AN INVESTIGATION OF ELECTRON TUNNELLING AND CONDUCTION IN LANGMUIR FILMS

by

Tariq Mahmood Ginnai

A thesis presented in part fulfilment
of the requirements for the Degree of
Doctor of Philosophy of the Council for
National Academic Awards

School of Physics,
Leicester Polytechnic,
LEICESTER.

SEPTEMBER, 1982.

ABSTRACT

AN INVESTIGATION OF ELECTRON TUNNELLING AND CONDUCTION IN LANGMUIR FILMS

Tariq Mahmood Ginnai

Langmuir films offer the possibility of obtaining uniform, well-ordered, insulating structures of defined and controllable thickness.

In this thesis, techniques for the fabrication of these films and the nature of the conduction process in single and multi-layer films of stearic acid/stearate sandwiched between metal electrodes (MIM devices) are discussed.

A sophisticated film fabrication system has been designed and implemented and methods necessary for obtaining films of high integrity established. Structural characterisation studies using various techniques demonstrate that the resultant films are uniform, of predictable composition and substantially free of defects.

In single layer MIM devices, detailed observations of the voltage and temperature dependence of the current suggest that the predominant conduction mechanism is direct electron tunnelling between the metal electrodes. This has been confirmed with the aid of additional experiments, including consideration of the role of the oxide film(s) invariably present in the completed device and investigation of the inelastic component of the tunnel current. It is argued that the latter provides unequivocal evidence that a significant proportion of all conduction is by electron tunnelling.

In multilayer (3-5 layers) MIM devices, the importance of Schottky emission as a mechanism for conduction has been confirmed through a careful examination of the current-voltage relationship and on the basis of the temperature dependence of the current at fixed voltage.

Finally, the techniques of Auger and X-ray photoelectron spectroscopy have been employed to provide further insight into the nature of film adhesion and composition. These observations, where possible, have been correlated with the results of electrical measurements.

ACKNOWLEDGEMENTS

The author would like to thank his supervisors, Dr.D.P.Oxley and Dr.R.G.Pritchard for invaluable guidance and encouragement in the course of this work. I am also indebted to numerous other members of the School of Physics, Leicester Polytechnic - in particular, thanks are due to :

Dr.R.E.Thurstans and Mr.Steve Reynolds for help and stimulating discussions and,

Mr. N.Bevan for assistance in the preparation of devices.

It is a pleasure also to acknowledge the advice and help of Dr.S.Proudfoot of the School of Pharmacy, Leicester Polytechnic.

The author wishes also to express his appreciation for the encouragement of Professor G.G. Roberts of the Department of Applied Physics and Electronics, University of Durham, and Mrs.S. Mellanby for her patience and expertise in the typing of this thesis.

My thanks are due to the Science Research Council for the award of a Research Studentship and to the Director and Governors of Leicester Polytechnic for the provision of laboratory facilities.

Finally, I am indebted to my wife and my parents for all the help, encouragement and support, I have received from them over the last few years.

CONTENTS

Pages

CHAPTER 1

INTRODUCTION

The subject of this thesis is the nature of the conduction process in mixed built-up films of stearic acid/stearic acid salts sandwiched between thin film metal electrodes (MIM structures).

These built-up films are fabricated (see Fig 1.1) by first introducing the material of interest onto an uncontaminated aqueous surface. If the material consists of ampliphilic molecules, e.g. fatty acids, then it may, under favourable conditions, form a monomolecular layer on the surface. With the application of suitable lateral compression, a monomolecular sheet may result with the molecules all aligned approximately normal to the surface and touching so as to allow Van der Waal's interactions along their lengths to form in effect,a two dimensional solid. If a suitable solid substrate is then dipped and withdrawn through the water surface, a film can be built up a monolayer at a time. Of course, as some of the monolayer is transferred onto the substrate, a system for maintaining the original state of compression or surface pressure (π) of the monolayer becomes necessary. The technique described offers a method of obtaining films of great precision for electrical studies. The films so formed have become known as Langmuir-Blodgett or Langmuir films (LF)(1-6).

Langmuir monolayers can be added sequentially, a monolayer at a time to give insulating films from about 2.5 nm in thickness to about 300 nm or so upwards. The main advantages in using Langmuir films for electrical studies derive from an accurate knowledge of their thickness, their high dielectric strength and the fact that they can be obtained in a form which is oriented, defect-free and uniform, even for thicknesses as low as 2.5 nm.

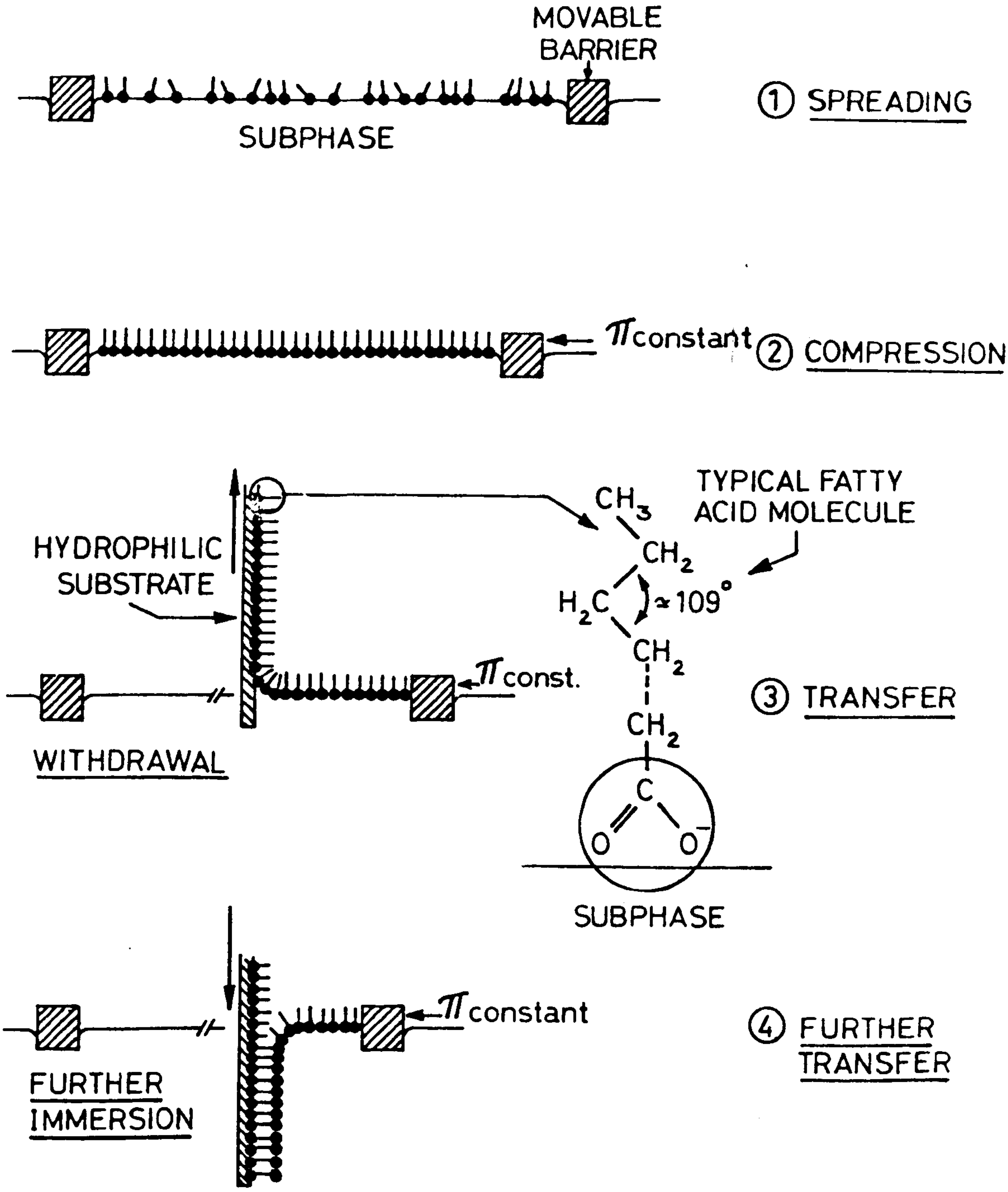

π = SURFACE PRESSURE = $\gamma_0 - \gamma$

γ_0 = SURFACE TENSION OF CLEAN SUBPHASE

γ = SURFACE TENSION OF SUBPHASE WITH SPREAD FILM

FIGURE 1.1 : Principle of Langmuir Film Fabrication

The electrical properties of thin insulating films are particularly sensitive to the twin parameters of uniformity of thickness and structural perfection. It is known that defects to an extent even as low as one part in 10^5 can significantly modify results$^{(7)}$. Studies on conventional insulating thin films, such as vacuum deposited films or metal oxides for the lower thickness range have suffered in the past from irreproducibility in results because of defects inevitably introduced into these films as a consequence of the fabrication processes$^{(8)}$. These problems become particularly acute when studying phenomena (e.g. tunnelling) which are of importance only in the thickness range below 10 nm. Although these conventional films have begun to yield more reliable results with improved understanding of the importance of conditions pertaining during preparation (i.e. with the understanding that the factors which determine the observed conductivity of these films are often extrinsic in nature) the Langmuir-Blodgett technique appears a most attractive method for obtaining films which are uniform, structurally oriented and with accurately known, controllable thickness. Also, since it is a low temperature deposition technique, it is anticipated that little or no thermal damage will be induced to the underlying substrate surface or the Langmuir film itself. These advantages over conventional insulating films are offset however, in practice, by one or two limitations.

In the first instance, meticulous care in fabrication is required if good quality films are to result. With the improved sophistication in Langmuir-film fabrication methods which has become available recently, this is now a tractable (although still a little daunting) task, as the increasing reproducibility in experimental results testifies.

Secondly, and this still forms a major bone of contention amongst workers, every MIM device incorporating a Langmuir film that has been fabricated to-date, has invariably had a metal oxide built into the structure, i.e. it has been found impossible to fabricate defect-free M-LF-M devices using non-reactive base metal films such as gold.

The presence of an oxide film in the system is not however uniform in its significance across the broad spectrum of electrical investigations that have been carried out on Langmuir films up until now. This point, viz. the significance of the oxide film receives particular attention at the relevant place in this thesis.

The major work on the electrical properties of Langmuir films has been performed on what have come to be known as conventional Langmuir films consisting of fatty acid systems (the term 'fatty acid' here is used in a general sense to include their salts). This may be due to the fact that the Langmuir-Blodgett technique was originally pioneered using these materials. However, not only do fatty acids (with some obvious limitations of the size of the long chain molecule) possess all the essential properties for spreading into a monolayer and its subsequent transfer onto a solid substrate, but they are also good insulators with, as has been mentioned already, high breakdown strengths(6). For these reasons, in the work to be described, stearic acid/metal stearate has been the Langmuir film system employed for study. It is interesting to note, however, that very recently the electrical properties of a number of unconventional materials have also been studied. These studies, on materials which range from unconventional long chain molecules(9) to lightly substituted aromatics(10) have opened up the exciting possibility of several new technological applications. The whole field of potential applications of Langmuir films (using both conventional and unconventional materials) has been extensively reviewed recently(11) and is also the subject of a brief discussion in the concluding chapter of the present work.

Although, with the realisation that the use of Langmuir films offered several advantages in studying electrical phenomena, investigations were carried out as early as 1938, it was not until the last decade that meaningful results began to emerge. To place the present work in context, a brief review is given in the next section of the more important electrical measurements that have been reported on fatty acid Langmuir films.

1.1 BRIEF REVIEW OF ELECTRON TRANSPORT PROPERTIES

Considerable work has been done on the electrical properties of Langmuir films. These measurements can be discussed under the following broad headings (approximately following the scheme of Vincett and Roberts(11)).

(1) Electron transport phenomena in single layer Langmuir films.

(2) Conduction properties of multilayers.

(3) Dielectric properties including dielectric breakdown.

(4) Sporadic internal voltage effects within the M-LF-M structures.

(5) Properties of electroformed MIM junctions incorporating multilayer Langmuir films.

The present section is taken up with a brief review of the more important contributions in the field. Only those measurements which have direct relevance are discussed - more general and rather more comprehensive reviews can be found in the literature(11). Dielectric properties, internal voltage and electroforming are discussed at relevant places in the thesis.

1.1.1 Electron Transport Properties of Single Layer Langmuir Films

The earliest reported measurements on electron transport phenomena in single layer Langmuir films are due to Miles and McMahon(12). With the use of thin oxide films grown on metal films to provide insulating spacers for studying electron tunnelling by Giaver and Megerle(13), it was soon realised that all the necessary requirements could perhaps be fulfilled more elegantly by Langmuir films. Miles and McMahon utilised a monolayer of barium stearate as an insulating spacer between tin-lead and tin-indium metal electrodes. They found, however, an irreproducible and strongly time-dependent device resistivity. These experiments, although obviously limited by the effects of film imperfections (the Langmuir-Blodgett technique was still being developed) nevertheless stimulated other investigations into the nature of the conduction process in Langmuir films.

Handy and Scala(14) and Horiuchi et al(15) subsequently carried out extensive studies on various Langmuir film MIM systems. Again, reproducibility of results was found to be poor. Interpretation of these results was made in terms of a combination of tunnelling and Schottky emission effects.

The only detailed studies carried out on superconductive tunnelling effects in Langmuir films are those reported in an unpublished internal report due to Clark(16) who interpreted superconductive tunnelling characteristics on the basis of a simple one-dimensional model of the energy spectrum of a superconductor proposed in the BCS theory(17) and found good agreement with the model. However, in common with other reported electrical measurements up until that period in time, quite a large scatter in the results was observed. Incidentally, Giaver himself did conduct some preliminary experiments utilising Langmuir films as tunnelling spacers but was not entirely convinced that the role of the substrate metal oxide was insignificant(18).

It was not until the last decade that the monolayer transfer technique had progressed to the stage,where for the first time, quantitative substantiation of the tunnelling mechanism in single layer Langmuir films was allowed. This was due in large measure to the experiments of Kuhn and co-workers(7,19), who demonstrated for the first time the exponential dependence of the tunnelling conductivity on Langmuir film thickness. By analysing their data in terms of the tunnelling model proposed by Sommerfield and Bethe (see Chapter 2) and after arguing that the thin oxide film on the base metal film in the MIM system did not affect the results too significantly, Kuhn and his co-workers succeeded in obtaining work function values which were in good agreement, within experimental error, with those determined from relevant photoelectric measurements. The effects expected due to changes in electrode material were also confirmed by experiment. Kuhn and co-workers began their analysis by assuming that each insulator had a total conductivity made up of some impurity-dependent conductivity (more significant with larger film thicknesses) and a tunnelling component of the total conductivity and separating out the two contributions. They were able to conclude that imperfections in their films (to an extent as low as covering one part in 10^5 of the area) were largely absent.

The work of Kuhn and co-workers has been extended by Polymeropoulos(20) to a wider range of film thickness. He demonstrated an essentially temperature independent conductivity which again shows an exponential dependence on film thickness. The impurity-dependent component of the total conductivity was found however to be negligible in contrast to the results of Mann and Kuhn(7). This difference has been attributed by Vincett and Roberts(11) to effects related to the different ambients in which measurements were made; a conclusion which is confirmed by the work of Honig(21).

Evidence for tunnelling at low applied bias and low temperature has been presented by Leger et al(22) who used organic films of cyanine with two grafted stearic chains. They demonstrated the expected modification in the I-V characteristic when an electrode becomes superconducting.

Since the start of the present work, other workers(23) have confirmed experimentally the theoretically predicted dependence of the tunnelling current on applied voltage and temperature. Roberts et al(24) however, have found an unusual $\log J \propto V^{1/4}$ relationship for single layer arachidate films. A similar dependence has been observed previously for thicker films(25) where it was attributed to interfacial Schottky barriers influenced by image force effects. However, Roberts et al point out that this mechanism is precluded as an explanation of their results as these were found to be essentially temperature and field-polarity independent whereas the mechanism predicts a substantial dependence on these parameters. Such a mechanism would also predict considerable deviations from a $V^{1/4}$ law for low voltages and thus our understanding remains incomplete.

1.1.2 Conduction Properties of Multilayers

The low field ($\lesssim 10^7$ V m^{-1}) conduction properties of fatty acid multilayers have received considerable attention from workers in the field. The current is found to be approximately proportional to the applied voltage(21,26-27). Most of the low field d.c. and low frequency a.c. results have been interpreted on the basis of conduction by hopping of carriers.

Workers are generally agreed that the conductivity shows an ω^n dependence on frequency with n between ~ 1 at low and room temperatures and ~ 0.5 at higher temperatures(26-27).

Sugi and co-workers(28-35) have been particularly active in the field. Their main findings may be summarised as follows :-

(1) Comparisons of the d.c. conductance(29) (obtained as a frequency-independent component of the a.c. admittance at low frequencies (10^{-1}-10^{-5}Hz) and low fields ($< 5 \times 10^6$ V m^{-1})) of fatty acid multilayers at liquid nitrogen temperatures with monolayer tunnelling(7) experiments suggest that the hopping distance corresponds to one monolayer rather than two (i.e.the repeat distance of the lattice) as proposed by other workers.

(2) The conductivity demonstrates an $\exp(-AT^{-\frac{1}{2}})$ dependence on temperature(30), which is consistent with a hopping carrier model.

(3) By producing synthetic disordered structures(31-33) and determining their conduction properties, they were further able to verify predictions of dispersion effects in conduction as a function of frequency - this is again consistent with a hopping carrier model(34).

(4) Peaks in the conductivity versus frequency characteristics for a single fatty acid system were obtained as expected(35) when the energies of the hopping electrons were clamped. They showed this by incorporating chromophores in the system, so that photo-excited electrons gave a sharp distribution in energy, and by then measuring the photo-induced a.c. conductance. The relationship between the critical frequencies and the film thickness was as predicted.

Jonscher and co-workers(26-27,36-41) report extensive measurements on stearic acid multilayers and have in fact distinguished two contributions to the a.c. conductivity(36-37).

The low frequency contribution to the conductivity ($\propto \omega^n$) was seen in terms of a hopping carrier model with carriers injected from the electrodes. Such a model is consistent with the observed electrode dependence of the d.c. and low frequency conduction process(36). The other contribution ($\propto \omega$) at $\omega >$ 1 Hz demonstrated temperature peaks which were identified with known phase transitions in the structures, i.e. this component is considered to be associated with the response of the lattice, mainly from the dipolar COOH group.

Before moving onto the high field conduction properties of multilayers, it should be noted that some workers(24,28) have reported an anomalous dependence of the a.c. conductivity on the number of monolayers. This is attributed to first-layer effects, i.e. the first monolayer or so is thought to demonstrate a higher conductivity than the rest.

TABLE 1.1 : Recent Observations on the Nature of the High Field Conduction Process in Langmuir Film Multilayers

Author(s)	Number of Monolayers N	Temperature Dependence	Polarity Dependence	Suggested Mechanism
Nathoo(42)	3-9			Schottky
Careem & Hill(23)	3-9	Temperature-activated characteristics		Schottky
	≥ 9	Temperature-activated characteristics	Weak only	Poole →Poole-Frenkel at high fields
Honig(21)	<15		Electrode-dependent currents	Schottky or Poole-Frenkel
Roberts et al(24)	≥ 3	Weak only	None	Poole-Frenkel

Roberts et al(24) have associated this with the presence of substrate metal ions in the insulator.

Early work into the nature of the high-field conduction process in Langmuir film multilayers was carried out by Handy and Scala(14) and Horiuchi et al(15). The observations of Handy and Scala for film thicknesses in the range N ≈ 1-9 (where N is the number of monolayers) seemed to suggest that electron tunnelling at small thicknesses probably gave way to thermionic emission at higher temperatures and larger thicknesses.

The other group(15) found a nearly temperature independent current below 200 K which became strongly temperature dependent above that temperature. This behaviour,however, was modified when the field polarity was reversed, suggesting that a tunnelling mechanism at lower temperatures probably gave way to Schottky emission as the temperature was increased.

More recently, workers have usually interpreted high field conduction in terms of either the Schottky effect or for the larger thicknesses, the Poole-Frenkel mechanism. All these investigations have demonstrated $\log J \propto V^{\frac{1}{2}}$ behaviour and are best summarised in Table 1.1.

1.2 COMMENTARY

It may seem to appear from the foregoing that a reasonably clear picture of the nature of the conduction process in Langmuir single and multilayer films has begun to emerge-especially so with regard to low field conduction in multilayer films. However, considerable disagreements still exist among workers in the subject and there are areas where little or no work has been done. This section aims to delineate some of these.

1.2.1 Electron Transport in Single Layer Films : Tunnelling

The evidence for this comes mainly from the experiments of Mann and Kuhn(7) and Polymeropoulos(20) with regard to the thickness dependence of the low field conductivity of single layer films. Further substantiation of the tunnelling mechanism comes from those experiments where one or both electrodes have been made superconducting (16,22) ; usually regarded as the unequivocal test.

Criticism of this evidence usually centres around the role of the inevitable oxide film in the system (43). It is generally recognised that this oxide layer is subject to wide variations depending on how it is formed. If the Langmuir film has pinholes, it is possible to form small area metal-oxide-metal structures which would yield results essentially similar to those of Giaver and Megerle (13) in those experiments where superconducting electrodes are used as a diagnostic test for electron tunnelling. It is also worth noting incidentally that these experiments would provide evidence of tunnelling only for low biases and temperatures. Furthermore, Gundlach and Kadlec (44) have attributed the non-linearity in the I-V characteristic found by many workers (22,44) at low biases ($\approx$ 50 mV) to additional conductance channels being opened up due to impurities in the oxide film in series with the Langmuir film monolayer. Normal tunnelling theory would predict a linear current-voltage relationship in this region of the characteristic . The role of the oxide film is thus an additional factor to consider when interpreting results.

In view of the above comments regarding tunnelling in single layer Langmuir films therefore, experiments were conducted accordingly to provide a fuller substantiation of the mechanism in barium stearate films. This was done through detailed investigations of :-

(1) the temperature and voltage dependence of the tunnelling current in MIM structures with and without (to determine the role of the oxide film) incorporated Langmuir films.

(2) the inelastic component of the tunnelling current for a bias extended up to ∿ 500 mV (Inelastic Electron Tunnelling Spectroscopy or IETS) and at liquid helium temperatures,

The theoretical rationale for these themes is developed in Chapter 2 with the experimental evidence presented in Chapter 5.

1.2.2 Conduction in Multilayers

Previous evidence from high field measurements points to injection limited conduction via the Schottky mechanism(21,23,42) or in other cases and for thicker films, to bulk-limited processes via the Poole(23) or Poole-Frenkel effects(21,23-24). These previous measurements have been extended through consideration of the temperature dependence of the current-voltage characteristic and results are presented in Chapter 6. The physics of the processes is developed in Chapter 2.

1.2.3 Structural and Other Considerations

The nature of the conduction process will obviously depend critically on the method of preparation of the films and on the conditions pertaining during measurement. The pH and ionic concentration of the subphase will determine the percent conversion of acid to the equivalent salt(10-12,45) and thus govern stability of the multilayer. The surface pressure during deposition may well be another factor to consider(14). Significant variations may also arise from the different ambients in which films have been tested(11) and possible removal of film in vacuum is another possibility(4,6). It is obvious therefore that a substantial part of the present work involved investigation of the fabrication of films (Chapter 3) and their characterisation. Accordingly, detailed investigations of the composition of these films was carried out using X-ray Photoelectron Spectroscopy (XPS) and Auger Electron Spectroscopy (AES). These results, where possible, were correlated with the results of electrical investigations and in particular the IETS results and are presented in Chapter 7.

Thus, to summarise, the aims of the present work were set out as :-

(1) Establish techniques for the fabrication of M-LF-M structures.

(2) Characterise these films and where possible correlate results of structural investigations with results obtained from electrical measurements.

(3) Study the electron transport phenomena in these structures with especial regard to :-

(a) electron tunnelling in thinner films, including the role of the oxide film and

(b) conduction in thicker films through consideration of the temperature dependence of the current-voltage relationship.

CHAPTER 2

THEORETICAL ASPECTS OF CONDUCTION IN THIN INSULATING FILMS

This chapter will attempt to provide the theoretical basis for the present work. Of the various mechanisms that have been invoked to explain d.c. conduction in thin insulating films, it is generally believed (see Chapter 1) that electron tunnelling predominates in the case of single layer Langmuir films, whilst in the case of multilayer films at high applied fields charge transport is much more likely to be due to the Schottky effect or its bulk analogue, the Poole-Frenkel effect. At low applied fields other conduction mechanisms will be of significance, but as the low-field conductivity properties of multilayer Langmuir films are already well documented, the present study of d.c. conduction in Langmuir film multilayers was restricted to the high field regime. Consequently, this chapter begins by considering electron tunnelling across a simple hypothetical rectangular barrier potential before extending the theory to tunnelling in a MIM junction. Since under certain circumstances, a tunnelling electron may make an inelastic transition across the barrier, inelastic electron tunnelling (IET) and the spectroscopic technique to which it gives rise (IETS) is also discussed at this stage. The final section in this chapter examines the physics underlying the Schottky and Poole-Frenkel effects.

The applicability and relevance of the results of this chapter to the present work are discussed in Chapters 5 and 6 when the experimental results are presented.

2.1 BASIC CONCEPTS OF ELECTRON TUNNELLING

Consider the simple, rectangular barrier potential illustrated in Fig 2.1. This potential is

$$\begin{aligned} V(x) &= V_o \quad ; \quad o < x < a \\ V(x) &= 0 \quad ; \quad x < o,\ x > a \end{aligned} \tag{2.1}$$

According to classical mechanics, an electron of total energy E in region I incident upon the barrier in the direction of increasing x, will have unity probability of being reflected if $E < V_o$ and unity probability of being transmitted if $E > V_o$. Neither of these conclusions obtains in quantum mechanics.

The equation that conveniently describes the behaviour of the electron is the time independent Schrödinger equation viz,

$$-\frac{\hbar^2}{2m} \frac{\partial^2\psi(x)}{d\,x^2} + V(x)\,\psi(x) = E\psi(x) \tag{2.2}$$

where $\psi(X)$ is the electron wave function, m is the electron mass and V(x) is the potential in which the electron moves.

Considering only the case when $E < V_o$, the general solutions of this equation in the regions I, II and III are,

$$\left.\begin{aligned} &\text{I} & \psi_1(x) &= Ae^{ik_1x} + Be^{-ik_1x}, & x &< 0 \\ &\text{II} & \psi_2(x) &= Ce^{-k_{11}x} + De^{k_{11}x}, & 0 &< x < a \\ &\text{III} & \psi_3(x) &= Fe^{ik_1x} + Ge^{-ik_1x}, & x &> a \end{aligned}\right\} \tag{2.3}$$

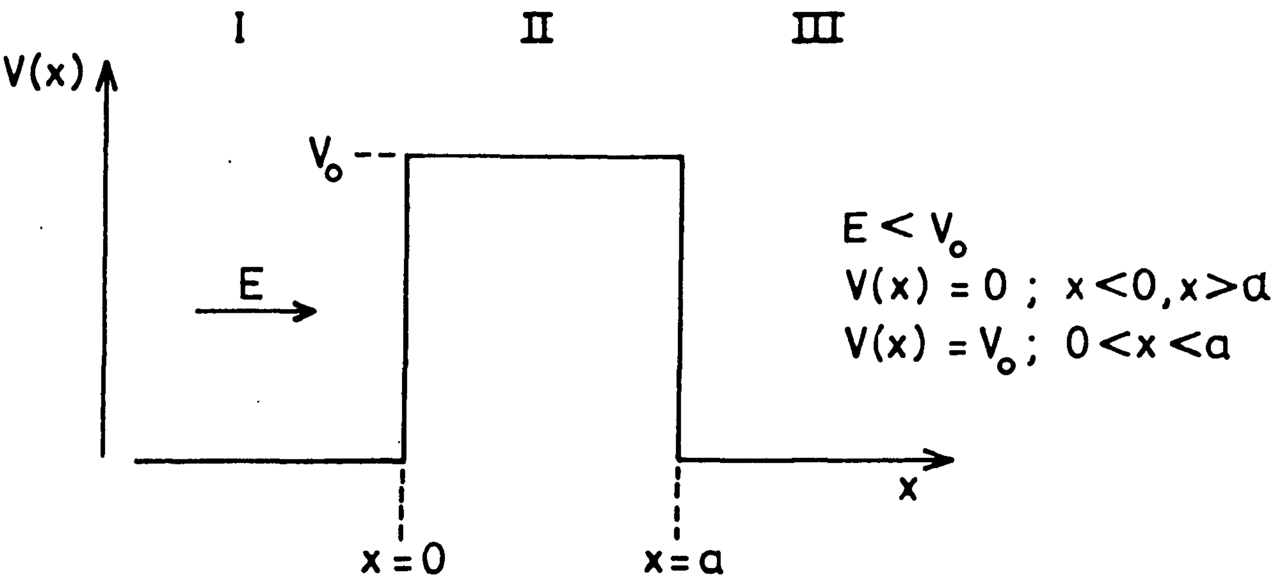

Fig 2.1: An electron with total energy E incident upon a hypothetical rectangular barrier potential.

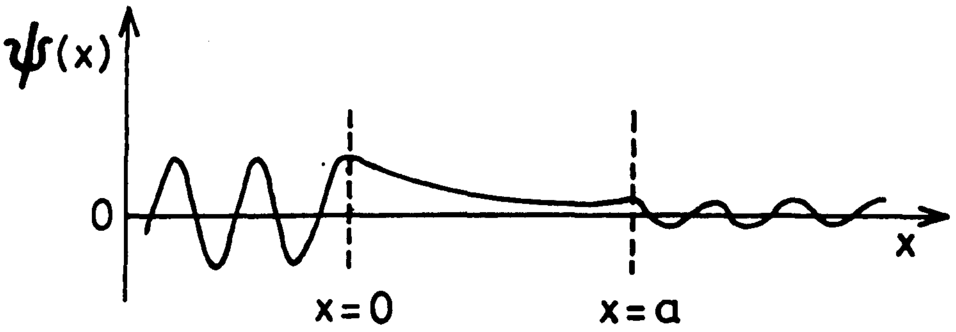

Fig 2.2: Real part of the barrier penetration eigenfunction (after Eisberg$^{(1)}$).

where k_1 and k_{11} are propagation numbers and may be written

$$k_1 = [2mE/\hbar^2]^{\frac{1}{2}} \quad ; \quad k_{11} = [2m(V_o - E)/\hbar^2]^{\frac{1}{2}} \qquad (2.4)$$

In evaluating the motion of an electron incident in the direction of increasing x, G may be set equal to zero since there can only be a transmitted wave in region III$(x > a)$. However, in the present situation D cannot be set equal to zero also, since the solution must satisfy the continuity condition that $\psi(x)$ remain finite in region II. By applying the continuity conditions which require that $\psi(x)$ and $\partial\psi(x)/dx$ be everywhere finite and continuous, the constants B, C, D and F may be determined in terms of A. The form of the eigenfunction obtained is indicated in Fig 2.2. This is meant to be only an indication however, since the exact form of $\psi(x)$ in region II as well as the ratio of its amplitude in region III to its amplitude in region I depends on the values of E, V_o, a and m. Furthermore, $\psi(x)$ is of course actually a complex function whereas in the figure only the real part of $\psi(x)$ has been plotted.

The most interesting result of the calculation is the probability of an electron being transmitted through the barrier. The transmission coefficient T is defined in terms of the intensity of the probability flux transmitted into region III and the intensity of the incident probability flux. The probability flux is the probability per second of finding the electron at a particular reference point and is proportional to both the velocity of the electron and the intensity of the wave at that point. Hence the transmission coefficient, as defined by Eisberg(1), is

$$T = \frac{v F^* F}{v A^* A} \qquad (2.5)$$

where v is the group velocity and F^* and A^* are the complex conjugates of F and A respectively. Substituting the values of F and A into (2.5) results in the following expression,

$$T = \left[1 + \frac{\left(e^{k_{11}a} - e^{-k_{11}a} \right)^2}{16 \frac{E}{V_o} \left(1 - \frac{E}{V_o} \right)} \right]^{-1} , \quad E < V_o \qquad (2.6)$$

which is

$$T = \left[1 + \frac{V_o^2}{4E} \; \frac{\sinh^2 k_{11}a}{(V_o - E)} \right]^{-1} , \quad E < V_o \qquad (2.7)$$

If $E << V_o$ and if the barrier is not too thin, the expression is further simplified to

$$T \approx 16 \frac{E}{V_o} \left(1 - \frac{E}{V_o} \right) e^{-2k_{11}a} \qquad (2.8)$$

These equations thus predict that an electron of total energy E, which is incident on a potential barrier of height $V_o > E$ and finite thickness a, actually has a certain probability T of penetrating the barrier and appearing on the other side. The electron is said to have tunnelled through the barrier. Of course, T is vanishingly small in the classical limit because then the exponent of the exponential term in (2.8) is extremely large. Simple calculation shows that for $V_o = 4$ eV and $E = V_o/10$, when a = 1 nm, T is equal to 8.5×10^{-5} ; when a = 10 nm, T is equal to 10^{-42} !

The discussion in this section has attempted to provide some physical insight into the nature of quantum-mechanical tunnelling by using the simple model of an electron incident upon a finite barrier potential. The extension of this model to the real case of tunnelling in a metal-insulator-metal junction forms the subject of the next section.

2.2 ELASTIC ELECTRON TUNNELLING IN METAL-INSULATOR-METAL JUNCTIONS

There is a considerable literature available on electron tunnelling in MIM junctions but for the present it will be sufficient to refer to the comprehensive review by Duke(2). The theoretical approach to the problem is formulated by examining the density of states and Fermi functions for the metals in addition to what has been dealt with above.

2.2.1 Basic Formulation

Consider the energy diagram (Fig 2.3) of a MIM junction at OK with a bias voltage V applied between the electrodes. This causes the Fermi energies E_{F1} and E_{F2} of the metals to separate by an amount eV. Here $Z_1(E)$ and $Z_2\ (E)$ represent the density of electron energy states in the metals with the occupied states denoted by the shaded regions.

The elastic tunnelling of electrons in a MIM junction involves the transfer of electrons, without loss of energy, from occupied states in one metal to unoccupied states in the other. In the situation represented by Fig 2.3, the number of electrons per unit time available for tunnelling from metal 1 to metal 2 with energies in the incremental range dE is proportional to the number of occupied states in metal 1, namely

$$Z_1\ (E)\ f\ (E) \tag{2.9}$$

where f(E) represents the Fermi distribution function and energies are measured using the Fermi energy of metal 1 as origin. The number of tunnelling electrons is also proportional to the number of unoccupied states in metal 2,

$$Z_2\ (E + eV)\quad [1 - f(E + eV)] \tag{2.10}$$

If the probability of transfer across the barrier is denoted by $P_{1-2}(E)$,

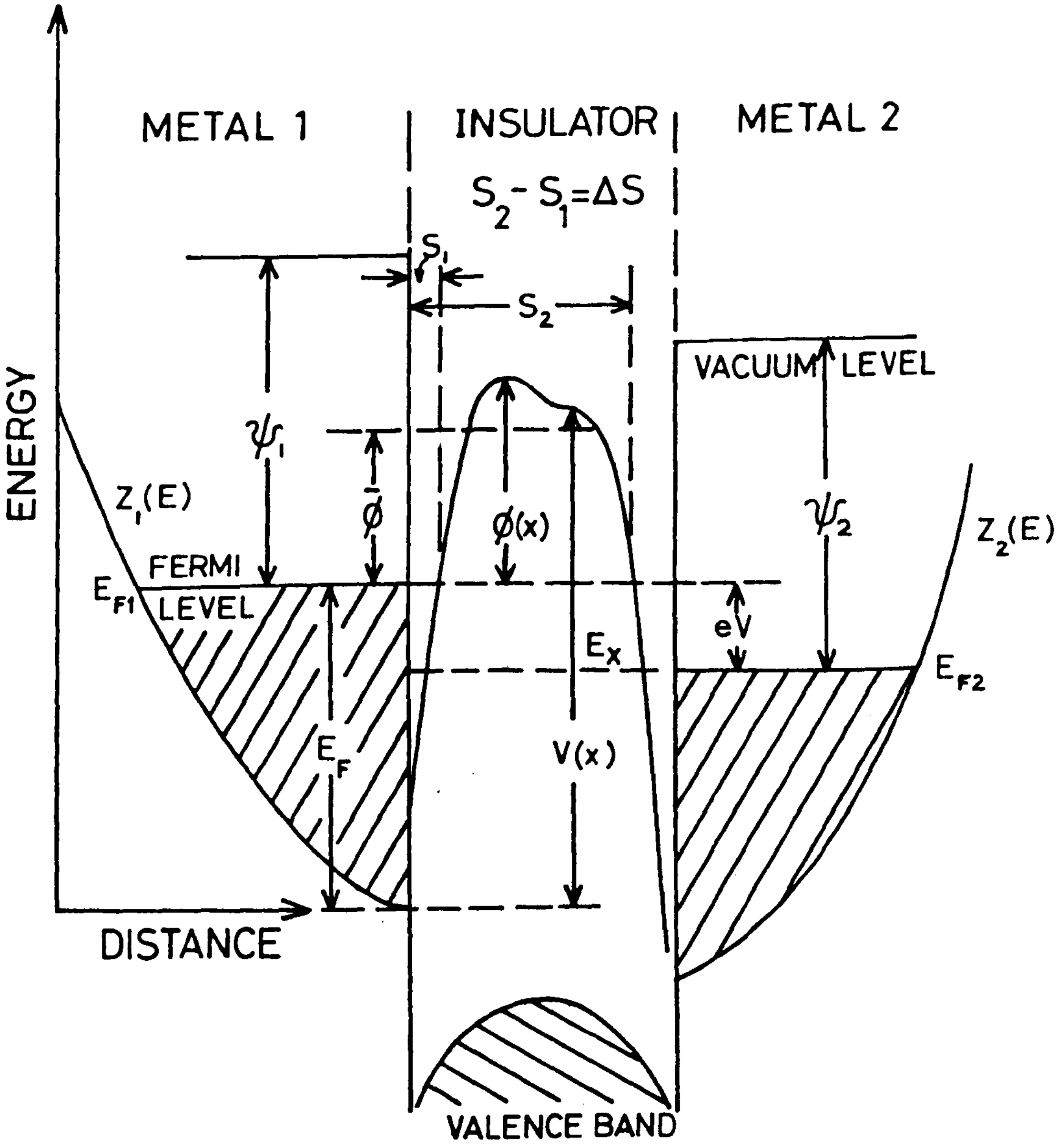

Fig 2.3: Schematic Representation of a general practical barrier in a MIM junction at temperature 0 K and with a negative voltage V applied to metal 1, $\bar{\phi}$ represents the mean metal-insulator interfacial barrier height and ψ refers to the metal work function. Other symbols are defined in the text (modified after Simmons(8)).

then the incremental current dI, from metal 1 to metal 2 can be written as

$$dI_{1-2} \propto P_{1-2}(E)\ Z_1(E)\ Z_2(E + eV)f(E)[1-f(E + eV)]\ dE \qquad (2.11)$$

A similar expression can be obtained for the incremental tunnel current dI_{2-1} in the opposite direction. Thus

$$dI_{2-1} \propto P_{2-1}(E)\ Z_1(E)\ Z_2(E + eV)f(E + eV)[1 - f(E)]dE \qquad (2.12)$$

Assuming that an electron has the same probability of tunnelling in either direction, so that

$$P_{1-2}(E) = P_{2-1}(E) = P(E) \qquad (2.13)$$

the net total tunnelling current is given by

$$I = I_{1-2} - I_{2-1} \propto \int P(E)Z_1(E)Z_2(E + eV)[f(E)-f(E + eV)]dE \qquad (2.14)$$

Since the current will be mostly due to electrons with energy $E \approx E_F$, the density of states functions can be taken as slowly varying functions and their values can be taken as those at the Fermi energy, i.e,

$$Z_1(E) \approx Z_1(0)$$

$$Z_2(E + eV) \approx Z_2(E) \approx Z_2(0)$$

By making the further assumption that P(E) is independent of energy for small applied voltages, equation (2.14) may be written as

$$I \approx A\ P\ Z_1(0)Z_2(0) \int [\ f(E) - f(E + eV)]\ dE \qquad (2.15)$$

where A is a constant. Furthermore, for small applied voltages, the Fermi functions can be expressed as

$$f(E) - f(E + eV) \simeq - eV \frac{df}{dE} \qquad (2.16)$$

and if $\frac{df}{dE}$ is approximated by a delta function, then equation (2.15) reduces to

$$I \simeq A\ P\ Z_1(0)\ Z_2(0)\ eV \qquad (2.17)$$

i.e. the tunnel current increases linearly with applied voltage for small applied voltages and temperature T = 0 K.

The above discussion serves as a useful introduction to the theory of inter-electrode tunnelling in MIM junctions. However, it is more usual to express tunnelling in terms of the current density. This is given by the number of electrons incident upon the barrier, per unit area per second, multiplied by the probability that tunnelling will occur. Consider first the tunnelling of electrons in the x direction from metal 1 to metal 2. Now, the number of quantum states in the elemental volume of momentum space $dp_x\ dp_y\ dp_z$ is given by$^{(3)}$

$$\frac{2m^3}{h^3}\ dv_x\ dv_y\ dv_z \qquad (2.18)$$

where v_x, v_y and v_z are components of electron velocity in the x, y, z directions. Of these states, a fraction f(E) are expected to be occupied. Thus, the total number of electrons per unit volume in the electrode is

$$\int_{-\infty}^{\infty}\int_{-\infty}^{\infty}\int_{-\infty}^{\infty} \frac{2m^3}{h^3}\ f(E)\ dv_x\ dv_y\ dv_z$$

Denoting the transition probability by $P(E_x)$, then the rate at which electrons tunnel through unit area normal to the x direction is

$$N_{1-2} = \frac{2m^3}{h^3} \int_{-\infty}^{\infty}\int_{-\infty}^{\infty}\int_{-\infty}^{\infty} f(E) \quad P(E_x) \; v_x \, dv_x \, dv_y \, dv_z \qquad (2.19)$$

This integral may be simplified by putting

$$mv_x \, dv_x = d\,E_x$$

and converting to spherical polar coordinates where$^{(3)}$ $dv_y \, dv_z$ can be written $v_r \, dv_r \, d\Theta$. Here v_r denotes the radial component of electron velocity in a plane normal to the direction of tunnelling. Thus, equation (2.19) becomes (assuming momentum conservation in the plane of the junction).

$$N_{1-2} = \frac{2m}{h^3} \int_0^{\phi} P(E_x) \; dE_x \int_0^{\infty}\int_0^{vf} f(E) \, dv_\Theta \, dE_r \qquad (2.20)$$

which in turn simplifies to

$$N_{1-2} = \frac{4\pi m}{h^3} \int_0^{\phi} P(E_x) \; dE_x \int_0^{\infty} f(E) \; dE_r \qquad (2.21)$$

where ϕ is the metal-insulator interfacial barrier height and E_r denotes the radial component of electron energy in a plane normal to the direction of tunnelling.

Thus the current density J_{1-2}, due to electrons tunnelling from metal 1 to metal 2 is given by

$$J_{1-2} = \frac{4\pi me}{h^3} \int_0^{\phi} P(E_x) dE_x \int_0^{\infty} f(E) \; dE_r \qquad (2.22)$$

Similarly, the current density J_{2-1}, due to electrons tunnelling in the opposite direction can be calculated. Hence, the net current density is given by

$$J = J_{1-2} - J_{2-1} = \frac{4\pi me}{h^3} \int_0^{\phi} P(E_x)dE_x \int_0^{\infty} [\, f(E)-f(E + eV)]dE_r \qquad (2.23)$$

which assumes that $P(E_x)$ is the same in both directions.

It is necessary at this stage to consider the transmission coefficient $P(E_x)$ in more detail. Denoting the amplitudes of the waves associated with the electron at the first and second interfaces of the barrier by ψ_o and ψ_1 respectively, then

$$P(E_x) = (\psi_1/\psi_o)^2 \qquad (2.24)$$

The time-independent Schrödinger wave equation can be written

$$\frac{\partial^2\psi(x)}{\partial x^2} - \frac{2m}{\hbar^2} [\, V(x) - E_x] \, \psi(x) = 0 \qquad (2.25)$$

Putting

$$k^2(x) = \frac{2m}{\hbar^2} [\, V(x) - E_x] \qquad (2.26)$$

equation (2.25) becomes

$$\frac{\partial^2\psi(x)}{\partial x^2} - k^2 (x) \, \psi(x) = 0 \qquad (2.27)$$

Assuming a solution of the form

$$\psi(x) = a \exp - f(x)$$

equation (2.27) then becomes

$$\frac{-\partial^2 f(x)}{\partial x^2} + \left(\frac{\partial f(x)}{\partial x}\right)^2 - k^2(x) = 0 \tag{2.28}$$

Here the analysis follows other workers$^{(3)}$ and considers that f(x) is a slowly varying function of x. Thus

$$\frac{\partial f(x)}{\partial x} = k(x)$$

and therefore

$$\psi(x) = a \exp - \int k(x)\, dx$$

Thus, if the limits of the barrier occur at $x = s_1$ and $x = s_2$ (see Fig 2.3) then

$$P(E_x) = \exp \left\{ -2\left(\frac{2m}{\hbar^2}\right)^{\frac{1}{2}} \int_{s_1}^{s_2} [V(x) - E_x]^{\frac{1}{2}}\, dx \right\} \tag{2.29}$$

Furthermore, returning to the model in Fig 2.3, it can be seen that the potential at any point on the surface of a barrier of arbitrary shape may be expressed by

$$V(x) = E_F + \phi(x)$$

where E_F is the Fermi energy of metal 1.

Thus, equation (2.29) may be written,

$$P(E_x) = \exp\left\{ - 2 \left(\frac{2m}{\hbar^2}\right)^{\frac{1}{2}} \int_{s_1}^{s_2} [\, \phi(x) + E_F - E_x]^{\frac{1}{2}}\, dx \right\} \qquad (2.30)$$

This is known as the WKB approximation to the transmission coefficient and has been discussed by various authors$^{(4)}$. The value of the transmission coefficient calculated from the WKB approximation has been compared with values obtained from a direct numerical solution of the wave equation for tunnelling through insulating films for a range of particle energies (see reference 3). It was concluded that the WKB approximation to the transmission coefficient is acceptable for low fields and electron energies approximately equal to the Fermi energy.

2.2.2 Models of Interelectrode Tunnelling in MIM Junctions : An Overview

Several authors have discussed the solution of equations (2.23) and (2.30) for MIM tunnelling. The earliest calculations were made by Frenkel$^{(5)}$. Since the integral in (2.30) cannot in general be evaluated in a closed form, approximations of one form or another must be made. One approach, developed by Sommerfield and Bethe$^{(6)}$ and Holm$^{(7)}$, is to simplify $\phi(x)$ by substituting a rectangular barrier of height equal to the average of $\phi(x,V)$. More recently, Simmons$^{(8-11)}$ generalised Holm's concept of the average height approximation and extended it to an arbitrary barrier shape, and symmetric (equal electrodes) as well as asymmetric potential barriers. Another method, basically running parallel to that of Holm and Simmons and giving substantially similar results is due to Chow$^{(12)}$.

An alternative to the Holm-Simmons-Chow approach to the evaluation of equation (2.30) is to expand the integral in a Taylor series with respect to $(E_F - E_x)^{(13)}$. This expansion is justified if the tunnel current is due predominantly to electrons with $E_x \simeq E_F$. This was the approach used by Stratton(14) in deriving general tunnel formulas for MIM tunnelling. In particular, Stratton's model considers a broader class of arbitrary barrier shapes and temperatures than Holm's or Simmons', and is therefore necessarily more complicated.

Whatever the approximations and errors (and a number are evident in the literature), the functional form of the current-voltage dependence is the same in all cases. Both the Holm-Simmons-Chow approach and Stratton's are equivalent at T = 0 K and V → 0. Furthermore, Simmons introduced a temperature-dependent distribution function in his generalised model(10-11) and obtained temperature dependence identical to the Stratton model.

An outline of the Simmons' method(8-9) for evaluating the current density for a barrier of arbitrary shape will be presented in the next section. These generalised results will then be applied to an idealised rectangular barrier shape for both symmetric and asymmetric MIM junctions to obtain analytical expressions relating J and V. Section 2.24 is taken up with a discussion of Stratton's approach and where practicable, his results are compared with the Simmons' model.

2.2.3 The Simmons Generalised Model

Returning to the model in Fig 2.3, Simmons first step is to replace $\phi(x)$ in equation (2.30) with a mean barrier height. This is defined by

$$\bar{\phi} = 1/\Delta s \int_{s_1}^{s_2} \phi(x)\, dx \qquad (2.31)$$

where $\Delta s (= s_2 - s_1)$, is the width of the potential barrier at the Fermi level of the cathode (metal 1).

Equation (2.30) yields (after integration)

$$P(E_x) \approx \exp\left[- A(\bar{\phi} + E_F - E_x)^{\frac{1}{2}} \right] \tag{2.32}$$

where $A = [4\pi\beta(\Delta s/h)]\ (2m)^{\frac{1}{2}}$ and β is a function of the barrier shape, approximately equal to unity. Equation (2.23) can now be solved yielding (at T = 0 K)

$$J = J_o\{ \bar{\phi} \exp - (A\bar{\phi}^{\frac{1}{2}}) - (\bar{\phi} + eV)\exp[-A(\bar{\phi} + eV)^{\frac{1}{2}}]\} \tag{2.33}$$

where $J_o = e/2\pi h(\beta\Delta s)^2$.

For the case of very low voltages, this equation can be further simplified. Since $eV \ll \bar{\phi}$, it can be written as

$$J = J_o\ [\bar{\phi} - (\bar{\phi} + eV)\ (-A\ eV/2\bar{\phi}^{\frac{1}{2}})]\ \exp\ (-A\bar{\phi}^{\frac{1}{2}}) \tag{2.34}$$

Expanding $\exp(-AeV/2\bar{\phi}^{\frac{1}{2}})$ and neglecting terms containing V^2 and higher orders, equation (2.34) becomes

$$J = J_o[\bar{\phi} - (\bar{\phi} + eV)\ (1 - AeV/2\bar{\phi}^{\frac{1}{2}})]\exp\ (-A\bar{\phi}^{\frac{1}{2}})$$

$$J = J_o\ eV\ [(A\bar{\phi}^{\frac{1}{2}}/2) - 1]\ \exp\ (-A\bar{\phi}^{\frac{1}{2}})$$

Since $A\bar{\phi}^{\frac{1}{2}}/2 \gg 1$, this reduces to

$$J = J_L\ \bar{\phi}^{\frac{1}{2}}\ V \exp(- A\phi^{\frac{1}{2}}) \tag{2.35}$$

where $J_L = [\ (2m)^{\frac{1}{2}}/\Delta s]\ \ [e/h\ ]^2$

Equation (2.35) predicts that for applied biases $eV \ll \phi$, the J-V characteristic is ohmic.

Equation (2.33) is applicable to any shape of potential barrier providing the mean barrier height is known. If applied to the idealised rectangular barrier for a symmetric junction (Fig 2.4) the following results relating J and V are obtained$^{(15)}$.

When $eV \approx 0$,

$$J = \left(\frac{e^2 V}{h^2 s} \right) (2m\phi)^{\frac{1}{2}} \exp - \left[\frac{4\pi s}{h} \quad (2m\phi)^{\frac{1}{2}} \right] \qquad (2.36)$$

in general agreement with the Sommerfield-Bethe$^{(6)}$ result for $eV \ll \phi$.

When $eV < \phi$,

$$J = \left(\frac{e}{2\pi h s^2} \right) \left\{ \left(\frac{\phi - eV}{2} \right) \exp \left[- \frac{4\pi s}{h} (2m)^{\frac{1}{2}} \left(\frac{\phi - eV}{2} \right)^{\frac{1}{2}} \right] \right.$$

$$\left. - \left(\frac{\phi + eV}{2} \right) \exp \left[\frac{-4\pi s}{h} \quad (2m)^{\frac{1}{2}} \left(\frac{\phi + eV}{2} \right)^{\frac{1}{2}} \right] \right\} \qquad (2.37)$$

When $eV > \phi$,

$$J = \frac{2.2\ e^3 V^2}{8\pi h \phi s^2} \left\{ \exp \left[- \frac{8\pi s}{2.96\ heV} \quad (2m)^{\frac{1}{2}} \phi^{3/2} \right] \right.$$

$$\left. - \left(1 + \frac{2eV}{\phi} \right) \exp \left[- \frac{8\pi s}{2.96\ heV} \quad (2m)^{\frac{1}{2}} \phi^{3/2} \left(1 + \frac{2eV}{\phi} \right)^{\frac{1}{2}} \right] \right\} \qquad (2.38)$$

When $eV > \phi + E_F$,

$$J = \frac{2.2\ e^3 V^2}{8\pi h \phi s^2} \exp \left[- \frac{8\pi s}{2.96\ heV} \quad (2m)^{\frac{1}{2}} \phi^{3/2} \right] \qquad (2.39)$$

which, except for very small numerical differences is the same result

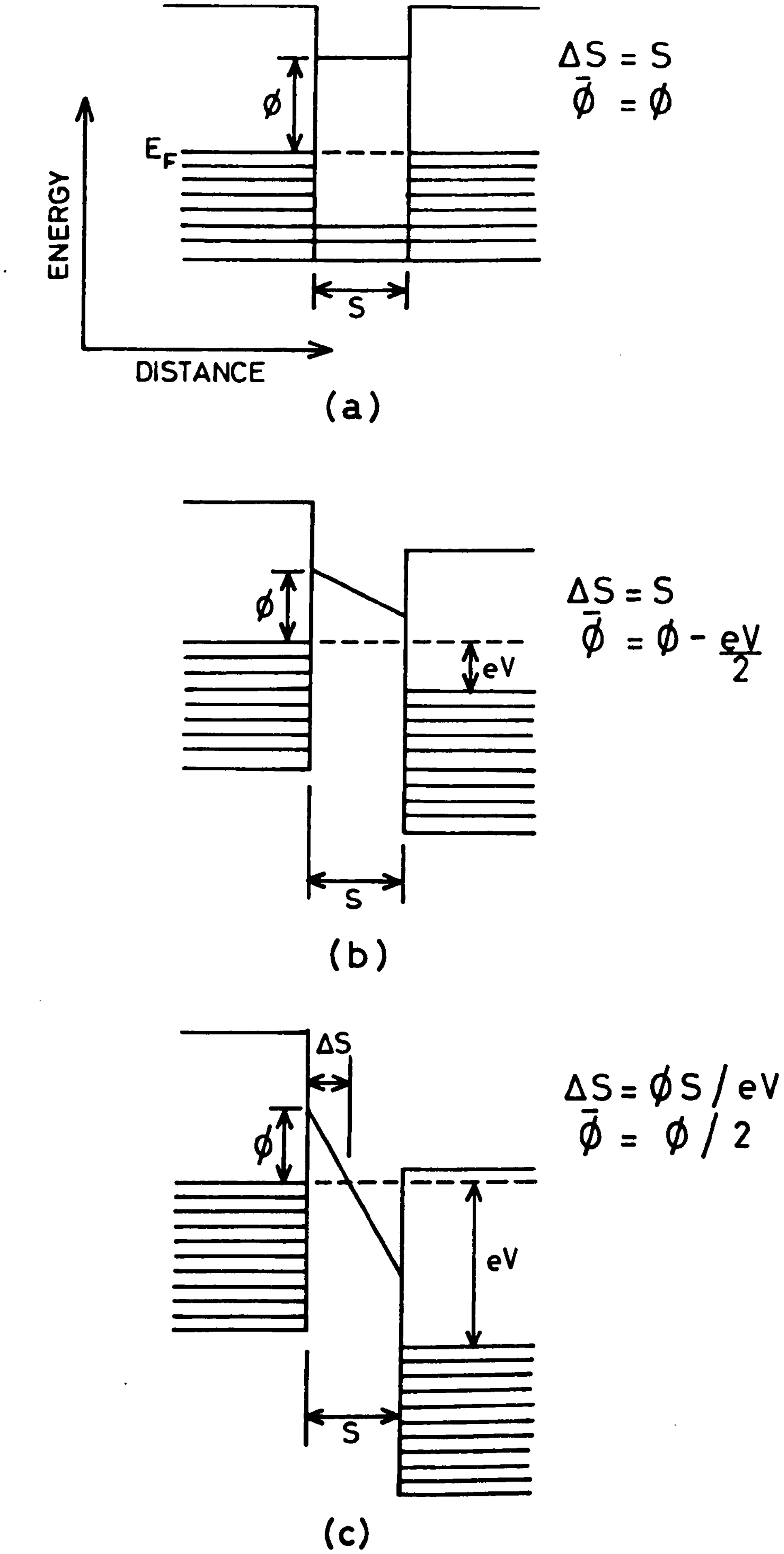

Fig 2.4: A rectangular potential barrier for a symmetrical MIM junction when (a) V = o, (b) eV < ϕ and (c) eV > ϕ (see text).

as the Sommerfield-Bethe(6) equation for this voltage range , and the Fowler-Nordheim(16) equation for tunnelling at very high fields.

If the junction is asymmetric, equation (2.33) is still applicable. Adopting the convention that any electrical characteristic is described as the forward characteristic when the electrode of lower work function is positively biased, and as the reverse characteristic if this electrode is negatively biased (see Fig 2.5), and denoting the reverse and forward current densities by J_1 and J_2 respectively, then the following results are obtained(9)

when $V \simeq 0$, $\bar{\phi} = (\phi_1 + \phi_2)/2$ and $\Delta s = s$. Equation (2.33) yields

$$J = \left[\frac{e^2}{h^2 s} \; m \; (\phi_1 + \phi_2)\right]^{\frac{1}{2}} V \; \exp\left[-\frac{4\pi s}{h} \, m^{\frac{1}{2}} \, (\phi_1 + \phi_2)^{\frac{1}{2}}\right] \qquad (2.40)$$

which predicts that the junction resistance is ohmic at very low voltages. When $0 \lesssim V \lesssim \phi_1/e$, $J_1 = J_2$ is obtained by substituting $\bar{\phi} = (\phi_1 + \phi_2 - eV)/2$ and $\Delta s = s$ in equation (2.33).

For $V > \phi_2$, J_2 is obtained by substituting $\bar{\phi} = \phi_2/2$ and $\Delta s = s\phi_2/(eV + \Delta\phi)$ where $\Delta\phi = (\phi_2 - \phi_1)$. J_1 is given by using $\bar{\phi} = \phi_1/2$ and $\Delta s = s\phi_1/(eV - \Delta\phi)$. Thus $J_1 \neq J_2$ and the J-V characteristic is asymmetric. For very high voltages, the familiar Fowler-Nordheim(16) form is again obtained.

Current-voltage characteristics for asymmetric junctions have also been calculated by Hartman(17) who has pointed out some errors in Simmons' treatment. He has shown that in fact rectification effects can be expected even at low voltages for rectangular barriers.

It is interesting to consider the result for the intermediate voltage range $V < \phi/e$ for the symmetric barrier in more detail. The calculations of Sommerfield and Bethe(6) were extended to this voltage range by Holm(7). His expression for this range has been found to be in error however in

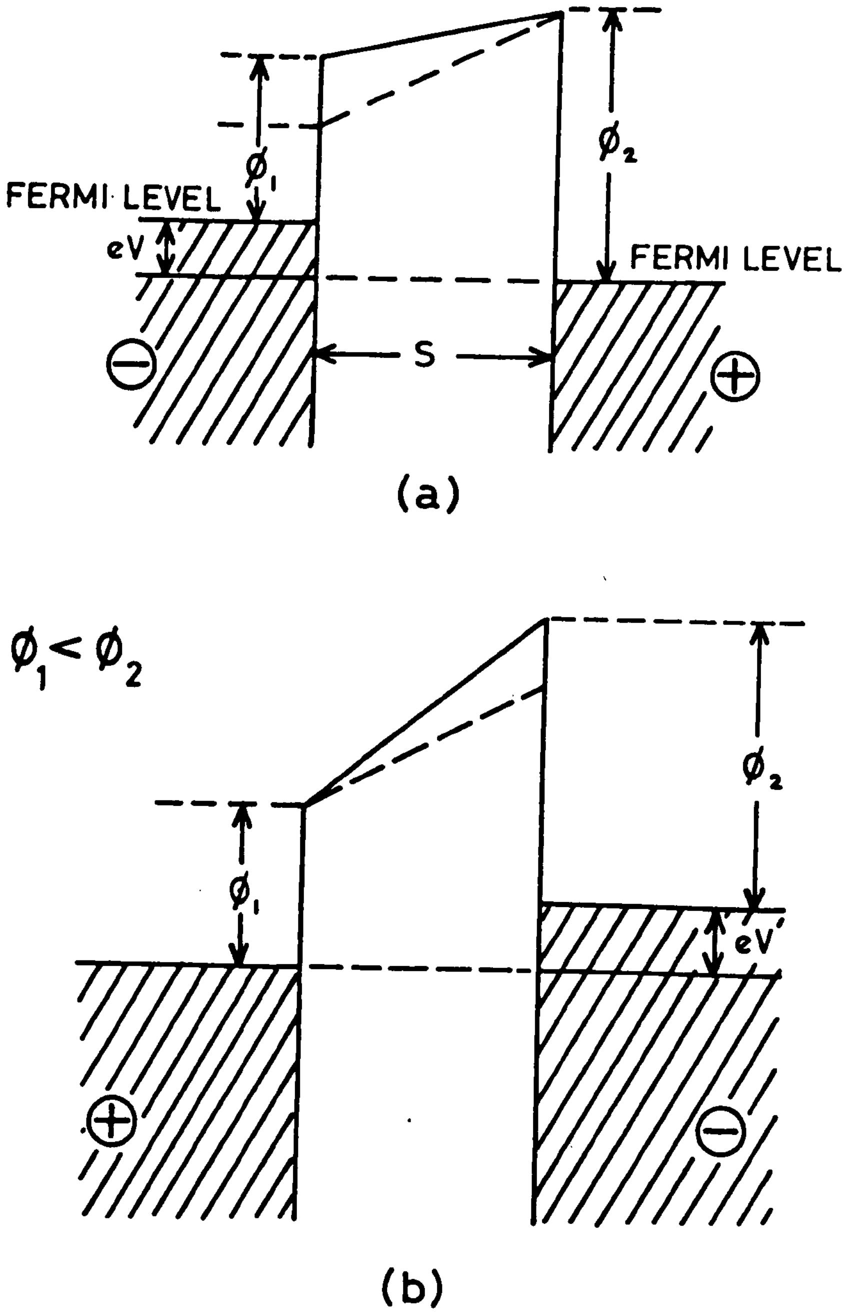

Fig 2.5: Rectangular barrier for an asymmetrical MIM junction for $0 \leqslant eV \leqslant \phi_1$ (a) under reverse-bias, (b) under forward-bias. The dotted lines illustrate the shape of the barrier (with respect to the Fermi level of the positively biased electrode in both cases) under zero-bias conditions.

that it does not (unlike equation 2.37) reduce to the corresponding Sommerfield-Bethe result when V → 0 (equation 2.36). It has been shown in fact that this is the result of mathematical error (12) and if due allowance is made, Holm's expression is essentially similar to equation (2.37).

Alternatively, it is possible to show (12) that in this voltage range

$$J = \frac{3e\phi}{2\pi s^2 h} \exp\left[-\frac{4\pi s(2m\phi)^{\frac{1}{2}}}{h}\right] \exp\left[\frac{\pi s e^2 (2m)^{\frac{1}{2}} V^2}{8h\ \phi^{3/2}}\right] \sinh\left[\frac{\pi s e (2m)^{\frac{1}{2}} V}{h\phi^{\frac{1}{2}}}\right] \tag{2.41}$$

This is in a form which allows ready comparison with the equivalent expression of Stratton (14).

2.2.4 The Stratton Approach

The approach used by Stratton (14) is to expand $\ell n\ P(E_x)$ (equation 2.30) in a Taylor series, retaining only the terms linear in E_x, such that

$$\ell n\ P(E_x) \simeq \left[-b_1 + c_1(E_F - E_x)\right] \tag{2.42}$$

where

$$b_1 = 4\pi(2m)^{\frac{1}{2}}/h \int_{s_{11}}^{s_{21}} \left[\phi(x)\right]^{\frac{1}{2}} dx \tag{2.43}$$

$$C_1 = 2\pi(2m)^{\frac{1}{2}}/h \int_{s_{11}}^{s_{21}} \left[\phi(x)\right]^{-\frac{1}{2}} dx \tag{2.44}$$

The limits s_{11} and s_{21} are values of x for which $\phi(x) = 0$, with respect to the Fermi level E_F. It should be noted also that b_1 and C_1 are functions of the applied voltage. The justification for equation (2.42) is that the tunnel current is predominantly due to electrons with $E_x \simeq E_F$.

Stratton then follows the method of Murphy and Good$^{(13)}$ in carrying out the integration in equation (2.23), yielding

$$J = (4\pi me/C_1^2h^3)\ \exp(-b_1)\ [1 - \exp(-C_1eV)] \qquad (2.45)$$

which is Stratton's general expression for arbitrary barriers at absolute zero temperature.

If equation (2.45) is generalised to include finite temperatures, then the equivalent expression becomes$^{(14)}$,

$$J(V,T) = \frac{4\pi me}{C_1^2h^3} \cdot \frac{\pi C_1 kT}{\sin\pi C_1 kT} \cdot \exp(-b_1)[1 - \exp(-C_1eV)] \qquad (2.46)$$

For a symmetrical barrier in the applied bias range $0 \lesssim eV \lesssim \phi$, equation (2.45) can be further simplified$^{(14)}$ to yield (for T = 0 K),

$$J = (8\pi me/C_{10}^2h^3)\ \exp(-b_{10})\ \exp(-b_{12}V^2)\sinh(C_{10}\ eV/2) \qquad (2.47)$$

where the b's and c's are coefficients of a power series in V such that,

$$b_1 = b_{10} - b_{11}\,eV + b_{12}\,eV^2$$

$$C_1 = C_{10} - C_{11}\,eV + C_{12}\,eV^2$$

It can be shown$^{(14)}$ that subsequent coefficients in these expressions differ from preceding ones by a factor $(1/\phi)$ and also that $b_{11} = C_{10}/2$. This last result is used in arriving at equation (2.47). To derive an analytical solution for equation (2.47), Stratton computes the coefficients for various barrier geometries (see Table 1 in reference 14).

For a rectangular barrier

$$\left.\begin{aligned} b_{10} &= 4\pi s(2m\phi)^{\frac{1}{2}}/h \\ b_{12} &= -\pi e^{2} s(2m)^{\frac{1}{2}}/6h\phi^{3/2} \\ c_{10} &= 2\pi s(2m)^{\frac{1}{2}}/h\ \phi^{\frac{1}{2}} \end{aligned}\right\} \qquad (2.48)$$

Substitution of equations (2.48) into (2.47) yields

$$J = \frac{e\phi}{\pi s^{2} h} \exp - \left[\frac{4\pi s\ (2m\phi)^{\frac{1}{2}}}{h}\right] \exp\left[\frac{\pi e^{2} s(2m)^{\frac{1}{2}}\ V^{2}}{6h\ \phi^{3/2}}\right] \times \sinh\left[\frac{\pi s\ (2m)^{\frac{1}{2}}\ eV}{h\ \phi^{\frac{1}{2}}}\right] \qquad (2.49)$$

which is the same result as equation (2.41) except for very small numerical differences. Further, as V tends to zero, equation (2.49) reduces to

$$(J)_{V\to 0} = \left[e^{2}V(2m\phi)^{\frac{1}{2}}/h^{2}s\right] \exp\left[-\ 4\pi s(2m\phi)^{\frac{1}{2}}/h\right] \qquad (2.50)$$

which is the same result as equation (2.36) and the Sommerfield-Bethe result for $V \simeq 0$.

2.2.5 Temperature Dependence of the Tunnelling Characteristic

The discussion of electron tunnelling presented above has neglected the effect of smearing of the Fermi surface for $T \neq 0$ K. The $J(V,T)$ characteristic for a tunnel junction was first derived by Stratton(14). His expression, generalised to include finite temperature has already been given (equation 2.46).

The temperature dependence of the tunnelling characteristic has also been considered by Simmons$^{(10)}$ in terms of his generalised model. This involved an accurate integration of the Fermi functions in equation (2.23) rather than using the approximations valid for T = 0 K. Using the approximation valid for the transmission coefficients (2.30), the current density can be written$^{(3)}$ as,

$$J(V,T) = \frac{4\pi me}{h^3} \exp - A\bar{\phi}^{\frac{1}{2}} \int_0^{\phi} \exp -B(E_F-E_x)dE_x$$

$$\times \int_0^{\infty} \left(\frac{1}{1 + \exp(E_F-E_x-E_r)/kT} - \frac{1}{1 + \exp(E_F-E_x-E_r + eV)/kT} \right) dE_r \qquad (2.51)$$

where the total electron energy $E = E_x + E_r$ and $B = A/2\,\bar{\phi}^{\frac{1}{2}}$

By making the substitutions :

$$a = \exp\,(E_F-E_x-E_r)/kT$$

$$b = \exp(eV/kT)$$

the second integral in (2.51) can be evaluated and for eV << kT is equal to

$$kT \;\ln \left[\frac{1 + \exp(E_F-E_x)/kT}{1 + \exp(E_F-E_x-eV)/kT} \right]$$

The integration over E_x can only be carried out by extending the upper limit to infinity. Thus, it is possible to finally obtain

$$J(V,T) = \frac{4\pi me}{h^3 B^2} \left(\frac{\pi B kT}{\sin \pi BkT} \right) . \exp\left(-A\bar{\phi}^{\frac{1}{2}} \right) \left[1-\exp(-BeV) \right] \qquad (2.52)$$

The similarity between this equation and the corresponding expression given by Stratton (equation 2.46) is to be expected.

The above analysis is of course equally valid for asymmetric junctions where $\phi_1 \neq \phi_2$.

Thus, the tunnel current J(V,T) at temperature T is given by

$$\frac{J(V,T)}{J(V,0)} = \frac{(\pi AkT/2\bar{\phi}^{\frac{1}{2}})}{\sin(\pi AkT/2\bar{\phi}^{\frac{1}{2}})} \qquad (2.53)$$

where J(V,0) is the tunnel current at 0 K given by equation (2.33). It should be remembered that Δs, the width of the potential barrier at the Fermi level of the cathode and $\bar{\phi}$, the mean barrier height above the Fermi level of the cathode (see Fig 2.3) both vary with applied bias. Expressing $\bar{\phi}$ in electron volts and Δs in nm for convenience, equation (2.53) becomes

$$\frac{J(V,T)}{J(V,0)} \simeq 1 + \left[\frac{3 \times 10^{-7} (\Delta sT)^2}{\bar{\phi}} \right] \qquad (2.54)$$

i.e. a slight quadratic dependence of the current (at constant voltage) on temperature. This weak dependence is typical of the tunnel effect and in general it will be feasible to use J(V,0) to determine the tunnelling characteristic at any reasonable temperature.

An interesting result(10) is obtained if equation (2.54) is rewritten as

$$\hat{J} = 100 \left\{ \frac{J(V,T) - J(V,0)}{J(V,0)} \right\} = \frac{3 \times 10^{-7} \Delta s T^2}{\bar{\phi}} \qquad (2.55)$$

If follows from this that a plot of $\hat{J}$ against V will have a peak when $V = \phi$ for a symmetrical junction. Similarly, plots $\hat{J}_1$-V (reverse-biased characteristic) and $\hat{J}_2$-V will yield ϕ_2 and ϕ_1 for asymmetrical junctions.

2.2.6 Tunnelling into Superconductors

The unequivocal test for electron tunnelling between metal electrodes involves the employment of at least one superconducting electrode(18). The theory of superconductivity of Bardeen, Cooper and Shrieffer(19) (BCS) postulates the existence of a forbidden energy gap centred at the Fermi level of superconductors and as a consequence, deviations from the low-voltage ohmic tunnelling characteristic obtained when using normal metal electrodes can be expected.

This is readily understood on the basis of a one-particle approximation of a BCS superconductor. Briefly, the BCS theory proposes that below the superconducting transition temperature, electrons in a metal may interact via lattice phonons to form electron pairs called 'Cooper pairs'. These pairs have a strong tendency to collect into a single energy state - the BCS ground state, which has the net effect of producing a new electron energy distribution in which the total energy of the system is less than that found in a normal metal at the same temperature. The new electron energy spectrum is characterised by a forbidden energy gap 2Δ, centred at the Fermi level of the superconductor, of width equivalent to the energy required to break-up a Cooper pair at the temperature of interest, and a new density of states function given by(20),

$$N_s(E) = \begin{cases} N_n(E)\dfrac{|E|}{(E^2 - \Delta^2)^{1/2}} & |E| \geq \Delta \\ 0 & |E| < \Delta \end{cases} \qquad (2.56)$$

where 2Δ is the energy gap and subscripts n and s refer to the normal and superconducting states of the metal, respectively. Thus the density of states in a superconductor is very large near the energy gap and approaches the gap asymptotically from above and below (see Fig 2.6).

For inter-electrode tunnelling, the tunnel current is proportional to the product of the density of electrons at a particular energy in the emitter metal and the density of unoccupied states at the same energy level in the absorber metal. Assuming that the transition probability is proportional to the density of states in a superconductor, the tunnel current from electrode 1 to 2 is given by(18),

$$I_{1-2} = Gn_1 n_2 \int_{-\infty}^{\infty} \rho_1(E)\rho_2(E + eV)\left[\, f(E) - f(E + eV)\,\right] dE$$

where Gn_1n_2 is the conductance when both metals are normal and ρ_1, ρ_2 are the ratios between the superconducting and normal densities of states in the two metal electrodes. The derivation of this equation has been discussed in detail by Giaver and Megerle(18). If one of the electrodes is normal, then at T = 0 K, the relative conductance (dI/dV) obtained from this equation is directly proportional to the relative density of states in the superconducting electrode. If the density of states in the two metals is constant over the applied voltage range, ohmic behaviour is expected (Fig 2.6a). If the Fermi level of a normal metal faces the forbidden energy gap of a superconducting metal electrode (Fig 2.6b), then

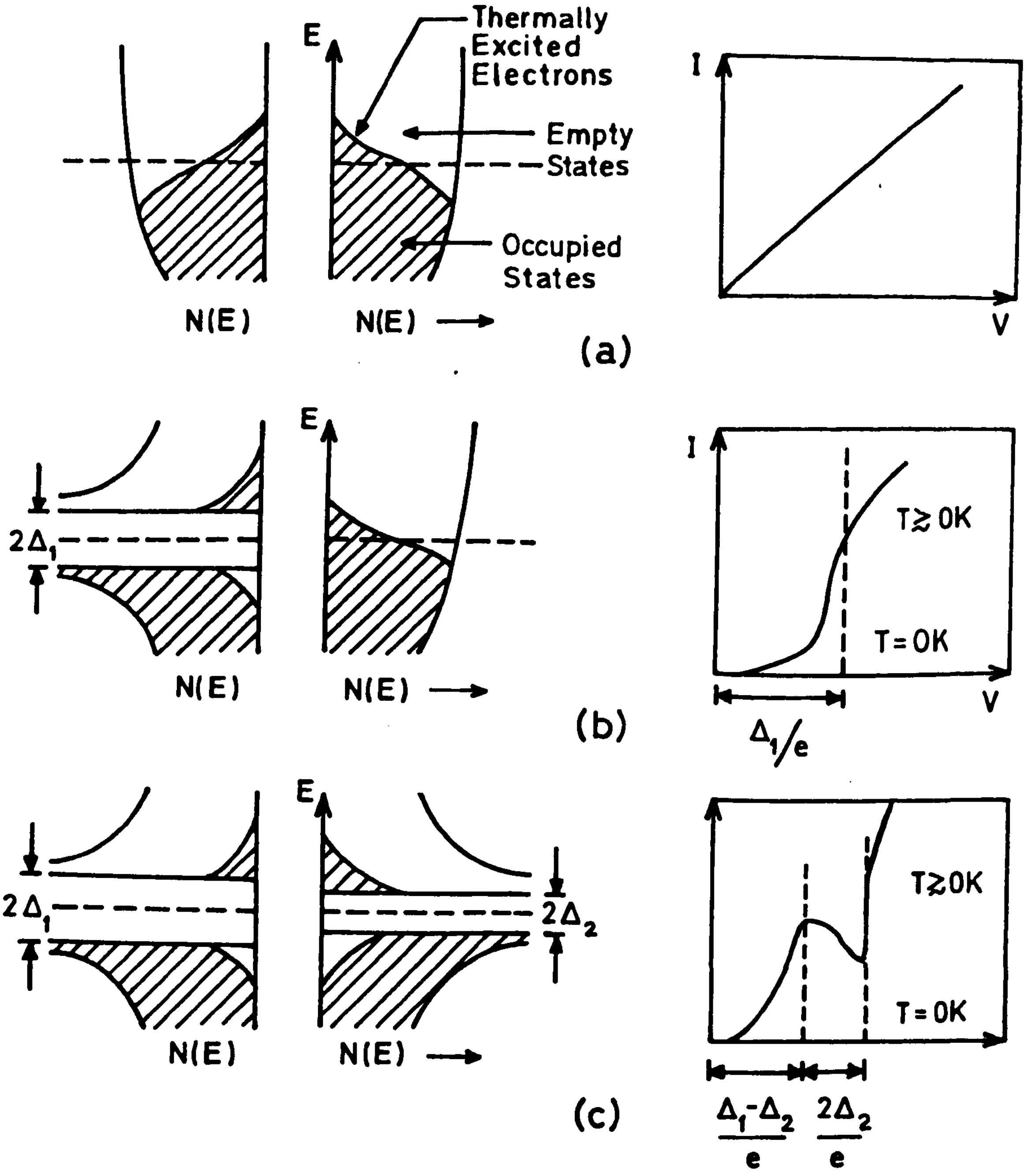

Fig 2.6: Density of states curves and expected I-V characteristics of various tunnelling junctions near absolute zero temperature (a) Both metals normal (b) one metal superconducting, one metal normal (c) both metals superconducting (after Giaver & Megerle$^{(18)}$).

at T = 0 K a potential across the junction must be raised or lowered by Δ_1 (i.e. half the superconductor energy gap) to allow any tunnel current to flow. At finite temperatures however, some current will flow before $V = \pm \Delta_1/e$, because of thermal smearing of electron energies around the Fermi levels.

If both metals are superconducting with energy gaps $2\Delta_1$ and $2\Delta_2$ (Fig 2.6c), tunnelling can occur only when $V = (\Delta_1-\Delta_2)/e$. With increasing applied voltage however, the tunnel current decreases since the density of available states decreases with increasing energy above the gap. As the voltage is further increased to $V = (\Delta_1 + \Delta_2)/e$, the main body of unexcited electrons in one electrode is brought opposite the empty states of the other and the current starts increasing rapidly and asymptotically approaches the characteristic found when both metals are normal. This describes the case for finite temperatures. At T = 0 K of course, no current can flow until a voltage $V = (\Delta_1 + \Delta_2)/e$ is applied. Thus electron tunnelling in MIM structures can be identified with certainty from the voltage and temperature dependence of the current if one of the electrodes is allowed to go superconducting.

2.2.7 Refinements to the Theory of Electron Tunnelling in MIM Junctions

The detailed analysis of electron tunnelling in MIM junctions presented in this chapter has in the main been restricted to the idealised case of a rectangular barrier. The rectangular barrier however is physically unrealisable because of the effect of the image force. Thus, when a charge moves from one electrode to another in a MIM junction, induced charges appear on the electrodes which exert forces on the initial charge. The net effect of this is that the potential seen by an electron tunnelling between the electrodes is not simply the rectangular barrier of height $E_F + \phi$ but in fact the rectangular barrier modified by the image force potentials. This reduces the area of the potential barrier by rounding off the corners and reducing the thickness.

The image force correction to the idealised rectangular barrier has been considered by various authors(6-8, 21-22). As a result of its inclusion, the dielectric constant is introduced into the theory. It is not the intention here to produce a critique of the relative merits of the different approximations, rather it is to stress that the principal effect of the image force is to reduce the barrier height and lower the junction resistance, especially for very thin films and materials of low dielectric constant. The general functional form of the results obtained for the idealised rectangular barrier however is unaffected and as far as the tunnel effect is concerned, the image force connection will not be considered again.

There have been many other studies of a more detailed nature in addition to the basic literature that has already been cited. Space-charge effects have been considered by Geppert(23) and Pitteli(24). The effects of traps(25) and ions(26) in the insulator and of electric-field penetration(27) of the electrodes have also been examined. Stratton has extended the analysis to include the effect of a non-parabolic energy-momentum relation and an electron effective mass in the insulator not equal to the free electron mass(14).

Most of these contributions whilst providing an insight into the complex nature of electron tunnelling are of little quantitative help to the experimentalist, for various reasons. For instance, if there is a large density of surface states present at the interface, the interfacial potential barrier height is often found to be independent of the electrode work function. Since the factors determining the density of surface states are not quanitifiable, in part at least being a function of film preparation technique, it is difficult to determine their exact role in conduction processes. Also, all the analyses of MIM tunnelling are based on the assumption that it is possible to achieve a perfectly planar electrode geometry, neglecting the effect of surface irregularities on a molecular scale. Since electron tunnelling is critically dependent on electrode separation, it is obvious that this assumption may not always be valid. Thus it is important to realise that in many respects, the analysis of MIM tunnelling presented above is an oversimplification. The main justification for its use is that it gives the correct functional form of the J-V-T relationship and whilst there are obvious dangers in trying to fit experimental data to expressions containing disposable parameters, the analysis can certainly be used in a qualitative sense to support or otherwise, the belief that a particular conduction process is electron tunnelling.

Finally, before closing this section and to introduce the next, mention should be made of deviations from the ideal tunnelling behaviour discussed above. These are referred to as tunnelling anomalies and can be divided into two broad categories.

The first of these, known as zero-bias anomalies, usually manifest themselves as either a peak or dip in the junction conductance about zero applied bias and have been studied by Shen and Rowell(28). They are not of direct relevance here and will not be discussed further. The second category of anomalies, known as finite-bias anomalies, involve an energy exchange between the tunnelling electron and some internal mode in the barrier. These may involve phonon excitations in the electrodes and the oxide or the excitation of the vibrational modes of molecules trapped in the insulator. Hence, the tunnelling electrons may act as spectroscopic probes of the tunnel junction. Since there is an exchange of energy by the tunnelling electron in exciting any internal degree of freedom in the barrier, the process is known as inelastic electron tunnelling (IET).

A discussion of the effect and its use as a spectroscopic tool forms the subject of the next section.

2.3 INELASTIC ELECTRON TUNNELLING

Consider the energy diagram of a typical MIM junction at absolute zero, where one of the metals is superconducting (Fig 2.7). As discussed previously, the electron energy spectrum of the superconductor is characterised by a band of forbidden energies of width 2Δ ($\simeq$ 2-5 meV), centred at its Fermi level E_{F2}, where all the electron energy states (at 0 K) are filled below the gap and empty above it.

When a voltage V is applied to the junction, the Fermi levels of the two electrodes become separated by an amount eV. It is clear from the diagram that elastic tunnelling, i.e. electron tunnelling from a filled level in metal 1 to an empty level at the <u>same</u> energy in metal 2, can only occur when $V \gtrsim \Delta/e$. However, in addition to the elastic tunnelling of electrons, it is also possible for a small proportion (typically < 1%) of the electrons to tunnel inelastically, losing energy to excite molecular vibrations in the barrier. While elastic tunnelling begins at $V = \Delta/e$, it is evident from Fig 2.7, that in the low temperature limit, the requirements of the exclusion principle applied to the final state of the tunnelling process cause the inelastic tunnelling channel to open abruptly only at $eV = h\nu + \Delta$, where $h\nu$ is the energy lost to a molecular oscillator. The consequences of this sharp onset of the inelastic tunnelling process cause linear increases (typically several μA) in the magnitude of the total tunnel current, step-function increases in the conductance and peaks in d^2I/dV^2 at $eV = h\nu + \Delta$, as shown in Fig 2.8.

The excitations leading to the opening of inelastic tunnelling channels include infra-red and Raman-like molecular vibrations (29), phonon excitations in the electrodes, and electronic transitions (30). Hence, a plot of d^2I/dV^2 versus V (Fig 2.8c) is called a tunnelling spectrum and

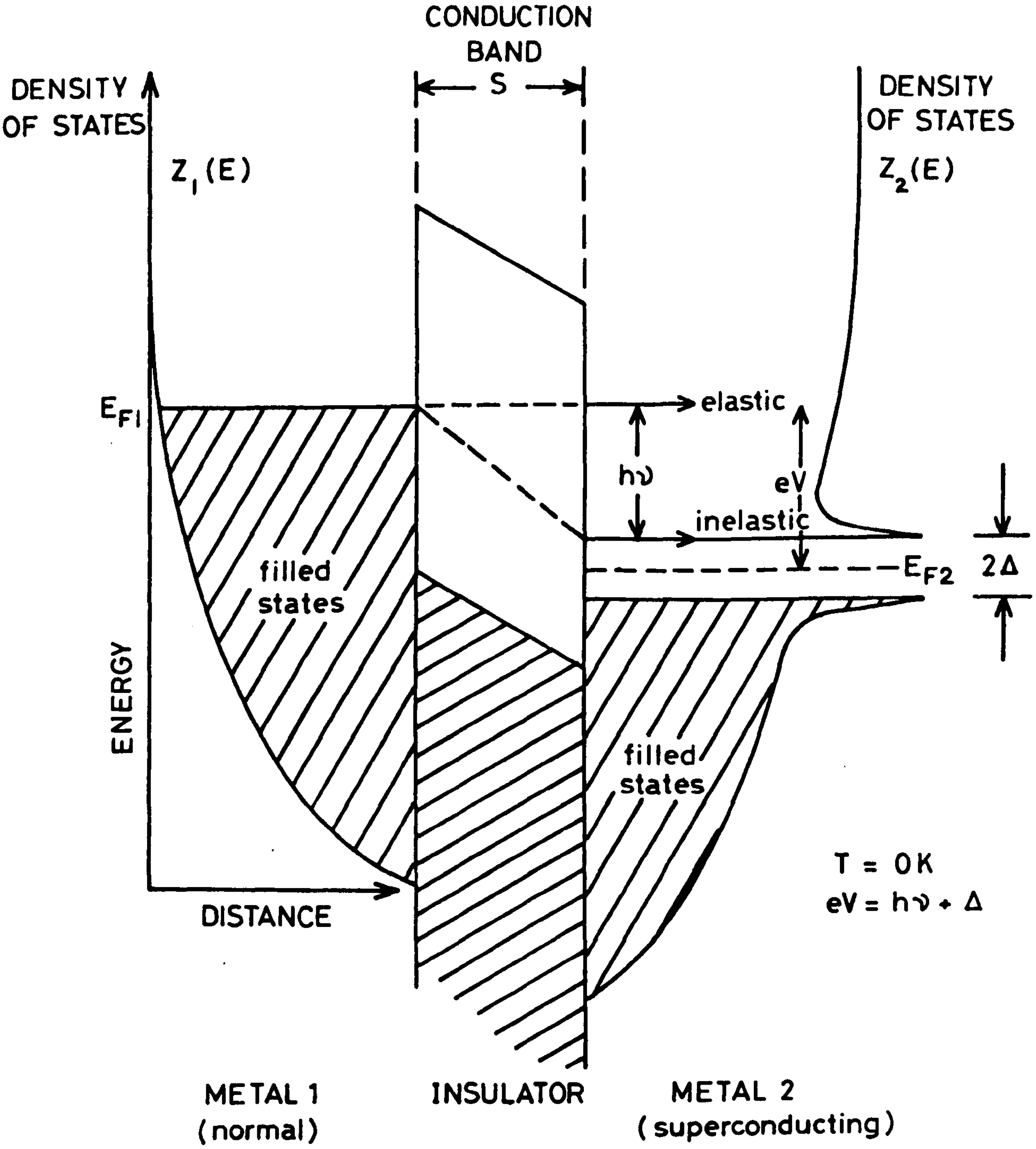

Fig 2.7: Electron energy diagram for a normal metal-insulator-superconducting metal junction at T = 0 K. Both the elastic and inelastic tunnelling of electrons is illustrated (after Keil et al (30)).

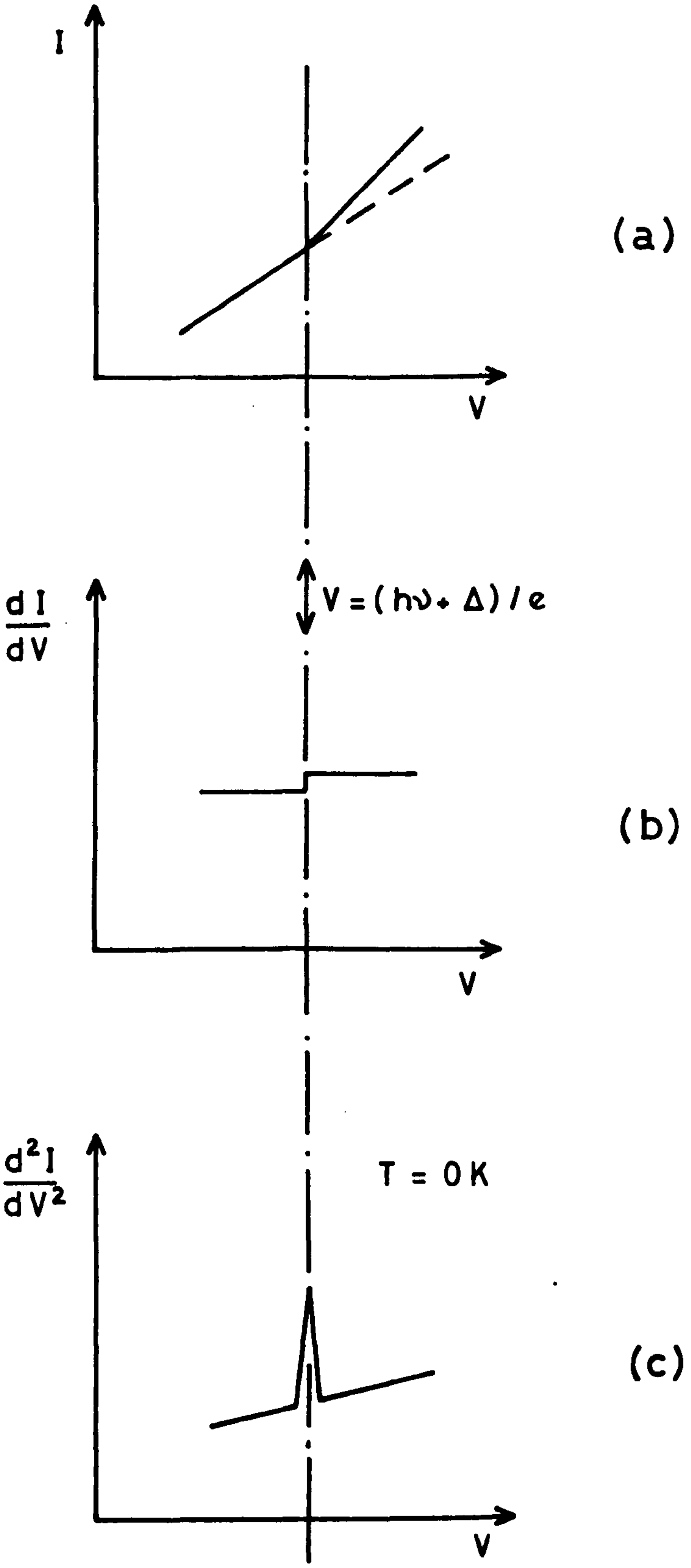

Fig 2.8: Schematic of inelastic tunnelling effects seen in MIM junctions - (a) The I-V characteristic (b) its first and (c) second derivatives for a vibrational mode excited at $V = (h\nu + \Delta)/e$. One metal is superconducting.

the technique is known as Inelastic Electron Tunnelling Spectroscopy (IETS)(30-31). The theoretical lineshape in Fig 2.8c will depend on the natural lineshape of the excitation, broadening due to the thermal smearing of the Fermi surface of the metals and density of states effects related to the use of superconducting electrodes.

Inelastic electron tunnelling via the vibronic excitation of molecules in the barrier can be understood in terms of a one-electron model that was first advanced by Scalapino and Marcus(32) and extended by Lambe and Jaklevic(33). The model is examined in the next section, before the effect of finite temperatures and superconducting electrodes on the observed linewidth in inelastic tunnelling experiments is discussed in section (2.3.2).

2.3.1 Inelastic Electron Tunnelling : One-electron Model

Scalapino and Marcus(32) considered a simple model where the tunnelling electron interacts via its electric field with the Coulomb potential of a molecular dipole (and its image) situated near one of the electrodes in an MIM system. The electron-molecule coupling was thought of in terms of a perturbation of the barrier height and it was shown how the interaction led to the usual infra-red selection rules. This model was subsequently extended by Lambe and Jaklevic(33) to include electronic interactions with the polarizability of the molecule, thus accounting for the Raman-active modes also observed in IETS.

Consider a molecular dipole, inside the insulator of a tunnel junction and near the metal-insulator interface (Fig 2.9). The probability (P_{1-2}) that an electron tunnelling from metal 1 to metal 2 interacts with the dipole may be obtained from the 'Golden Rule' of quantum mechanics(30). Thus

$$P_{1-2} = \left(\frac{2\pi}{\hbar}\right) \left| M_{1-2} \right|^2 \delta \left(E_{\text{metal }1} - E_{\text{metal }2} - h\nu\right) \tag{2.57}$$

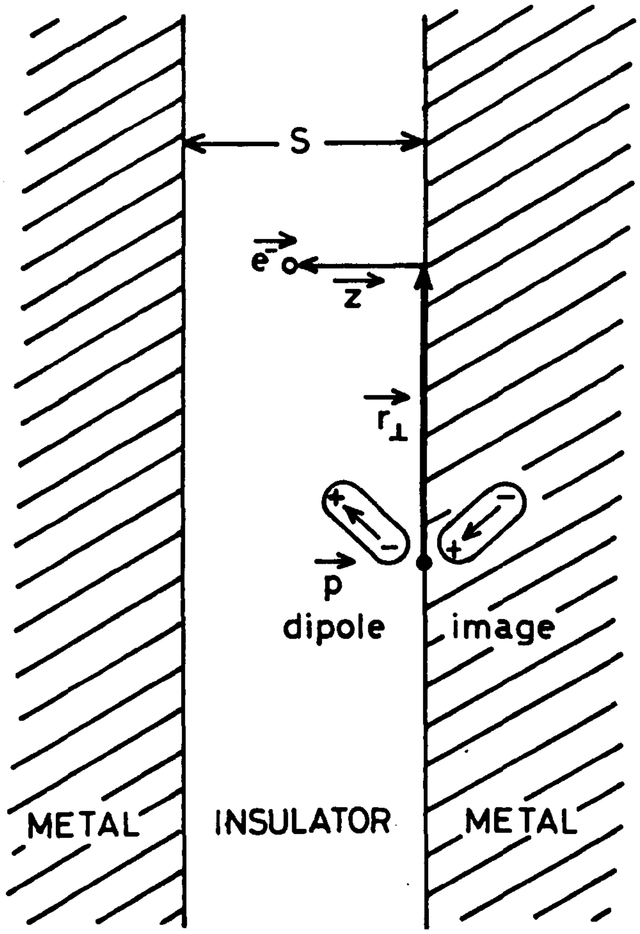

Fig 2.9: An electron at position $(z, r_\perp)$ interacts with a molecular dipole moment (and its image) at the origin at the interface in a tunnel junction (after Hansma (31)).

Here, P_{1-2} is called the inelastic tunnelling transition rate, $|M_{1-2}|$ describes the electron-molecule interaction for electron transfer from metal 1 to metal 2 and is termed the matrix element for the transition, and the quantity $\delta(E_1-E_2-h\nu)$ is a delta function that ensures $\delta(x) = 0$ unless $x = 0$, thus implying $E_1 = E_2 + h\nu$.

Scalapino and Marcus(32) considered that the electron-molecule interaction could be approximated by a Coulomb interaction between the electron and the dipole moment of the molecule, given by

$$U_{int}(Z) = \frac{2\,ep_z Z}{(Z^2 + r_\perp^2)^{3/2}} \qquad (2.58)$$

where the co-ordinates of z and $r_\perp$ are defined by Fig 2.9 and p_z is the component of the dipole moment perpendicular to the barrier. This interaction potential $U_{int}(z)$ is then treated as a perturbation on the barrier potential U(z) which is assumed to be rectangular and the electronic matrix element $|M_{1-2}|$ is evaluated using a WKB approximation(3-4). This gives(33)

$$|M_{1-2}| \propto \exp\left\{ - \int_0^s \left(\frac{2m}{\hbar^2}\right)^{\frac{1}{2}} \left[U(z) + U_{int}(z) - (E-E_\perp)\right]^{\frac{1}{2}} dz \right\} \qquad (2.59)$$

where E is the total electron energy and $E_\perp$ is the component of its kinetic energy perpendicular to the z direction. If it is assumed that the tunnelling electron excites the molecule from its ground state to the mth vibrational state, then the dipole matrix element for the transition is written $|\langle m|\, p_z|\, 0\rangle\,|$. If there are N molecular dipoles in the barrier, then the expression for the inelastic tunnel current due to electron-dipole moment interactions is given by Lambe and Jaklevic(33) as,

$$I_i(v) = N\,G_o \left[\frac{4\pi m e}{\hbar^2\,\Phi}\right] \ell n \left|\frac{s}{r_o}\right| \sum_m \left|\langle m|\,p_z\,|\,o\rangle\right|^2$$

$$\times \int_{-\infty}^{\infty} f(E)\left[1-f(E + eV-h\nu)\right]\left\{N_1(E)N_2(E+eV-h\nu)\right\}dE \qquad (2.60)$$

where the transition rate has been summed over 0 to m vibrational states, N_1 and N_2 represent the density of states in the two metals, G_o is the elastic conductance of the junction and Φ is the maximum barrier height. The Fermi functions here have been written assuming the transition is one-way only, from metal 1 to metal 2. The term $\ell n\left|\frac{s}{r_o}\right|$ represents an effective cross-section for tunnelling, where r_o defines a cut-off radius below which the dipole approximation no longer holds.

The Scalapino and Marcus model thus predicts that the size of the conductance increase due to this interaction is proportional to $|\langle m|p_z|0\rangle|^2$. This is the same quantity that determines the integrated intensity of peaks in infra-red absorption and therefore the model suggests a strong correspondence between infra-red and tunnelling intensities. Furthermore, Scalapino and Marcus(32) estimate a value of ∿ 1% for the increase in conductance due to the onset of a vibrational mode, which compares well with measured conductance changes(33).

The model was extended by Lambe and Jaklevic(33) to include electron-molecule interactions through the polarisability of the molecule, where the electric field of the molecule induces a dipole moment in the molecule and interacts with it. In this case, the interaction potential is given by

$$U_{int}\,(\alpha) = -\,\frac{4\,e^2\alpha\,Z^2}{(Z^2 + r_\perp)^3} \qquad (2.61)$$

where α is the polarisability of the molecule. Using essentially the formalism discussed above, Lambe and Jaklevic derived an expression for $I_i(V)$, similar to equation (2.60), where the term $|\langle m|p_z|o\rangle|$ is replaced by $|\langle m|\alpha|o\rangle|$, normally associated with Raman-active modes.

An evaluation of the increase in conductance due to this interaction predicts(33) a value of $\sim 0.5\%$, as opposed to 1% for the electron-dipole interaction. Thus, the model predicts that although Raman-active modes should also be observed in tunnelling spectroscopy, they should perhaps be less intense than infra-red vibrational modes.

The simple one-electron formulation discussed above has been used with reasonable success to predict magnitudes in the range found experimentally. However, a serious shortcoming is its inability to explain relative peak intensities in IETS. More rigorous models have thus been proposed which use a many-body approach. One such theory has been discussed by Kirtley, Scalapino and Hansma(34) in terms of the transfer Hamiltonian formalism where each metal electrode is described by a distinct many-body Hamiltonian and a third Hamiltonian, the transfer or barrier one, is added to describe the interaction of the tunnelling electrons with the molecules comprising the barrier. Furthermore, rather than making the dipole approximation used by Scalapino and Marcus, they assume that the charge distribution within the molecule can be broken up into partial charges localised on particular atoms. However, this theory and other refined approaches(2,35) to the problem have still proven incapable of calculating the relative intensities of the various inelastic modes with any certainty and thus the theory of inelastic tunnelling remains approximate.

2.3.2 Temperature Dependence and the Effect of Superconducting Electrodes

In the one-electron model of inelastic electron tunnelling presented above, it will have been noted that the effect of thermal smearing of the Fermi surfaces has been neglected. In fact, at finite temperatures, because of the Fermi tail, the applied voltage required to cause a vibrational transition may be greater or less than hν/e. This can be seen from Fig 2.10, where f(E) represents the thermally smeared Fermi function in metal 1 and 1-f(E) represents unfilled states in metal 2. It is obvious therefore, that there is a range of applied voltage over which the vibrational mode of energy hν is excited. This was first discussed by Lambe and Jaklevic(33).

For normal metal electrodes, the inelastic tunnelling current can be written

$$I_i = C\int_{-\infty}^{\infty} f(E)\ [1-f(E + eV-h\nu)]\ dE \qquad (2.62)$$

This follows naturally from equation (2.60) if the density of electron states is assumed to be slowly varying near the Fermi energies in the two metals (see section 2.2.1). Here the parameter C contains all the details of the electron-molecule interaction, and the integral thus simply expresses the condition that electrons must tunnel from a filled state in one electrode into an empty one in the other. On evaluation, equation (2.62) yields

$$I_i = C(eV - h\nu)\frac{e^x}{e^x-1} \qquad (2.63)$$

where $x = (eV-h\nu)/kT$.

However, since in inelastic tunnelling experiments the experimentally measured quantity is d^2I/dV^2, taking the second derivative of (2.63) with respect to voltage yields,

$$\frac{d^2I}{dV^2} = \frac{Ce^2}{kT}e^x\ [(x-2)e^x + (x + 2)] \Big/ (e^x-1)^3 \qquad (2.64)$$

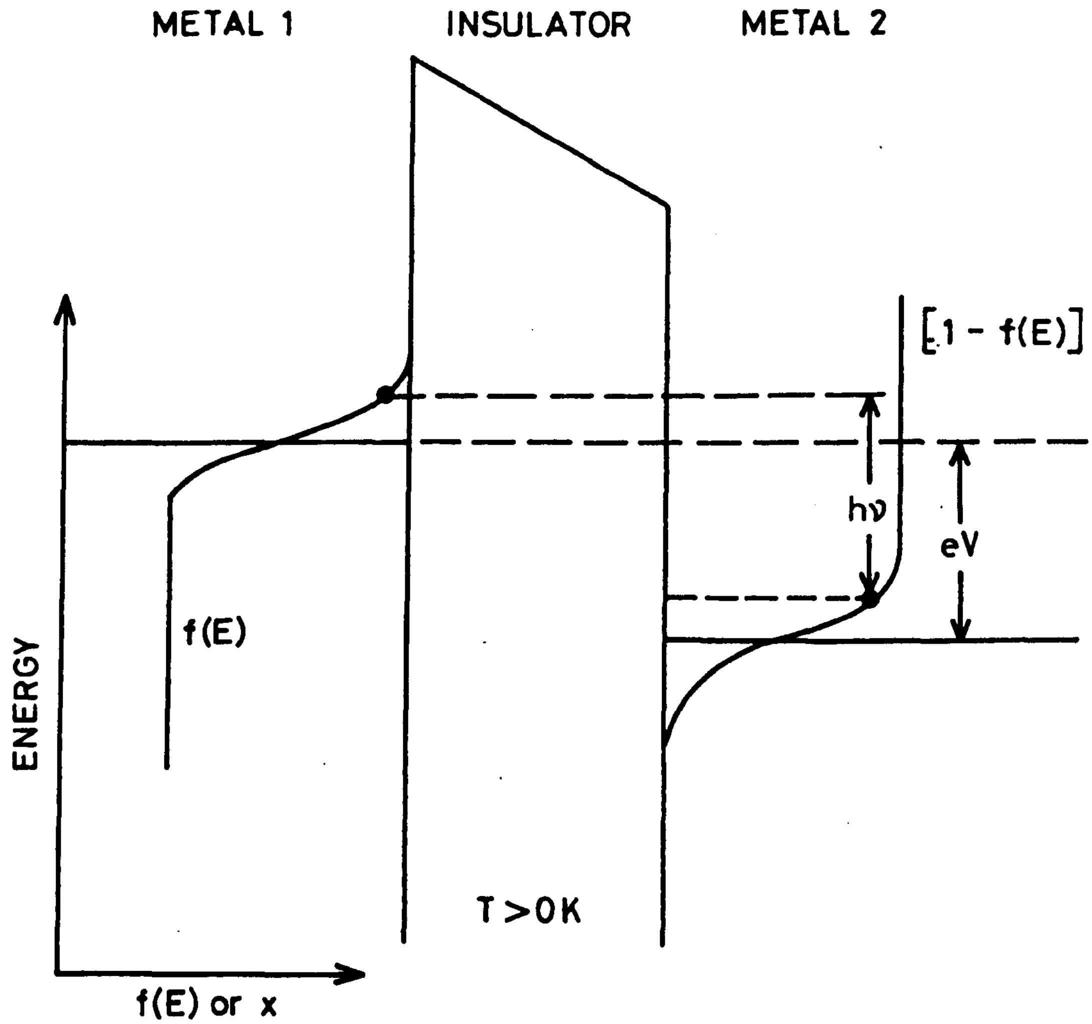

Fig 2.10: Schematic energy diagram of a MIM junction indicating the origins of thermal linewidth. The filled {unfilled} states are bounded by the curve f(E) {[1-f(E)]} (after Keil et al (30)).

This function thus describes the linewidth expected at a finite temperature in a tunnelling spectrum for a vibrational excitation of negligible natural width, i.e. it is assumed that the observed linewidth is due entirely to the smearing in energy of the electron distribution in the metals. The function has a bell-shaped form (see Fig 2.11), with a width at half-maximum equal to 5.4 kT, which is in good agreement with experiment(36). Simple calculation shows that this broadening of the linewidth ranges from ∿ 150 meV at room temperature to ∿ 2 meV at 4 K.

In the case of superconducting electrodes, the situation is different to that described by the above analysis, since now the effect of changes in the tunnelling density of states must be considered.

As discussed in section (2.2.6), when one of the metals in a MIM junction is superconducting, an energy gap 2Δ, centred at the Fermi level of this electrode is introduced (see Fig 2.7). At finite temperatures, below the superconductor transition temperature T_c, there will be a number of electrons which have been thermally excited across the superconductor energy gap. This number will be governed by the Fermi distribution, which in the tail, is approximately equal to the Boltzmann distribution, $\exp-(E+\Delta)/kT$ where E is the electron energy. However, since $\Delta >> kT$ at the temperatures of interest, it can be assumed that there will be a sharp boundary in energy between filled and unfilled states, i.e. the Fermi tail is much reduced.

Another significant effect is that the superconducting density of states, given by equation (2.56), is very large and sharp near the gap, as indicated in Fig 2.7. Since the tunnel current into a superconductor is directly proportional to the superconductor density of states (see section 2.2.6), and since for $E \simeq \Delta$, the number of states in a small energy range is so large, tunnelling into these states will dominate. Thus, when the electrodes are superconducting, the threshold of the inelastic tunnel

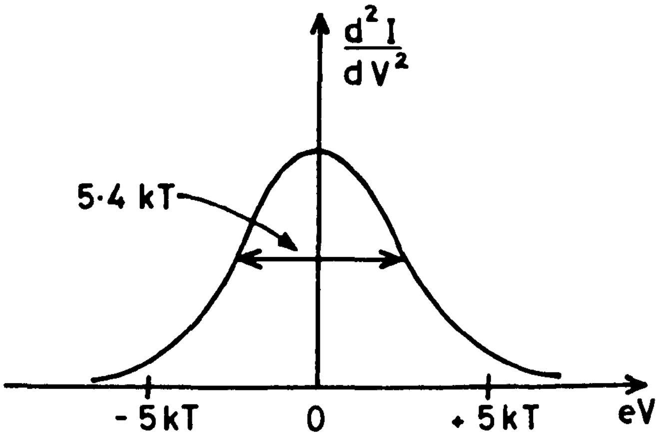

Fig 2.11: The lineshape due to thermal broadening for a MIM junction with normal electrodes (after Hansma(31)).

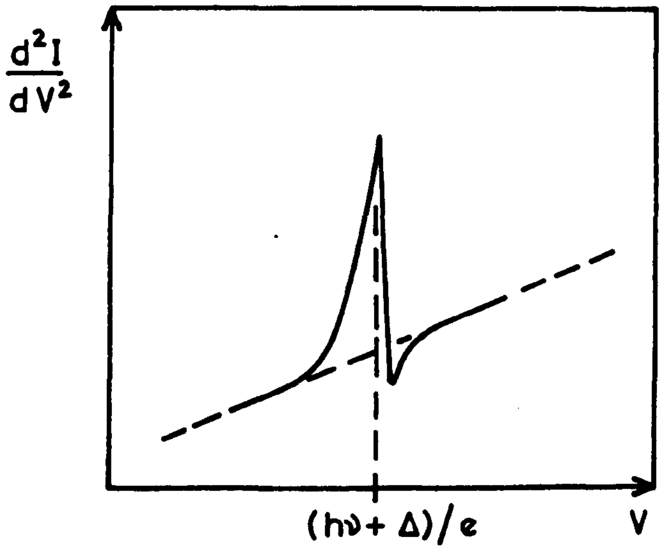

Fig 2.12: Characteristic lineshape of second derivative of I-V characteristic of a MIM junction when one (or both) electrode(s) superconducting (after Keil et al(30)).

current occurs over a much narrower voltage range (Fig 2.12). It will also be noted from Fig 2.12, that there is a modification of the lineshape from that obtained with normal metal electrodes (Fig 2.11), with an undershoot on the high energy side of the peak. The position of the peak is given by $eV = h\nu + \Delta$. However, this is strictly true only at T = 0 K since the energy gap itself is temperature dependent(20), and in fact at finite $T(< T_c)$, the peak is displaced from $eV = h\nu$ by slightly less than the full value (at T = 0 K) of Δ.

It is reasonable to conclude therefore that a significant reduction in linewidth broadening due to thermal effects is obtained with the use of superconducting electrodes. In practice however, experiments(33) show that the sharply defined density of states at the gap is rounded off compared with the ideal BCS prediction, resulting in a smearing of the threshold and thus the decrease in linewidth expected with superconducting electrodes though significant may not be dramatic.

Of course, thermal broadening and any reduction of it by superconducting electrode density of state effects will not be the only factors contributing to the observed linewidth, i.e. the resolution capability in tunnelling spectroscopy. Tunnelling spectra (d^2I/dV^2 versus V plots) are obtained using modulation techniques and lock-in amplification, and significant effects on second derivative linewidths can be expected as a consequence. Theoretical aspects governing the use of these techniques however are best examined in Chapter 4, when measurement methods are discussed.

2.4 CONDUCTION IN THICKER FILMS: SCHOTTKY EMISSION AND THE POOLE-FRENKEL EFFECT

It is obvious from the discussion in this chapter of electronic conduction in thin insulating films that electron tunnelling is a most unlikely mechanism for electron transfer in MIM junctions where the insulating film is much thicker than ∿ 5 nm. In fact at high applied fields, the observed current is much more likely to be due to either Schottky emission or the Poole-Frenkel effect.

The Schottky effect can best be illustrated by considering the potential barrier at the metal-insulator interface (Fig 2.3). Clearly, in addition to electron tunnelling there exists also the possibility that electrons from the electrode at negative potential will be emitted over the barrier and into the conduction band of the insulator. This is essentially the same effect as thermionic emission, except that in the case of the Schottky effect the applied field lowers the interfacial barrier height. Since this barrier to electron transfer across the MIM junction arises at the contact, the effect is clearly electrode-limited. In addition, another very similar mechanism is possible if there is a high density of donor centres (localised states) in the <u>bulk</u> of the insulator. In this effect, the application of an electric field assists the thermal excitation of electrons from these donors (which then become ionised) into the conduction band of the insulator. This process is known as the Poole-Frenkel effect. Since the barrier in this case arises in the insulator itself, the process can be termed bulk-limited.

Since workers are generally agreed (see section 1.1) that these mechanisms play an important role in determining the high-field conduction properties of multilayer Langmuir films, the essential physics of these two processes will now be discussed.

2.4.1 The Schottky Effect

A consideration of the theory of the Schottky effect must take into account the effect of the image force on the potential barrier at the metal insulator interface (see section 2.2.7). Consider an electron at a distance x from the surface of an uncharged metal. The image force f_{im} on the electron can be calculated simply by assuming that it is equivalent to replacing the metal surface by a 'mirror' charge a distance 2x away. This gives

$$f_{im} = \frac{e^2}{4\pi\varepsilon_o\varepsilon_r} \frac{1}{(2x)^2} \tag{2.65}$$

where ε_r is the high-frequency relative permittivity of the insulator. The potential energy associated with this force is

$$\phi_{im} = - \frac{e^2}{16\pi\varepsilon_o\varepsilon_r . x} \tag{2.66}$$

Thus, the potential step (with respect to the Fermi level) at the metal-insulator interface with this image potential included can be written (Fig 2.13),

$$\phi(x) = \phi_o + \phi_{im} = \phi_o - \frac{e^2}{16\pi\varepsilon_o\varepsilon_r x} \tag{2.67}$$

where ϕ_o is the potential barrier (idealised) in the absence of the image potential.

The barrier $\phi(x)$ in the presence of image forces is illustrated by the line AB in Fig 2.13. It is obvious that equation (2.67) is invalid at the electrode surface, since there $\phi = -\infty$. This anomaly is circumvented by assuming that the image force holds only for x greater than some critical distance x_o. For $x < x_o$, a constant image force is assumed such that the

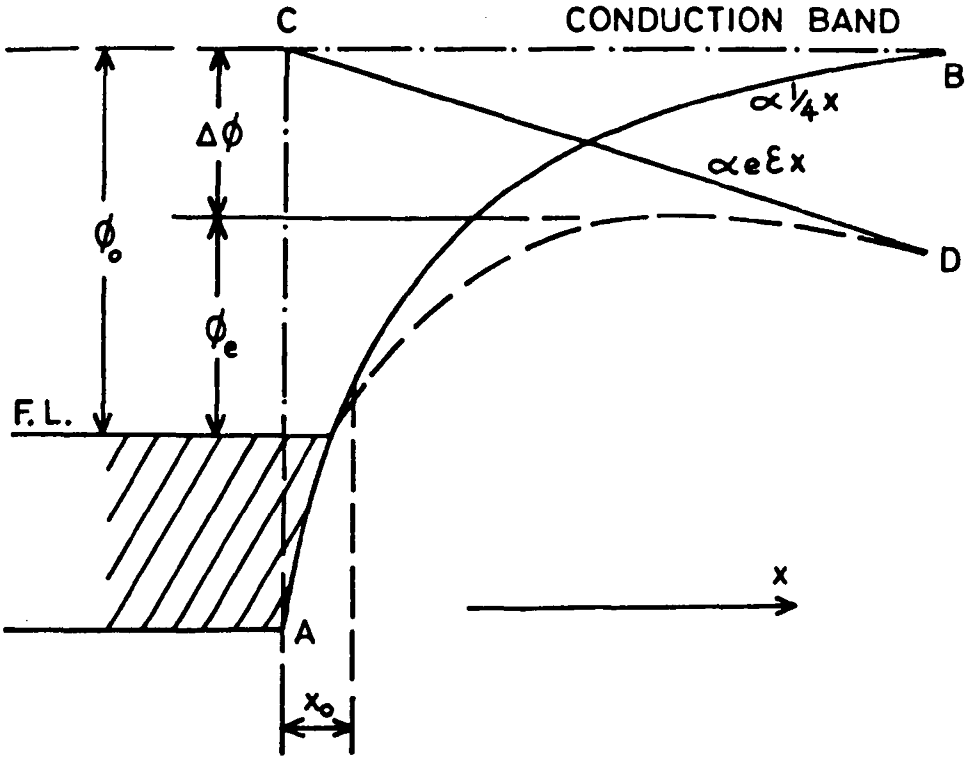

Fig 2.13: Schematic representation of the Schottky emission process.

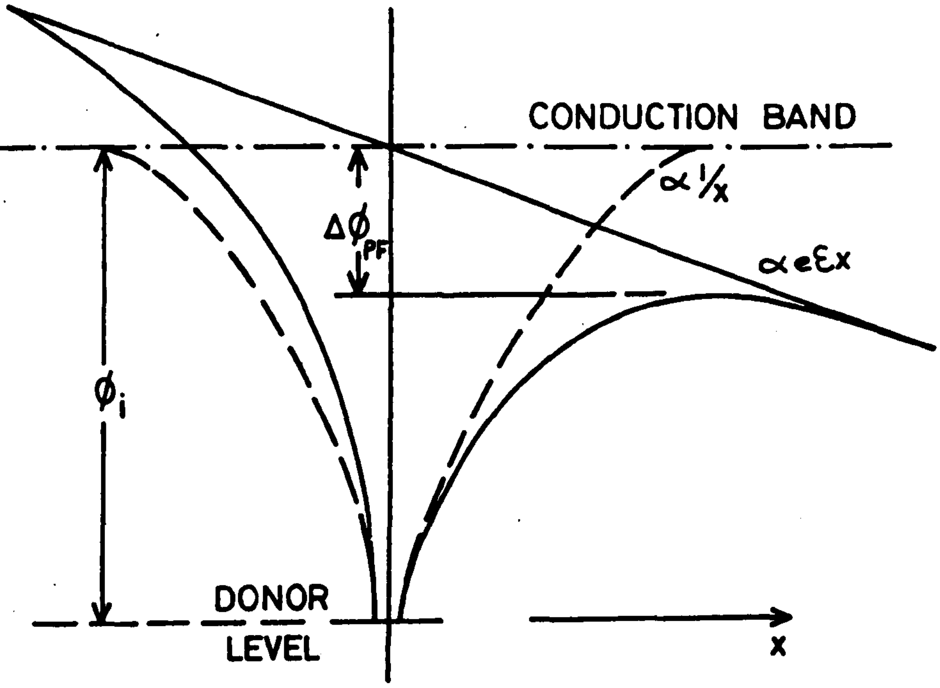

Fig 2.14: Schematic of the Poole-Frenkel effect at a donor centre.

potential energy is a linear function of x which matches the bottom of the electrode conduction band.

If the metal is now negatively charged by the application of a constant electric field $\mathcal{E}$, then the potential (line CD) due to this field must also be taken into account. Thus, the potential energy of the barrier with respect to the Fermi level of the electrode is now given by

$$\phi(x) = \phi_o - \frac{e^2}{16\pi\varepsilon_o\varepsilon_r} - e\mathcal{E}x \tag{2.68}$$

and is illustrated by the dotted line in Fig 2.13. The maximum barrier height is given at a distance x_m from the interface where

$$x_m = \left(\frac{e}{16\pi\varepsilon_o\varepsilon_r\mathcal{E}}\right)^{\frac{1}{2}} \tag{2.69}$$

This gives the reduction in barrier height $\Delta\phi$ [$= \phi_o - \phi(x_m)$] as,

$$\Delta\phi = \left(\frac{e^3}{4\pi\varepsilon_o\varepsilon_r}\right)^{\frac{1}{2}} \mathcal{E}^{\frac{1}{2}} \equiv \beta_s\mathcal{E}^{\frac{1}{2}} \tag{2.70}$$

where β_s is the Schottky field lowering coefficient. The effective barrier height is thus given by

$$\phi_e = \phi_o - \beta_s\mathcal{E}^{\frac{1}{2}} \tag{2.71}$$

Using Richardson's equation (37) for the current density due to thermionic emission over a barrier, and substituting for the Schottky barrier and neglecting electron reflection yields the simplified Richardson-Schottky equation

$$J = A_o T^2 \exp\left(-\frac{\phi_o}{kT}\right) \exp\left(\frac{\beta_s\mathcal{E}^{\frac{1}{2}}}{kT}\right) \tag{2.72}$$

where $A_o = 4\pi mek^2/h^3$ and ϕ_o are constants for a given system.

Thus (2.72) may be written in the form

$$J = J_o \exp\left(\frac{\beta_s \mathcal{E}^{\frac{1}{2}}}{kT}\right) \tag{2.73}$$

where J_o is a constant for a given temperature.

This expression neglects the complicating influence on the emission current of barrier shape, space-charge effects and traps etc. In addition, large deviations of the constants may be observed, although most of the these can be attributed to the assumptions used to keep the theory as simple as possible. Lamb (15) has discussed some of the more obvious sources of error.

2.4.2 The Poole-Frenkel Effect

The arguments for the Poole-Frenkel effect are very similar to those outlined above for Schottky emission except that here the electron is emitted from a donor centre, e.g. an impurity atom, in the bulk of the insulator. The removal of an electron from a donor becomes subjected to the Coulombic potential of the ionised donor. However, since the ionised donor is fixed in space the Coulombic potential varies simply as 1/x rather than (1/4x) as for Schottky emission. The barrier $\phi(x)$ separating the donor level from the conduction band is now given by (see Fig 2.14),

$$\phi(x) = \phi_i - \left(\frac{e^2}{4\pi\varepsilon_o\varepsilon_r x}\right) - e\mathcal{E}x \tag{2.74}$$

where ϕ_i is the difference between the donor level and the conduction band in the absence of the applied field, i.e. the ionisation energy of the donor, and the second term is the Coulombic potential. Proceeding as for the Schottky effect, the effective barrier is now given by

$$\phi_e = \phi_i - 2\left(\frac{e^3\mathcal{E}}{4\pi\varepsilon_o\varepsilon_r}\right)^{\frac{1}{2}} \tag{2.75}$$

which gives the attenuation in the barrier height as

$$\Delta\phi_{PF} = \left(\frac{e^3}{\pi\varepsilon_o\varepsilon_r}\right)^{\frac{1}{2}} \mathcal{E}^{\frac{1}{2}} \equiv \beta_{PF}\mathcal{E}^{\frac{1}{2}} \tag{2.76}$$

from which it can be seen that the barrier lowering is twice that found in Schottky emission. The probability of thermal excitation over the lowered barrier is,

$$P \propto \exp\left(-\frac{\phi_i - \beta_{PF}\mathcal{E}^{\frac{1}{2}}}{kT}\right) \tag{2.77}$$

and hence the current will be of the form,

$$J = A(T)\exp\left(\frac{\beta_{PF}\mathcal{E}^{\frac{1}{2}}}{kT}\right) \tag{2.78}$$

where A(T) is a function of temperature and includes exp $(-\phi_i/kT)$ as well as other factors.

Thus, it can be seen that the functional dependence of the current on the applied field is identical for the Schottky and Poole-Frenkel mechanisms. Both mechanisms would yield straight-line plots of ℓn J versus $V^{\frac{1}{2}}$ from which the gradient and intercept points could be used to determine various constants. In the basic situation just analysed, the two mechanisms will vary by a factor of two in the gradient and so can be easily separated. However, it should be noted that this consideration of Poole-Frenkel conduction is not general as it deals with only one specific situation. A particularly interesting case is where the donor centres lie beneath the

Fermi level. With this situation, equation (2.78) is altered so as to have an extra factor of two in the denominator and so becomes virtually identical to the Schottky conduction equation (2.73). One method of distinguishing between the two therefore would be to use the temperature dependence, as a plot of log J/T^2 versus $1/T$ would yield a straight line only for the Schottky process. Also, since the Poole-Frenkel mechanism is essentially a bulk property it will scale with film thickness whereas the Schottky mechanism is independent of this but will vary with electrode material. Interpretation of data is also likely to be complicated by the fact that at very high fields, where the barrier width is reduced to a large extent, direct tunnelling into the insulator conduction band can also take place (see section 2.2.2). The expression relating J and V is then expressed by equation (2.39).

Finally, it is possible that a different form of field dependence may be observed when the spacing between donor centres is sufficiently small so that their Coulombic fields overlap. If the centres are spaced at a distance of 2a, then the lowering of the Coulombic barrier due to the action of the field will be $ea\mathcal{E}$, and the current dependence will be of the form

$$J = B(T) \exp\left(\frac{ea\mathcal{E}}{kT}\right) \tag{2.79}$$

where B(T) is the temperature dependent pre-exponential factor which also contains $\exp(-\phi_i/kT)$. This is known as the Poole effect and has been invoked by some workers to explain conduction in multilayer Langmuir films(38).

CHAPTER 3

FABRICATION METHODS

The main advantages and several limitations of using Langmuir films for electrical studies have already been discussed in the opening chapter. Briefly, the fact that insulating films can be obtained with accurately known and controllable thicknesses, and in a form which is near-perfect makes them eminently suited for the purpose of these studies. However, the fabrication of defect-free, 'electrical-quality' Langmuir films is an involved procedure requiring great care and attention to detail. It is the purpose of this chapter to provide a description of the particular methods developed in this regard during the course of this work and to examine the factors which contribute to the final film quality. The chapter begins by discussing the basic philosophy of Langmuir film fabrication and identifying the various considerations on which the design of any fabrication system must be based. This is followed by a detailed description of the particular system developed during the present investigation and a discussion of the general fabrication techniques which were implemented to produce the MIM devices used in this study.

3.1 BASIC CONCEPTS AND CONSIDERATIONS

As discussed previously, the fabrication of a Langmuir film basically entails the spreading of a small amount of material on the uncontaminated surface of a liquid subphase and its subsequent compression into a monomolecular sheet (see Fig 1.1). The film is transferred onto a solid substrate by repeatedly passing the latter through the monolayer-covered subphase surface, picking up one layer each time.

The subphase normally used is water. It is required to be pure, especially with regard to surface-active contamination, since this may considerably influence the properties of the monolayer. However, in Langmuir films where the material is a fatty acid it is usual to add a small number of metal ions, usually in the form of the soluble metal chloride, to increase the stability of the monolayer and the final transferred film (discussed in greater detail at a later stage in this chapter).

There are certain requirements on the film material also. In particular, it must be insoluble in the subphase and it must consist of amphipathic molecules in order that these align approximately normal to the subphase surface. This means that the molecules must have a hydrophobic group at one end, and a hydrophilic group at the other, thus ensuring that the material forms a regularly ordered structure when compressed to form the solid monolayer. Although there are many materials which fulfil these conditions, the present investigation was restricted to stearic acid and one or two of its metal salts.

Once spread, the film is compressed by the application of suitable lateral compression. Normally, this is done by employing a suitable compression barrier lying across the rims of the trough used to contain the subphase. These rims are initially rendered hydrophobic by coating with paraffin wax or alternatively the trough can be constructed out of a hydrophobic material such as polytetrafluoroethylene (PTFE). Thus, when the trough is filled to the brim, the positive meniscus ensures that the level of the subphase is slightly above that of the trough rims and that any film spread on the subphase surface is amenable to manipulation (see Fig 1.1). It is obviously of great importance to ensure that the film is not over-compressed to the point that it collapses and no longer consists of a monomolecular sheet. The state of compression of the film is defined in terms of its surface pressure (π). This is equivalent to the reduction in surface tension of the uncontaminated subphase surface by the film. Thus,

$$\pi = \gamma_o - \gamma \qquad (\mathrm{mN\ m^{-1}}) \tag{3.1}$$

where γ_o is the surface tension of the clean subphase and γ is the surface tension of the subphase when covered with a film. It is essential therefore to monitor the surface pressure of the spread monolayer during the compression stage. Usually, the surface area available to the monolayer is also monitored at the same time. Thus, it is possible to plot the surface pressure of the monolayer (π/mN m^{-1}) against the surface area available per molecule (A/Å^2) and from this curve determine the behaviour of the spread film. An idealised π-A curve(also called an isotherm)for stearic acid is shown in Fig 3.1. By analogy with the compression of a normal gas, it is possible to distinguish three distinct regions on the curve which correspond to the gaseous, liquid and solid phases of the monolayer. Beyond the solid phase, the monolayer collapses due to the piling up of molecules on each other. Transfer of film onto a solid substrate will normally only be undertaken when the monolayer is in the solid phase. Furthermore, it is obvious that unless there is a system for ensuring that the surface pressure remains constant <u>during</u> transfer, the spread film will no longer remain as a <u>solid</u> monomolecular sheet. In the early work(1-3), this was achieved by the use of a 'piston-oil'. This was a hydrophilic oil which always spread to exert a constant surface pressure, provided it was present on the surface in amounts in excess to that necessary for monolayer-coverage, e.g. oleic acid was used to exert a constant surface pressure of 29.5 mN m^{-1}. The monolayer film was separated from the 'piston-oil' by a floating waxed thread clamped at the ends to the trough edges. As some of the monolayer was removed, the 'piston-oil' pushed the thread to take up the area vacated, thus ensuring that the original state of compression of the film was maintained. This system for maintaining constant surface

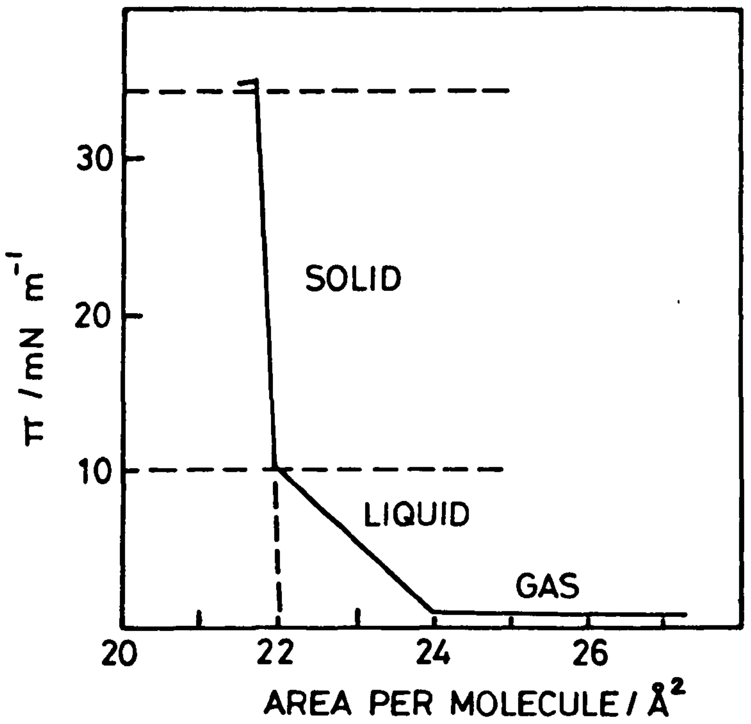

Fig. 3.1 Idealised π-A isotherm for stearic acid

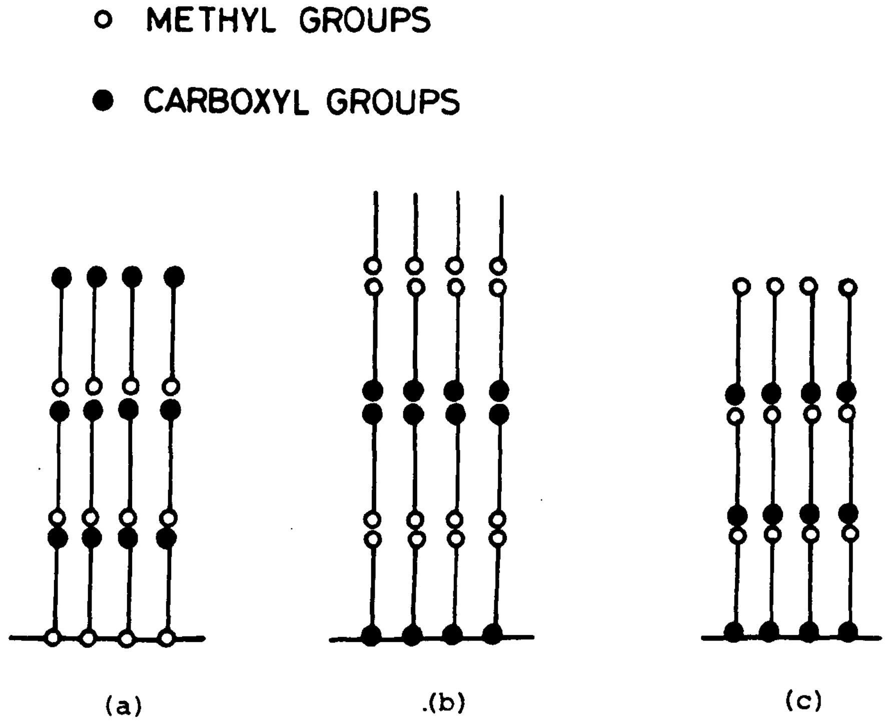

(a) .(b) (c)

Fig 3.2 Schematic representation of the molecular orientation in (a) X-type, (b) Y-type and (c) Z-type films of stearic acid.

pressure however suffers from the obvious problem of possible leakage at the points of attachment of the floating thread and hence possible contamination of the spread monolayer by the 'piston-oil'. In more recent designs of fabrication system, these problems are eliminated by the use of electronic feedback mechanisms which monitor the surface pressure of the film and compare this with a reference value. Any error signal is then amplified and used to drive the compression barrier so as to maintain the desired surface pressure. A similar system was developed for use in the present work. During film transfer, it was found capable of giving a precision in π of $\pm$ 0.05 mN m^{-1} whereas for well-defined monolayers $\pm$ 0.2 mN m^{-1} is usually held to be adequate(4).

Once a method for controlling surface pressure has been incorporated into the system, the monolayer can be deposited onto a solid substrate by simply passing the latter through the film-covered surface of the subphase. Depending on conditions, there are three different modes of monolayer transfer (Fig 3.2). These are ; transfer on immersion of the substrate only (termed X-type), on withdrawal only (Z-type), and in both directions (Y-type). Thus, the Langmuir technique not only provides an eminently elegant method for obtaining films of accurately defined and controllable thickness, but it also provides films that are ordered and furthermore, films whose molecular orientation can be varied. In practice however, the mode of film transfer will be chiefly governed by the substrate surface and its pre-conditioning and these are factors which will usually be dictated by the final functional requirements impingent on the completed device. Additional conditions that have a bearing on the mode of film transfer and final film quality have been identified(1-4). With most Langmuir films, it is found that the pH and temperature of the subphase are of critical importance and any variation of these from optimal values will adversely affect film quality.

It is useful at this stage to draw some general conclusions as to the considerations which must govern the design and implementation of a suitable fabrication system :-

(1) Contamination : As with any work involving aqueous surfaces and the accurate measurement of surface tension, it can hardly be overstressed that the system must introduce rigorous checks to reduce contamination to an acceptable level. Thus, any material used in the design of the system and which is likely to come into contact with the monolayer must not be a source of involuntary contamination. Generally, all materials used in the fabrication of films must be of the purest grade available and furthermore thier purity, especially with regard to surface-active contamination, must be verified occasionally. Precautions to reduce the other possibility, that of airborne contamination, must also be introduced into the system.

(2) Vibration : A monolayer film spread on the surface of a subphase is in a rather delicate state of equilibrium and it is obvious that the reduction of vibration must be of paramount importance. Thus, the fabrication system will generally need to be mounted on an anti-vibration table and it will have to be ensured that the design of any compression barrier and constant surface pressure mechanism reflects the need to reduce vibration to a minimum.

(3) Surface Pressure Control : The need for a system for the precise control of surface pressure has been discussed already.

(4) Control of pH and Temperature : These parameters are of significance in affecting the stability and final quality of the transferred film and hence methods for their control must be another design feature. In general, preliminary experiments must also be conducted to determine optimum values for these parameters before any film transfer takes place.

(5) The Dipping Mechanism : In general, any movement of the substrate through the subphase surface must be smooth and at relatively low speed, since the speed of transfer is obviously another factor which will affect film quality. The design of the dipping mechanism must therefore reflect these requirements.

The next section shows how these considerations were met with in the design of the present fabrication system.

3.2 DESIGN AND INSTRUMENTATION

The main components of the fabrication system developed during the present investigation are the trough and barriers, the systems for maintaining constant temperature and surface pressure and the sample dipping mechanism. A schematic of the system is shown in Fig 3.3 and a detailed description of the various component parts will now be undertaken.

3.2.1 Trough and Barrier Construction

The trough was constructed out of pyrex plate glass using Araldite adhesive (A.D. Whitehead, Instruments for Research and Control, Colchester). Materials such as plastics and metals should generally be avoided because of the attendant risk of contamination. In this respect, frequent blank runs under controlled conditions, where the surface tension of a clean subphase was monitored for extended periods were carried out to ensure that the adhesive was not a source of contamination. The results were always satisfactory but it should be noted that the glass trough can become contaminated from another source as a result of metal ions introduced into the subphase or because of organic solvents used in preceding experiments. This therefore necessitated a rigorous cleaning schedule not only for the trough, but for all components coming into contact with the monolayer system. These procedures are discussed in detail in section 3.3.

It is also necessary that the rims of the trough are perfectly flat and hydrophobic in order that the monolayer on the subphase surface can be

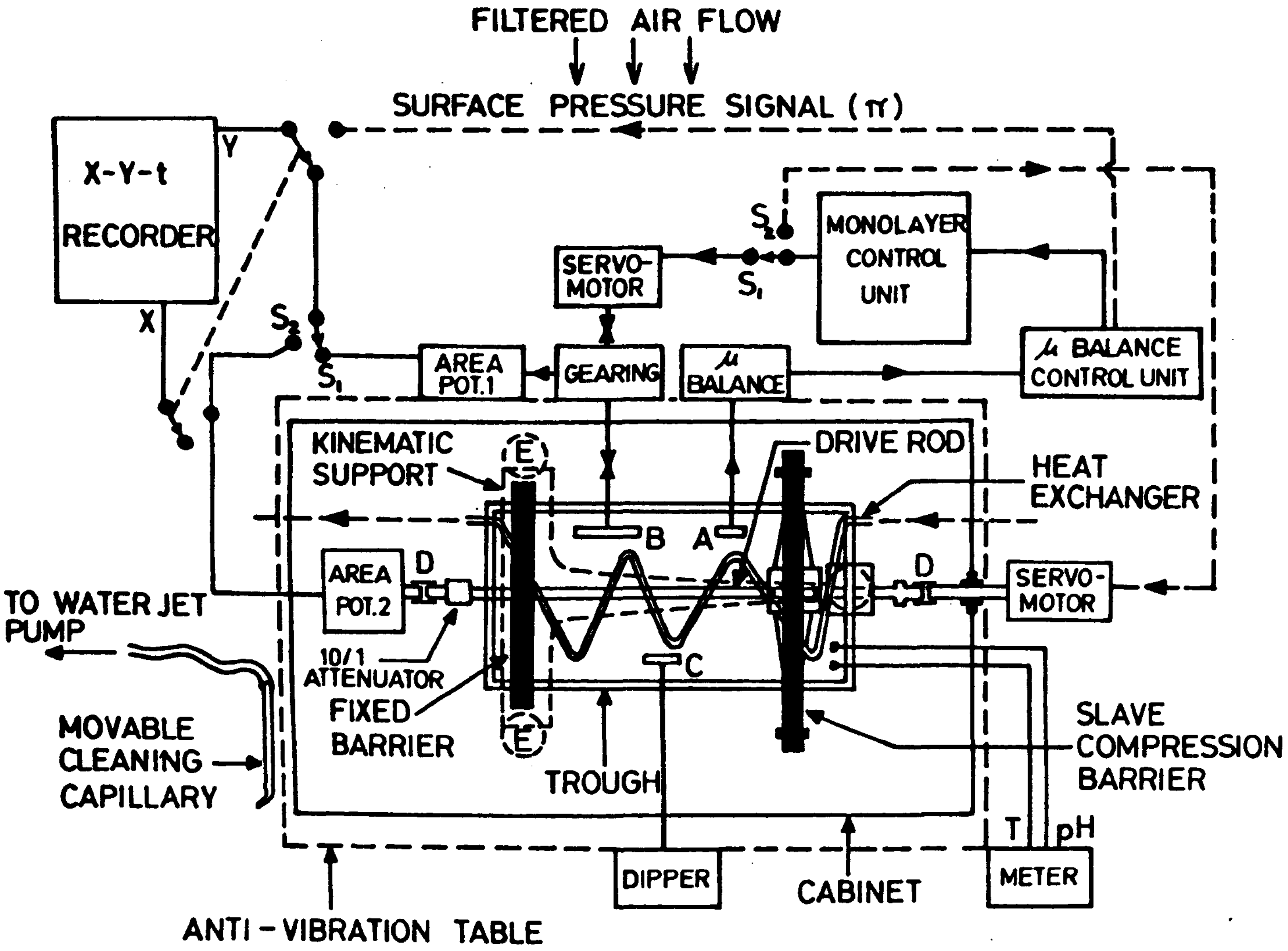

A	Wilhelmy sensor
B	Filter paper plate (monolayer reservoir)
C	Sample
D	Flexi-couplings
E	Levelling feet.

Fig. 3.3 Schematic of the Langmuir film fabrication system

manipulated by the compression barriers. This was achieved by applying a thin coat of paraffin wax to the rims from a saturated solution of paraffin wax in petroleium ether (the exact details are given elsewhere) and blank runs in the same way as for the adhesive were carried out from time to time, to ensure that the wax coating was not a source of involuntary contamination.

The dimensions of the trough are not critical, except that it has to be deep enough to coat the standard size of sample used in the present work and deep enough to accommodate the heat-exchange tube which was a feature of the temperature control system employed in the design of the fabrication system. The dimensions of the trough were 337 mm x 143 mm x 22 mm and the thickness of the plate glass used was 6.5 mm.

For the compression barriers, PTFE was found to be a satisfactory material. However, this material tends to deform slowly with time and since it is necessary for the compression barriers to be absolutely flat so as to prevent monolayer leakage between them and the trough rims, a stainless steel stabilising bar was screwed into the PTFE barriers. This arrangement was found to be satisfactory. As an alternative, waxed glass bars were also employed occasionally as compression barriers.

The trough was mounted on a kinematic support system(5). Levelling screws in the support feet permitted the subphase surface to be adjusted such that it was absolutely flat. The drive for the compression barrier was a screw rod located directly underneath the trough and built into the support. It was flexi-coupled at one end to the drive motor which was located outside the cabinet in which the monolayer system was housed. A precision potentiometer mounted at the other end of the drive rod through another flexible coupling, permitted displacements of the compression barrier and hence monolayer area to be monitored. The complete arrangement is shown in Figs 3.4 and 3.5.

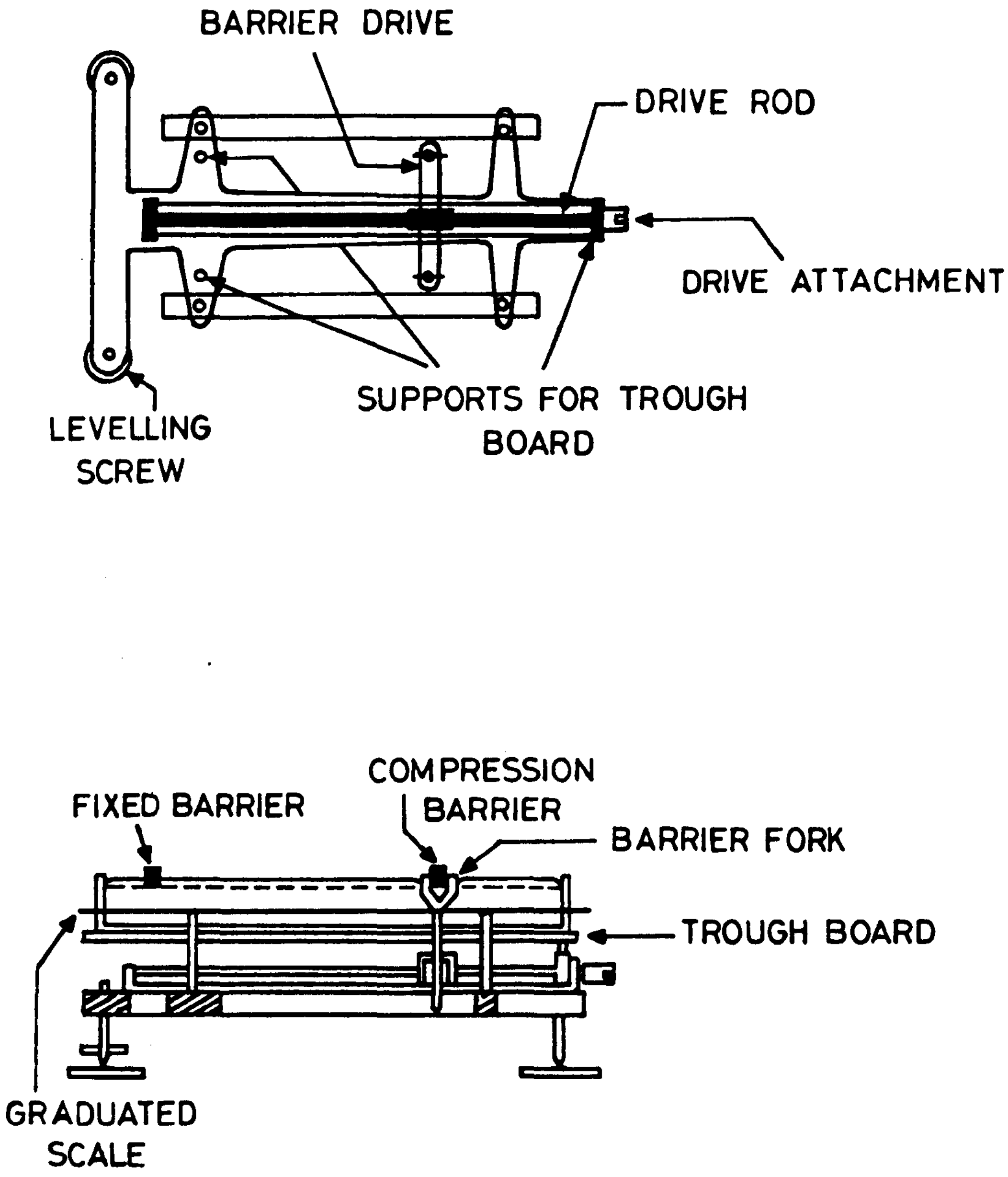

Fig. 3.4 Langmuir trough support

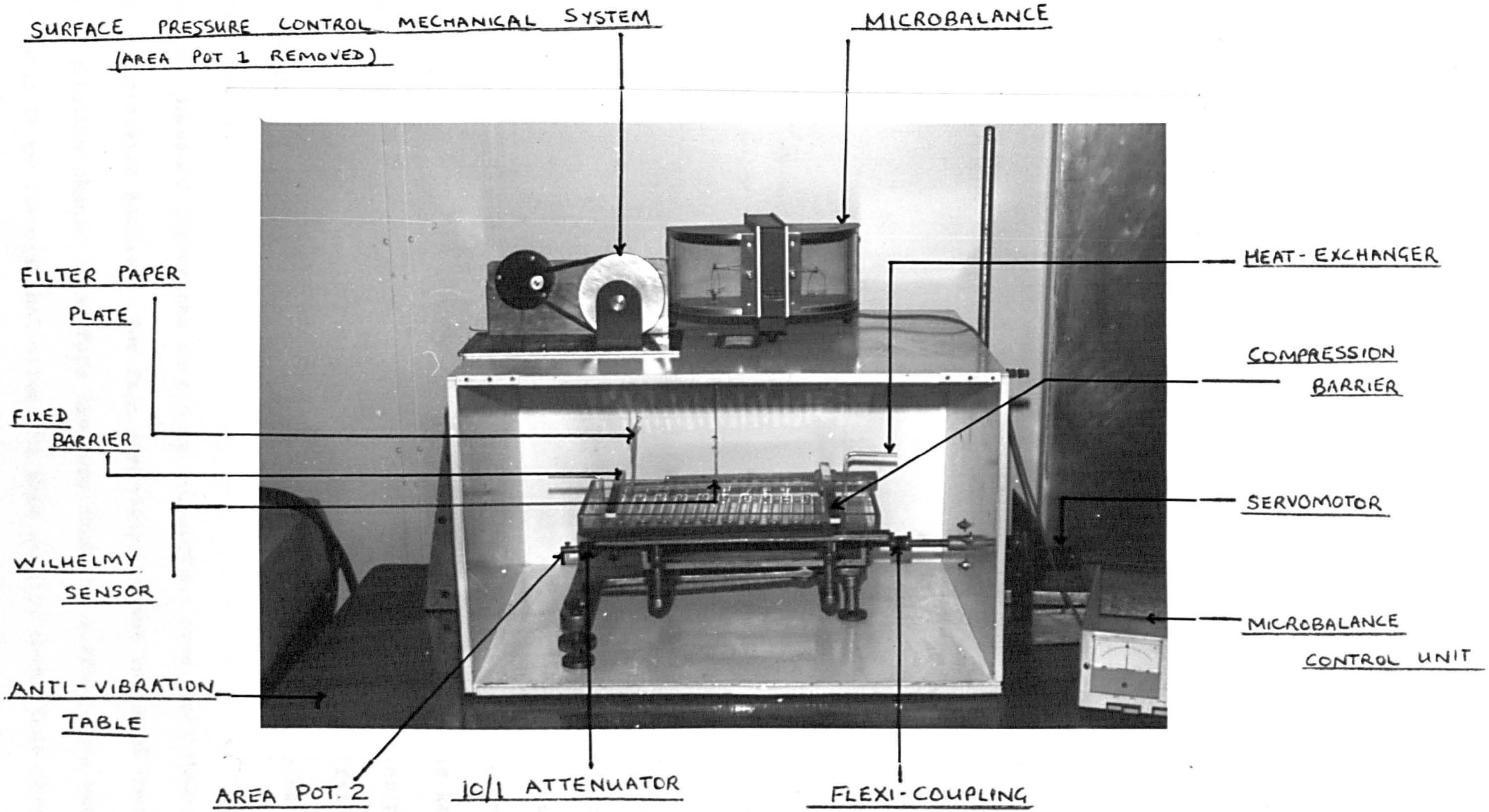

Fig. 3.5 The Langmuir Film fabrication system

3.2.2 Precautions against Vibration and Airborne Contamination

Vibration presents a major problem in any work with monolayers. In the present system, this was countered by locating the trough on a massive anti-vibration table made of terrazo stone (Gallenkamp, London), isolated from the floor and walls as far as possible by using rubber dampers. In addition, the glass trough itself was located on its support via rubber mounts and any attachments of the drive rod to the motor etc. were made through bellows-type flexible couplings. The motors (Maxon-type 2325-912/2332-908, Trident Eng., Berks) were chosen so that they did not contribute any significant vibration to the system at normal speeds of operation. The total elimination of vibration no matter how desirable, is in practice however, impossible. Any additional measures in this regard would entail diminishing returns and it is probably more profitable to introduce checks on other factors contributing in the introduction of artifacts into the monolayer system.

Airborne contamination presented a lesser problem in the design of the fabrication system. The film balance was housed inside a cabinet and the whole experimental rig located in a clean room with filtered airflow such that a slight atmospheric over-pressure could be maintained. In addition, a stringent check on the clothing of personnel was kept and generally standard clean room techniques were followed as far as possible.

For initial cleaning of the subphase surface prior to film spreading, a fine glass tube connected to a water jet pump was employed. The cleanliness of the surface was checked by monitoring the residual surface pressure (described later) as the surface area was reduced with the compression barrier. For film spreading, it was required that there be negligible change in surface pressure when the surface area was reduced to about 5% of its original value and this usually meant that this procedure had to be repeated several times before the criterion was met.

3.2.3 The Control and Measurement of Temperature and pH

In the present system, temperature control of the subphase (to within ± 0.2°C) was achieved by means of pumping water from a thermostatically controlled water-bath through a pyrex heat-exchange tube resting on the bottom of the trough (see Fig 3.5) and in thermal contact with the subphase. There was no evidence that any vibration set up in the subphase by the water flowing through the heat exchange tube promoted leakage or collapse of the monolayer since switching off the flow of water did not cause any change in the surface pressure of the spread monolayer.

The control of pH was a more difficult task. In general, buffers need to be avoided in any work involving spread monolayers(4), as they can modify the properties of the film. In the present system, dilute HCl or NaOH were used to adjust the pH of the subphase and it was generally found that these subphase solutions were stable with respect to pH for the length of time required for fabrication of the device. Both the subphase pH and temperature were continuously monitored using a temperature sensor and digital pH meter (Havant Instruments Ltd).

3.2.4 The Sample Dipping Mechanism

In order to deposit defect-free Langmuir films onto solid substrates, the transfer of the monolayer from the subphase surface has to be done in a smooth and sensitive manner. Generally, the speed of transfer must also be relatively low, so as to avoid tearing the transferred film and also disturbing the spread monolayer. For the dipping of samples in the present fabrication system, a motorised screw drive system was developed. It consisted of a micrometer thread, friction-coupled to the spindle of a d.c. motor (Maxon type 2325-912, Trident Eng., Berks) and is shown in Fig 3.6. Vibration from the motor was negligible at normal speeds of operation and the lower limit for smooth friction-free operation was about 0.1 mm s^{-1} vertical movement. The sample was mounted on the dipping rod of the mechanism with a small pressure clamp.

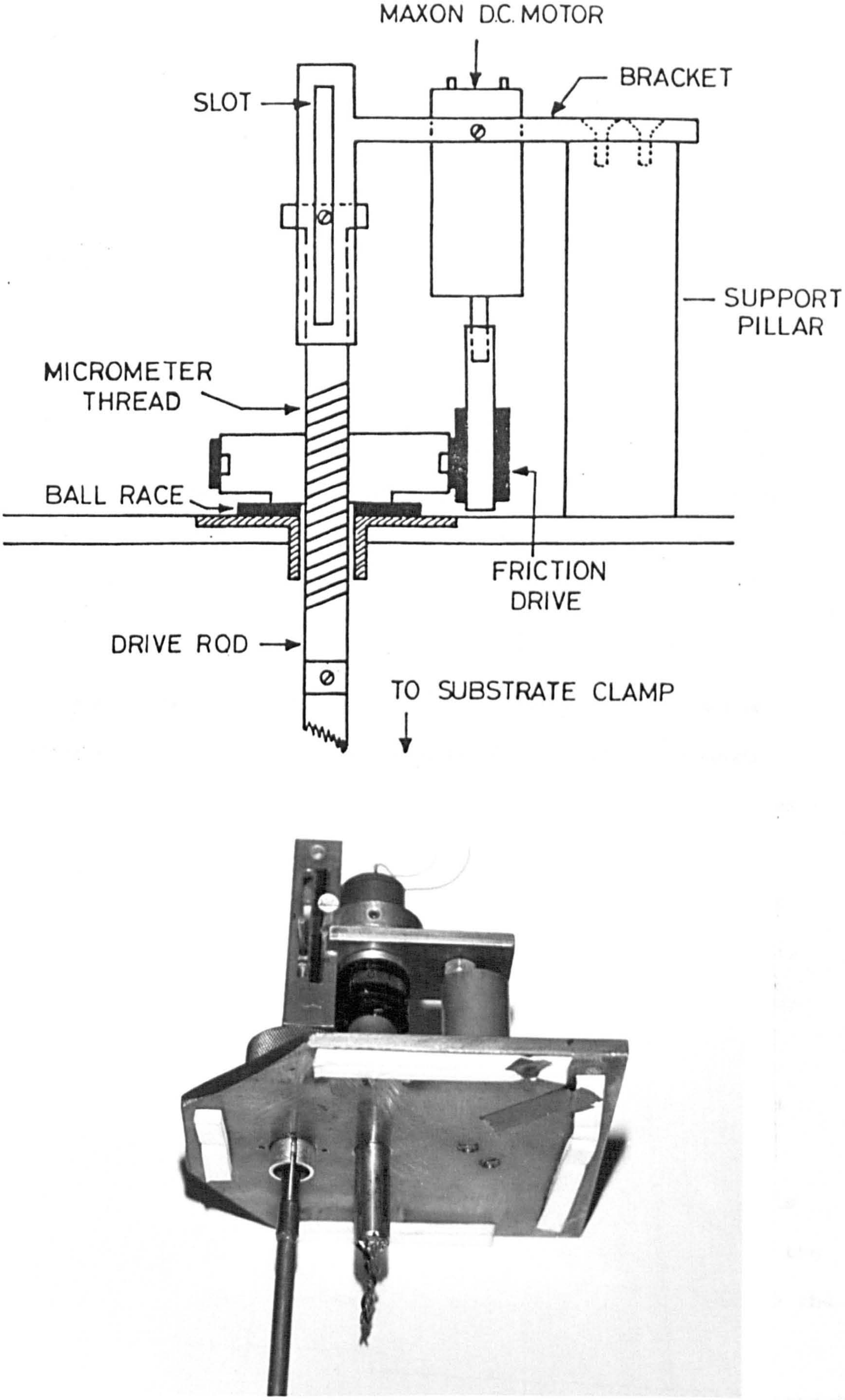

Fig. 3.6 The sample dipping mechanism

In use, the dipping mechanism was located on top of the cabinet housing the monolayer system, for ease of exchange of samples. Foam dampers on the underside of the dipping mechanism support base eliminated any vibration when it was removed from the cabinet.

3.2.5 Surface Pressure Measurement and Control

This is at the heart of any system for the fabrication of Langmuir films and the design of the present surface pressure control system will be treated in some detail.

3.2.5.1 Measurement of surface pressure

The surface pressure (π) of an insoluble monolayer is given by equation (3.1) as

$$\pi = \gamma_o - \gamma$$

where γ_o is the surface tension of the clean subphase and γ is the surface tension of the subphase when covered with a film. The usual methods of monitoring the surface pressure fall into one of two classes:-

(1) Langmuir's method(1-3) : In this method a movable float separates a clean portion of the subphase surface from that area of it covered by the monolayer and the force acting on the float is measured.

(2) Wilhelmy methods(6) : Here a relative measurement is made by determining the force due to surface tension on a plate (the Wilhelmy sensor) partially immersed in the subphase (γ) and comparing it with a similar measurement for the clean surface (γ_o).

Both methods suffer from some disadvantages(6). However, it is possible to avoid most of the difficulties associated with the use of the Wilhelmy method by suitable choice of materials and this was therefore the method employed in the present system.

Consider a thin plate which is completely wetted (i.e. zero contact angle) and partially immersed in the subphase as shown in Fig 3.7. The forces acting on the plate consist of gravity and surface tension downwards and buoyancy due to the displaced water upwards. If the density of the plate is ρ_p, then the downward force on the plate is given by

$$F_d = \rho_p g l \omega t + 2\gamma\ (t + \omega) \qquad (3.2)$$

where g is the acceleration due to gravity, γ is the surface tension of the subphase and the other symbols are defined by Fig. 3.7. The upward force due to the buoyancy effect is

$$F_u = \rho_p g l^1 \omega t \qquad (3.3)$$

and hence the total force on the plate (downwards) is given by

$$F_t = \rho_p g l \omega t + 2\gamma\ (t + \omega) - \rho_p g l^1 \omega t \qquad (3.4)$$

This expression neglects the effects of the second phase which is air with negligible density. The usual method of measurement is to hold the plate stationary so that l^1 remains constant, and to determine the change in F_t when the surface tension of a clean subphase is reduced by the presence of a monolayer. Thus

$$\pi = -\Delta\gamma = -[\Delta F_t/2(t + \omega)] \qquad (3.5)$$

which indicates a plate of large periphery for high sensitivity.

This method of surface pressure measurement suffers from two main disadvantages. Firstly, the contact angle θ must be zero. This is not really a problem until the monolayer is spread. Then, since the monolayer is also spread onto the Wilhelmy plate, the contact angle may

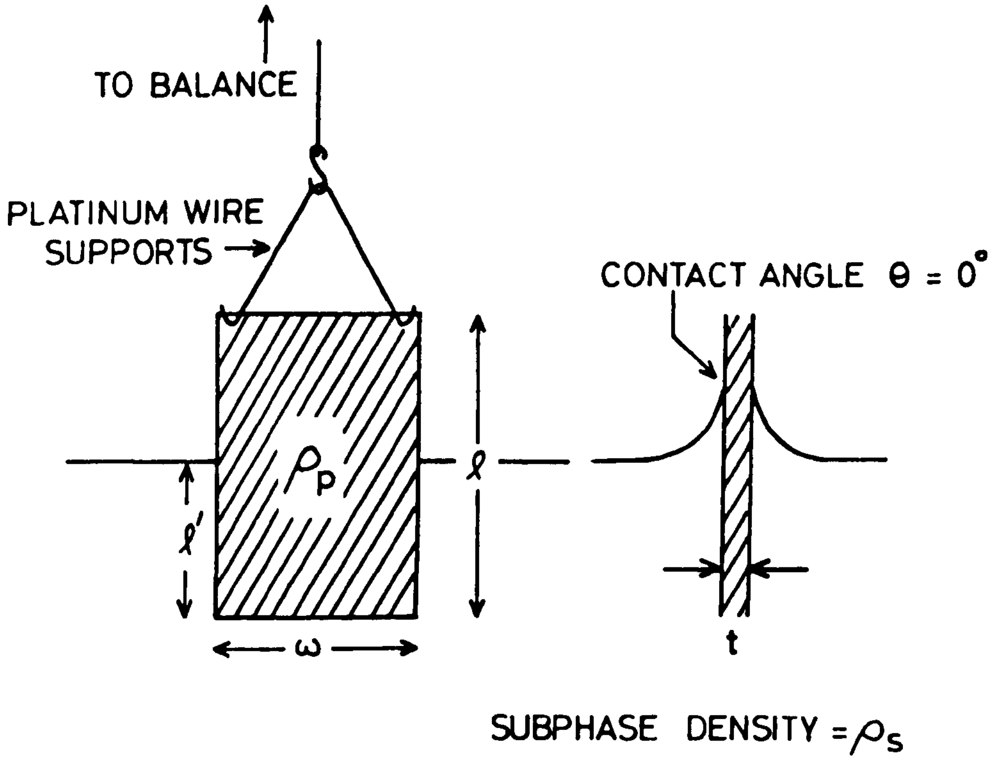

Fig. 3.7 Principle of the Wilhelmy method of measuring surface pressure (see text)

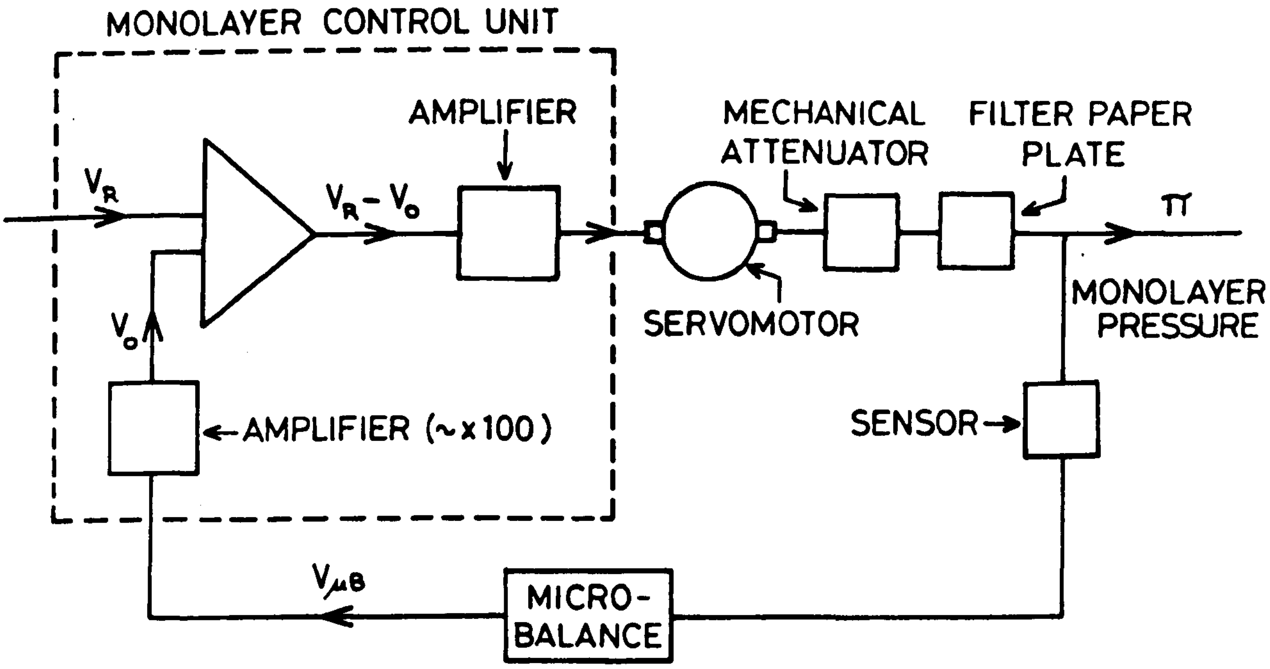

Fig. 3.8 The basic feedback system for surface pressure control

well be far from zero, especially if the fixed position of the plate is altered during measurement. The second problem with the method is that the reference surface tension value γ_o is not measurable during the experiment. Thus, it is necessary to ensure that factors which may alter this e.g. surface-active contamination or temperature do not vary after its determination.

The Wilhelmy sensor used in the present system was cut out of filter paper (Schleicher and Schull No. 589 or Whatman No. 50), and wetted to a constant weight. Kuhn et al$^{(7)}$ have shown that this avoids the problems of zero contact angle associated with materials such as glass and mica which have often been used for this purpose. The dimensions of the sensor were 50 mm x 10 mm x 0.1 mm . If the thickness is assumed to be negligible, then (3.5) becomes

$$\pi = -\Delta\gamma = - \Delta F_t/2\omega \qquad (3.6)$$

and thus for the sensor of width 10 mm used in the system, the weight measured in milligrams is equal to twice the surface pressure in mN m^{-1}.

Changes in the surface tension of the subphase were measured with a Beckmann LM600 microbalance which has further advantages with regard to the problem of maintaining zero contact angle. The constant horizontal position of the microbalance beam is maintained by an electronic relay system coupled to a pair of matched photocells; the position of the Wilhelmy sensor (hung from the beam) is thus constant in the subphase and problems associated with advancing/retarding contact angle hysteresis do not arise. Use of the microbalance afforded excellent sensitivity and reproducibility over several intercalibrated weight ranges and also the ability to monitor the surface pressure directly on a chart recorder.

The microbalance head was located on the cabinet housing the trough and the sensor suspended from the beam with a length of fine cotton thread and platinum wire supports (see Fig. 3.5). Special draught shields were incorporated so that an overall sensitivity of 0.01 mN m^{-1} could be achieved

3.2.5.2 Surface Pressure Control

A block diagram of the basic feedback system for maintaining constant surface pressure is shown in Fig. 3.8. For this, a special control unit was constructed which compared the actual surface pressure measured by the microbalance with a desired value and fed the error signal to a mechanical system which after suitable amplification allowed compensating changes in monolayer area and hence surface pressure to be made. A circuit diagram of the monolayer control unit, comprising the comparator circuit and independent controls for both forward and reverse movement of the servomotor is shown in Fig. 3.9. The circuit was arranged to have zero output (V_{out}) when the amplified (gain $\sim$ x 100) input signal V_o from the microbalance and the reference channel signal V_R were adequately similar but which became positive or negative if deviation occurred. A series of readings of $V_{\mu B}$ and V_R for balance conditions ($V_{out} = 0$) are plotted in Fig. 3.10, from which it can be seen that the characteristic is linear within the range of operation shown.

The error signal was used after suitable scaling to drive a servomotor,which through a suitable mechanical attenuator(about 10/1) adjusted the position of a filter paper plate (10 cm x 10 cm x 0.01 cm) relative to the subphase surface. This filter paper plate effectively acted as an extension of the subphase surface (7) and during the initial spreading of the film it too got covered with a monolayer, thus constituting a reserve of film to replenish that withdrawn during transfer. A precision potentiometer flexi-coupled to the servomotor allowed

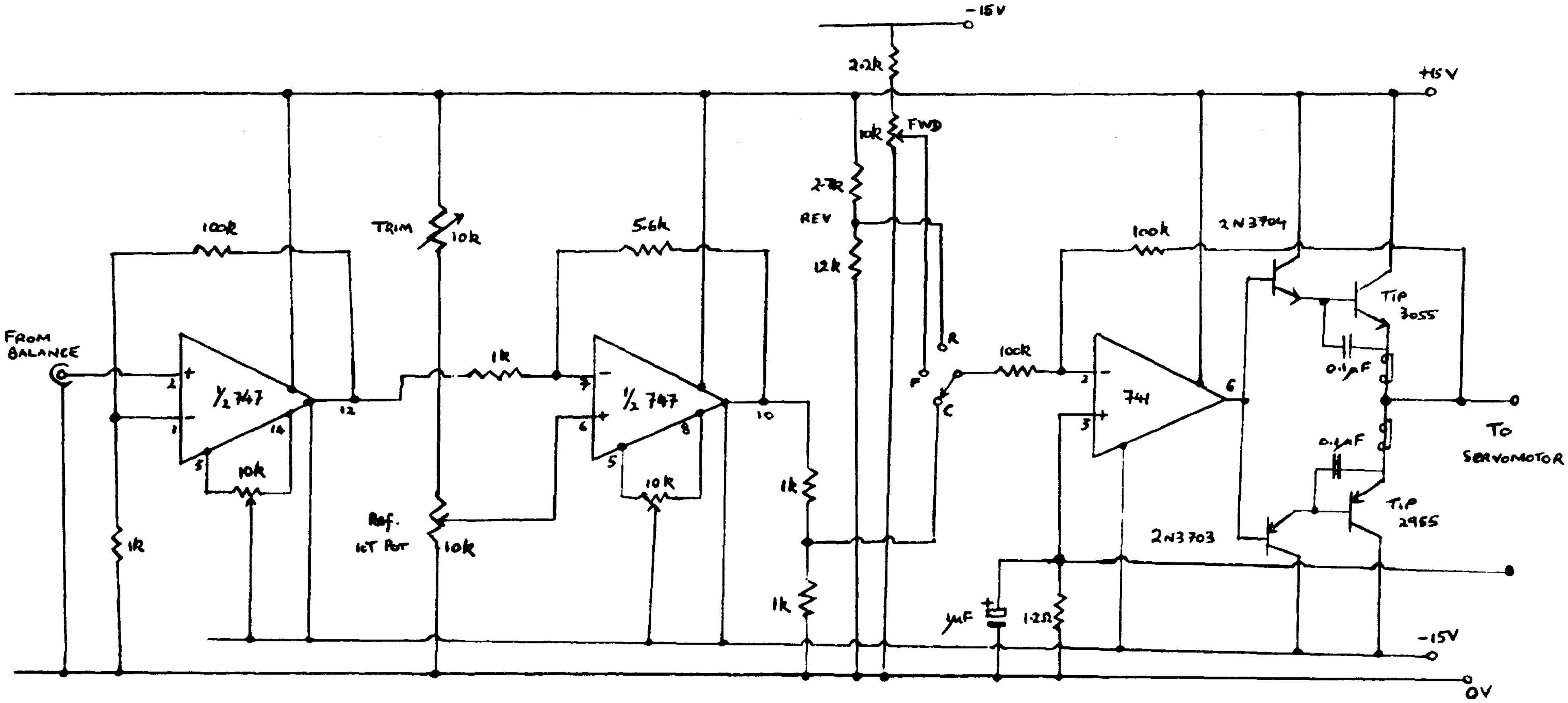

Fig. 3.9 Circuit diagram of the monolayer control unit

displacements of this filter paper and hence changes in the area of the spread monolayer to be monitored. The arrangement is visible in Fig. 3.5 and is also shown in more detail in Fig. 3.11.

For the automatic control of surface pressure, the initial calibration of the reference signal in terms of surface pressure was carried out as follows. The surface of the subphase was first swept clean by using the fine glass vacuum tube described earlier and the cleanliness of the subphase surface verified. With the Wilhelmy sensor located in the clean subphase, the microbalance was adjusted to give zero output. This corresponded to the reference surface tension value γ_o (equation 3.1). Various weights were then located on the opposite pan of the microbalance and the reference signal which had to be derived from the monolayer control unit to achieve balance ($V_{out} = 0$) for each weight noted. Since the dimensions of the sensor were known, the surface pressure corresponding to each weight could be calculated. A typical calibration curve is shown in Fig. 3.12.

The main advantages of the system just described is that it avoids problems of monolayer leakage associated with conventional compression barriers and allows increased precision in surface pressure control. However, the arrangement could only maintain constant surface pressure over a limited range, and it was usual therefore to first employ the slave compression barrier (independently of the servo feedback loop) to permit coarse adjustments of the monolayer area and hence surface pressure. Since pressure changes, first detected by the sensor, took more time to affect the molecules further away from the sensor, this preliminary compression had to be made slowly so as to prevent localised collapse of the monolayer near to the barrier. As described earlier, this compression barrier was also equipped with a precision potentiometer flexi-coupled to the screw drive, thus

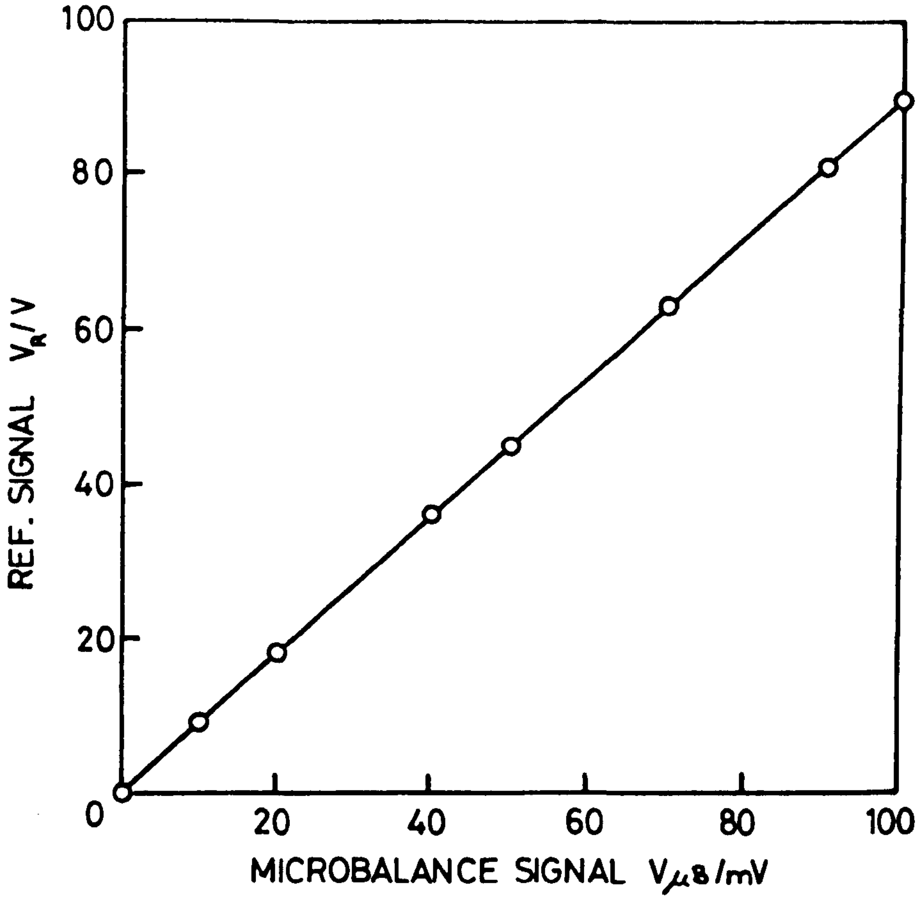

Fig. 3.10 Servo characteristic

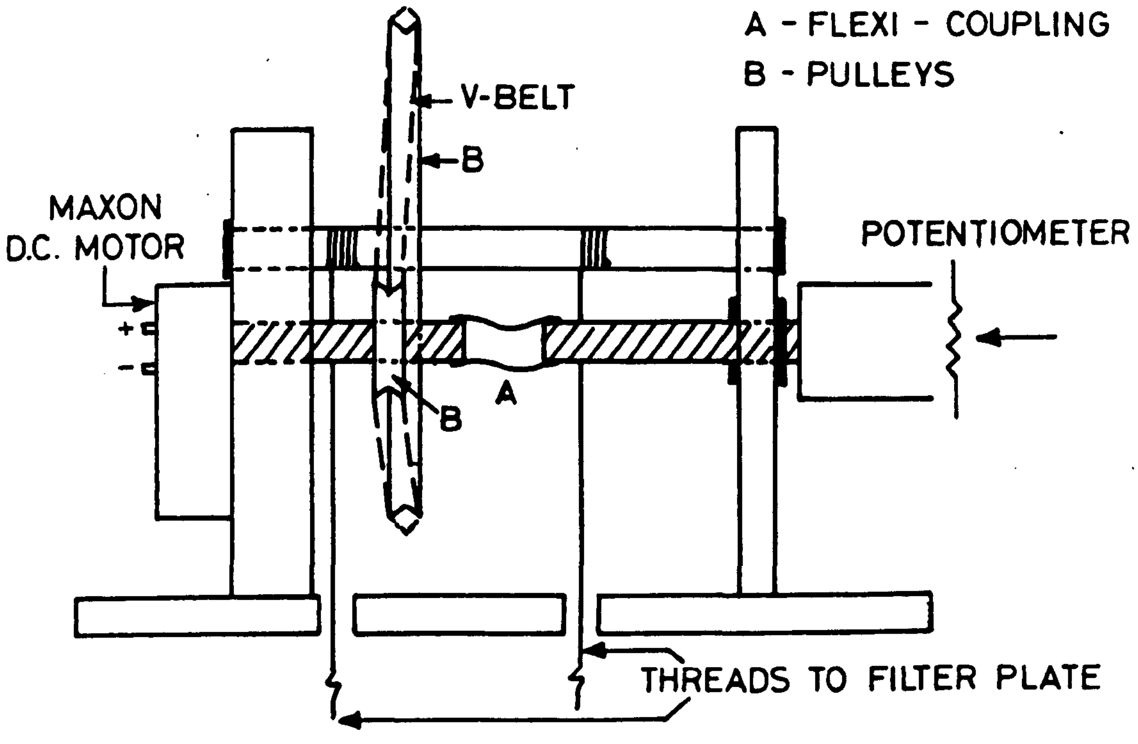

Fig. 3.11 The mechanical system for surface pressure control (Diagrammatic).

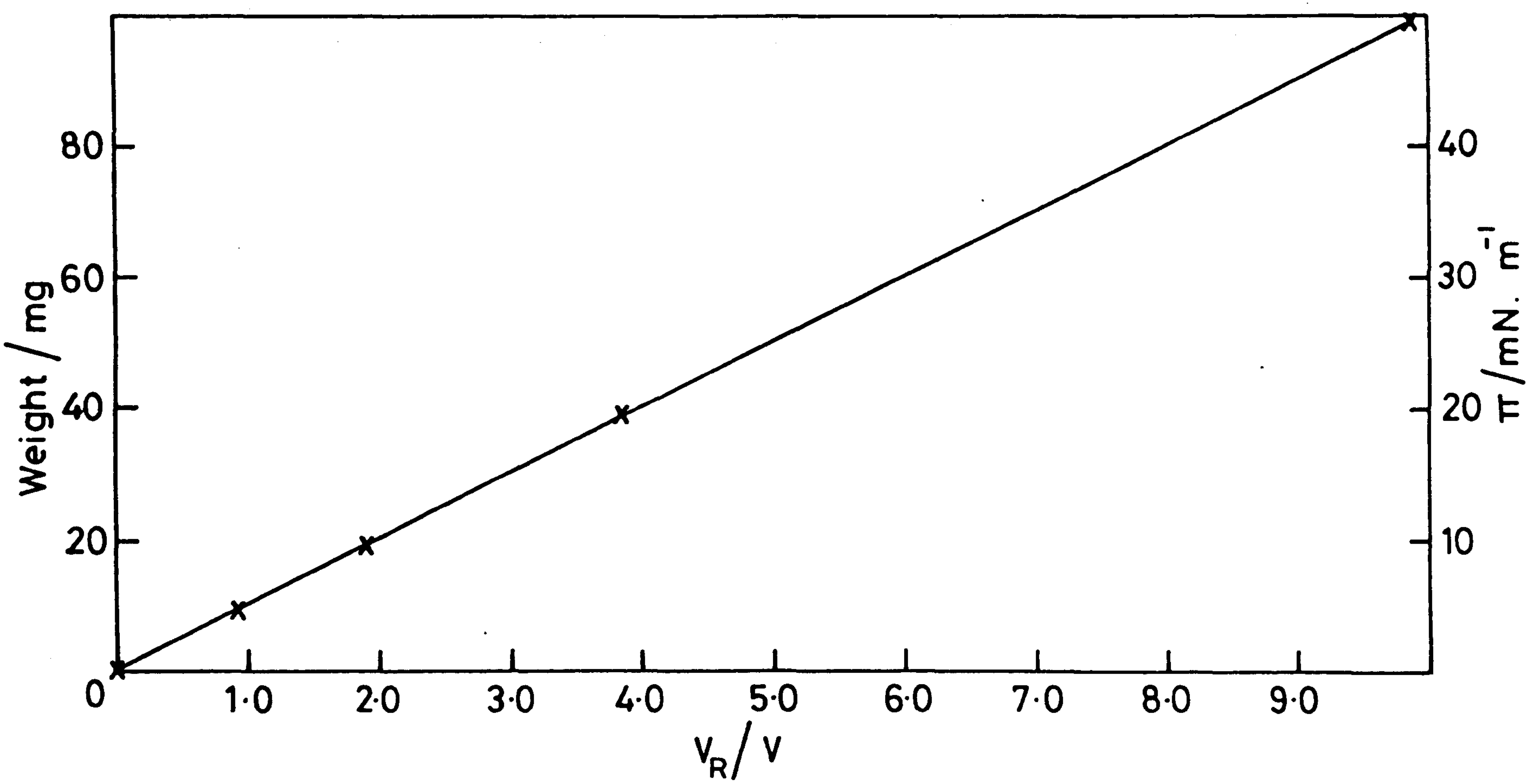

Fig. 3.12 Servo calibration curve

facilitating the measurement of pressure-area curves for the monolayer system. This is discussed in detail in section 3.4.

3.3 FABRICATION TECHNIQUES

The last section described the design of the fabrication system developed during the present investigation. Since Langmuir film fabrication is very much an area where meticulous attention to detail is necessary for obtaining consistent results, other details of the experimental procedure will now be delineated.

3.3.1 Materials

Generally, it is essential to use the purest grade of materials available and this is true especially with regard to surface-active contaminants. The materials employed in the fabrication system e.g. pyrex, PTFE etc. have already been discussed. It is obviously necessary to pay particular attention to the cleaning of those solid surfaces which come into contact with the monolayer system and accordingly, this subject is discussed in some detail in a later section (3.3.2). The chemicals and reagents used in the fabrication of samples are dealt with below.

3.3.1.1 The Film Material : Stearic Acid

It is necessary that the film material fulfil certain requirements, quite apart from the general condition that it should spread spontaneously or when dispersed from a solution of a suitable solvent. Firstly, the molecules must be amphipathic i.e. they should be hydrophilic at one end and hydrophobic at the other so that their alignment is possible after compression on the subphase surface. Secondly, the film material should be insoluble in water. Although other materials satisfy these requirements, most of the work to date has been performed on fatty acids and their salts.

The structure of the material used in the present work, Stearic acid, is shown in Fig. 3.13. The H^+ ion in the hydrophilic end group

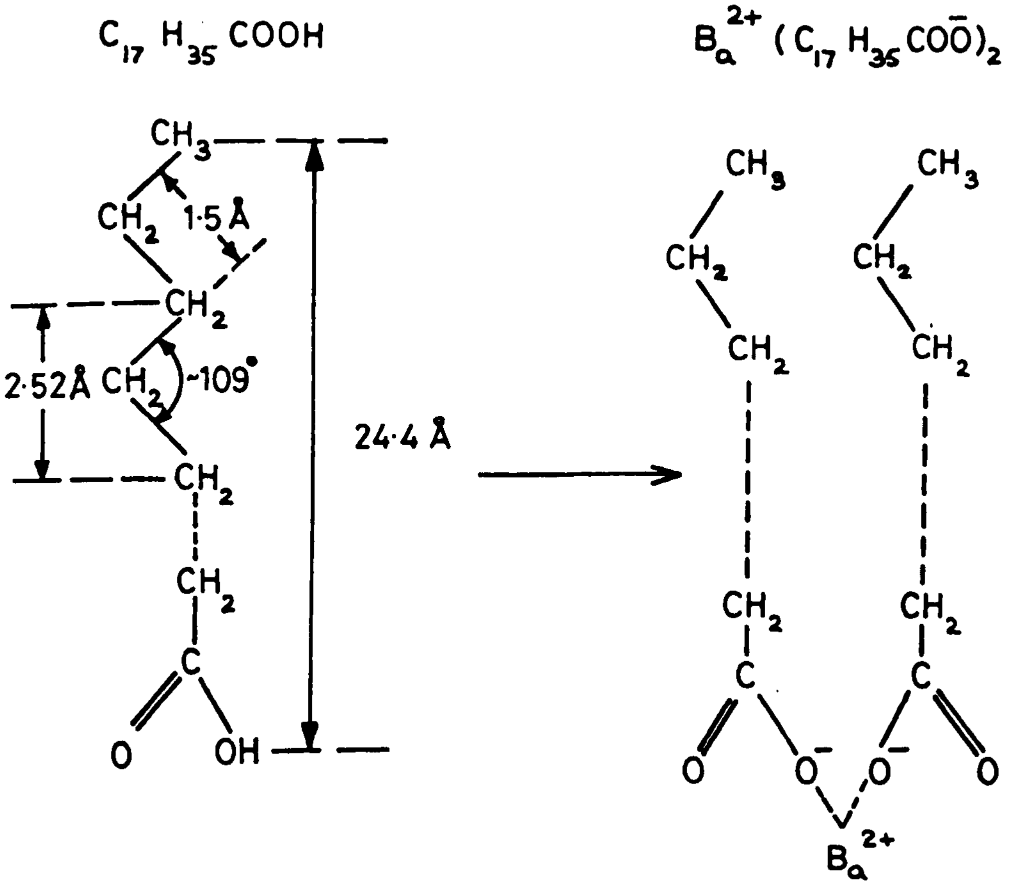

Fig. 3.13 The chemical structure of stearic acid and its barium salt

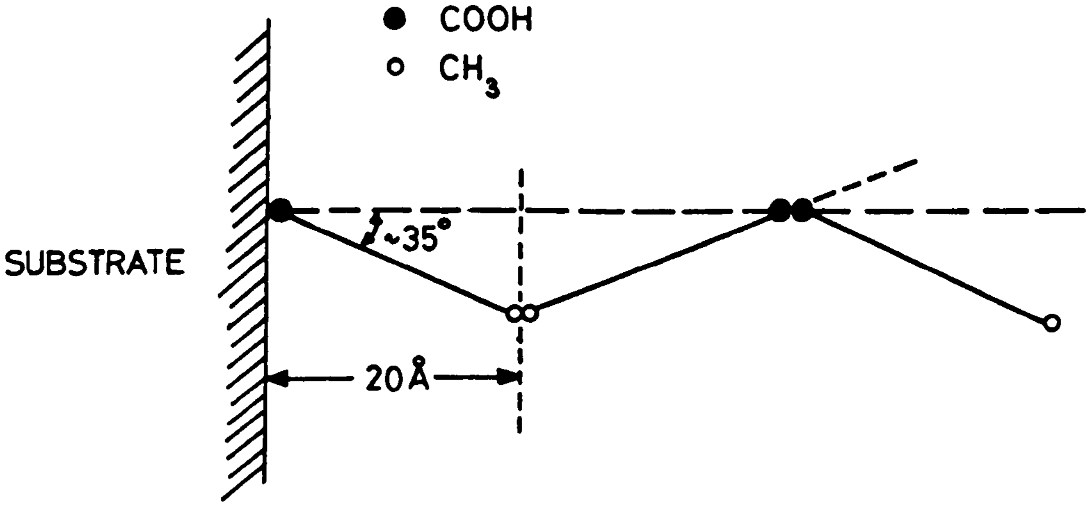

Fig. 3.14 Possible arrangement of molecules in stearic acid/stearate multilayer films (see text).

may be replaced by a divalent metal ion (e.g. Ba^{2+} or Cd^{2+}), introduced into the subphase in the form of a soluble salt (usually the chloride) of the desired metal. The metal ion combines two acid molecules following the reaction

$$2\ (C_{17}H_{35}COOH) + M^{2+} \rightleftharpoons M^{2+}\ (C_{17}H_{35}\ COO^{-})_2 + 2H^{+}.$$

This reaction and hence the extent of conversion of the stearic acid to its salt depends critically on the subphase pH. Generally, increased stability of the monolayer results from metal ion inclusion. However, this advantage is partially offset by the fact that as a result, the monolayer becomes more rigid and consequently the risk of defects in the transferred film increases(3, 8). Clearly therefore, in practice preliminary experiments need to be conducted to optimise the subphase pH, and this will be discussed further in section 3.4.

According to detailed X-ray studies of single crystal stearic acid(9), the length of the molecule is 2.44 nm. Thus the spacings and angles between successive CH_2 groups will be as shown in Fig. 3.13. However, X-ray measurements reported by Carcem(10) on stearic acid Langmuir films give the length of the molecules as 2.0 nm, which would imply that the molecules are not aligned quite perpendicularly to the substrate surface. A possible arrangement of the molecules in the Langmuir film is shown in Fig 3.14.

The stearic acid used in the present work was supplied by Fluka A. G. ('puriss' grade) and Fisons (Analar, nominally 99.5%) and used without further purification. These materials were generally stored in a dessicator.

3.3.1.2 Solvents

In its normal form, stearic acid is a crystalline powder, and will not therefore spread spontaneously on the subphase surface. To aid dispersion, the stearic acid was spread from solution of a suitable solvent. The requirements on the solvent are relatively simple; it should have sufficient solvent power for the material concerned, be chemically inert with respect to other materials used in the monolayer system and it should evaporate completely after dispersion. In practice, the following solvents were found to be satisfactory for making dispersion solutions:-

(1) Petroleum ether (60-80°C) - 'Special for chromatography' grade and

(2) n-Hexane (60-80°C) - 'Special for Spectroscopy' grade.

Both of these materials were supplied by BDH and used without further purification. Solvent purity with respect to surface-active contaminants was verified ocassionally by blank solvent spreading experiments and found satisfactory.

3.3.1.3 Water

The water used in film fabrication should have low conductivity, but more importantly it should have high surface tension. In the present system, the water was obtained from a Quickfit double distillation still fitted with silica-sheathed heating elements. Mean surface tension values for this water, obtained at 25°C were within the range 71.9 - 72.1 m Nm^{-1} which is generally believed to be adequately high(4). Resin de-ionised water was not used as it usually contains organic material(6).

3.3.1.4 Subphase Additives

As discussed above, it is usual to add a small number of divalent metal ions to the subphase. These were generally added in the form of the metal chloride since this salt was found to be readily soluble in the subphase. Depending on the stearate desired, the chlorides of barium, calcium and cadmium were employed and these were added to the subphase to a concentration of 2.5×10^{-4} M. This concentration was chosen so as to avoid the possibility of the precipitation of metal hydroxides and carbonates at higher pH values(8). All the chlorides were of Analar grade and were supplied by BDH. Occasionally, it was necessary to add a few drops of either sodium hydroxide solution or hydrochloric acid to the subphase in order to adjust the pH. These were of 'Aristar' grade and prepared to 0.1 M strength.

3.3.1.5 Paraffin wax and its application

The rims of the glass trough used in the present fabrication system were made hydrophobic by the application of paraffin wax. It was important to ensure that this was not a source of surface-active contamination and thus the paraffin wax was generally purified before use following a method due to Davdani(11). The purified wax was stored as a saturated solution in petroleum ether and applied to the trough with the aid of some gauze wrapped around a glass rod. After evaporation, this left a smooth, hard surface with high contact angle. However, the coated trough was generally left to dry for a further period (10-20 hours) before being rinsed repeatedly in double-distilled water. Before use, it was usual to monitor the surface tension of a clean subphase contained in the trough for 1-2 hours, to ensure that the wax was not contributing surface-active contaminants.

3.3.2 Cleaning Methods and Handling

It was necessary to establish a rigorous cleaning schedule for all components in the system which were likely to come into contact with the spread monolayer. Most items were cleaned by ultrasonic agitation in a 10% Decon solution for 1-2 hours. Residual cleaning was effected by soaking the items in 10% Decon overnight and then thoroughly rinsing them in running double-distilled water. The items were oven-dried in a dust-free area and then stored in a dust-free cabinet.

There were several components which required more specific treatment. Wax from the trough rims was removed by using tissues soaked in acetone before the trough was subjected to the cleaning treatment described above. With the compression barriers, it was necessary to occasionally separate the stainless steel backing from the PTFE barrier and polish the two components separately before ultrasonic cleaning in 10% Decon. This polishing was done using Balzer's No. 2 substrate cleaner for the barrier while for the backing, fine wet-grinding was found to be most effective.

The Wilhelmy sensor and filter paper plate were cut out of filter paper and generally left in double-distilled water for extended periods of up to two weeks before use. Regular changes of the water ensured the leaching-out of any surface-active contaminants. The platinum wire supports were first soaked in acetone before following the same procedure. The complete items were stored in double-distilled water in a dust-free cabinet.

In addition to components actually used in the fabrication system, a considerable amount of glassware was also necessary. The cleaning of these items generally followed the cleaning schedule described above.

Once clean, scrupulous care was taken in the handling of all items. Generally, tweezers or tongs (for the larger items) were used. As an additional precaution, it was usual to wear disposable rubber gloves to further eliminate the possibility of the transfer of grease etc. during handling. Finally, most items were rinsed with the appropriate clean solvent immediately before use.

3.3.3 Substrate Preparation and Electrode Deposition

The transfer of Langmuir films onto metal substrates for electrical measurements has received considerable attention(7, 12-13). It has been noted that the subsequent properties of the device depend critically on the nature of the substrate and in particular on its degree of surface smoothness. Accordingly, this section will describe the procedures adopted in the present investigation to produce substrates for Langmuir film deposition. Since it is an equally important theme in the preparation of devices for electrical studies and in particular for inelastic tunnelling experiments, particular reference will be made to the various additional precautions which were taken during this stage to minimize contamination.

The majority of structures investigated in the present work were metal-insulator-metal (MIM) devices prepared on glass microscope slides. The initial preparation of these samples consisted of the evaporation in vacuum ($\sim 10^{-5}$ Torr) of base metal electrodes onto carefully cleaned 'Chance Select' glass microscope slides (76mm x 11mm). The electrode geometry was defined by a brass mask held close to the substrate during the evaporation. In addition to these samples, a different type of structure was fabricated for structural studies. For these, it was found more convenient to coat the whole of the glass slide (38mm x 18mm) with the desired base metal film and hence masks were not generally required; the glass slide being simply located in a special holder.

The initial preparation of glass slides for base metal evaporation was carried out as follows. Chance select microscope slides which were free of obvious defects were first cleaned with Balzer No.2 substrate cleaner. This was followed by an additional de-greasing operation consisting of ultrasonic agitation for 15-30 minutes in 10%

Decon. To remove all traces of the detergent, the microscope slides were then rinsed several times in running tap water and double-distilled water before finally being hung to dry in a clean oven at 70°C. At all times during this cleaning procedure and subsequently the slides were handled with tweezers to avoid re-introducing contamination. Generally, since contamination can also be introduced from the mask and slide holder used during evaporation of the metal electrodes, a similar cleaning procedure was followed for these items prior to their use. It was usual however in this case to remove all traces of previous evaporations from these items with fine wire-wool prior to any further cleaning.

The next stage in the preparation of substrates consisted of the evaporation of the base metal film from one of two evaporation plants (NGN type 12-SG-2/ Nanotech Autocoater 300). Several special precautions were taken at this stage in an attempt to further eliminate contamination:-

(1) In addition to the usual liquid nitrogen trap before the diffusion pump, a series of baffles and an extra cold trap in the roughing line were incorporated in the evaporation plant to further reduce pump fluid back-streaming.

(2) 'Santovac 5', a polyphenyl ether specially designed for use in clean vacuum systems, was used as the diffusion pump fluid.

(3) Since a vacuum system is invariably 'dirty' after a shutdown, an aluminium evaporation was performed at the start of each day to remove any contaminants from the system.

(4) It was usual to clean the evaporator prior to any evaporation by establishing a glow discharge in oxygen (partial pressure ∿ 40 m Torr) using a current of 60 mA for about five minutes.

(5) Prior to the deposition of the base metal film, the microscope slides were further cleaned by exposure to an identical glow discharge for about 30 s.

The base metal film was generally evaporated to a thickness of about 200 nm in vacuum better than 10^{-5} Torr, with the evaporation being carried out slowly ($\sim$ 3-5 nm s^{-1}) in order to ensure smooth coatings. Generally, the purest grade (at least 99.99%) metals were used for these film evaporations. In the case of samples to be used for electrical investigation, the electrode geometry was defined by a brass mask so that the completed device could be used with a modified Radio Spares PCB edge connector sample holder which permitted four-point probe electrical measurements (described in the next chapter). The slide holder and mask are shown in Fig. 3.15, from which it will be seen that the arrangement allowed the fabrication of five MIM junctions on one glass slide. The metals usually employed for the base electrode were aluminium, tin or more rarely, lead.

From the viewpoint of electrical measurements, it was important to ensure that the whole of the base electrode was covered as far as possible by a coherent oxide layer. In the case of aluminium electrodes, this was achieved by simply exposing the electrodes to room air. For the tin electrodes however, since tin does not oxidise so readily, it was usual to promote the initial growth of oxide in an oxygen glow discharge. This was carried out at a partial pressure of oxygen of $\sim$ 50 m Torr using a discharge current of 8 mA for about 30s. It was anticipated that this would ensure complete oxide coverage. As discussed earlier, the growth of subsequent oxide layers, either in air or when in contact with the aqueous subphase, is an inevitable feature of Langmuir film fabrication. In this work however, attempts were made to treat all junctions on an equivalent basis so that the formation of further oxide was as reproducible as possible.

Usually, Langmuir film deposition was undertaken as soon as base-electrode evaporation was complete. The transfer of these films

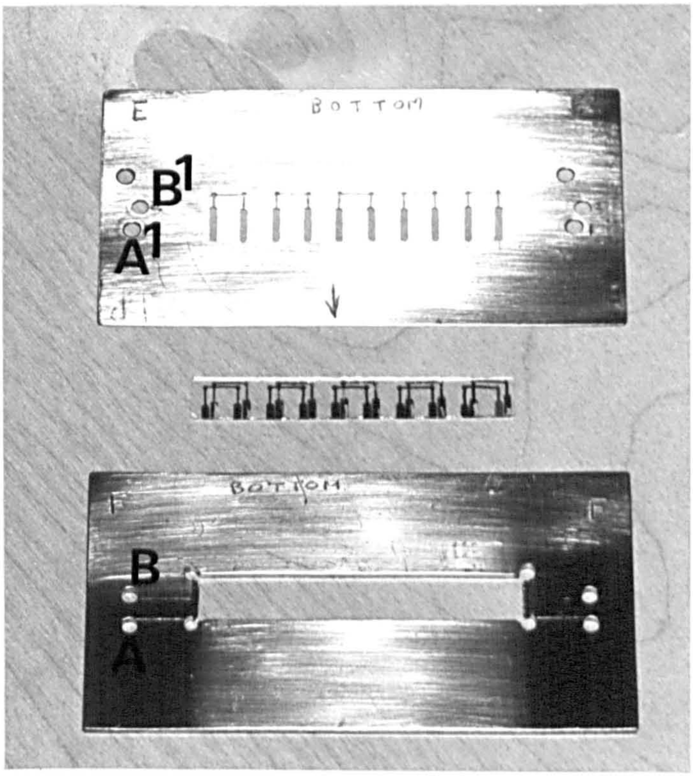

<u>Fig. 3.15</u> Photograph of the mask, slide holder and a completed device. The aligning holes $A^1/_A$ and $B^1/_B$ were aligned for the first and second evaporations respectively.

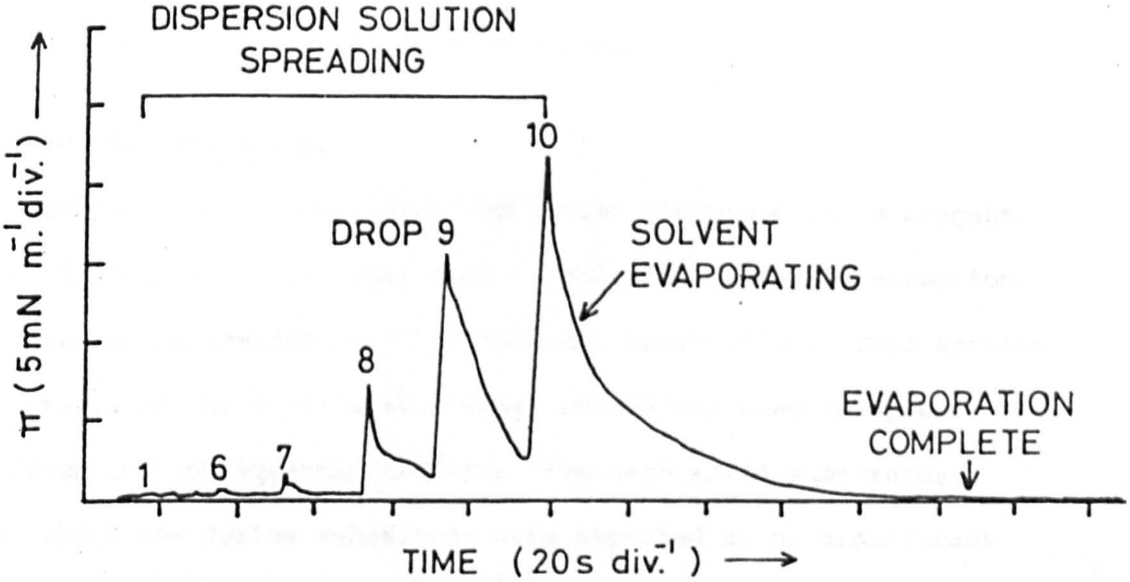

<u>Fig. 3.16</u> Typical surface pressure versus time plot obtained during film spreading

is discussed in detail in section 3.4, but for now it will be assumed that the requisite film has been transferred and that the samples are ready for counter-electrode evaporation. For this, a similar procedure to that described above for the evaporation of the base electrode was generally adopted. The metals used for the counter-electrodes were lead and aluminium, and occasionally tin. Particular care was taken to ensure that this evaporation was carried out slowly so as to reduce the possibility of damage to the organic film. In this regard, lead is eminently suitable for use as a counter-electrode since it evaporates at a relatively low temperature. With the other metals used as counter-electrodes, it was decided after some preliminary experiments where substrate cooling was employed, that no particular advantage accrued as a result, and generally counter-electrodes were evaporated without this precaution being taken. For this, the same slide holder and mask as that used for the first evaporation were employed - the correct electrode geometry being produced by a different alignment of the locating holes (see Fig. 3.15). The completed junction (also shown in Fig. 3.15) was generally stored over silica-gel in a dessicator.

3.4 LANGMUIR FILM DEPOSITION

Although the Langmuir film deposition technique is an elegantly simple one in concept, it is clear that considerable care and attention to detail need to be expended in its practical application. This section presents details of the various additional procedures used to spread Langmuir films and subsequently transfer them onto solid substrates. Since the conditions during deposition were expected to be significant in determining final film quality(6-7, 12), considerable effort was made to define optimum conditions for film transfer and these also will be discussed in this section.

3.4.1 Film Spreading

It is usual to spread monolayers from a suitable dispersion solution. In this work, the monolayer dispersion solution was mixed in a 10 ml volumetric flask, using stearic acid and one of the two solvents, n-Hexane or petroleum ether (see section 3.3.1.2) at a concentration of ∿ 1 mg ml^{-1}. Higher concentrations were avoided since in this case, the fast evaporation of the solvent could result in patches of agglomerated material, whereas with lower concentrations there was always the possibility of solvent molecules becoming trapped in the monolayer.

Prior to the spreading of this solution, the subphase surface was cleaned and the surface pressure system calibrated using the procedures discussed previously. It was necessary to arrange initially that a sufficient surface area was available for film spreading to ensure an area per molecule of ∿ 60 - 80 Å^2. This estimate was based on the consideration that at this value of area/molecule, the monolayer is in the gaseous phase (see Fig. 3.1) and thus complete spreading would result. For spreading, the working area of the subphase surface was maximised by reversing the compression barrier and the filter paper plate film reservoir (see section 3.2.5.2) to their limits. Since this area was known the amount of dispersion solution of concentration 1 mg ml^{-1} to ensure an area/molecule of 60-80 Å could easily be calculated.

Spreading of the film was accomplished by applying a few drops of the stearic acid dispersion solution to the subphase surface. Since the amount of liquid required to produce monolayer coverage was extremely small (20-30 µl), a micrometer syringe (Agla/Gallenkamp) was used for this purpose. The syringe was normally first flushed out with the appropriate solvent before being filled with the dispersion solution. This solution was then applied, one drop at a time and very close

(∿ 2mm) to the subphase surface to ensure maximum evaporation of the solvent. To further aid the rapid evaporation of the solvent, it was usual to leave the door of the trough cabinet open for a few minutes. The surface pressure was monitored on the chart recorder during the whole of the film spreading operation, thus providing a useful check on solvent evaporation. A typical trace is shown in Fig. 3-16, suitably annotated to make clear the various stages in the spreading operation. This procedure was particularly useful in helping to check on effects occasionally found by workers$^{(6)}$, where a significant amount of solvent becomes trapped in the monolayer and persists for long periods. No such artifact due to a 'solvent effect' was found in the present work with either of the two solvents used. However, as an additional precaution to ensure quantitative spreading, it was usual to allow at least half an hour (with the cabinet door open) before compressing the monolayer.

3.4.2 Deposition Conditions

Several parameters were expected to be of critical importance in determing the final quality of the Langmuir film. An examination of these, forms the subject of this section.

3.4.2.1 Surface Pressure and Subphase pH

As discussed earlier, for effective transfer it is important to ensure that the monolayer be compressed to a point where the molecules are tightly packed together, i.e. the solid phase. On the other hand, it is equally important to ensure that the film is not over-compressed to the point where it collapses and is no longer monomolecular. The optimisation of the surface pressure for film transfer was achieved by studying the appropriate surface pressure - area/molecule (π - A) relationship. since the π-A isotherm is known to be pH dependent, this procedure had the additional benefit of providing a guide for the optimisation of the subphase pH.

Typical π-A curves for stearic acid/barium stearate monolayers obtained using the apparatus developed in this work are shown in Fig. 3.17. They were obtained by slowly compressing ($\sim$ 5 cm^2/minute) the spread monolayer and monitoring the surface pressure as a function of surface area (later converted to area per molecule in $Å^2$/molecule) on the X-Y recorder. The compression was undertaken at this relatively slow rate to ensure that the film remained in equilibrium at all times during the compression operation(14).

Leaving aside the effect of pH for the moment (see Fig. 3.17), it has been found that all saturated fatty acid/salt films exhibit essentially similar behaviour(6) and that there are three distinct regions in the π-A curve. Critical changes in the compressibility of the monolayer occur at 25-26 $Å^2$/molecule when initial close-packing of the carboxylate end groups occurs (the liquid-condensed phase) and at $\sim$ 23 $Å^2$/molecule. This was considered by Adam(15) to correspond to a re-arrangement of the polar end-groups of the molecules, permitting closer packing of the hydrocarbon chains of adjacent molecules. Beyond this solid phase, the film collapses due to the piling up of molecules.

The isotherm is strongly influenced by the presence of surface-active contamination, resulting in pronounced deviation from ideal behaviour. This was usually cured by a thorough cleaning of the whole system. In addition, it was customary to occasionally plot π-A isotherms as a routine procedure to check on the cleanliness of the system.

For film transfer onto solid substrates, it is important that the spread monolayer is compressed to the solid phase, such that the molecular area remains sensibly constant for a large change in pressure. This avoids the possibility of transferring inhomogenities such as would occur if transfer was accomplished with the molecules loosely packed (i.e. in the gaseous or liquid-condensed phase) or that of

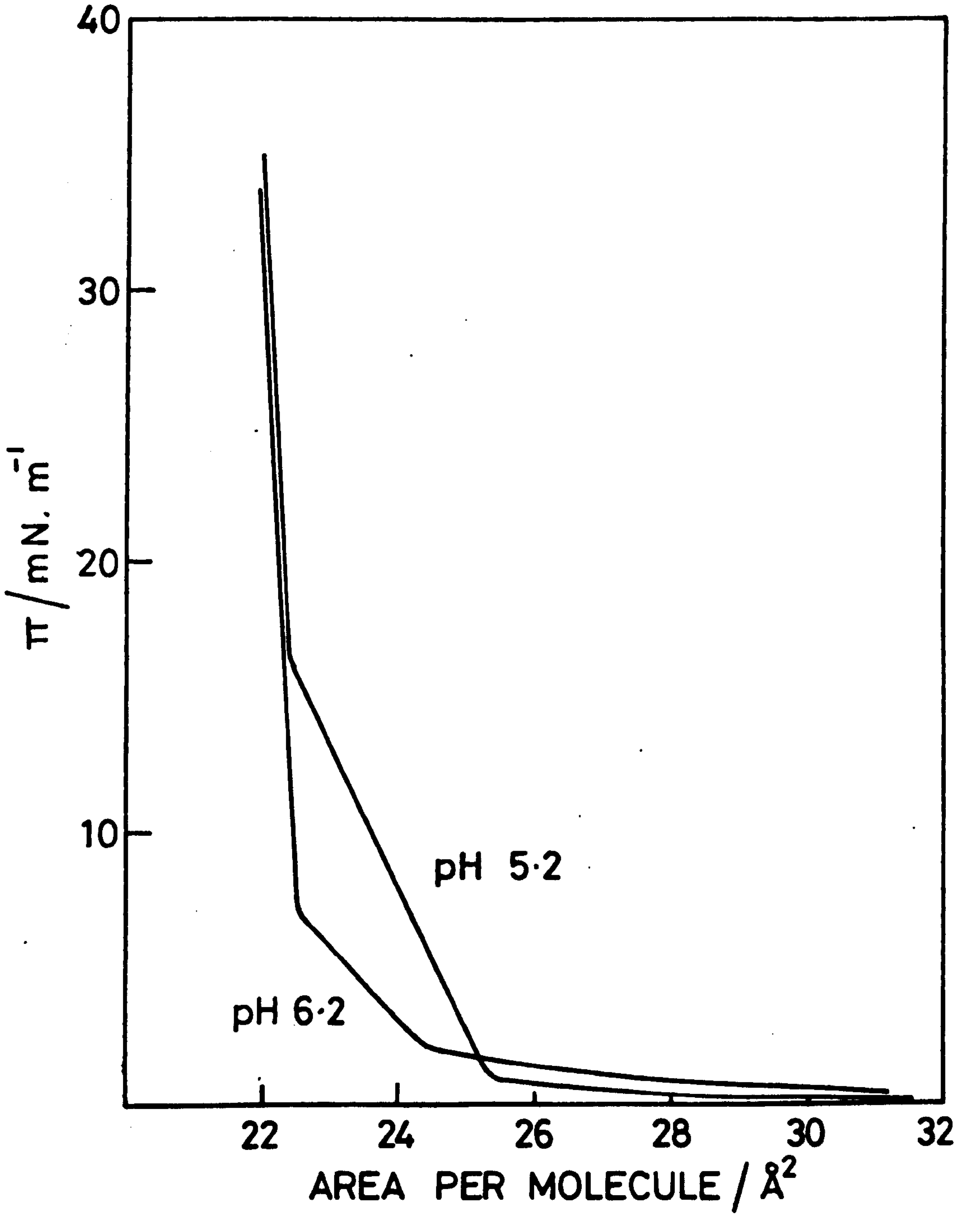

Fig. 3.17 Pressure-Area/molecule (π-A) isotherms for a stearic acid/barium stearate monolayer at pH 5.2 and pH 6.2

transferring agglomerated patches if the monolayer had collapsed under the application of excessive pressure. The typical π-A curves obtained in the course of the present work suggested that the optimum surface pressure for the transfer of the films used, would be in the range 25-30 mN m^{-1}.

The π-A curve is modified by an increase in pH so that the liquid-condensed phase is effectively eliminated (see Fig. 3.17) and the monolayer goes to all intents, directly to the solid phase at ∿ 22 $Å^2$/molecule. The typical behaviour observed was that up to pH ∿5.2, the subphase pH has little effect on the isotherm shape. Above this value of pH however, the isotherm is considerably modified with the effect becoming more noticeable with increasing pH, until at pH 6.5 the liquid-condensed phase disappears completely. This behaviour is readily understood in the following terms. Above pH 5.2, the dissociation of the acid molecule becomes significant and results in the formation of barium stearate. Here, a barium ion combines two acid molecular together which, because of the increased cohesiveness between molecules, helps to stabilise the monolayer (see section 3.3.1.1.). The reduction of the liquid condensed phase at pH 5.2. and the lowering of the pressure at which the transition into the solid phase occurs are thus symptomatic of this enhanced stability. Furthermore, since the degree of dissociation of the acid and hence its conversion to the salt increases with subphase pH, it can be expected that the liquid-condensed phase will be further reduced at higher values of pH, which of course is precisely the effect that is observed.

In addition to the enhanced stability of the monolayer at higher values of pH as a result of metal ion inclusion, it has been found that relatively high pH values improve film-substrate adhesion(16). These effects are offset however by an increased solubility in the subphase and also the possibility of the precipitation of metal hydroxides and carbonates(8), Clearly thus, there is a need for optimisation of the pH. Analysis of the π-A isotherms obtained in this work suggested that films fabricated approximately in the middle of the range pH 5.2 - 6.5 would probably produce the correct proportion of stearic acid and salt to give a flexible monolayer covering with good adhesion to the substrate. Generally therefore, films were transferred in the pH range 5.7 - 6.0, which also avoided metal hydroxide precipitation and reduced the risk of transferring defects which has been found to increase as monolayers become more rigid with increased pH(3, 8, 17). Transfer in this range had the additional benefit of not necessitating any pH adjustment, since this range coincides well with the pH of distilled water in equilibrium with the atmosphere.

3.4.2.2. Subphase Temperature and Transfer Rate

Generally, the subphase temperature has a less crucial effect on Langmuir film transfer and films were transferred satisfactorily in the range 20 - 24°C. Its primary effect is to limit the rate of film transfer(16). To obtain good quality films, it is vitally important that the first layer is transferred relatively slowly and without defects. In the case of multilayer films, faults in this initial layer can be replicated in subsequent layers. Thus, dipping speeds as low as 5 mm/minute were used for this first layer and it was possible to increase this to ∿ 10-15 mm/minute for further layers.

Table 3.1 summarises the deposition conditions found satisfactory for the films fabricated in the present work.

3.4.3 Film Transfer

Before film transfer, it was necessary to establish the optimum deposition conditions (summarised in Table 3.1) adopted in the present work. This generally meant allowing about 1-2 h for the pH and

TABLE 3.1 SUMMARY OF DEPOSITION CONDITIONS

Film Material		Stearic Acid $CH_3(CH_2)_{16}COOH$
Dispersion Solution	Solvents	Petroleum Ether (60-80°C) n-Hexane (60-80°C)
	Concentration	1 mg ml^{-1}
Subphase	Metal ion and concentration	2.5×10^{-4} M $Ba^{2+}/Cd^{2+}/Ca^{2+}$ double-distilled water
	pH	5.8 - 6.0
	Temperature	20 - 24°C
Surface Pressure		25 - 30 mN m^{-1}
Deposition Rate		5 mm min^{-1} (Initial layer) 10 mm min^{-1}
Substrates		Evaporated Al/Sn/Pb (200 nm) on glass (MIM junctions) Au/Ag/Al/Sn (200 nm)

temperature of the subphase to stabilise. Following this, the subphase surface was cleaned and the surface pressure system calibrated as discussed previously. The desired operating surface pressure (usually in the range 25-30 mN m^{-1}) was then dialled up on the reference channel potentiometer of the servo system.

Spreading of the film has been described in section 3.4.1. After adequate time had been allowed for the complete evaporation of the solvent, the spread monolayer was slowly ($\sim$ 5 cm^2/minute) compressed with the slave compression barrier to bring the surface pressure approximately close to the desired value set on the servo system; the surface pressure being monitored during the whole of this operation. It was then usual to allow approximately five minutes for final re-arrangement and stabilisation of the monolayer to take place before the feedback system was employed to maintain constant surface pressure and dipping commenced.

Transfer was accomplished by dipping and retracting a prepared substrate slowly through the subphase surface. Generally, it was found that the transfer of the initial layer was the most crucial part of the whole fabrication process, especially when it was intended to deposit further layers. This was so not only because any faults in this initial layer would be replicated in subsequent layers but also because the bonding at the metal-monolayer interface is of a relatively weak and tenuous nature. By contrast, the bonding in the bulk of the film (in multilayers) relies on a stronger interaction due to the head/head and tail/tail stacking sequence (see Fig. 3.2). Thus, it was usual to transfer the initial layer (the only layer of course in the case of single-layer MIM junctions) at a relatively slow rate (5 mm/minute) and also to wait $\sim$20-30 minutes for the evaporation of any water molecules which may have been transferred along with the film(12) before further deposition. These subsequent layers could then be transferred at a faster rate (5-10 mm/minute). The configurations adopted for both MIM devices and those samples fabricated for structural characterisation are illustrated in Fig. 3.18. For these latter samples, it was found more convenient to fabricate stepped monolayer structures of several thicknesses on the same substrate.

During the deposition operation, it was usual to monitor the surface area of the spread monolayer on a chart recorder and to observe its decrease as some of the film was transferred onto the substrate (Fig. 3.19). Generally, deposition ratios (transferred film area/ substrate geometrical area) of approximately unity (± 10%) were found. The surface area-time plot also enabled the particular mode of film transfer to be distinguished. It will be recalled (see Fig. 3.2) that these are of three types, referred to as X, Y and Z type deposition, and that the particular mode operating at any one time is largely determined by the subphase pH and the nature of the substrate surface. Most of the evaporated metal substrates used in the present work produced hydrophilic surfaces which resulted in straightforward Y-type deposition. Here, no film was transferred on the first downstroke but all subsequent strokes (up and down) of the substrate through the subphase surface resulted in monolayer deposition (see Fig. 3.19). In contrast, the evaporated noble metal substrates produced hydrophobic surfaces which in principle, should have resulted in monolayer transfer on the first downstroke. In fact, with occasional exceptions, the deposition observed was similar to that observed for the hydrophilic substrates. On those occasions where transfer was indicated on the first downstroke, very low deposition ratios (∿0.1 ±10%) were found. The reasons for this anomalous behaviour are not clear. However, it is now known that the simple classification into X, Y and Z type depositions may be an oversimplification(18-20),

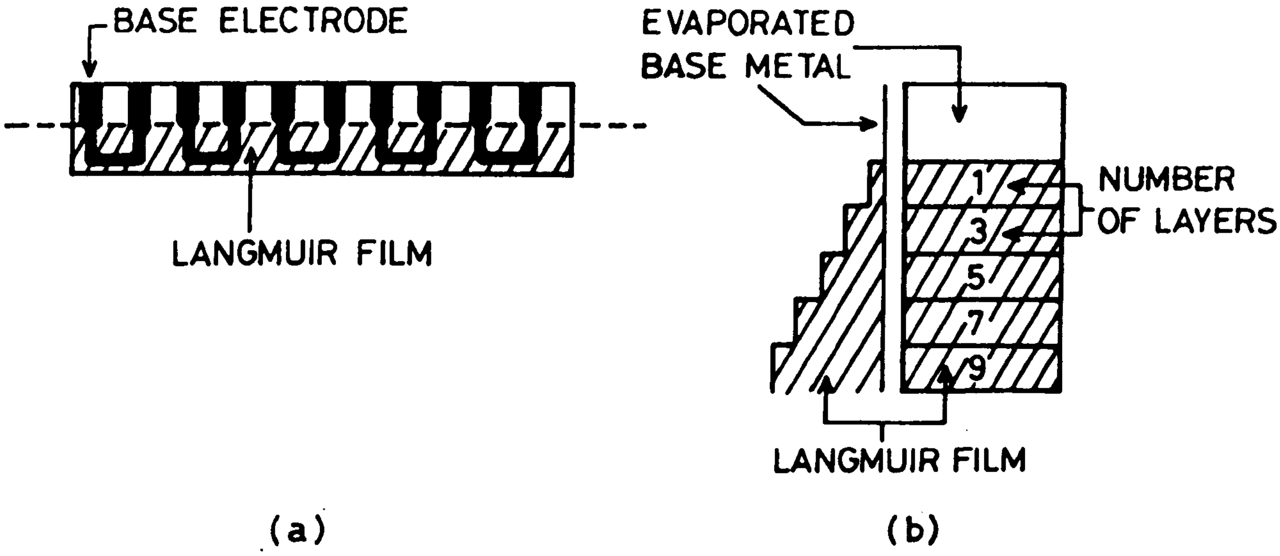

Fig. 3.18 Configurations for (a) MIM devices and (b) samples fabricated for structural characteristion. Both types of sample were prepared on glass microscope slides.

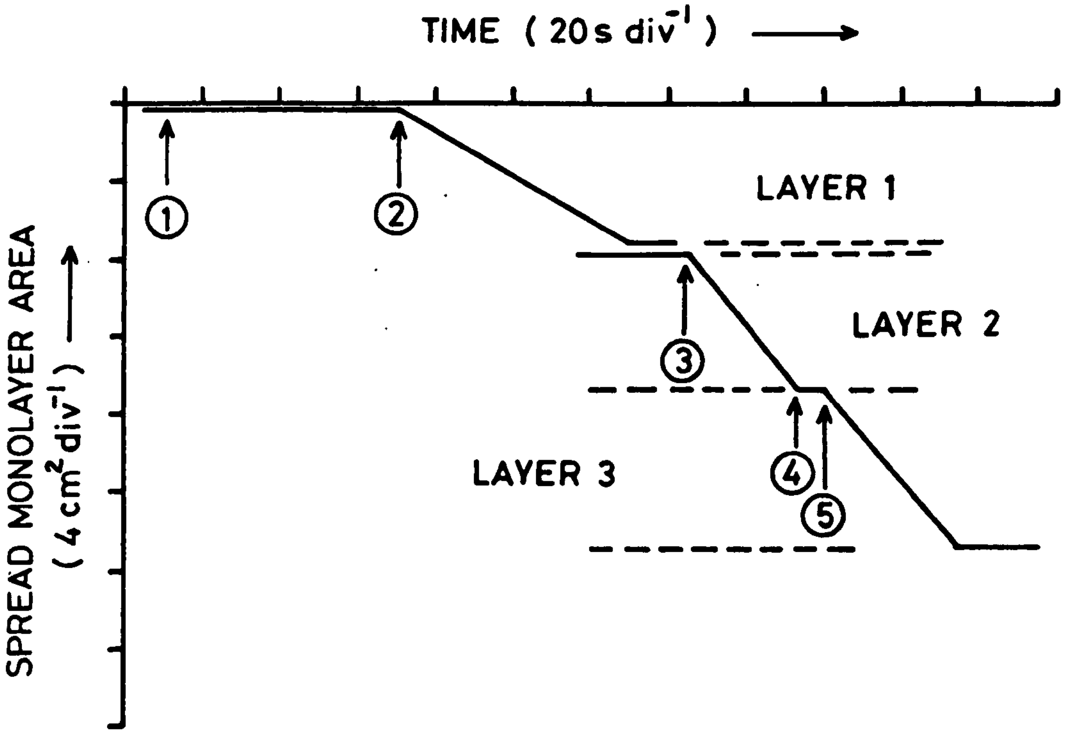

Fig. 3.19 Typical monolayer area versus time plot (1) dipping commenced, (2) sample retracted, (3) dipping re-commenced, (4) dipping stopped and (5) sample retracted. After the first retraction the sample is allowed to dry for 20-30 minutes (see text) before re-commencing dipping at point (3).

and that in fact the real process is considerably more complex. Consequently, the subject of monolayer orientation will be discussed in more detail at a later stage in this thesis (Chapter 7).

In addition to monitoring the surface area, a DVM was used to check that the surface pressure remained constant during film deposition. This was normally found to be so to within $\pm$ 0.05 mN m^{-1}. Other indications of smooth transfer were the even rolling back of the subphase meniscus as the slide emerged from the surface and the fact that they appeared completely dry after doing so. Once transfer was complete, devices were stored over silica gel for about 12-15 hours to remove any water molecules which may have been transferred along with the monolayer(21). In the case of MIM devices, this was followed by the slow evaporation of the counter-electrode (see section 3.3.3).

It will be apparent from the discussion in this chapter that the fabrication of Langmuir films is a considerably involved process where the increased precision in film transfer is only obtained at the expense of rigorous checks on vibration, surface pressure and attention to trace contaminants. The consistency and reliability of the final results reflects directly the care taken during the fabrication stage. The films obtained by using the methods developed here were characterised by Auger Electron Spectroscopy (AES) and X-ray Photoelectron Spectroscopy (XPS) in addition to the electrical methods, and the quality of results can be taken as reasonably indicative of an adequate fabrication technique.

CHAPTER 4

ELECTRICAL MEASUREMENT METHODS

This chapter describes the various methods which were utilised to obtain the electrical data presented in this thesis. It begins with a description of the sample experimental chambers and the general procedures for device handling before discussing in detail the theoretical and practical considerations which guided the use of the more specialised techniques. Methods used for the structural characterisation of the films fabricated during this work are described in a later chapter.

4.1 EXPERIMENTAL CHAMBERS

Electrical measurements at room temperature were made with the device located in the rig illustrated in Fig 4.1. This consisted of a hollow open-ended cylinder with flats machined on the outer face to facilitate the mounting of vacuum gauges. The top and bottom were sealed with conventional 'O' rings and flat brass plates. The sample holder consisted of a Radio Spares printed circuit board (PCB) 2.5 mm edge connector (type 446-551) and was mounted on the inside of the top plate. A multi-cored, shielded cable was used to take measurement leads through an Edwards vacuum coupling to the outside of the chamber where they were then soldered to a Radio Spares 25-pin connector (type 467-857). In use, this chamber was 'continuously pumped' with a rotary pump (Edwards 25c20A) and oil diffusion pump which maintained a pressure of 10^{-5} Torr. No facility existed for temperature control and consequently a separate arrangement was used where it was necessary to study the device properties as a function of temperature.

This rig consisted of an Oxford Instruments CF500 cryostat fitted with automatic temperature control (VC30, Oxford Instruments) and an integral

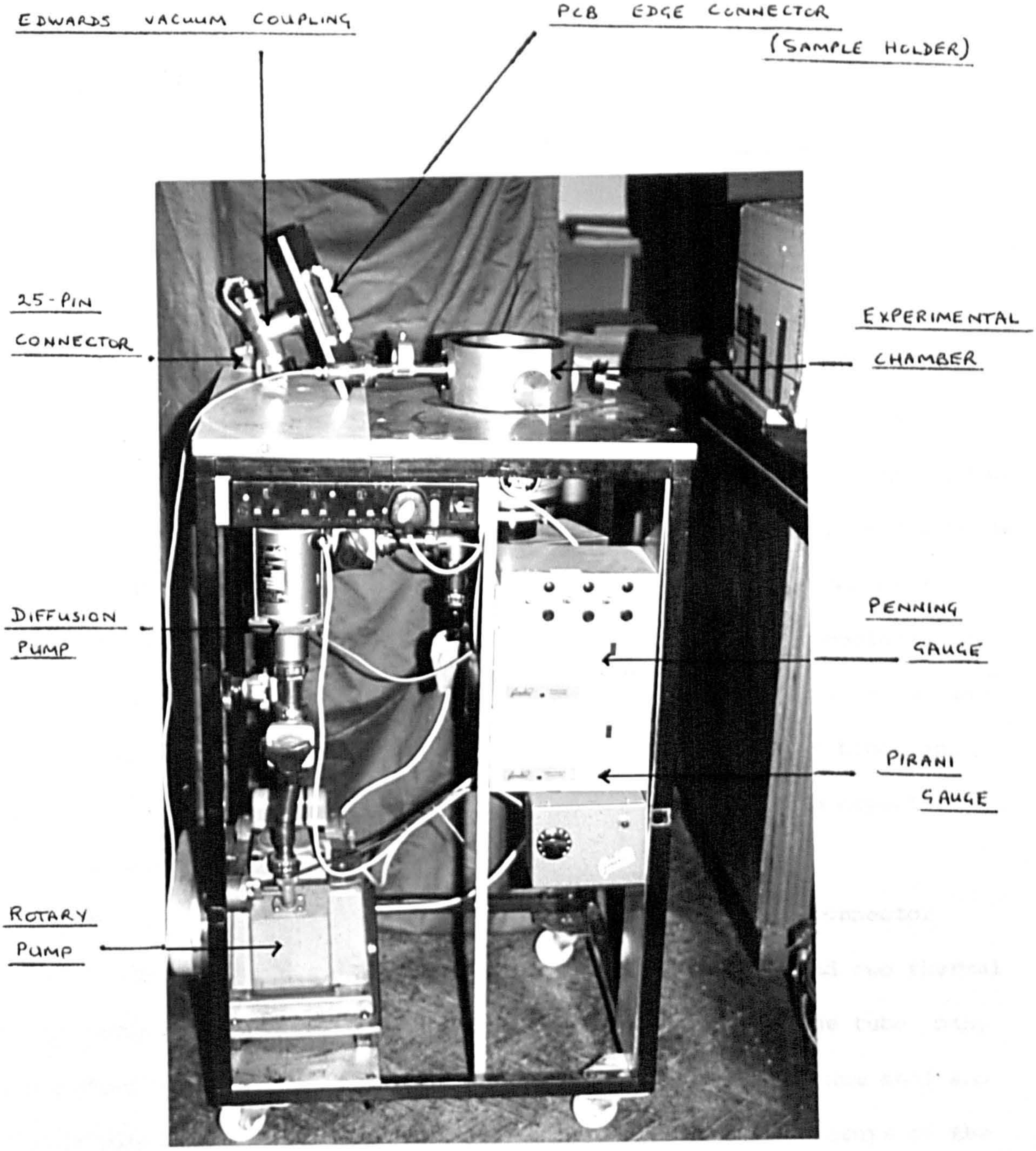

Fig 4.1: Photograph of the experimental chamber used for room temperature measurements.

transfer tube. The cryostat had an experimental chamber in the shape of a cylinder about 2 cm in diameter and ∿ 40 cm in length which was evacuated with a rotary pump through a pumping port at the top of the cryostat. The bottom 5 cm of the experimental chamber were surrounded by a copper block in good thermal contact with a cooling gas and a heater. In conjunction with the automatic temperature controller, this arrangement enabled the temperature of the experimental chamber to be maintained to within ± 0.1 K.

When in use, liquid helium (or nitrogen) was continuously drawn through the transfer tube and into the cryostat by the action of a carbon-vane oil free pump. The pumping speed was controlled by a needle valve incorporated in the temperature control unit. The temperature of the copper block in the cryostat was measured with a gold 0.03%/Fe/calomel thermocouple and deviations from a pre-set temperature were used by the temperature controller to regulate the needle valve and hence the flow of coolant. A port at the top of the cryostat allowed the admittance of helium exchange gas in order to ensure good thermal contact between the copper block and sample and an additional port allowed the enclosure around the cryostat to be evacuated with a rotary pump.

The sample holder consisted of the Radio Spares edge connector mounted at the end of a cupro-nickel tube (8 mm O.D.) which had two thermal baffles attached. The connecting wires were wrapped around the tube many times before being passed out through an improvised rubber vacuum seal and finished again in a Radio Spares 25-pin connector. The temperature of the sample holder was monitored separately with a cryogenic linear temperature senor (CLTS) consisting of fine manganin and nickel wire(Oxford Instruments). It was linear in the range 4.2-300 K and was calibrated with melting ice and liquid nitrogen by measuring the voltage across it (∿ 35 mV), with a constant drive current of ∿ 10^{-4} A supplied from an accumulator and resistance box. It thus provided a useful check on the temperature controller thermocouple.

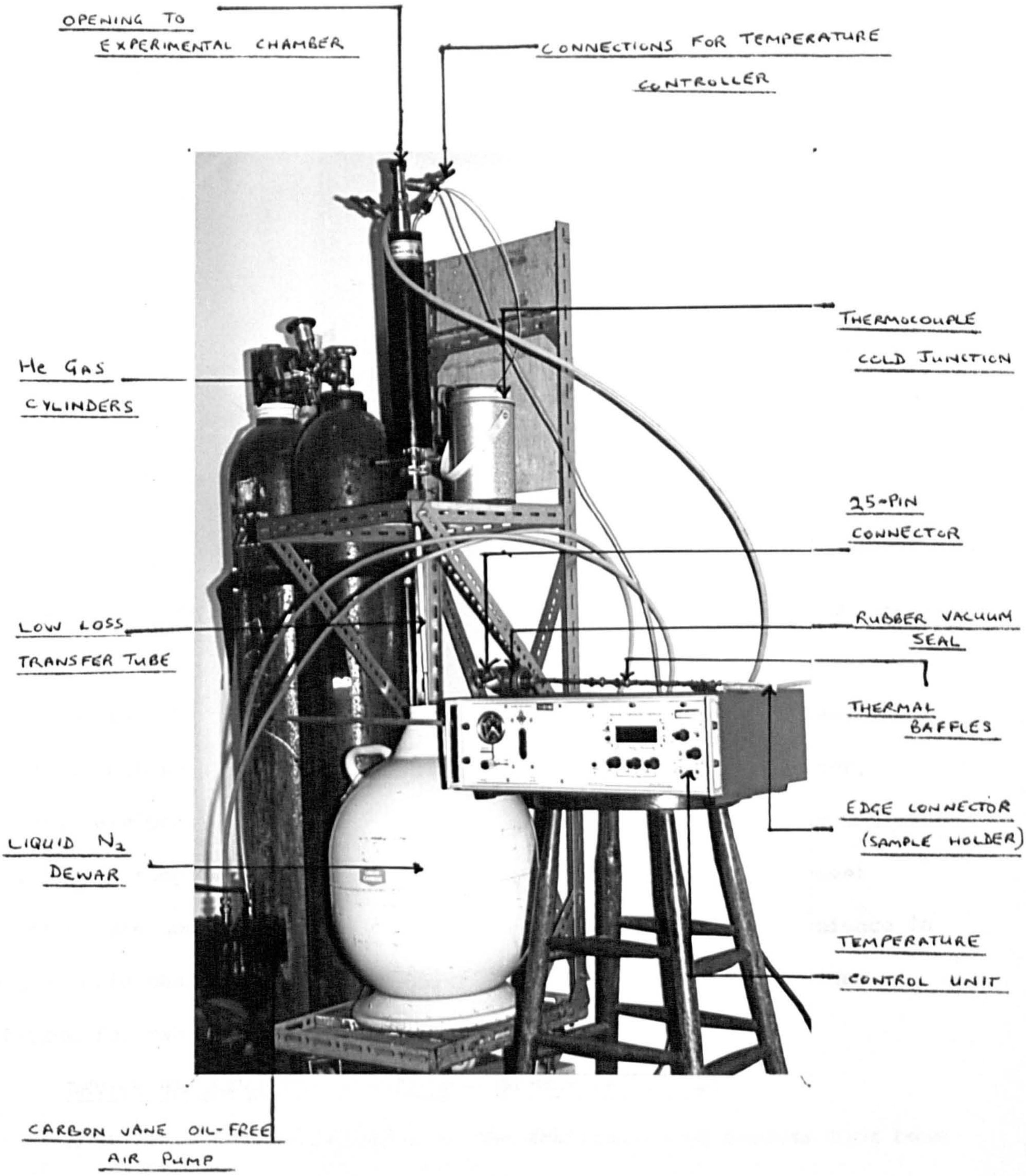

Fig 4.2: The cryostat and associated cooling equipment

An external view of the cryostat and sample holder is shown in Fig 4.2.

For making many conductivity and inelastic tunnelling measurements at liquid helium temperature, it was found convenient to simply use the liquid helium dewar itself as an experimental chamber. The sample holder consisted of a length of cupro-nickel tubing (8mm O.D.) carrying the required wiring from a 25-pin connector to another Radio Spares PCB edge connector mounted using aluminium brackets, at the other end of the tube (see Fig 4.3). In order to facilitate entry through the narrow neck (18 mm diameter) of a standard British Oxygen Company Ltd, (BOC) liquid helium dewar, the overall dimensions of the edge connector were reduced by removing all surplus plastic and by bending back the gold-plated contacts at the rear of the connector. An Oxford Instruments liquid helium dewar adaptor completed the sample holder and enabled the sample, mounted in the edge connector, to be lowered slowly and directly into the liquid helium (see Fig 4.8). No facility existed for pumping on the liquid helium and thus all the data obtained using this arrangement were at 4.2 K.

During the course of this work, slightly different arrangements for the sample holders were used where instead of the edge connector, contacts were made using conducting paint (Silver dag 915, Acheson Colloids Ltd), onto a sample mounted on veroboard. The use of the arrangement described here however, offered very definite advantages of convenience in use and rapid changeover time and for the most part was the technique preferred for making sound and reliable contacts to samples.

4.2 DEVICE HANDLING AND GENERAL MEASUREMENT PRINCIPLES

Most of the stages involved in the fabrication of devices have been discussed in the last chapter. An important step that has only been mentioned in passing however, is the drying stage, prior to counter-electrode evaporation. With freshly dipped Langmuir films, there are inevitably some water molecules picked up during the deposition process.

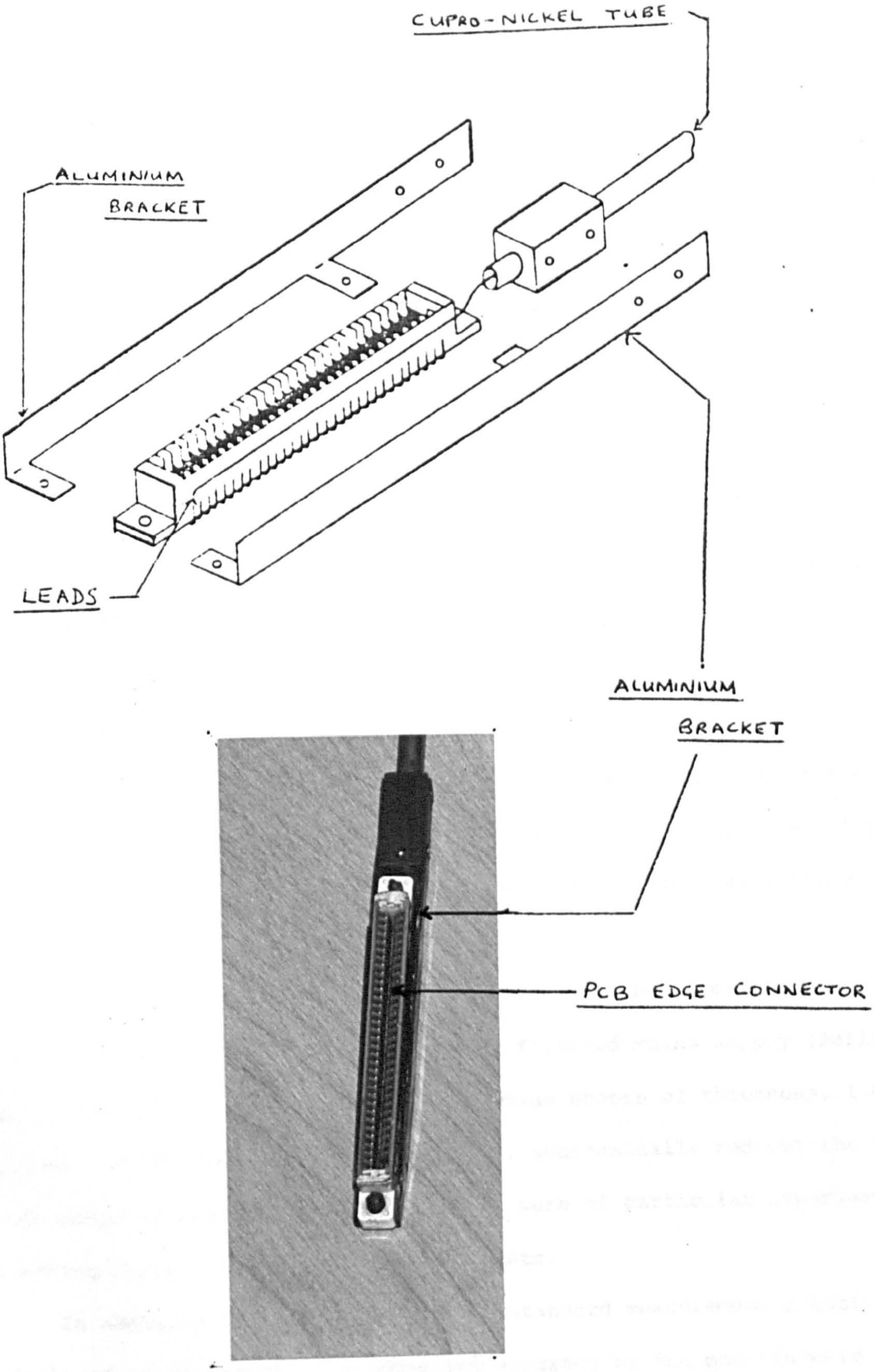

Fig 4.3: The sample holder used in conjunction with the liquid helium dewar for making measurements at 4.2 K.

Thus in common with other workers(1-2), it was usual to subject all samples to a 12-15 hours drying period over silica gel in an evacuated dessicator, before evaporating the top electrode. If this was not done, it was found that the resultant devices showed strongly irreproducible electrical properties, often with large sporadic internal voltages (discussed in Chapter 5) and broke down at a comparatively low applied bias. This drying stage was therefore included in the normal production process as a matter of course. Once fabricated, devices were generally stored under similar conditions so as to avoid any degradation of device properties under normal atmospheric conditions.

The first step in the evaluation of devices was usually a careful check on electrode continuity and junction resistances at room temperature. For these measurements, a specially constructed low power ohmmeter(3) which operated at a voltage of 10 mV was used. It was usual for about 10% of all junctions to be rejected by this preliminary check because of short circuits. Acceptable devices were then tested using the more specialised methods such as current-voltage plotting and the inelastic tunnelling measurements.

All electrical measurements were made with the experimental chambers located in a screened room with a filtered mains supply (Belling-Lee Filter, type L1822). For screening, aluminium sheets of thickness, 1.6 mm were used. These precautions,it was found, substantially reduced the problem of both radiated and mains-borne noise and were of particular importance when making inelastic tunnelling measurements.

In addition to these precautions, standard measurement practice was followed in an effort to improve the accuracy of the measurements and reduce noise and interference problems. BNC connections were used throughout for the circuit wiring, with the shortest possible lengths to reduce capacitive noise pick-up. In addition, care was taken to avoid 'ground loops' by making all ground connections to one point only. An important factor to consider with regard to the accuracy of voltage measurements was the importance of making four-probe measurements in order to eliminate any potential drops across parasitic resistances associated with the leads and contacts. In general, if the voltage developed across the device is measured using a method other than the four-point technique, then part of the voltage measured will be that developed across the electrodes and connecting leads, e.g. if the actual effective resistance of the junction $R_J \approx 500\ \Omega$ and the resistance associated with the leads etc. $R_S \approx 10\ \Omega$, then a possible error of 2% is introduced. Generally therefore, care was taken to employ four-probe techniques in all electrical measurements and the electrode geometry was chosen (as described in section 3.3.3) with this in mind.

4.3 A.C. MEASUREMENTS

All a.c. measurements were made with a Wayne-Kerr bridge (model B224) in conjunction with a tuned amplifier and oscilloscope as detector (see Fig 4.4). The bridge enabled the capacitance and a.c. conductance of the devices to be measured simultaneously. Results were obtained at a frequency of 1 kHz and peak-to-peak amplitude of 100 mV.

4.4 D.C. MEASUREMENTS

A block diagram of the system used for making d.c. measurements is shown in Fig 4.5. For these measurements, a battery or stabilised power supply (Farnell L30B) with suitable attenuation was used in conjunction with two microprocessor digital voltmeters (Solatron-Schlumberger 7055), to measure both the junction bias (V_D) and the potential drop (V_S) across a resistance in series with the junction to give a value for the current. The very high input impedance of the instruments (100 G Ω) ensured negligible error in the measurements due to loading effects.

The voltmeters were connected to a DEC LSI 11 microcomputer via an RS232 serial interface. A printer was used to output the data and in

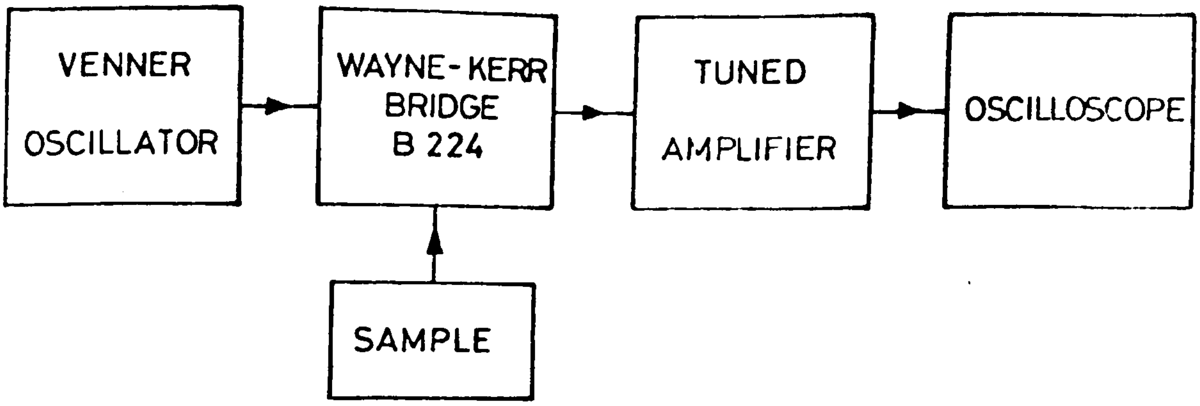

Fig 4.4: Block diagram of the arrangement used for a.c. measurements.

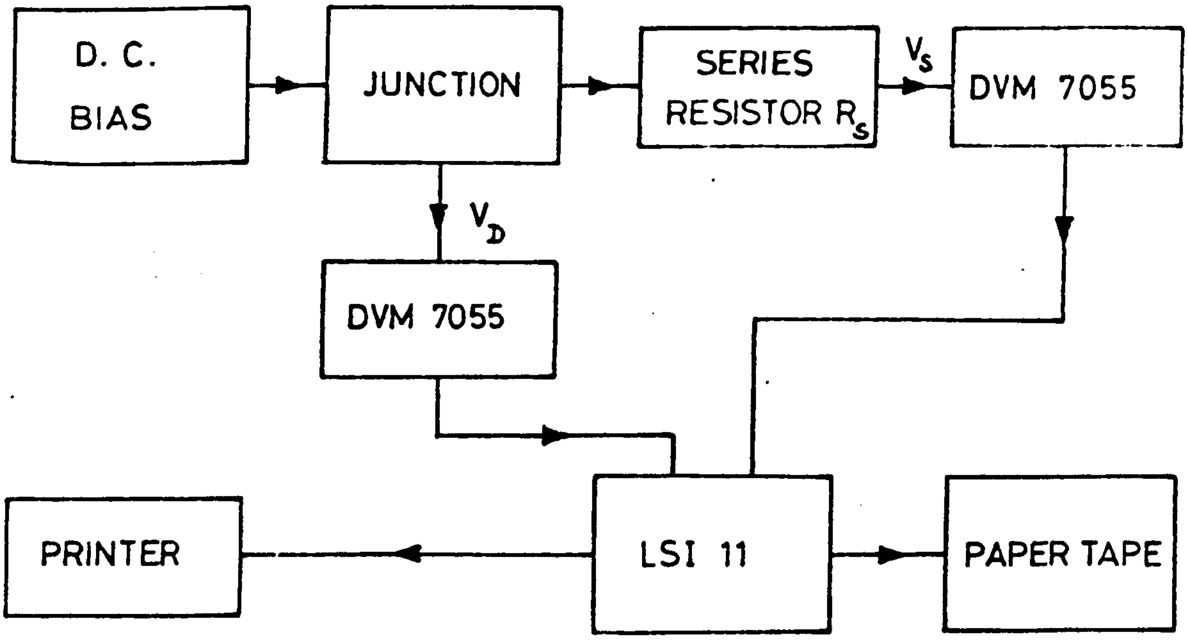

Fig 4.5: Schematic of the system used for d.c. measurements.

addition, if desired, data could be stored permanently on paper tape for ease of analysis at a later stage.

Data was normally recorded on a point by point basis with the applied bias varied in small steps. The power was switched off upon each change of bias to avoid transient spikes damaging the device. At each point, a large number of sequential readings (20-50) of both V_D and V_S were taken and these were averaged out during the course of each scan before their mean values were printed. At the end of the experiment, the pairs of averaged data (V_D and V_S) could be punched on paper tape if desired.

With multilayer Langmuir film devices, it was usual in common with other workers(4), to wait for the current to decay to a steady value for each individual applied voltage before taking a series of readings. This procedure was necessary to ensure the recovery of the true d.c. data as the decay effect is attributed(4) to injected charge or trapped ions, moving in response to the applied bias and as such represents a displacement current ; the true d.c. current being given by the lower steady values. With single layer films, this decay effect was not as pronounced and on application of bias, the current through the device attained a steady value which to all purposes was instantaneous.

Some of the earlier d.c. data were obtained using a stabilised power supply (Farnell L30B) with suitable attenuation, in conjunction with a Keithley 602 electrometer and a Schlumberger Solatron 7040 DVM. As with all measurements, all possible precautions were taken to ensure accurate measurements and the reduction of noise to a minimum level.

4.5 INELASTIC ELECTRON TUNNELLING SPECTROSCOPY METHODS

This section first discusses the principle of the inelastic tunnelling measurements made during this investigation before going on to describe the actual instrumentation and its operation.

4.5.1 Theoretical Aspects

The onset of an inelastic tunnelling event manifests itself as a slight break in the slope of the I-V characteristic of the junction (see Fig 2.8). In practice however, since this increase in the tunnel current is small, it is the second derivative of the I-V characteristic that is measured. This is most easily done through the use of modulation techniques and lock-in amplification. In the most common arrangement (see Fig 4.6) a small a.c. modulation current is superimposed on a steadily increasing d.c. current and applied to the junction. Because of the non-linearities in the I-V characteristic resulting from inelastic tunnelling, the a.c. response of the junction contains harmonics of the fundamental frequency of the modulation signal applied to it, which are proportional to the first and second derivatives of the I-V characteristic. This can be seen from the following analysis.

If the peak amplitude and angular frequency of the modulation current is denoted by δ and ω respectively, then for a direct current (I_o), the voltage developed across the junction (V) can be expanded as a Taylor series to give(5)

$$\begin{aligned} V(I) &= V(I_o + \delta \cos \omega t) \\ &= V(I_o) + \left(\frac{dV}{dI}\right)_{I_o} \delta \cos \omega t + \frac{1}{2} \left(\frac{d^2V}{dI^2}\right)_{I_o} \delta^2 \cos^2 \omega t + \ldots \\ &= V(I_o) + \left(\frac{dV}{dI}\right)_{I_o} \delta \cos \omega t + \frac{1}{4} \left(\frac{d^2V}{dI^2}\right)_{I_o} \delta^2 (1 + \cos 2\omega t) + \ldots \quad (4.1) \end{aligned}$$

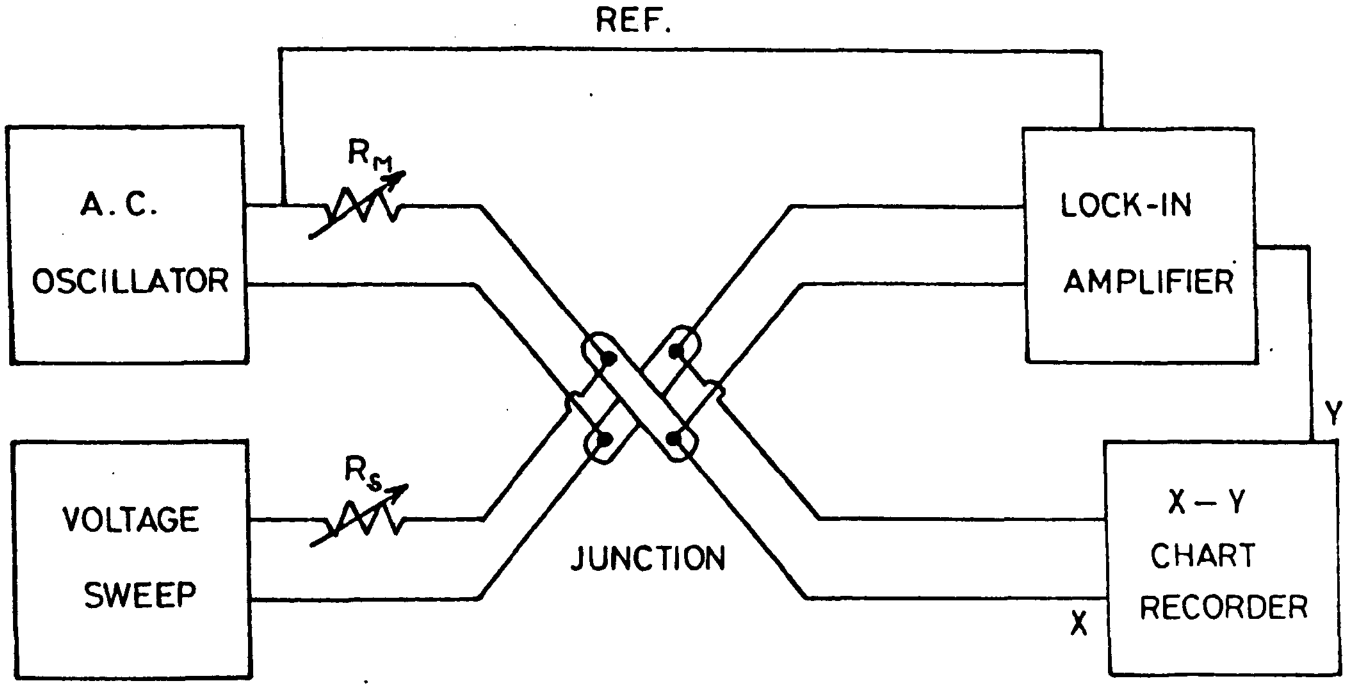

Fig 4.6: Schematic of a conventional tunnelling spectrometer.

From this, it can be seen that the voltage (V_ω) at the first harmonic frequency is proportional to the first derivative

$$V_\omega \propto \left(\frac{dV}{dI}\right)_{I_o} \delta \cos \omega t \qquad (4.2)$$

and the voltage ($V_{2\omega}$) at the second harmonic frequency is proportional to the second derivative,

$$V_{2\omega} \propto \left(\frac{d^2V}{dI^2}\right)_{I_o} \delta^2 (\cos 2\omega t) \qquad (4.3)$$

Both of these voltages are available across the junction and can be recovered using a lock-in amplifier.

It will have been noted that with this arrangement, it is the derivatives dV/dI, the dynamic tunnel resistance and d^2V/dI^2 that are obtained whereas the theoretical results (see Chapter 2) discuss dI/dV = G, the dynamic conductance and d^2I/dV^2. This is a consequence of the preference amongst workers for constant current circuits which offer certain advantages in respect of sensitivity and simplicity over constant voltage circuits(5). Since

$$\frac{d^2V}{dI^2} = - G^{-3} \left(\frac{d^2I}{dV^2}\right) \qquad (4.4)$$

and G is relatively constant over the voltage range of interest (0-0.5 V) and since at present no good theoretical calculations of mode intensity are available, d^2V/dI^2 is sufficient to determine mode frequencies and only the absolute intensity is lacking. The necessary instrumentation for measuring dI/dV and d^2I/dV^2 directly has been developed(6). The analysis for this arrangement is essentially similar to that discussed above - it corresponds to maintaining constant voltage conditions and expanding $I(V) = I\,(V_o + V_\omega \cos \omega t)$ as a Taylor series.

The modulation techniques just discussed will contribute broadening to the observed linewidth in addition to any thermal contribution (see section 2.3.2). This is because the response at the second harmonic is proportional to the second derivative averaged over the interval of the modulation signal. Following Klein et al$^{(7)}$, the effect of finite modulation voltages (corresponding to maintaining constant voltage conditions) on the measured linewidth in tunnelling spectroscopy can be analysed in the following terms.

Assuming that the modulation voltage is $eV_\omega \cos \omega t$ and that $f''(eV)$ is the exact second derivative (i.e. with no modulation voltage broadening), the tunnel current (I) can be written as

$$I \;=\; f(eV_\omega + eV_\omega \cos \omega t) \tag{4.5}$$

where V is the bias voltage. Now, the second derivative (d^2I/dV^2) is proportional to the current at the second harmonic frequency and is given by

$$I_{2\omega} \;=\; \frac{2}{\tau}\int_0^\tau f(eV_\omega + eV_\omega \cos \omega t)\,\cos 2\omega t\,dt \tag{4.6}$$

Integrating by parts twice gives

$$I_{2\omega} \;\propto\; \int_{-eV_\omega}^{eV_\omega} f''(eV + E)\,\left[(eV_\omega)^2 - E^2\right]^{3/2}\,dE \tag{4.7}$$

where $E = eV_\omega \cos\omega t$. Thus, $I_{2\omega}$ is a convolution of the exact second derivative with a function that is proportional to $\left[(eV_\omega)^2 - E^2\right]^{3/2}$ for $|E| < eV_\omega$ and zero for $|E| > eV_\omega$. This is a bell-shaped function with a width at half-maximum of 1.7 V_ω(rms) (7).

Now, the thermal broadening at 4.2 K is $\sim$ 2 meV(section 2.3.2). Thus, with normal electrodes at this temperature, modulation broadening will be comparable to thermal broadening when V_ω = 1.2 mV rms. With superconducting electrodes at 4.2 K, the width at half-maximum of the thermal broadening function is reduced to 2.9 kT (8). Hence, in order to take advantage of the reduction is linewidth consequent with the use of superconducting electrodes, would necessitate a modulation voltage of $\sim$ 0.6 mV rms. Since the second harmonic signal varies approximately with the square of the modulation signal (equation 4.3) and since the signal to noise ratio improves as the square root of the averaging time, it means that with this modulation voltage it would take a prohibitively long time to complete a tunnelling spectrum with the same signal/noise ratio as that obtained with V_ω = 1.2 mV rms. Thus in practice, for routine work broadening due to the modulation signal will be the limiting factor as far as the resolution in tunnelling spectroscopy is concerned.

4.5.2 Instrumentation

Tunnelling spectra and measurements of the dynamic tunnel resistance as a function of applied bias were obtained using a spectrometer designed and constructed by other workers (9). This employed a constant current modulation technique to measure the first and second derivatives of the current-voltage characteristic and the corresponding applied bias (see Fig 4.7).

A slowly increasing current from a d.c.power unit and motor-driven Rayleigh potentiometer (M.P.120) was supplied to the junction through a series resistance $R_1 - R_{11}$. This resistance was kept as large as possible relative to the junction resistance, consistent with sweeping the junction

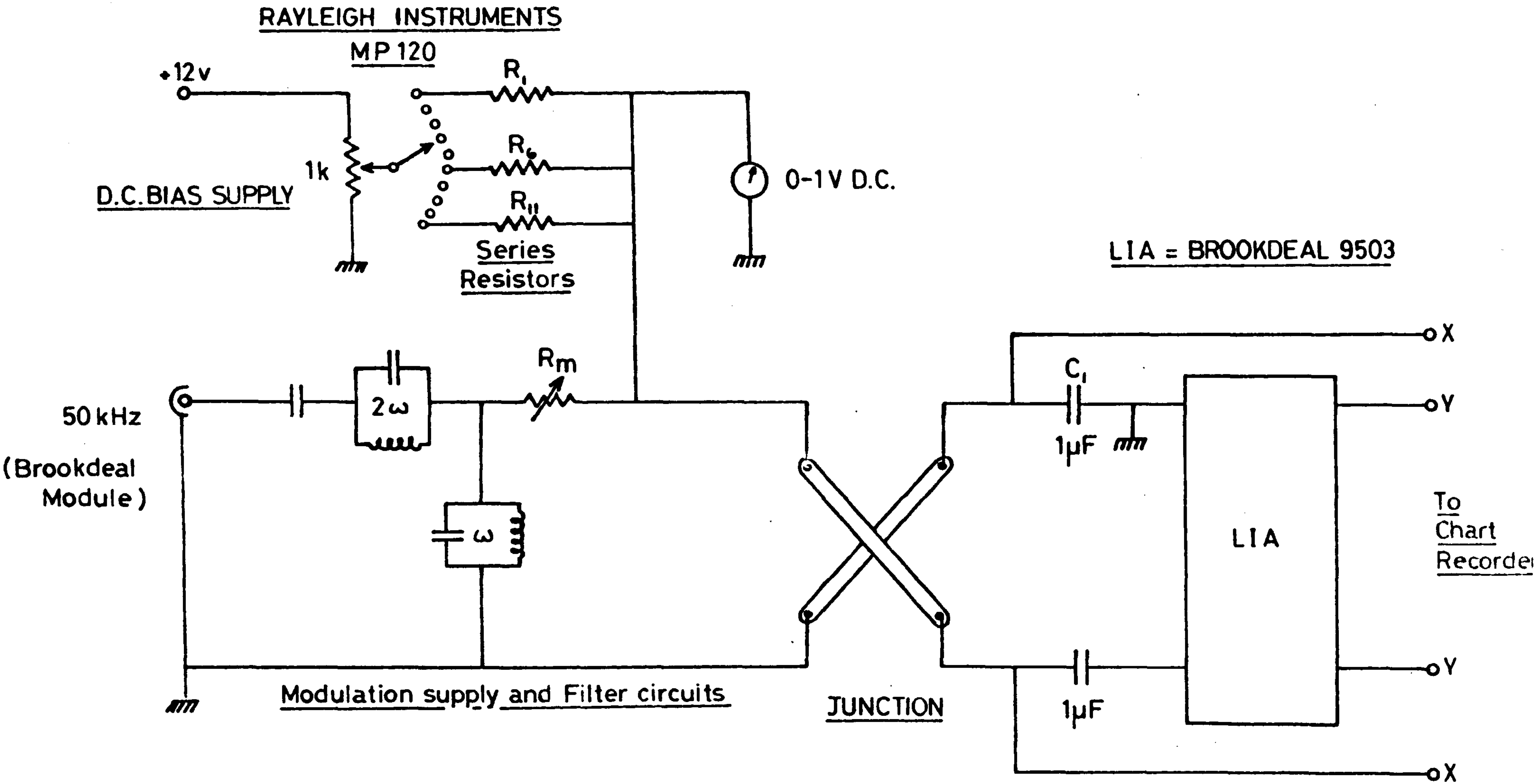

Fig 4.7: Circuit diagram of the tunnelling spectrometer.

to the desired voltage (0.5 V), and ensured that the current was insensitive to small changes in the junction resistance(5). In addition to this slow sweep, a small amplitude, filtered a.c. (50 kHz) modulation current generated by a low-distortion oscillator (Ortec Brookdeal module) was supplied to the junction through another resistance R_m which permitted the modulation voltage developed across the junction to be adjusted to the desired value (typically 0.5-4 mV peak-to-peak). The modulation current produced a second harmonic voltage $V_{2\omega}$, proportional to d^2V/dI^2, at the junction (as discussed in the last section) which was recovered with an Ortec Brookdeal precision lock-in amplifier (model 9503) with a high frequency modification. This was then applied as a larger d.c. signal to the y-axis of an x-y chart recorder (Bryans 25000). The corresponding bias voltage developed across the junction was taken to the x-axis of this recorder, thus giving a display of d^2V/dI^2 against V. A photograph of the spectrometer in operation is shown in Fig 4.8.

As described previously, the electrode geometry permitted four-point probe measurements of the voltage developed across the junction. An important feature in this regard with the earthing arrangements of the present circuit was the presence of the capacitor C_1. This eliminated the possibility of any voltage being developed across the measurement leads and thus ensured that correct four-point probe conditions were established.

Since the second harmonic signal developed at the junction could be as low as 10 nV, particular attention was paid to the problem of reducing noise. In addition to the usual precautions such as adequate screening of leads and the avoidance of 'ground loops' all measurements were made (as described earlier) in a room totally screened with 1.6 mm thick aluminium sheets and with a filtered mains supply. Furthermore, the fundamental frequency of operation of the spectrometer was chosen in common with other workers(10,11) to be 50 kHz, as in general it is found that noise from a

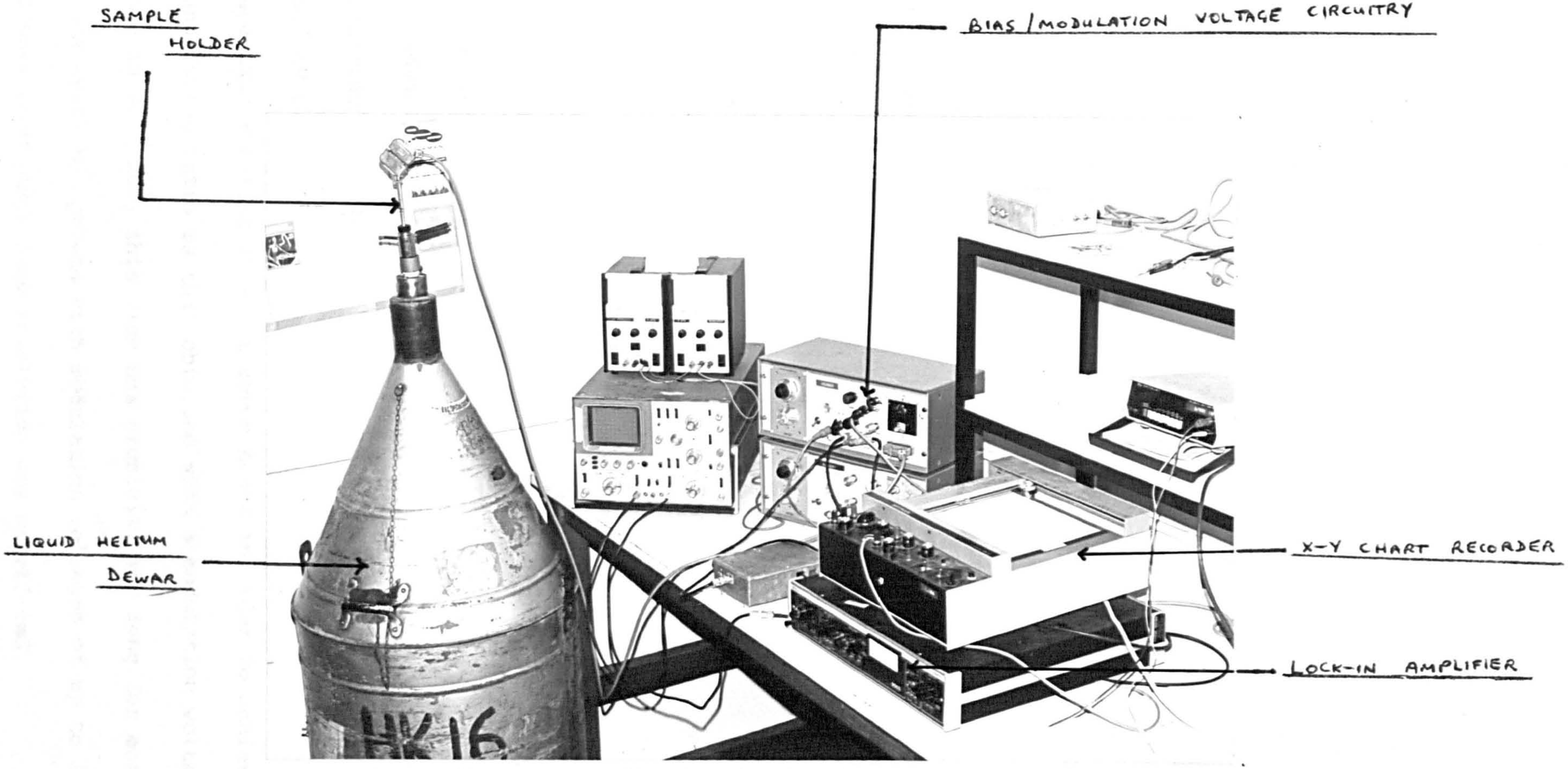

Fig 4.8: Photograph of the tunnelling spectrometer in operation.

given junction drops as the frequency of operation increases(10).

It was usual, prior to actual measurement, to carry out a preliminary assessment of the likelihood of a particular junction giving a tunnelling spectrum(9). As described earlier, junction resistances were first checked with a low power ohmmeter. It was found that junctions having a resistance outside the range 20-1000 Ω (junction areas ≃ 0.5x0.5 mm^2) seldom produced tunnelling spectra and were consequently rejected for this measurement. Next, the remaining junctions were tested for electron tunnelling at 4.2 K. This was undertaken by applying a modulation voltage of a few millivolts peak-to-peak at zero bias from a constant current source and observing the shape of the voltage waveform at the junction. Junctions with a non-linear low voltage current-voltage (I-V) characteristic (consistent with superconductive tunnelling), considerably distorted the sinusoidal voltage waveform obtained with junctions having linear I-V characteristics and could thus be easily differentiated. In this regard, one further method of assessing junction suitability consisted of measuring the second harmonic signal from the junction using the lock-in amplifier in the bias range 0-10 mV, where suitable junctions were indicated by variations in the second harmonic signal (due to a non-linear low bias I-V characteristic) greater than ∿ 5 μV.

It is necessary before concluding this section to briefly consider the resolution of the spectrometer used. As discussed earlier, to take full advantage of the increased resolution afforded by the use of superconducting electrodes would require at 4.2 K, a modulation voltage of ∿ 0.6 mV rms. With the present spectrometer, this would have necessitated a spectrum run-time of about seven hours in order to achieve the same signal/noise ratio as that obtained with a modulation voltage of 1.2 mV rms. Since in practice, this time was prohibitively long for most measurements, it was usual to operate with modulation voltages of up to 1.5 mV rms(∿4 mV p-p) and thus inevitably some resolution was sacrificed.

CHAPTER 5

ELECTRONIC CONDUCTION IN SINGLE LAYER LANGMUIR FILMS

This chapter presents the results of the various electrical investigations undertaken with a view to substantiating the conduction mechanisms thought to be important in Langmuir film MIM devices. It begins by describing some of the preliminary measurements that were carried out to characterise the devices before presenting the results of the more detailed experiments with single layer Langmuir film devices.

5.1 PRELIMINARY ELECTRICAL MEASUREMENTS

The results of preliminary a.c. measurements on about ten devices (mean area ∿ 0.25 mm^2) consisting of single layer films of barium stearate ($BaSt_2$) sandwiched between aluminium electrodes revealed a mean capacitance of 1.47 nF ± 20% and an a.c. resistance of 5.0 M Ω ± 20%. The measurements were made at 100 mV applied bias and at a frequency of operation of 1 kHz. The 20% variation in capacitance and resistance was typical even for samples on the same substrate and is too great to be accounted for simply by the accuracy to which electrode areas could be produced and measured (± 5%). The variation is therefore tentatively attributed to variations in oxide thickness and/or to pinholes and voids in the Langmuir film.

The mean junction area (A) of devices was 0.25×10^{-6} m^2. Assuming that the thickness (s) of a single layer of barium stearate is approximately 2.5 nm(1) and that for these films, the dielectric constant $\varepsilon = 2.6$(2), then the mean capacitance (C) of the devices used in these experiments is given by

$$C = \frac{\varepsilon_o \varepsilon A}{s} = 2.3 \text{ nF}.$$

where ε_o has been put equal to 8.85×10^{-12} F m^{-1}.

Comparison of this theoretical estimate with the mean experimental value for the device capacitance would imply a somewhat thicker junction than assumed. It is well known that there is an oxide layer on the base aluminium electrode and therefore, if it is considered that the capacitance of this thin oxide layer is in series with the capacitance of the monolayer, then the capacitance (C^1) of a system of N superimposed barium stearate monolayers is given by

$$\frac{1}{C^1} = \frac{1}{\varepsilon_o A}\left[\frac{s_{ox}}{\varepsilon_{ox}} + \frac{Ns}{\varepsilon}\right] = \frac{s_{ox}}{\varepsilon_o \varepsilon_{ox} A} + \frac{1}{C} \qquad (5.1)$$

where s_{ox} and ε_{ox} are the thickness and dielectric constant of the oxide layer respectively. Assuming that $\varepsilon_{ox} = 8$ (3) and putting N = 1, then

$$s_{ox} = (6.8 - 4.3)\ 10^8 \times 8.85 \times 0.25 \times 8 \times 10^{-18}\ [m]$$

$$\underline{s_{ox} = 4.4\ nm}$$

This value of s_{ox} is in reasonable agreemnt with Madden et al (4) (3-4 nm) but is somewhat lower than that quoted by Mann and Kuhn (5) (7 nm). An important point to note is that a reliable measurement of the true dielectric parameters of a monolayer is necessarily complicated even if measurements of these parameters are made as a function of the number of layers, since the effect of the oxide may mask the response of the stearate film itself and in addition it is possible that the first layer deposited may be significantly different from subsequent layers.

It was not possible in the author's laboratory to measure the capacitance of single layer films of barium stearate deposited on tin base electrodes as the a.c. resistance of these devices proved to be too low for both the capacitance and conductance terms to be balanced on the Wayne-Kerr bridge used (Model B224).

The specific junction resistances of $Sn/BaSt_2/Pb$ junctions were however measured at an applied bias of ∿ 10 mV using a low power ohmmeter (see Chapter 4) and were found to differ considerably (∿ k Ω) from similar measurements on equivalent aluminium-based junctions (∿ M Ω). In general, there was also a greater variation in tin-based junction resistances than for junctions based on aluminium. For the tin-based junctions, the resistances varied from ∿ 25 Ω to ∿ 4k Ω for a junction area of 0.25 mm^2. This is in reasonable accord with the values reported by Handy and Scala(6), where it is suggested that the lower resistance values were characteristic of the oxide and that the upper limit corresponded to those organic films possessing the smallest fraction of voids. Attempts made to form insulating $Sn/SnO_x/Pb$ junctions by dipping these substrates in the Langmuir trough but without incorporating a monolayer however generally showed junction resistances of less than 1 Ω, even when the base tin electrode was exposed to an oxygen glow discharge to promote oxide growth. In a very few of these junctions however, insulating behaviour was found at liquid helium temperatures but electrical breakdown invariably occurred at applied voltages of less than 20 mV.

The important observations that can be made from the results of these preliminary experiments are :-

(1) The junction resistance is influenced by the nature of the metal substrate and in particular by the extent to which this metal is oxidised. At low bias voltages, junctions with base electrodes of tin show much lower resistances (of the order of $10\text{-}10^3$ Ω) when compared with aluminium-based junctions ($R \gtrsim 10^6$ Ω) for a monolayer film and a junction area of 1 mm^2. These observations are in accord with results reported by other workers(5-6).

(2) The effect of the interfacial oxide layer must be considered when interpreting conduction data from Langmuir film MIM devices. This applies particularly to devices using an aluminium film as substrate.

For tin-based junctions the SnO_x film is relatively conducting, and is thus deemed to be of less importance in determining the conduction characteristics of tin-based Langmuir film junctions.

(3) The thickness of the interfacial oxide layer in Al-LF-Al junctions can be taken to be of the order of 4 nm.

5.2 THE CURRENT-VOLTAGE RELATIONSHIP

For a uniform insulating layer about 2.5 nm thick at applied voltage $V \lesssim \phi$(the interfacial barrier height), the predominant conduction mechanism is expected to be electron tunnelling. The corresponding J-V characteristic is governed by equation (2.47) or equations (2.36-2.37) which constitute a similar variation. These equations predict that the J-V characteristic is effectively ohmic at an approximate value of applied bias $V \simeq 0$ and thereafter increases approximately exponentially with the voltage.

The current-voltage characteristics of an Al-$BaSt_2$-Al device measured at various constant temperatures in the range 80-300 K are shown in Fig 5.1. These results were obtained using the cryostat experimental chamber and measurement methods described in the last chapter.

With these devices, the characteristics were found to be symmetrical with respect to the polarity of the applied field throughout the voltage range 0-1 V. Typical results for characteristics measured at room temperature and under opposite polarities of the applied field are shown in Fig 5.2.

These particular characteristics were obtained using the evacuated ($\sim 10^{-6}$ Torr) experimental chamber of Fig 4.1. During the course of this work, experiments have been performed in a number of experimental chambers (described in Chapter 4) and in no case was any discernible correlation detected between device properties and the sample chamber being used, i.e. it may be concluded that the results described are genuine properties of the devices being studied rather than characteristics determined by the chamber.

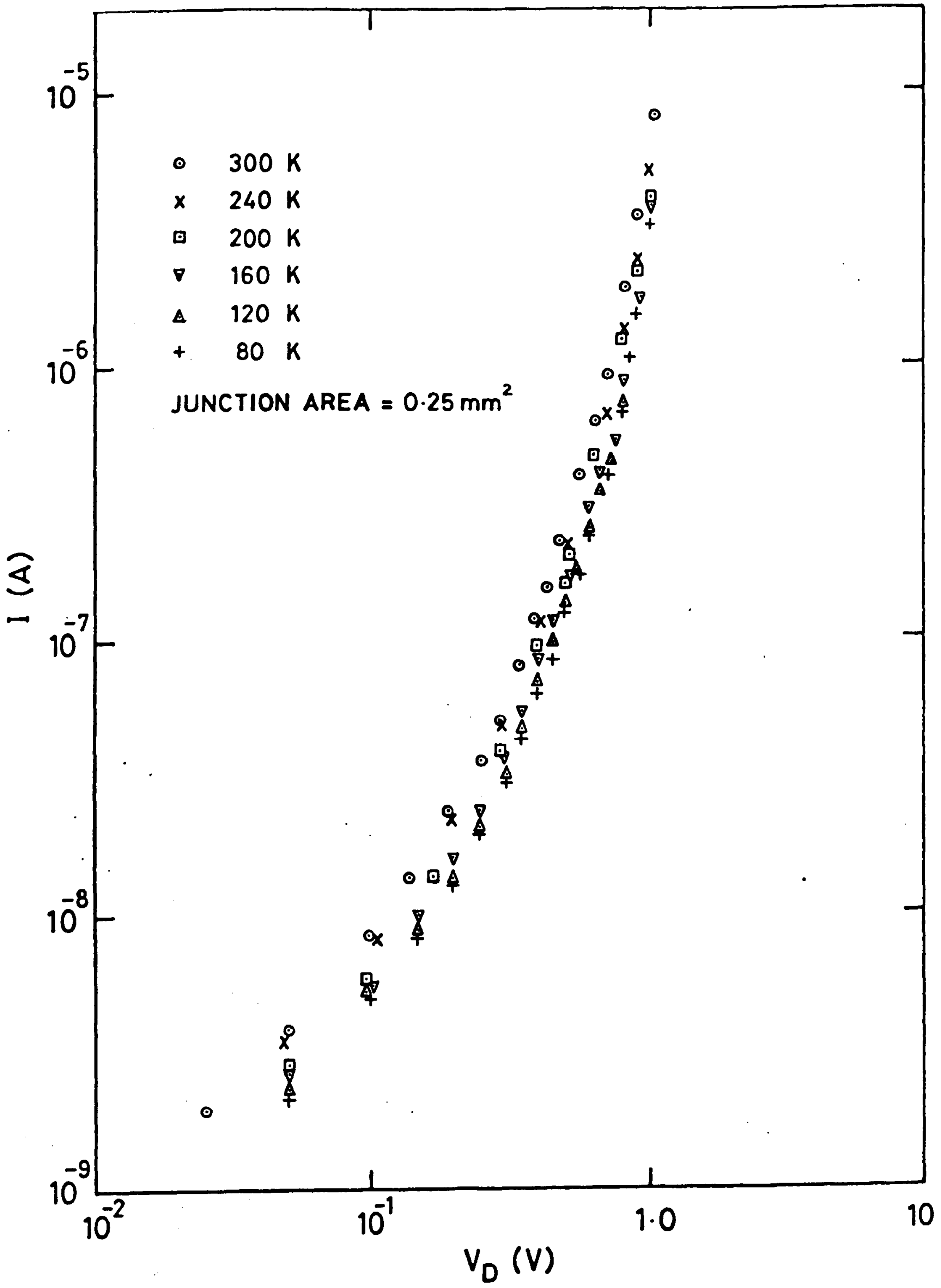

Fig 5.1: Current-voltage characteristics of a single layer Al-BaSt$_2$-Al device at various fixed temperatures. The base aluminium electrode was biased negatively.

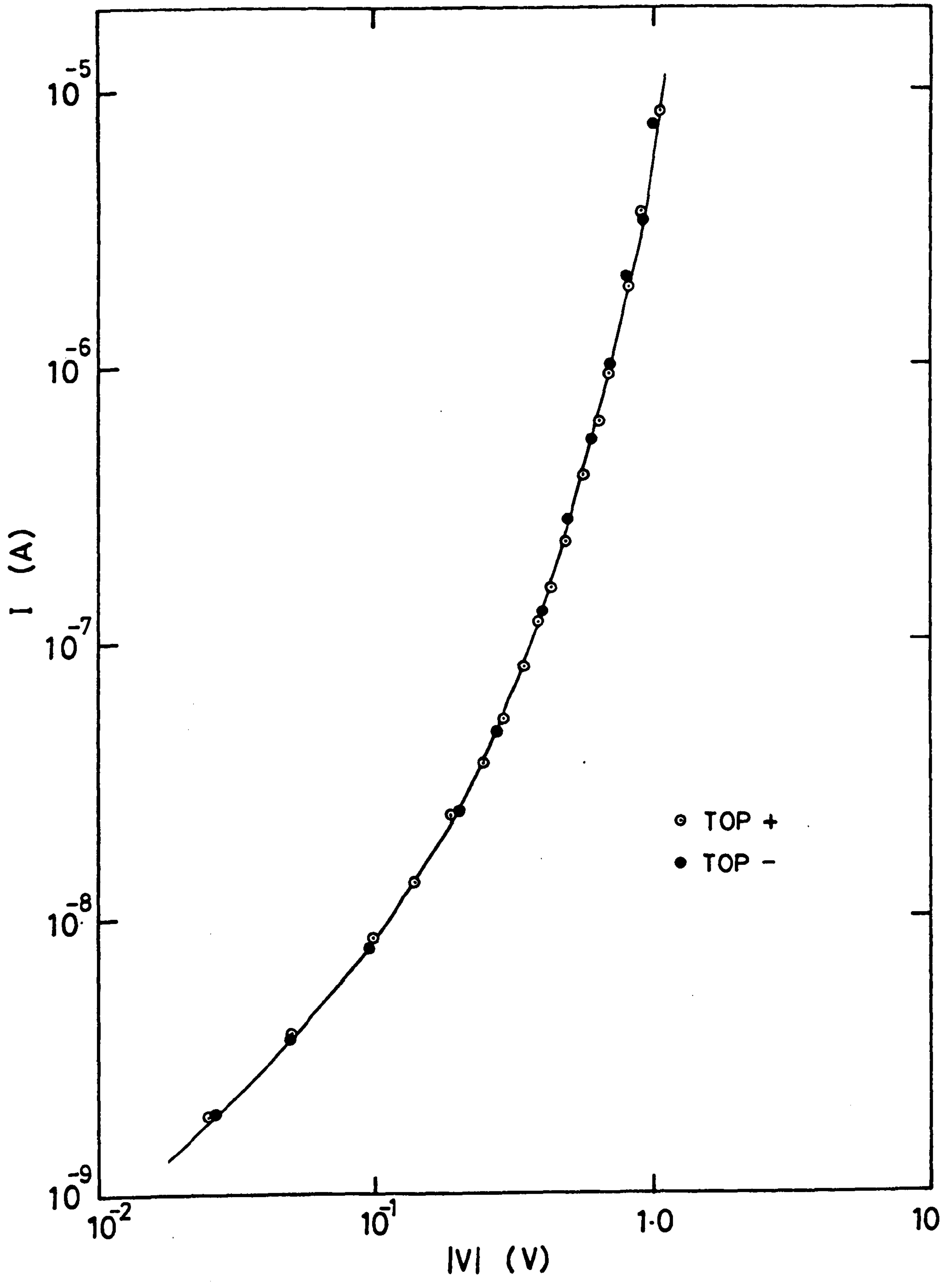

Fig 5.2: I-V characteristic under opposite polarities of bias for a single layer Al-BaSt$_2$-Al device at room temperature.

It is apparent from Fig 5.1 that the current-voltage characteristics display a weak temperature dependence. This makes it unlikely that the electron transport in these devices could be by a mechanism other than tunnelling. The characteristics at various fixed temperatures can be normalised to a single curve using the procedure suggested by Hill$^{(7)}$ - the individual curves are displaced along both the current and the voltage axes to demonstrate that a common characteristic is being exhibited (Fig 5.3), i.e. that a single conduction mechanism is being followed throughout the temperature and voltage range being investigated. The relative axial shift for each curve is shown by the temperature-labelled symbols in Fig 5.3.

Now, for a symmetrical barrier in the applied bias range $0 \lesssim eV \lesssim \phi$ equation (2.47) yields a current-voltage relationship of the form

$$J = \frac{8\pi me}{C_{10}^{2}h^{3}} \exp(-b_{10}) \exp(-b_{12}V^{2}) \sinh(C_{10}eV/2)$$

Assuming a rectangular barrier shape and substituting for the coefficients (2.48) yields

$$J = \frac{e\,\phi}{\pi s^{2}h} \exp\left[-\frac{4\pi s(2m\phi)^{\frac{1}{2}}}{h} \right] \exp\left[\frac{\pi e^{2}s(2m)^{\frac{1}{2}}\,V^{2}}{6h\phi^{3/2}} \right]$$

$$\times \sinh\left[\frac{\pi s(2m)^{\frac{1}{2}}\,eV}{h\,\phi^{\frac{1}{2}}} \right]$$

Now equation (2.47) can be written in the form

$$I = \text{constant} \times \exp\left[-\frac{K'}{K''}.V^{2} \right] \sinh K'V \qquad (5.2)$$

$$\text{where } K' = \frac{\pi se(2m)^{\frac{1}{2}}}{h\phi^{\frac{1}{2}}} \text{ and } K'' = 6\phi/e \qquad (5.3)$$

for direct tunnelling between the metal electrodes. A computer program (listed in Appendix 1) utilising a least squares fit routine was used to fit experimental results obtained from Al-BaSt$_2$-Al devices to equation (5.2)

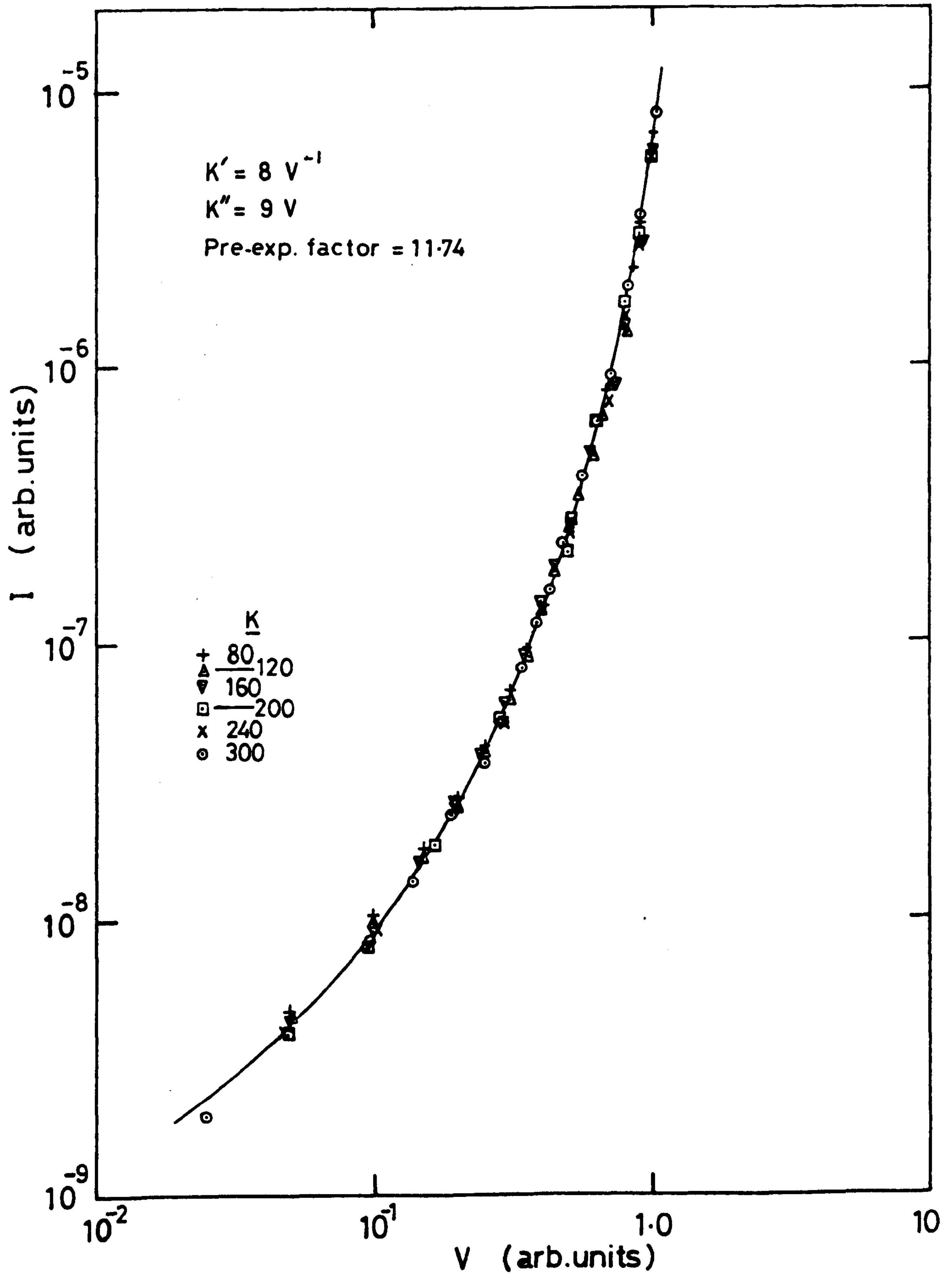

Fig 5.3: Temperature normalised I-V characteristic for a single layer Al-BaSt -Al device. The current and voltage scales have been shifted by the amounts indicated by the temperature-labelled symbols. The solid line is the best fit of equation (5.2) to the data with the parameters indicated.

in order to estimate a reasonable value for the interfacial barrier height ϕ.

The best fit of the model to the present results is shown as the solid line in Fig 5.3, and it is apparent that equation (5.2) is an excellent fit to the experimental data over almost four decades of the current and up to an applied voltage $V \simeq 1V$ at 300 K, the voltage scale being absolute for that value of temperature.

From the fit, the parameter K' is deduced and used to calculate a value for the interfacial barrier height ϕ given by equation (5.3). Substituting appropriate values for the constants and putting $s = 2.5$ nm, the thickness of the barium stearate monolayer$^{(1)}$, yields $\phi = 0.65$ eV. It will be seen that to obtain the fit, K'' has been used as an additional adjustable parameter and in fact the value of K'' obtained from the fit does not show very close agreement to the theoretical value. This discrepancy therefore represents some disagreement between the model and experiment and is one which has been noted previously by Stratton$^{(8)}$ when analysing data obtained from aluminium oxide films.

A point which must be made at this stage is that it is necessary to be cautious when interpreting data on the basis of a model which assumes an abrupt, rectangular barrier profile. Clearly, such a barrier shape is physically unrealisable since abrupt changes in potential imply infinite forces (see section 2.2.7). However, something which often seems to have been neglected in the literature is that the tunnelling width Δs(see Fig 2.3), at the Fermi level of the negatively charged electrode is itself bias dependent if a non-rectangular barrier shape is assumed. Thus as the applied voltage increases, it is possible to have direct metal to metal tunnelling across a reduced barrier width. This situation is quite apart from Fowler-Nordheim tunnelling where electron tunnelling into the conduction band of the insulator occurs at very high applied fields. It is quite reasonable therefore that strict (quantitative) agreement between theory and experiment not be obtained.

The absolute magnitude of the current density will now be considered. For the ohmic region at say V = 0.05 V, equation (2.36) gives the current density for tunnelling as

$$J = \frac{e^2 V}{h^2 s} (2m\phi)^{\frac{1}{2}} \exp\left[- \frac{4\pi s (2m\phi)^{\frac{1}{2}}}{h} \right]$$

Substituting values for s and ϕ of 2.5 nm and 0.65 eV respectively yields

$$J = \frac{(1.6 \times 10^{-19})^2 \, 0.05 (2 \times 9.1 \times 10^{-31} \times 0.65 \times 1.6 \times 10^{-19})^{\frac{1}{2}}}{(6.6 \times 10^{-34})^2 \times 2.5 \times 10^{-9}}$$

$$\times \exp\left[\frac{-4\pi \times 2.5 \times 10^{-9} \, (2 \times 9.1 \times 10^{-31} \times 0.65 \times 1.6 \times 10^{-19})^{\frac{1}{2}}}{6.6 \times 10^{-34}} \right]$$

$$= 5.16 \times 10^{2} \text{ A m}^{-2} \text{ or } 5.16 \times 10^{-4} \text{ A mm}^{-2}$$

Now it is found that typically the current density of an Al-BaSt$_2$-Al device is $\sim 1 \times 10^{-9}$ A mm^{-2} at an applied voltage of 0.05 V. Thus it seems that the current only flows through a small area of the device ($\sim$ 1 part in 10^5 perhaps) or alternatively this may be an oxide effect. The value of ϕ obtained from the theoretical fit is low compared with that quoted by Mann and Kuhn$^{(9)}$ (1.8 eV) for the Al-cadmium stearate interfacial barrier height obtained from a similar analysis and ϕ = 2.3 eV for the same interface obtained from photoelectric measurements. With the present results, if it is assumed that the oxide (or at least part of it) acts as an additional insulating layer in series with the Langmuir film then a higher value for ϕ is obtained and the predicted magnitude of the current density may well be in closer agreement with experiment. However, any estimate of the current density needs to be interpreted with extreme caution since the tunnel current is highly dependent upon s and ϕ. For example, if $s = 2.5$ nm and $\phi = 1.5$ eV then $J = 1.75 \times 10^{-8}$ A mm^{-2}. It can be seen from this that a change of ϕ from 0.65 eV to 1.5 eV changes J by almost four orders of magnitude and J is even more critically dependent on s. These points will be discussed again when considering the effect of the oxide at a later stage.

The current-voltage characteristics of single layer stearate films on aluminium base electrodes have been studied by a number of workers(5,9-14) who are generally agreed that the conduction in these films is due to electron tunnelling. One notable feature of the I-V characteristic that all these studies reveal is that it is markedly non-linear even for applied voltages $V < 100$ mV. Now it has been usual for workers to assume that the aluminium-stearate interfacial barrier height is of the order of 2 eV on the basis of relevant photoelectric measurements(5). Simple calculation shows (using equation 2.47) that for this voltage regime and $\phi = 2$ eV, $s = 2.5$ nm the tunnelling model predicts a linear relationship between J and V. A typical I-V characteristic for an Al-$BaSt_2$-Al device in this bias range is shown in Fig 5.4 from which it is apparent that the behaviour of the aluminium-based junctions fabricated in the present work confirm the results found by other workers. This point will be discussed in more detail in section 5.5.

Another interesting feature of the I-V characteristics obtained from aluminium based junctions is that the data can also be made to yield a linear plot of log I versus $V^{1/4}$. A typical result for a device at room temperature is shown in Fig 5.5. It is apparent that there is no deviation from $\log I \propto V^{1/4}$ within the bias range 0.05-1V which would indicate at least as good a fit as equation 5.2. The behaviour is similar to that reported by Roberts et al(11) for cadmium arachidate monolayers on aluminium substrates and has been noted previously also in thick porphyrin films by

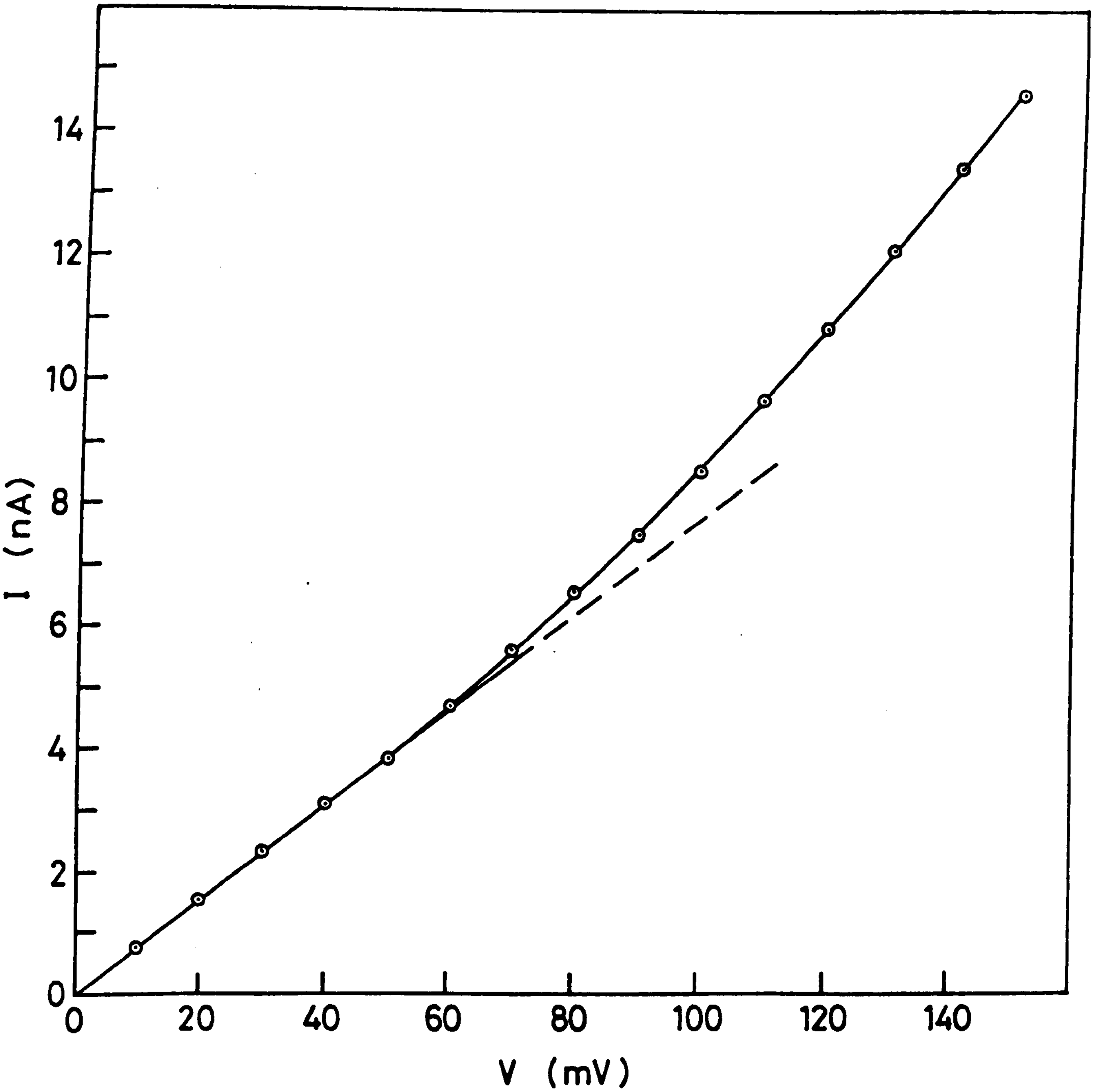

Fig 5.4: I-V at low applied voltages for a single layer Al-BaSt$_2$-Al device at room temperature.

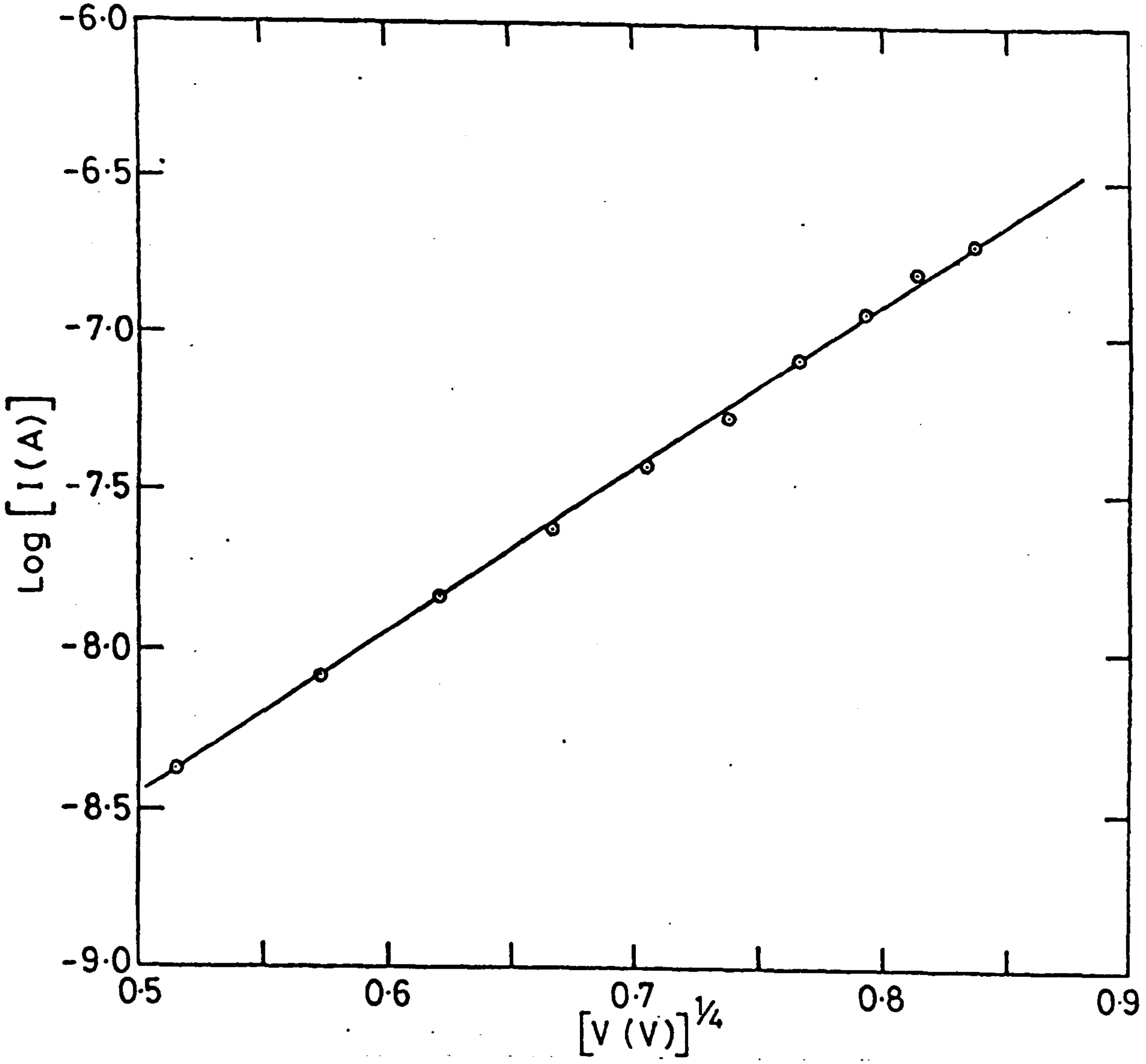

<u>Fig 5.5</u>: Log I versus $V^{1/4}$ plot for a single layer film Al-BaSt$_2$-Al device at room temperature.

Kampas and Gouterman(15) who attributed it to interfacial Schottky barriers whose shapes were influenced by image force effects. A mechanism of this type however predicts a substantial dependence of current on temperature and field polarity, as well as considerable deviation from a $V^{1/4}$ law for low voltages. All this is at variance with the observations on single layer Langmuir films made by Roberts et al and the results of the present work and as such is of doubtful validity as an explanation of the present results. In contrast to this, as will be shown in the next section, the current-voltage data does fit the weak temperature dependence indicated by the tunnelling model and thus suggests very strongly that the main conduction mechanism is these films is indeed electron-tunnelling.

In general, the I-V characteristics of Al-based devices were measured usually up to a maximum of about 1.2 V applied voltage in order to avoid device breakdown. The voltage at which this occurred varied considerably but as a rule was usually between 1.3 and 1.5 V.

The current-voltage characteristics of single layer stearate films deposited on tin base electrodes were found to differ considerably from the equivalent aluminium-based junction characteristics. The counter-electrode used for these junctions was lead and the device area was $\sim 0.25\ \text{mm}^2$. Typical results for various fixed temperatures in the range 80-280 K are shown in Fig 5.6 and 5.7. At low bias ($V \lesssim 0.3$ V) the characteristics are linear. As the applied voltage is increased however, the current begins to rise rapidly with bias before junction breakdown finally occurs at $V \simeq 0.8$V or occasionally, as in the example of Fig 5.7 at higher voltages $\sim$ 1.2 V. Above applied voltages of $\sim$ 0.6V, the characteristics display asymmetry when the bias polarity is reversed as predicted by Hartman(16) (see section 2.2.3).

As with the results obtained from Al-$BaSt_2$-Al junctions, it was again found possible to normalise the I-V characteristics at different

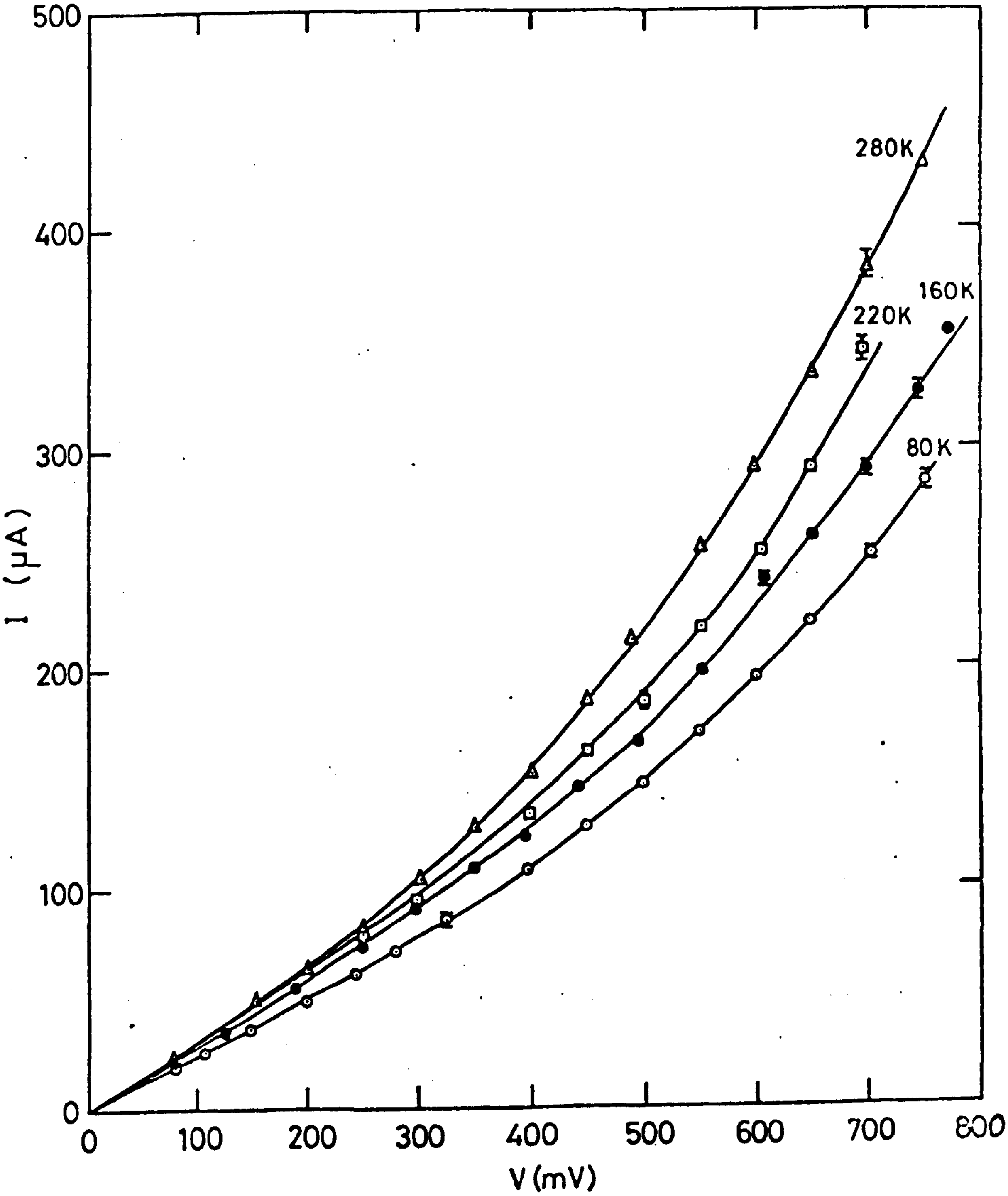

Fig 5.6 : I-V characteristics for a single layer Sn-BaSt$_2$-Pb device at various fixed temperatures. The tin electrode was biased negatively.

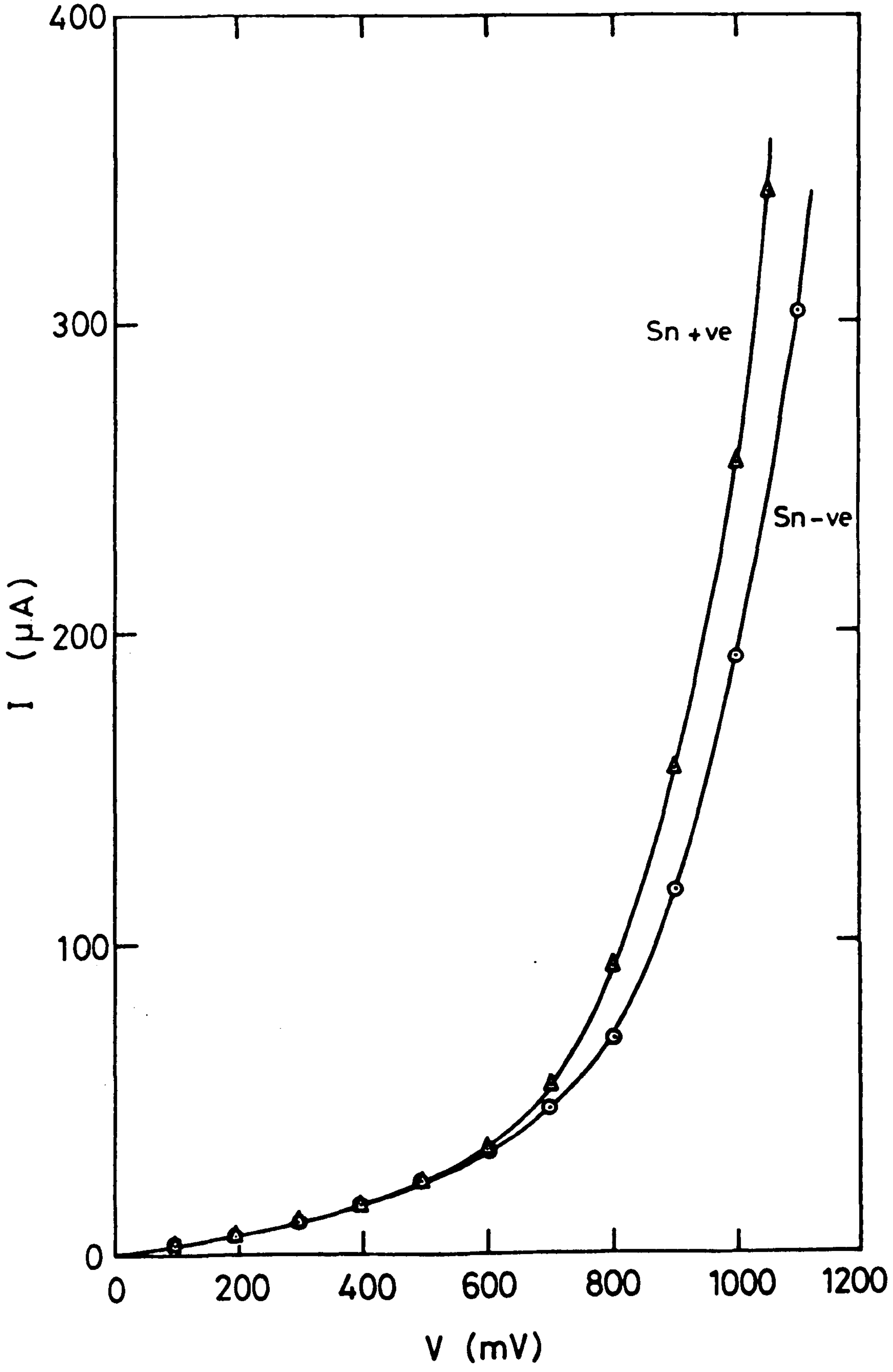

Fig 5.7: I-V characteristics under opposite polarities of bias for a single layer Sn-BaSt$_2$-Pb device.

temperatures to a single curve using the procedure due to Hill(7), thus demonstrating that a single conduction mechanism is being followed throughout the voltage and temperature range investigated.

A detailed analysis of the temperature dependence of the tunnel current in Sn-$BaSt_2$-Pb devices was undertaken and the results of this and a corresponding analysis for aluminium-based junctions are presented in the next section.

5.3 THE VARIATION OF CURRENT WITH TEMPERATURE

For these experiments, devices of the type Al-$BaSt_2$-Al and Sn-$BaSt_2$-Pb were fabricated, located in the cryostat and the small variation of current with temperature measured in the range 80-300 K and at fixed voltages from 0.05 to 0.8 V.

Typical results for a single layer film of barium stearate sandwiched between aluminium electrodes and at a fixed voltage of 0.1V are shown in Fig 5.8. The graph is of current density against T^2. It is apparent that within the limits of experimental error the graph is linear, thus implying a relationship of the form

$$\sigma = \sigma_o(1 + \alpha T^2)$$

where σ and σ_o are the conductivities at temperature T and absolute zero respectively.

The gradient yields the value of α as 0.9×10^{-5} K^{-2} and for a range of devices and voltages α was found to vary between 5×10^{-6} and 9×10^{-5} K^{-2}. The current is found to vary by $\sim$ 70% for a change in temperature of about 200 K. This is similar to the variation found by Hartman and Chivian(17) for tunnelling through thin films of aluminium oxide.

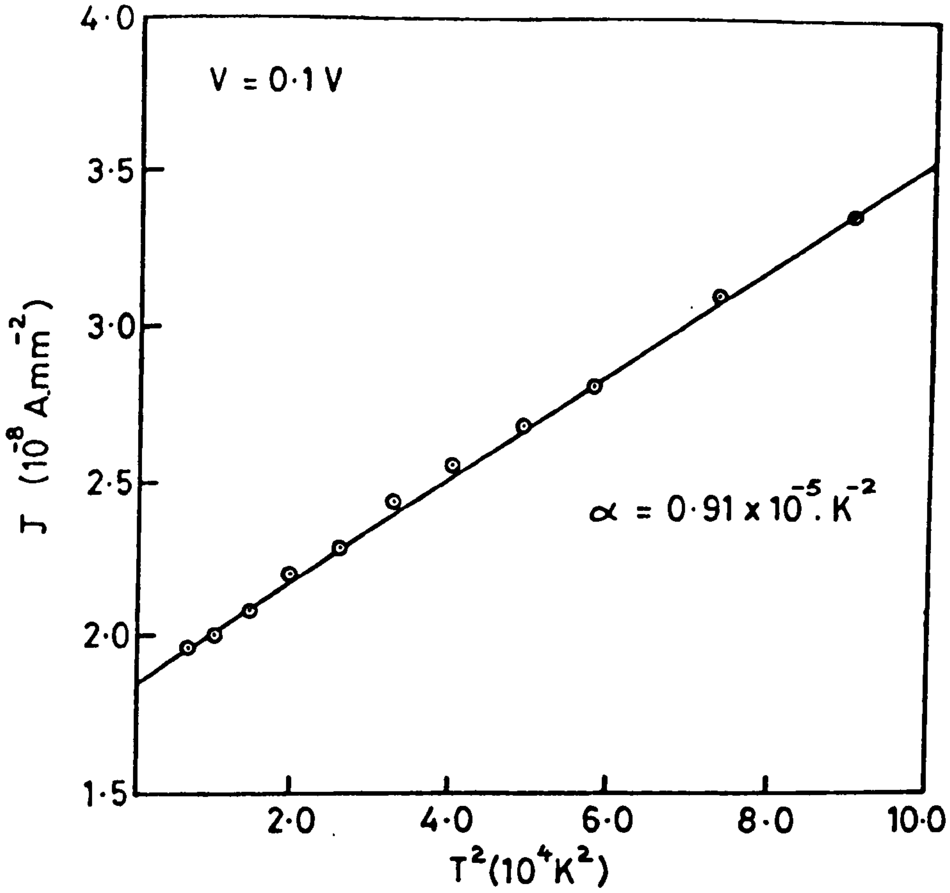

Fig 5.8: The variation of the current with (Temperature)^2 at a fixed voltage for a single layer Al-BaSt$_2$-Al device (Base Al negative).

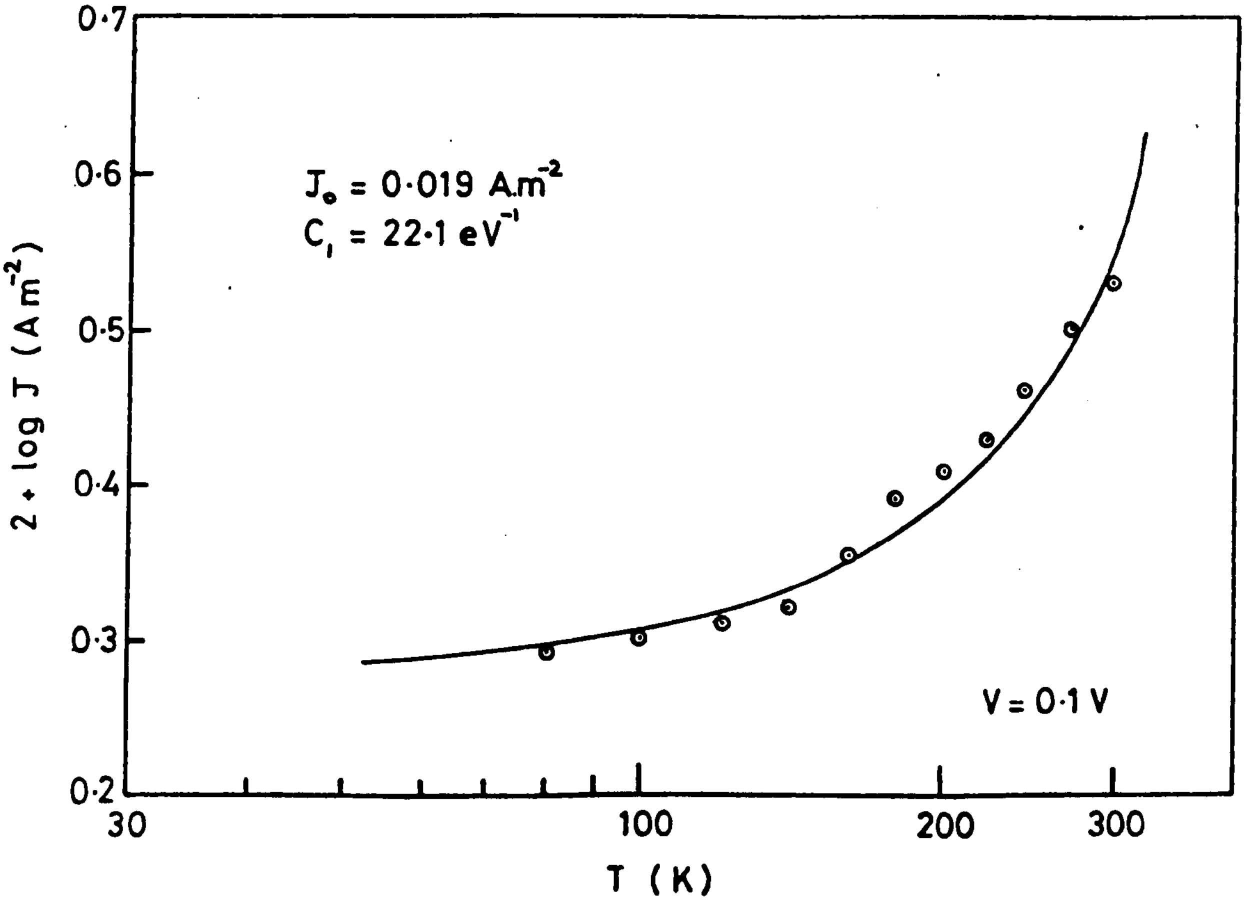

Fig 5.9: The dependence of the current density on temperature for a single layer Al-BaSt$_2$-Al device (Base Al negative). The curve is the best fit of equation (5.5) to the data.

Now the predicted variation of a tunnel current as a function of temperature is given by equation (2.53) as

$$\frac{J(V,T)}{J(V,0)} = \frac{\pi AkT/2\ \bar{\phi}^{\frac{1}{2}}}{\sin\ (\pi AkT/2\bar{\phi}^{\frac{1}{2}})}$$

where A $= 4\pi\ \Delta s\ (2m)^{\frac{1}{2}}/h$.

Putting $B = A/2\ \bar{\phi}^{\frac{1}{2}}$ and expanding the sine term as a power series yields

$$\frac{J(V,T)}{J(V,0)} = \frac{\pi BkT}{\pi BkT\ - 1/6(\pi BkT)^3}$$

Cancelling and employing the binomial expansion

$$\frac{J(V,T)}{J(V,0)} = 1 + \frac{1}{6}\ (\pi BkT)^2 \qquad (5.4)$$

where it has been assumed that all terms containing higher powers of T are negligible.

Equation (5.4) may be re-arranged and divided throughout by V. Thus

$$\sigma(V,T) = \sigma\ (V,0)\ (1 + \alpha\ T^2)$$

This is the variation found experimentally, which supports tunnelling as the electron transport mechanism.

Hartman and Chivian(17) have used a different approach in analysing their temperature dependence data obtained from aluminium oxide films. They fit their experimental data of log J(T) versus log T to the theoretical dependence given by equation (2.53) which is of the form x/sin x versus x. A similar method of analysis has been employed with the data obtained in the present work. A computer program (Appendix 1) using an iterative procedure was used to fit the data to the theoretical temperature dependence;

an approximate initial value of J(V,O) being estimated from a plot of the type shown in Fig 5.8. A typical example for an Al-BaSt$_2$-Al device is shown in Fig 5.9. The quality of the fit shown here for an applied potential of 0.1V is characteristic for all voltages between 0.1V and 0.7V. It should be noted that the scale of the ordinate axis has been greatly expanded compared to the abscissa in order that the relatively small (e.g. compared to Schottky emission) temperature dependence can be compared accurately with the theoretical form.

These results establish quite clearly that electron tunnelling directly between the two aluminium layers is the predominant conduction mechanism. Now the temperature dependence of the tunnel current given by equation (2.53) can be expressed in terms of Stratton's formulation as

$$\frac{J(V,T)}{J(V,O)} = \frac{\pi C_1 kT}{\sin(\pi C_1 kT)} \qquad (5.5)$$

Thus, by fitting the experimental current density data to the theoretical dependence given by equation (5.5) for a set of applied voltages in the range 0.05-0.7V, C_1 can be deduced as a function of V. For voltages V $\lesssim$ 0.4V, C_1 is found to be essentially independent of V and thus for the device of Fig 5.9,

$$C_1 \simeq C_{10} = 22.1 \text{ eV}^{-1}$$

to reasonable accuracy. If a rectangular barrier is assumed, then from equation (2.48)

$$C_{10} = 2\pi s \ (2m)^{\frac{1}{2}} \ / \ h \ \phi^{\frac{1}{2}}$$

On substituting known values for m and h and putting s = 2.5 nm, ϕ = 0.34 eV is obtained for the interfacial barrier height. This value is not in good agreement with that obtained from fitting the current-voltage data to equation (2.47). However, there are complications in the correct

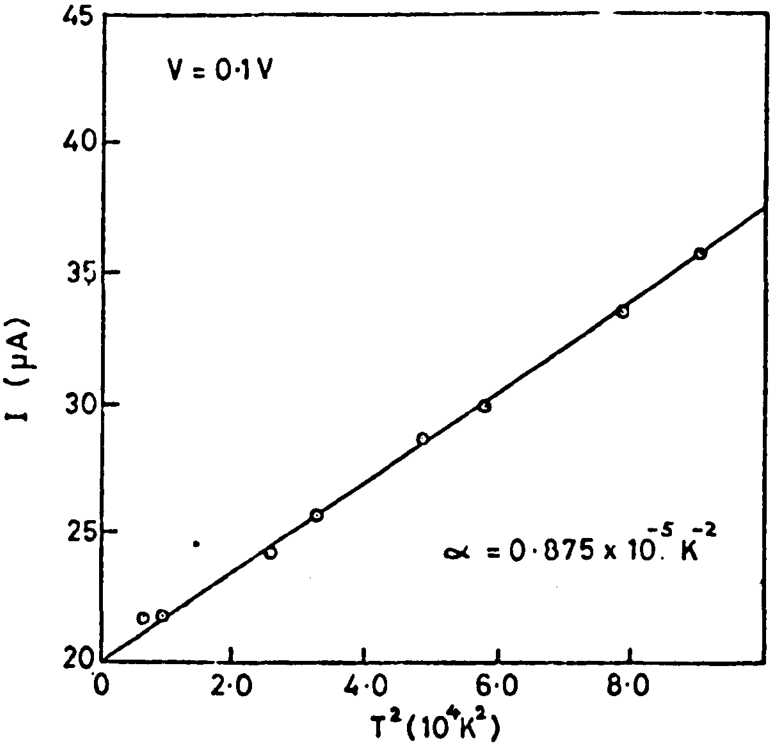

Fig 5.10: The variation of the current with (Temperature)^2 at a fixed voltage for a single layer Sn-BaSt$_2$-Pb device (Sn negative)

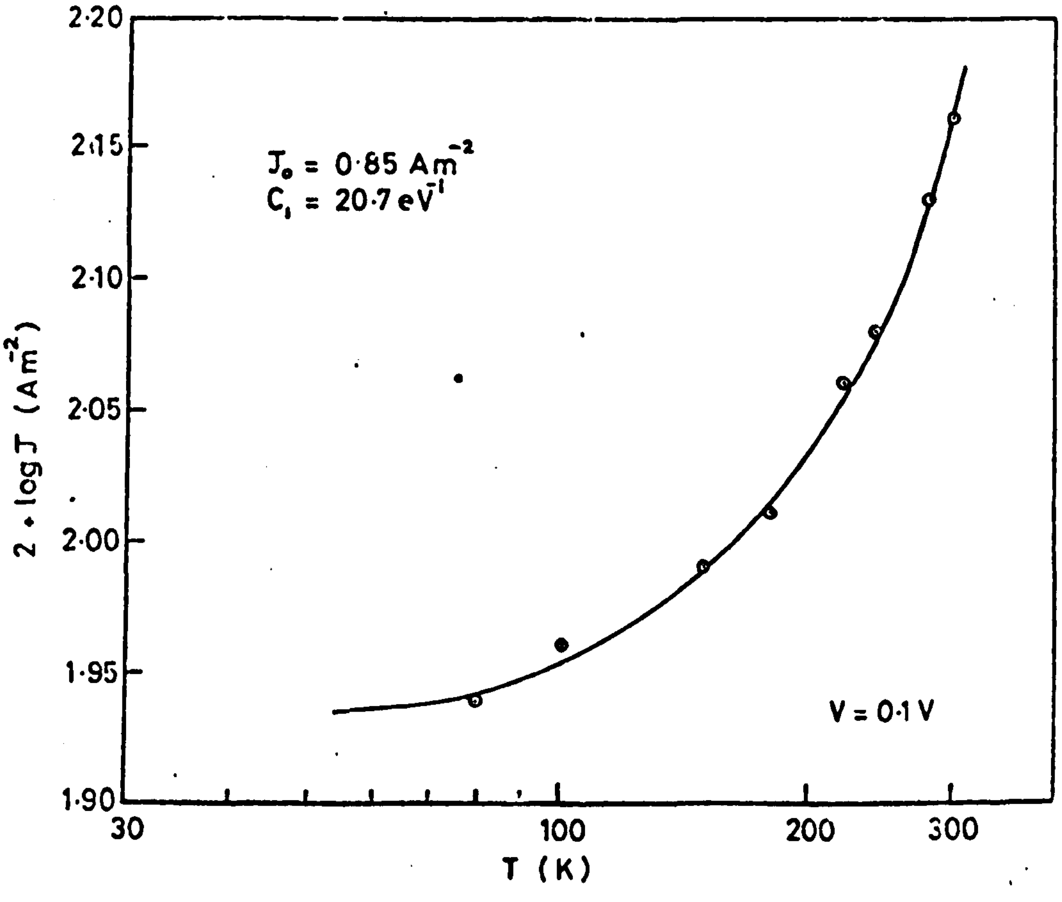

Fig 5.11: The dependence of the current density on temperature for a single layer Sn-BaSt$_2$-Pb device. The curve is the best fit of equation (5.5) to the data. The tin electrode was biased negative.

interpretation of these results because of the possible effects of the oxide layer. These will be considered in detail in section 5.7 after results from MIM devices without incorporated Langmuir films have been presented. Measurements of the variation of the current with temperature were made also for Sn-BaSt$_2$-Pb junctions in the temperature range 80-300K and at fixed voltages from 0.1 to 0.5V. Typical results obtained at a fixed voltage of 0.1V are shown in Figs 5.10 and 5.11. The detailed fit of the data to the theoretical temperature dependence offers strong support that the dominant conduction mechanism in these junctions is indeed electron tunnelling.

From the fit in Fig 5.11,

$$C_1 \approx C_{10} = 20.7 \text{ eV}^{-1}$$

can be deduced. Putting $s = 2.5$ nm yields a value of $\phi = 0.39$ eV for the Sn-BaSt$_2$ interfacial barrier height.

5.4 THE LOGARITHMIC CONDUCTIVITY AS A FUNCTION OF BIAS

The mean interfacial barrier height is an important parameter in determining the current-voltage characteristic of a tunnel junction. There are three methods which are commonly used for its determination. The first of these is to fit the experimental data to a tunnelling equation such as (2.47) and to use the tunnelling distance Δs and barrier height ϕ as adjustable parameters. This has already been described in section 5.2 for some of the results obtained in the present work. The second method is to plot $\hat{J}$ defined by equation (2.55) against V which should yield a peak at $V = \phi$. This method measures the change of current as a function of temperature and would thus be difficult and involve large errors since the current changes relatively little with temperature. The final method is to plot the logarithmic conductivity $d\,\ell n\,J/dV$ against V which should again yield a peak at $V = \phi^{(18)}$. The main advantage of this method is that it allows the determination of the barrier height to be made independently of the other parameters of the theory. This section describes the results of using the technique on the data obtained in the present work.

The arrangement described in section 4.4 was employed to measure values of current and voltage at 0.05V intervals and at temperatures between 80-300K. The logarithmic conductivity as a function of bias was obtained from these measurements by using a computer programme (see Appendix 1). Typical results for an Al-BaSt$_2$-Al device at room temperature are shown in Fig 5.12 for the voltage range 0-1.2V. It is clear that the logarithmic conductivity shows no peak within the limits of experimental error in the applied voltage range 0-1.2V. Although any peak is expected to be small if Δs is small$^{(18)}$, and Δs would be reduced further at higher bias because of the effect of a non-rectangular barrier shape (see section 5.2) a peak would still be noticeable if the barrier height ϕ were to be in the range 0-1.2V, as will be shown later in this section when results from Sn-BaSt$_2$-Pb junctions are considered. The fact that no peak is observed in the applied voltage range 0-1.2V makes it unlikely that the interfacial barrier height $\phi < 1.2$ eV. It was not possible to check for the presence of such a peak at higher voltage since device breakdown usually occurred at ∿ 1.3-1.5V.

These experiments were also undertaken with devices of the type Sn-BaSt$_2$-Pb. The result of plotting the logarithmic conductivity against applied voltage for such a device is shown in Fig 5.13. This yields a peak at V = 0.88 eV and thus it is possible to conclude a value of ϕ = 0.88 eV for the Sn-BaSt$_2$interfacial barrier height. Further confirmation of this is obtained from Fig 5.14 where the logarithmic conductivity against voltage has been plotted for another Sn-LF-Pb junction where this time the Langmuir film was a monolayer of an anthracene derivative (see Fig 5.14). This yields a value of ϕ = 0.94 eV for the Sn-anthracene interfacial barrier

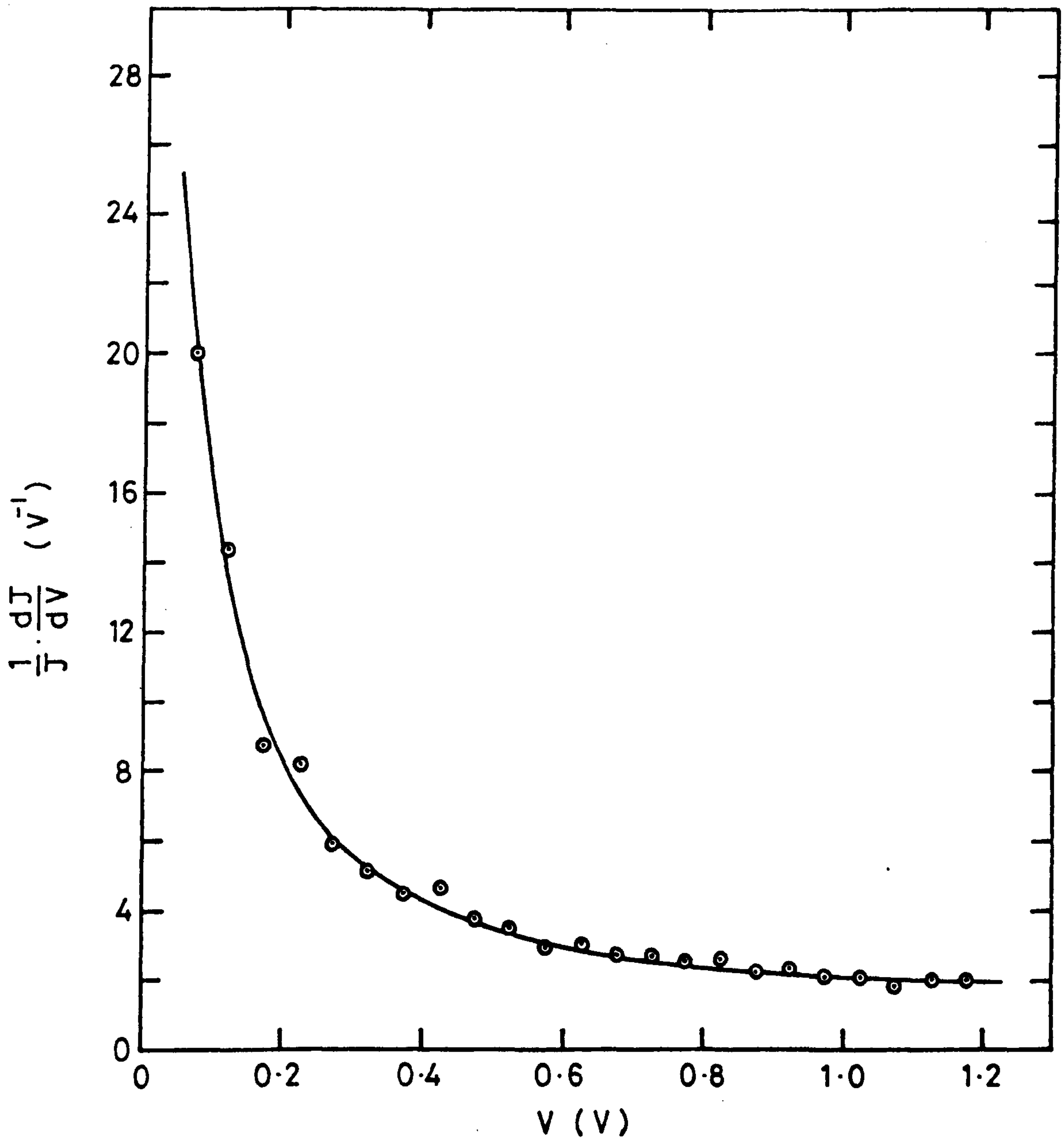

Fig 5.12 : The logarithmic conductivity d(ln J)/dV as a function of applied voltage for a single layer Al-BaSt$_2$-Al device at room temperature (Base electrode positive).

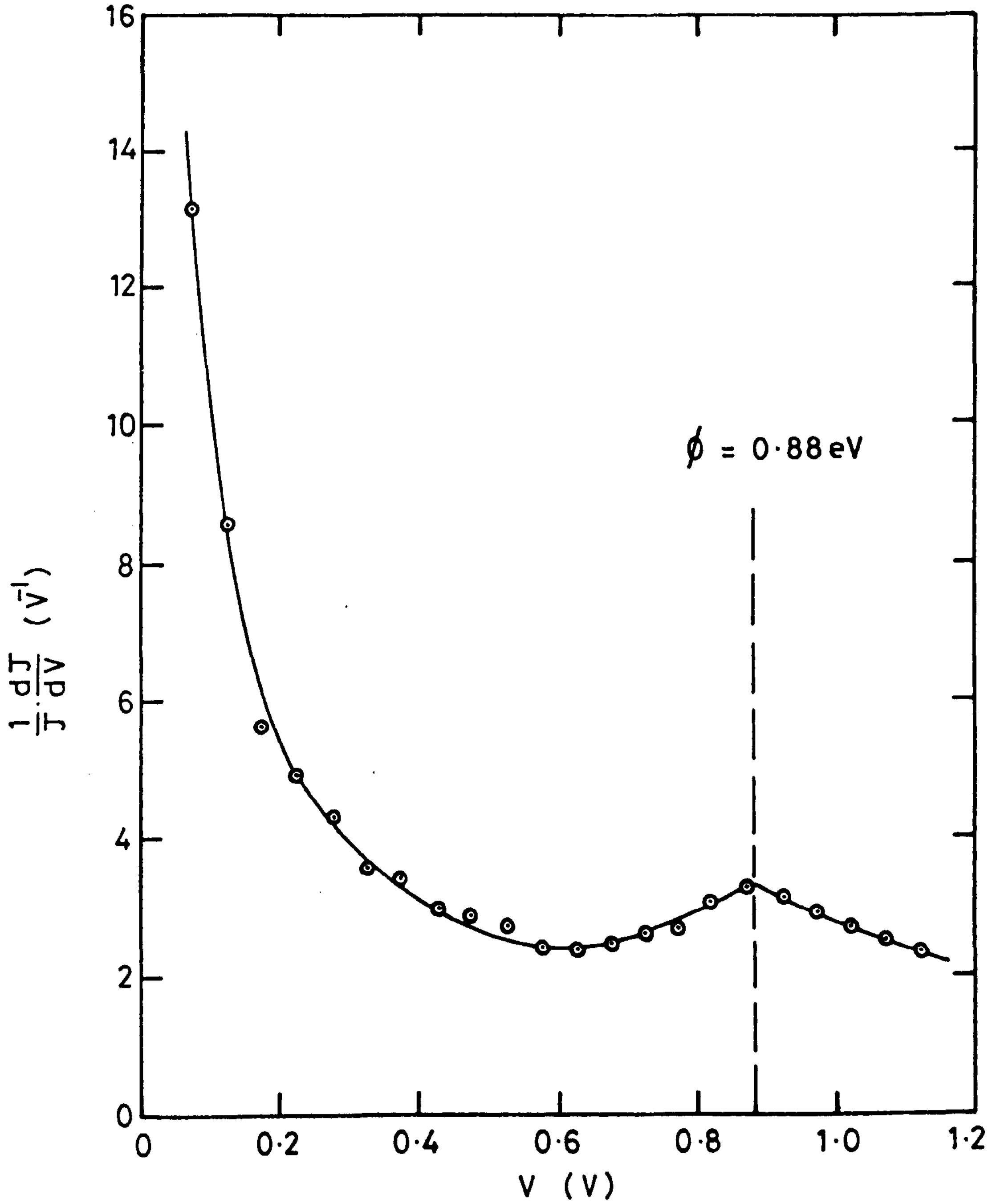

Fig 5.13: The logarithmic conductivity d(ln J)/dV as a function of applied voltage for a single layer Sn-BaSt$_2$-Pb device at 80 K (Sn electrode positive).

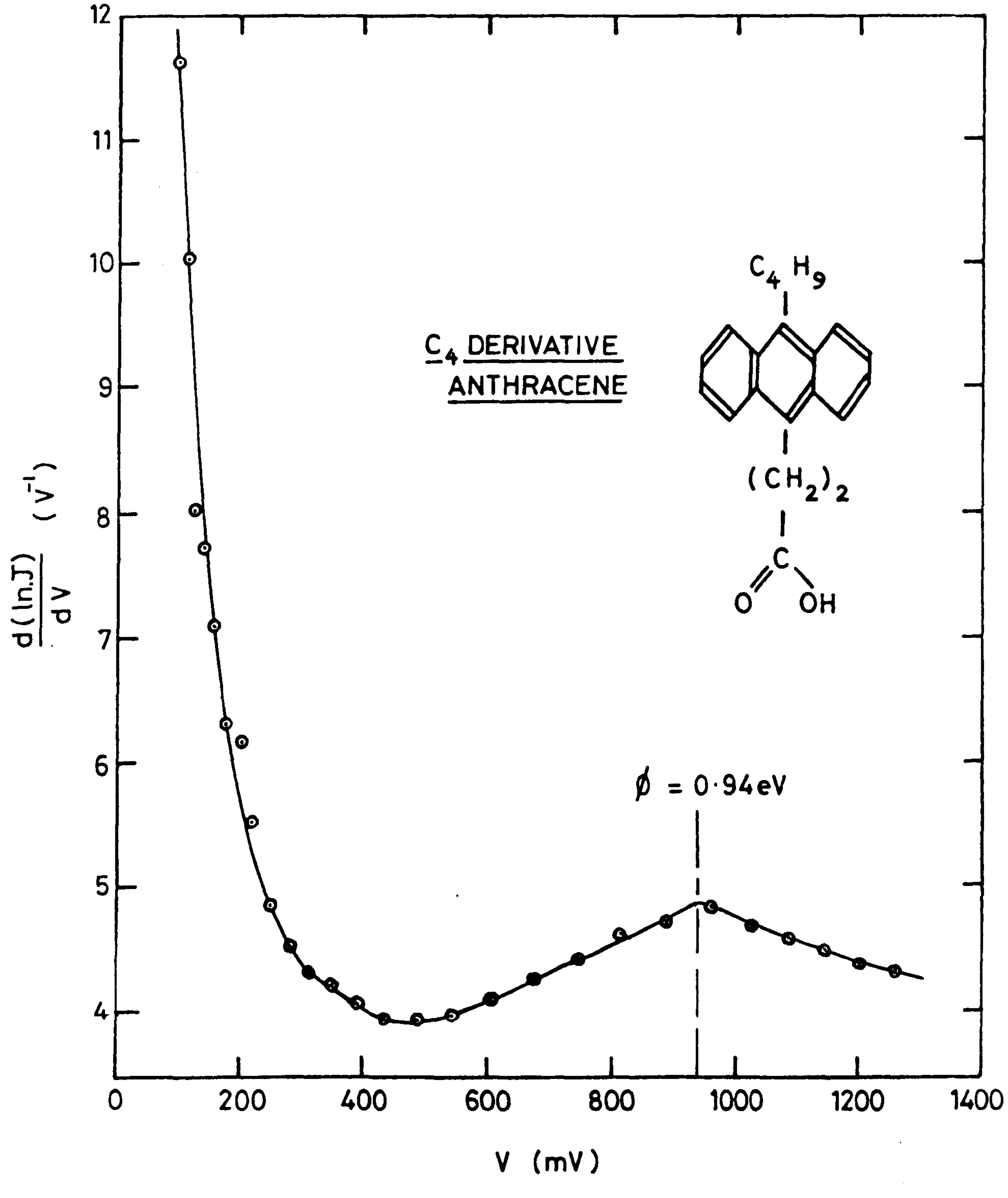

Fig 5.14: The logarithmic conductivity d(ln J)/dV as a function of applied voltage for a single layer Sn-Anthracene-Pb device (Sn electrode positive) at 77 K.

height. The value of ϕ = 0.88 eV obtained for the Sn-BaSt$_2$ barrier height does not agree with ϕ = 0.39 eV obtained from fitting the temperature dependence.

The interpretation of the results of these experiments is left until section 5.7 after the influence of the interfacial oxide layer has been considered.

5.5 THE CURRENT-VOLTAGE RELATIONSHIP AT LOW BIAS

This section considers the current-voltage relationship at low bias in more detail. If a metal-insulator barrier height of $\sim$ 2 eV and a thickness corresponding to the length of a barium stearate molecule is assumed, it is easy to shcw from equation (2.47) that the I-V characteristic of such a barrier should be linear up to approximately 100 mV. In fact, the current-voltage characteristics of the Al-BaSt$_2$-Al devices fabricated in this work and by others$^{(9-14)}$ show a marked non-linearity in this voltage range (see Fig 5.4). This discrepancy has been investigated in depth by Gundlach and Kadlec$^{(10)}$. By plotting the logarithmic derivative of the d.c. conductivity, that is d $\ell n(J/V)/dV$ versus the applied voltage V they demonstrated the existence of an additional barrier in the system of height $\sim$ 80 meV. Furthermore, by fabricating otherwise similar junctions <u>without</u> the organic layer and again demonstrating the existence of this low energy barrier, they were able to conclude that the effect was due to the interfacial oxide layer. Gundlach and Kadlec attribute this additional barrier to impurities in the oxide film, possibly from the subphase solution in the Langmuir trough, which give rise to trap-assisted tunnelling or an additional low energy barrier$^{(19)}$.

The low voltage I-V characteristics of Al-BaSt$_2$-Al junctions fabricated in the present work were studied in some detail. Measurements of current and voltage were made at 5 mV intervals in the temperature range 80-300 K and voltages from 5mV to 150 mV.

Typical results are shown in Fig 5.15, where the differential resistance dV/dI has been plotted against the applied voltage V for various fixed temperatures. The differential resistance as a function of bias was computed numerically from the I-V data (Appendix 1). Results obtained with the base aluminium electrode biased negative showed symmetrical characteristics. From Fig 5.15, several relevant observations emerge :-

(1) The differential resistance remains constant up to applied voltages V $\simeq$ 50 mV after which it decreases, implying an ohmic I-V characteristic for V $<$ 50 mV.

(2) The voltage at which the non-linearity sets in decreases with increasing temperature.

(3) There is no evidence of a zero-bias anomaly of the type investigated by Shen & Rowell(20). This would have been characterised by a peak in the differential resistance at zero bias which would show marked increases at lower temperatures and coalescence of the curves for different temperatures at higher bias.

In Fig 5.16, the logarithmic conductivity is plotted against the applied voltage for the device at a temperature 80 K and the voltage range 5-150 mV. This is essentially equivalent to plotting $d(\ell n\ J/V)/dV$ against V and the presence of an energy barrier of magnitude 5-150 meV would be revealed as a peak. It is clear from Fig 5.16 that there is no peak in the logarithmic conductivity in the whole of this bias range - a result which is at variance with the observations of Gundlach and Kadlec(10). Furthermore, aluminium-based junctions fabricated using an otherwise identical procedure but without incorporating Langmuir films produced I-V characteristics that were linear for applied voltages up to $\sim$ 0.3V.

It would appear from these results therefore that the non-linearity is not caused by the oxide layer but by the Langmuir film itself. These observations can be partly explained by assuming a two-barrier model where

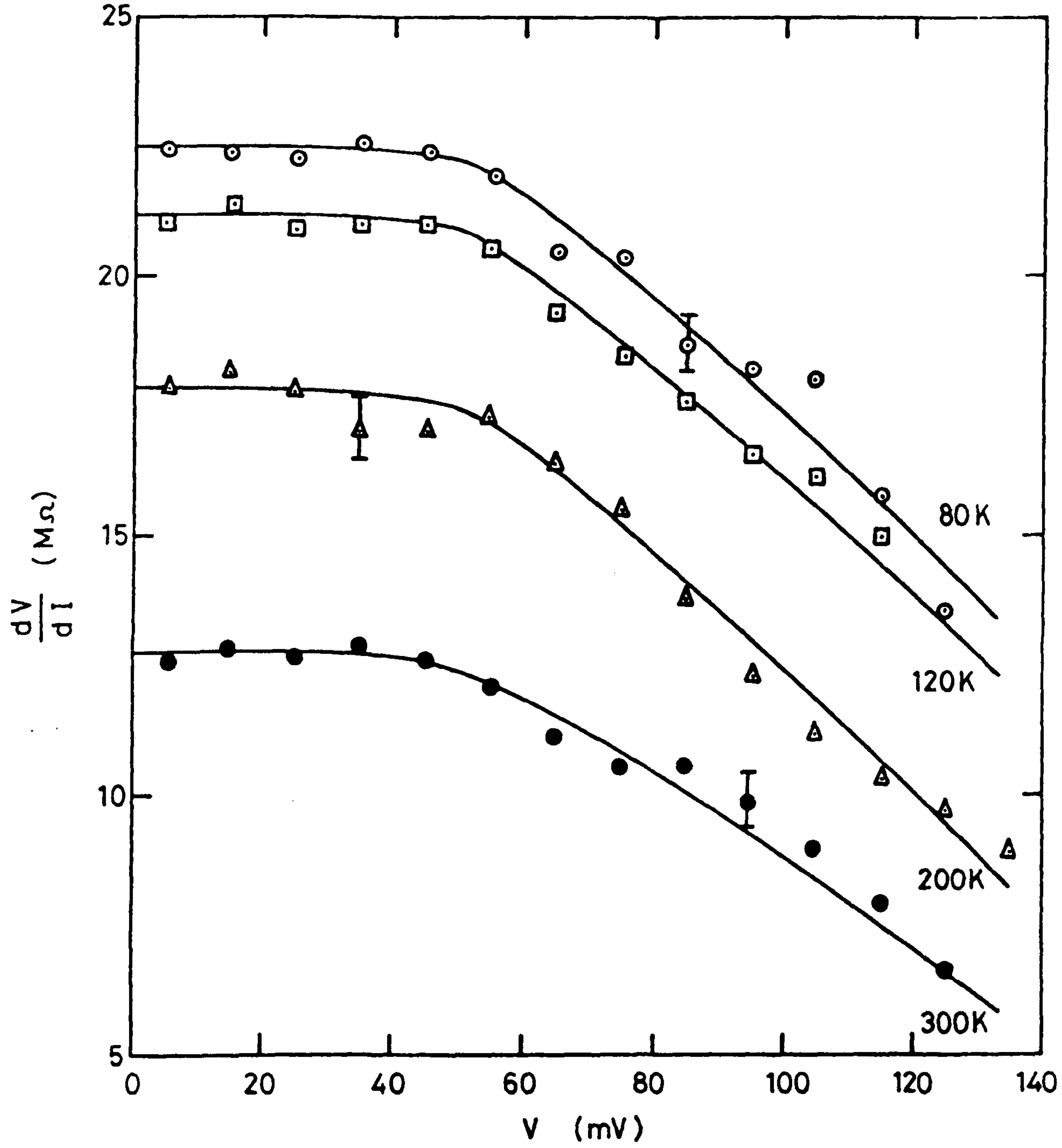

Fig 5.15: The differential resistance as a function of the applied voltage V at low biases for an Al-BaSt$_2$-Al device at various temperatures.

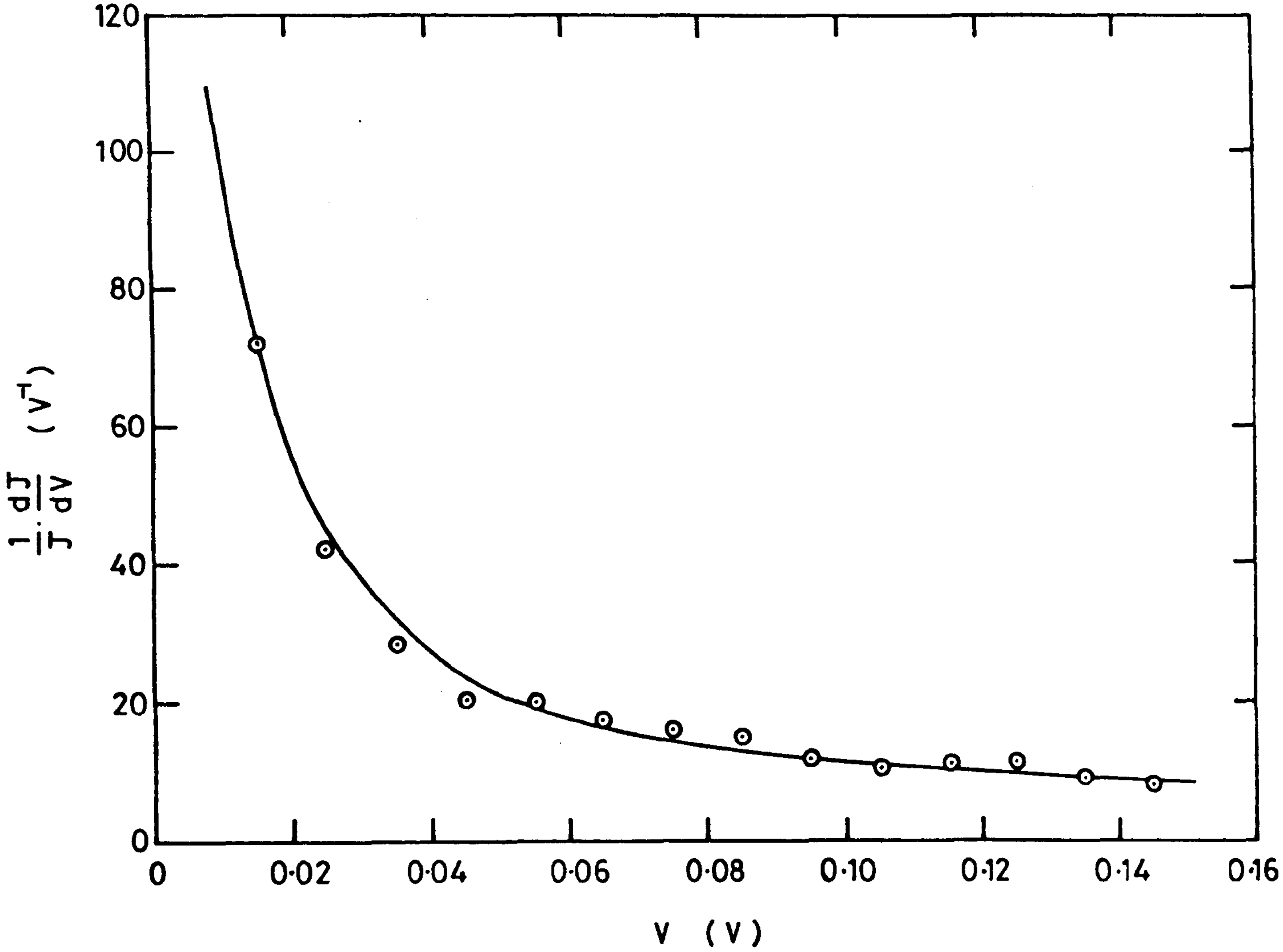

Fig 5.16: The logarithmic conductivity d(ln J)/dV against V plot for an Al-$BaSt_2$-Al device at 80 K and low applied bias (Base Al electrode positive).

the interfacial barrier due to the insulating oxide is in series with a lower energy barrier due to the Langmuir film(21). However, to explain the non-linearity in the characteristic this latter barrier height would have to be of the order of $\sim$ 0.8 eV or lower and would be revealed by a plot of $d(\ell n\, J)/dV$ versus V for the Al-$BaSt_2$-Al devices. It is known from results already presented (see Fig 5.12) that there is no such evidence for a barrier of this magnitude in the $d(\ell n\, J)/dV$ versus V plot and thus it is unlikely that this model is the correct explanation of the results.

5.6 THE EFFECT OF THE INTERFACIAL OXIDE LAYER

From the results presented so far, it is obvious that the effect of the interfacial oxide layer in Al-$BaSt_2$-Al junctions must be taken into account when interpreting data. The important observations arrived at from these results can be summarised as follows :-

(1) Capacitance measurements on Al-$BaSt_2$-Al junctions point to an oxide thickness 4-5 nm thick in series with the Langmuir film.

(2) The effect of this interfacial oxide layer is of considerably less importance in Sn-$BaSt_2$-Pb junctions where the oxide layer is relatively conducting.

(3) Since no rectification effects are observed in the I-V characteristics of aluminium-based junctions this can be taken as evidence of symmetry in Al-$BaSt_2$-Al systemsand thus possibly two interfacial oxide layers are present. Such an arrangement is quite possible because after transfer of the Langmuir film there are inevitably some water molecules present in the system and the diffusion of these to the top electrode and hence its subsequent oxidation cannot be ruled out(5).

The effect of the oxide film(s) in Al-$BaSt_2$-Al devices was investigated in considerable detail. For these experiments junctions of the type Al-Al_2O_3-Al were fabricated using an identical procedure to

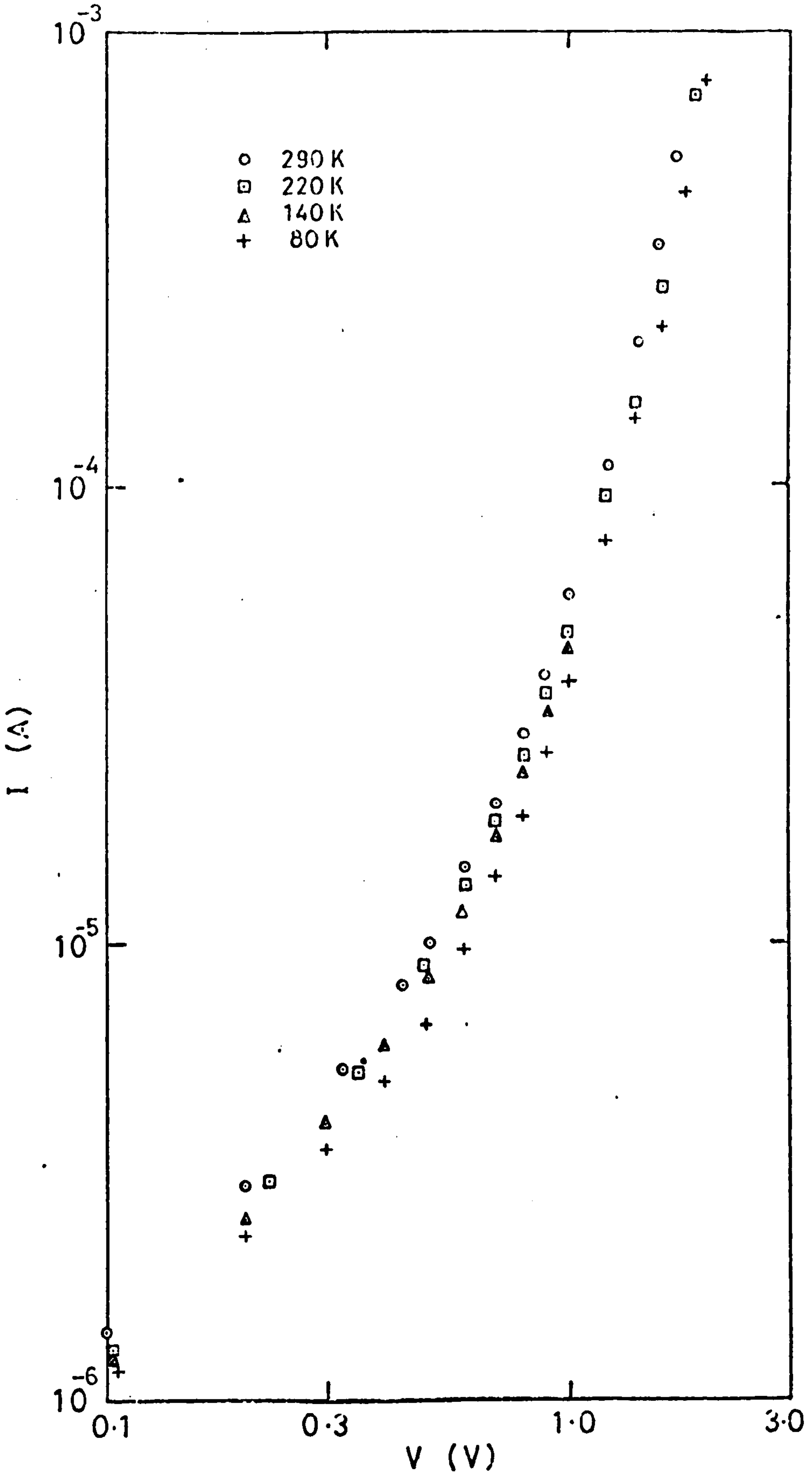

Fig 5.17: Current-voltage characteristics for an $Al-Al_2O_3-Al$ device at various fixed temperatures. (Base Al electrode negative).

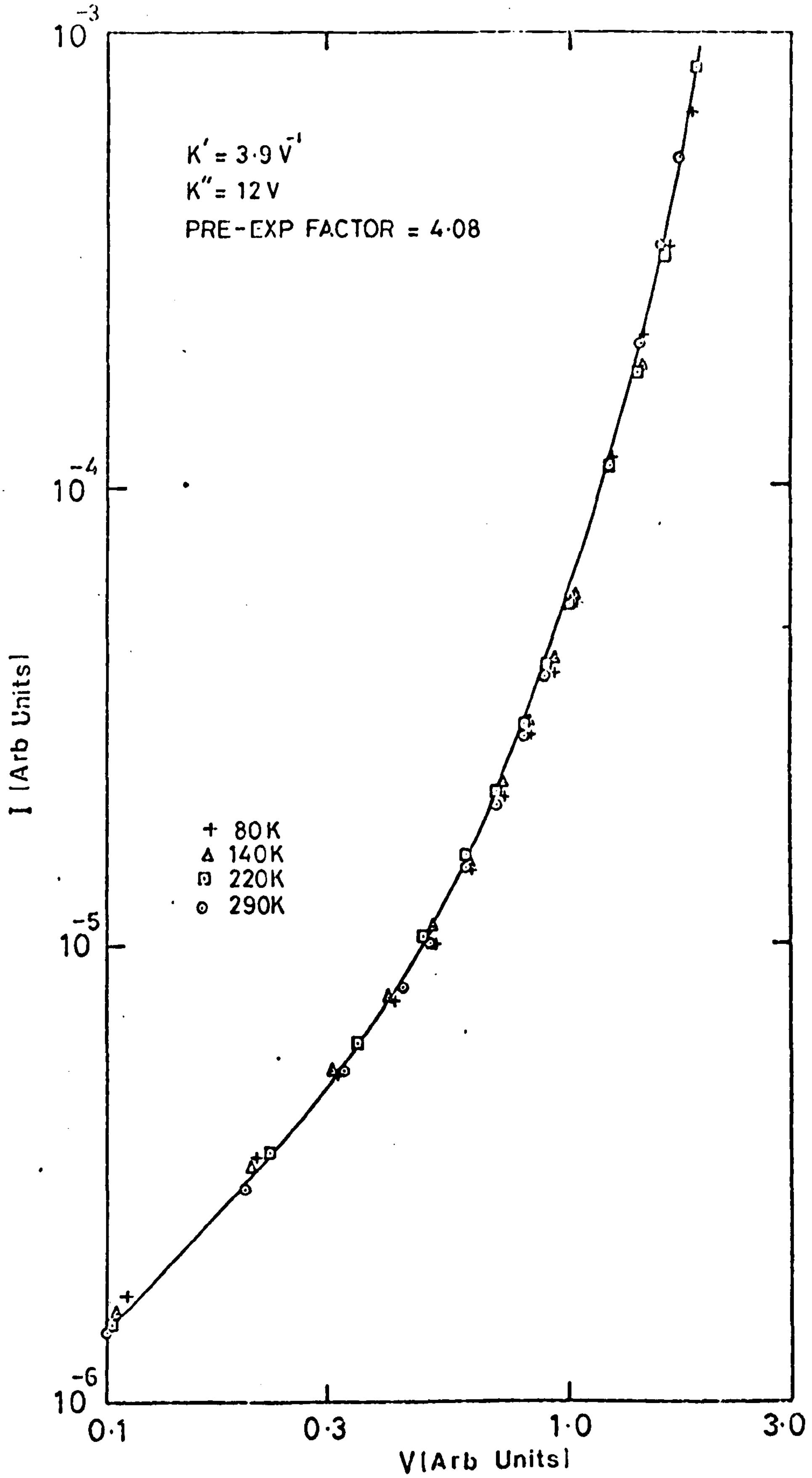

Fig 5.18: The temperature normalised I-V characteristic for an $Al-Al_2O_3-Al$ device. The solid line is the best fit of equation (5.2) to the data with the parameters indicated.

that used for fabricating Al-BaSt$_2$-Al devices but this time omitting to spread the monolayer on the subphase. The specific resistance of these junctions measured at low voltage (∿ 10 mV) was usually of the order of 10^3 Ω.

In Fig 5.17, typical current-voltage characteristics for an Al-Al$_2$O$_3$-Al device at various fixed temperatures in the range 80-290K are presented. As with the other characteristics presented, these results display a weak temperature dependence which make it unlikely that the conduction mechanism in these devices is by anything other than electron tunnelling. No rectification effects were observed when the polarity of the applied voltage was reversed. The characteristics were found to be linear for applied voltage $V < 0.4V$ in contrast to the results of Gundlach and Kadlec(10).

The I-V characteristics obtained at different temperatures can again be normalised to a single curve using the procedure due to Hill(7). This is demonstrated in Fig 5.18. Also shown here is the result of fitting equation (5.2) to the data for the voltage range 0.1-2.0V and it is apparent that the model is a good fit to the normalised characteristic throughout this voltage regime. From the fit the value of K' is deduced as 3.9 V^{-1}. If a value for the tunnelling distance of $s = 4.4$ nm as given by the capacitance measurement is assumed then $\phi = 8.40$ eV is obtained for the Al-Al$_2$O$_3$ interface. A more reasonable estimate of the tunnelling distance of $s = 2$nm yields a value of $\phi = 1.74$ eV which is in reasonable agreement with $\phi = 1.58$ eV quoted by Pollack and Morris(22) and $\phi = 1.5$ eV found by Furtlehner and Messier(23) for similar interfaces. The smaller estimate of the tunnelling distance is justified since electron tunnelling is most sensitive to thin spots in the insulating film whereas the capacitance measurement yields the <u>mean</u> thickness of the oxide.

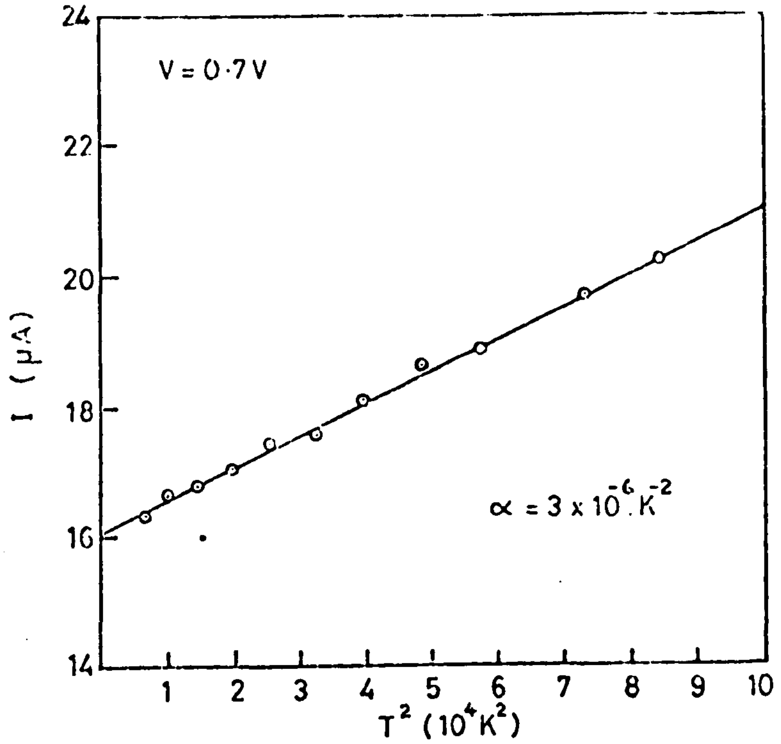

Fig 5.19: The variation of the current with $(\text{Temperature})^2$ at a fixed voltage for an $Al-Al_2O_3-Al$ device (Base Al negative)

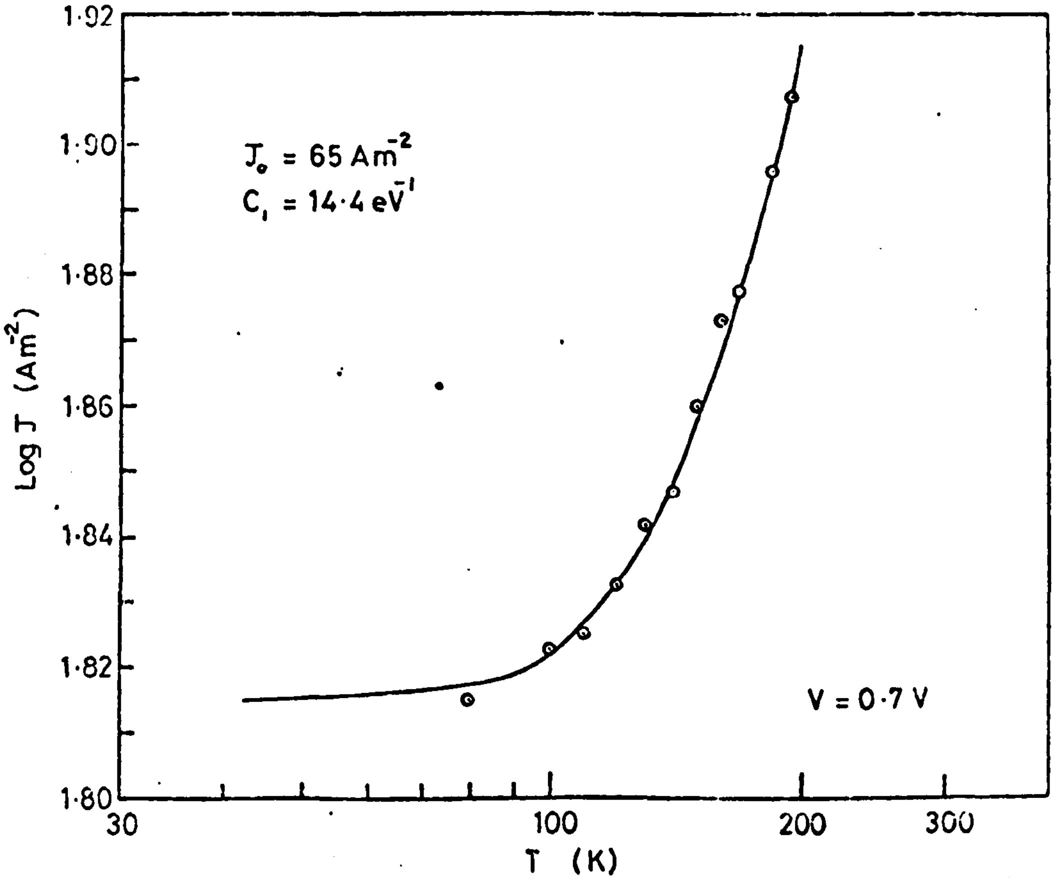

Fig 5.20: The dependence of the current density on temperature for an $Al-Al_2O_3-Al$ device. The curve is the best fit of equation (5.5) to the data.

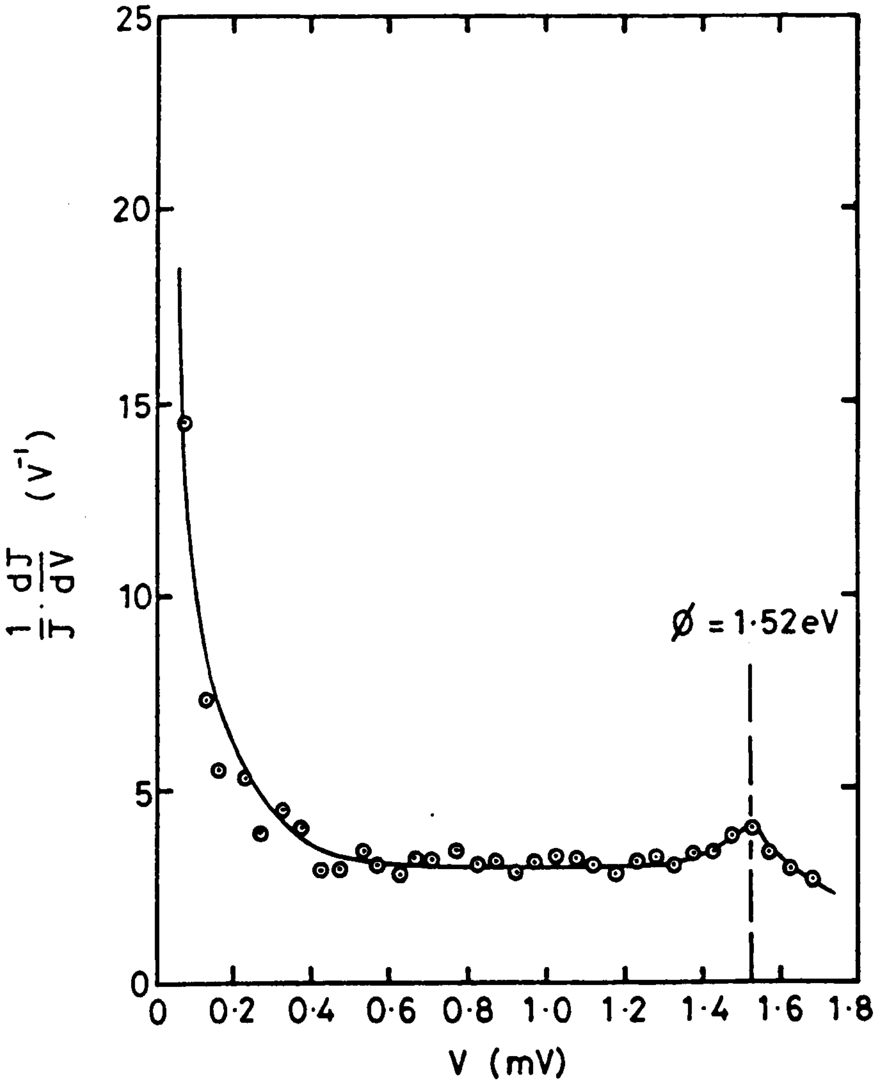

Fig 5.21: The logarithmic conductivity d(ln J)/dV as a function of applied voltage for an Al-Al_2O_3-Al device at liquid nitrogen temperature (Base Al electrode positive).

The temperature dependence of the current was investigated by measuring the variation of the current as a function of temperature at various fixed voltages in the range 0.1 to 0.9V. A typical result is shown in Fig 5.19. Within the limits of experimental error the graph is linear, thus implying a relationship of the form given by equation (5.4). Fitting of the data to the theoretical temperature dependence given by equation (5.5) yields $\phi = 0.51$ eV if a tunnel length of $s = 2$ nm is assumed. The quality of the fit is shown in Fig 5.20.

It is desirable to obtain an independent estimate of the barrier height for the Al-Al_2O_3 interface. This was done through plotting the logarithmic conductivity as a function of voltage as for the Sn-stearate and Sn-anthracene interfaces in section 5.4. A typical result for an Al-Al_2O_3-Al device at liquid nitrogen temperature is shown in Fig 5.21. This reveals a peak at $V = 1.52$ V and hence a barrier height $\phi = 1.52$ eV for the Al-Al_2O_3 interface which is in excellent agreement with the values of $\phi = 1.58$ eV(22) and $\phi = 1.5$ eV(23) quoted earlier.

If a value of $\phi = 1.52$ eV is assumed then a tunnelling distance of $s = 1.8$ nm is obtained from fitting equation (5.2) to the I-V data (Fig 5.18).

5.7 COMMENTS AND CRITICISMS

The various estimates of the interfacial barrier height obtained from the results presented so far have been tabulated in Table 5.1.

The major problem with the correct interpretation of these results is that apart from the method of plotting the logarithmic conductivity as a function of voltage, all the other estimates of the interfacial barrier height need to be treated with caution. This is because it is not possible to obtain ϕ independently of the other parameters of the junction by simply fitting a theoretical expression (equation 5.2 or 5.5) to the data. In

ϕ/eV	I-V	Temperature Dependence	Log Conductivity	Remarks
Al-BaSt$_2$	0.65	0.34	> 1.2 eV	Assuming S = 2.5 nm
Sn-BaSt$_2$	-	0.39	0.88	S = 2.5 nm
Al-Al$_2$O$_3$	1.5	0.41	1.5	S = 1.8 nm

<u>TABLE 5.1</u>: The values of the interfacial barrier heights obtained using the various techniques for three interfaces (see text).

each case it is necessary to perform independent experiments to justify the interpretation of each individual parameter.

Taking the results obtained from Al-Al_2O_3-Al junctions first, it can be seen that (Table 5.1) the values of ϕ obtained from fitting the tunnelling model to the I-V data and from the logarithmic conductivity can be made consistent with each other if a tunnelling distance of s = 1.8 nm is assumed. However, this value for s does not agree very closely with that estimated from the capacitance measurement which gives s = 4.4 nm. This discrepancy is not too serious because it is well known(10,14,22) that the aluminium oxide layer is non-stoichiometric and contains impurity states and that in fact it can be thought of as comprising of two regions - a semi-conducting transition region and a barrier-type oxide region. In addition, a tunnelling estimate of the thickness will favour the smaller value whereas a capacitance measurement yields a mean thickness. It would appear therefore from these measurements that this latter (insulating) region is approximately 1.8 nm thick.

If an insulating oxide layer of this thickness is assumed to be in series with the single layer Langmuir film in Al-$BaSt_2$-Al devices then the tunnelling distance becomes s = 4.3 nm and a value of ϕ = 1.90 eV is obtained for the Al-$BaSt_2$ interface. This is in good agreement with ϕ = 1.8 eV quoted by Mann and Kuhn(5) for the Al-$CdSt_2$ interface and would appear to explain also why no peak is observed in a $d(\ell n\ J)/dV$ against V plot for these junctions at V < 1.2 V. If the absolute magnitude of the current density is considered in the low voltage ohmic region, say at V = 0.05 V, for a rectangular barrier ϕ = 1.7 eV and s = 4 nm then equation (2.36) gives the current density for tunnelling as $J = 2.66 \times 10^{-12}\ A\ m^{-2}$ or $2.66 \times 10^{-18} A\ mm^{-2}$. This is much smaller than the typical current density of $J \simeq 1 \times 10^{-9}\ A\ mm^{-2}$ observed at V = 0.05V for Al-$BaSt_2$-Al devices. However, these estimates need to be treated with care because the tunnel current is highly dependent upon s and it may well be that the thickness of the insulating region of the oxide in Al-BaSt$_2$-Al devices is much smaller than in corresponding Al-Al$_2$O$_3$-Al devices.

This contention would seem to be supported by consideration of the breakdown voltages of the two types of device. For instance, Al-Al$_2$O$_3$-Al devices were found to undergo dielectric breakdown at much higher voltages ($V \sim 2.5$V) compared to those junctions where an intervening layer of barium stearate had been deposited ($\sim$ 1.3V). These results can be understood on the basis of a thicker insulating region in the former type of device which would support a greater applied voltage. If this is assumed then it would lead to a slight reduction in the interfacial barrier height estimate of $\phi = 1.90$ eV for the Al-BaSt$_2$ interface and an increase in the predicted magnitude of the tunnel current which may well be in closer agreement with that observed. It should be noted also that electron tunnelling is extremely sensitive to thin spots in the insulating film and the concept of a perfectly uniform and homogeneous oxide film may not necessarily be true for all the devices investigated. A possible energy diagram for the Al-BaSt$_2$-Al system constructed on the basis of the observations presented so far is shown in Fig 5.22. In view of the discrepancy in the magnitudes of the observed and predicted tunnel currents the thickness of each individual insulating region of the oxide layers may well be less than 0.9 nm. It should be noted however that these results are not unique in predicting tunnel current densities that are much smaller than those observed. Indeed, this seems to be a consistent feature of most attempts(22,24) to verify the tunnelling mechanism by comparison with an independent-electron model and is possibly a symptom of the inadequacy of the model to describe the experimental data even if the current through the junction is due to tunnelling(25).

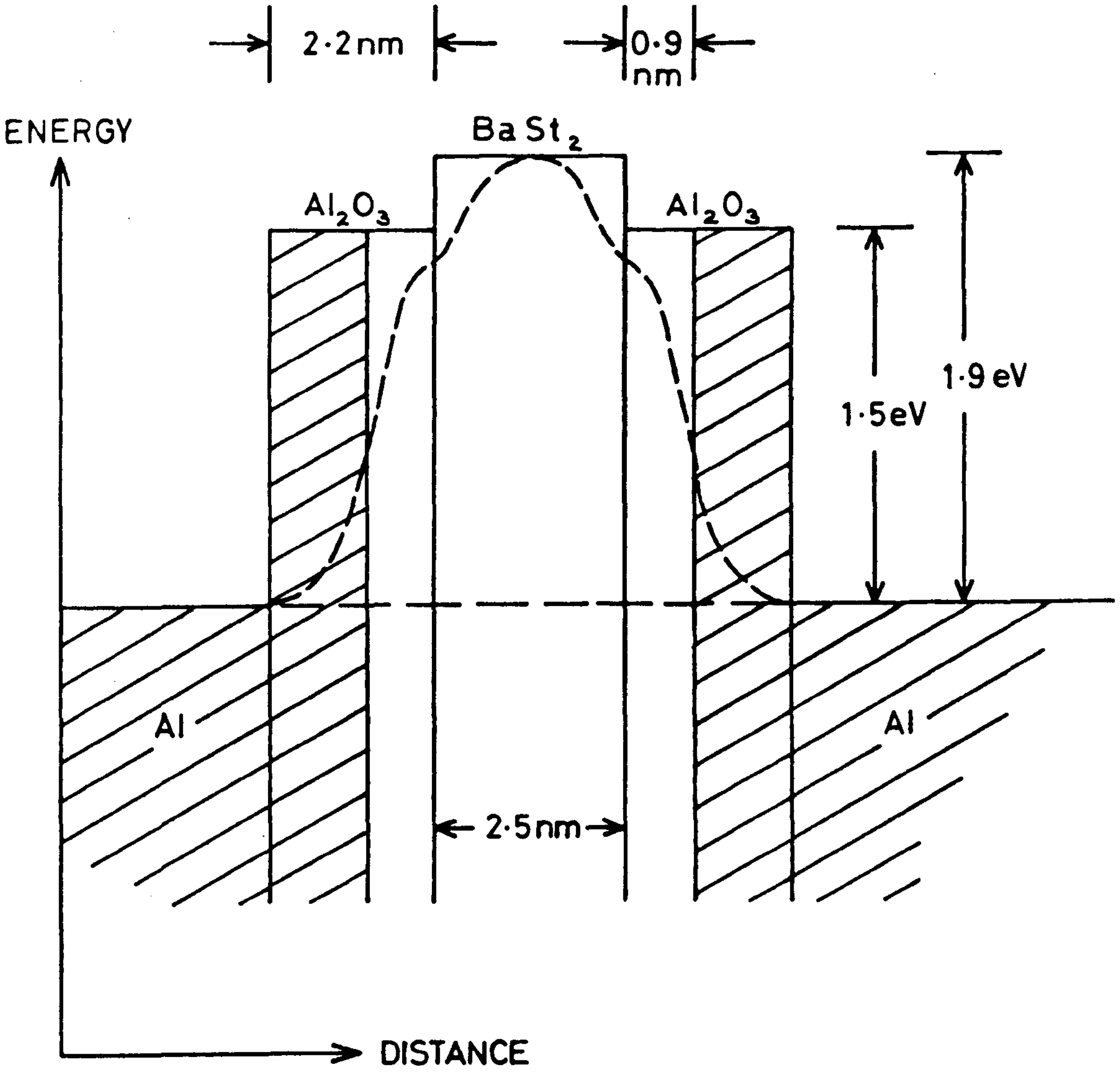

Fig 5.22: A possible energy diagram for the Al-Al$_2$O$_3$- BaSt$_2$- Al system. The hatched regions in the aluminium oxide layers represent the semiconducting transition region. The dotted line represents a more accurate estimate of the profile of the barrier.

It will be noted from Table 5.1 that the value of ϕ obtained from fitting the theoretical temperature dependence to the data is consistently lower than those obtained from the other methods for all types of junction. It is not clear why this should be but such low values as have been obtained are very unlikely since it would mean that the current-voltage relationship would then be given by the Fowler-Nordheim form (equation 2.39) for applied voltages $V \gtrsim 0.6$ V. Clearly, this is not the case and it must be concluded that the values of ϕ obtained from fitting to the theoretical temperature dependence are anomalous.

The logarithmic conductivity against voltage plot for Sn-BaSt$_2$-Pb junctions reveals a Sn-BaSt$_2$ interfacial barrier height of $\phi = 0.88$ eV in excellent agreement with $\phi = 0.8$ eV obtained by Horiuchi et al(26) for the same interface from fitting a tunnelling expression to their J-V data. In common with the other types of junction investigated, the value of ϕ obtained for the Sn-BaSt$_2$ interface from analysis of the temperature dependence is much lower than that obtained from the logarithmic conductivity plot. The former value is clearly anomalous in that it predicts a Fowler-Nordheim type J-V relationship given by equation (2.39) for $V \gtrsim 0.6$V. This is obviously not observed. It should be noted however that estimates of ϕ obtained from both the isothermal and thermal analysis would yield higher values if the effect of the image force is included. For very thin insulating films as are being dealt with here, this correction would be considerable and may well yield values which are in closer agreement with those obtained from the logarithmic conductivity plots.

It is necessary to briefly consider the absolute magnitude of the current density for Sn-BaSt$_2$-Pb junctions. At low voltages, these junction display symmetric characteristics and as a reasonable approximation, equation (2.36) may be used to calculate J. For $V = 0.05$ V, $\phi = 0.9$ eV and $s = 2.5$ nm this yields $J = 1.56 \times 10^{-5}$ A mm^{-2}. Now the typical current density observed in these junctions is usually of the order 10-100 μA mm^{-2} at applied voltages of 50 mV which is thus in good agreement with the predicted magnitude.

Although the results presented to date have been useful as evidence for electron tunnelling in single layer films they do not prove conclusively that the electron transport is indeed by electron tunnelling. It is necessary to examine the evidence with special regard to the following points :-

(1) What experimental verification of the tunnelling mechanism for charge transfer is proposed ?

(2) Is the physical interpretation proposed on the basis of the data analysis unique ? In particular, have other independent experiments been performed which support the proposed interpretation and demonstrate the internal consistency of the model parameterization of the J-V characteristics ?

The correspondence between equations (2.47) and (2.53) which describe the functional form of the bias dependence of the current at fixed temperature, and the temperature dependence of the current at fixed bias respectively, with the experimental results has been demonstrated already. However, at best, this correspondence is qualitative only and in particular it has not been possible to verify the value of each independent parameter used in the analysis by conducting independent experiments. The present analysis is by no means unique in this as all the studies of electron transport in Langmuir films which have proposed electron tunnelling as a mechanism for charge transfer(5,9-14) have also done so on the basis of similar analyses.

A major criticism of these studies is that often not enough importance has been attached to the role of the interfacial oxide layer(s) present in the M-LF-M system. The results of the present study have shown that it is possible to explain most of the results obtained by assuming a conduction process which is dominated by electron tunnelling through the oxide and then via pinholes and other defects in the Langmuir film. This is particularly so for those experiments where aluminium has been used as a base electrode. Since the majority of previous work has been undertaken with this material as a substrate for Langmuir film deposition, the interpretation of the results as evidence for electron tunnelling through the Langmuir film may well be justifiably criticised.

Now, a definitive verification of the tunnelling mechanism is to use at least one superconducting electrode and observe that only a small current due to thermally excited quasi-particles flows for bias $|eV|$ less than the energy gap of this electrode(27). The theoretical description of the I-V characteristic for such a junction has been discussed in section 2.2.6. This simple and relatively diagnostic test has been applied to Langmuir films only by Clark(28) and Leger et al(13). It is unfortunate that even the results of these studies can be criticised on identical grounds to those outlined above ; i.e. since there is inevitably an oxide film present in the structure the possibility that electron tunnelling is occurring through the oxide and through defects in the Langmuir film cannot positively be ruled out. In addition, the presence of structure related to the superconducting electrode energy gap in the I-V characteristic is evidence only for a tunnelling mechanism at low bias and does not substantiate electron tunnelling as the mechanism for charge transfer at higher applied voltages.

On the other hand, the detection of inelastic electron tunnelling (IET) signals in conventional tunnelling spectroscopy does fully support the interaction of tunnelling electrons with molecular adsorbates over a considerable energy range and more importantly would, if observed in a M-LF-M structure, substantiate tunnelling through the Langmuir film itself. The significant point here is that only a small fraction of tunnelling electrons (∿ 1%)[(29)] would lose energy to molecular oscillators in the organic film. Thus, the observation of this small number of relatively rare inelastic tunnelling events would be strong evidence of tunnelling through the Langmuir film over an extensive voltage range.

In the rest of this chapter, it will be shown how the results of additional experiments support the contention that the mechanism for charge transfer in single layer films is indeed electron tunnelling.

5.8 THE CURRENT VOLTAGE RELATIONSHIP AT LOW TEMPERATURES : SUPERCONDUCTIVE TUNNELLING

For these experiments the device was located in the cryostat and the current-voltage characteristic recorded at 0.1 mV intervals using the apparatus of Fig 4.5. Occasionally, these measurements were made at 4.2 K by simply locating a device on the sample holder and immersing it directly into the liquid helium.

A typical result for an Sn-$BaSt_2$-Pb junction at low bias and two different fixed temperatures is shown in Fig 5.23. At T = 4K, the lead electrode is superconducting and the I-V curve is expected to show a marked deviation from linearity due to its superconducting energy gap.

This structure in the I-V characteristic is displayed even more prominently when the differential resistance dV/dI is plotted against the applied voltage as shown in Fig 5.24 for a Pb-$BaSt_2$-Pb junction at 4.2K. It was obtained using the tunnelling spectroscopy circuitry described in Chapter 4 using a modulation voltage of 30 μV rms. These measurements establish beyond doubt the contention that electron tunnelling is the

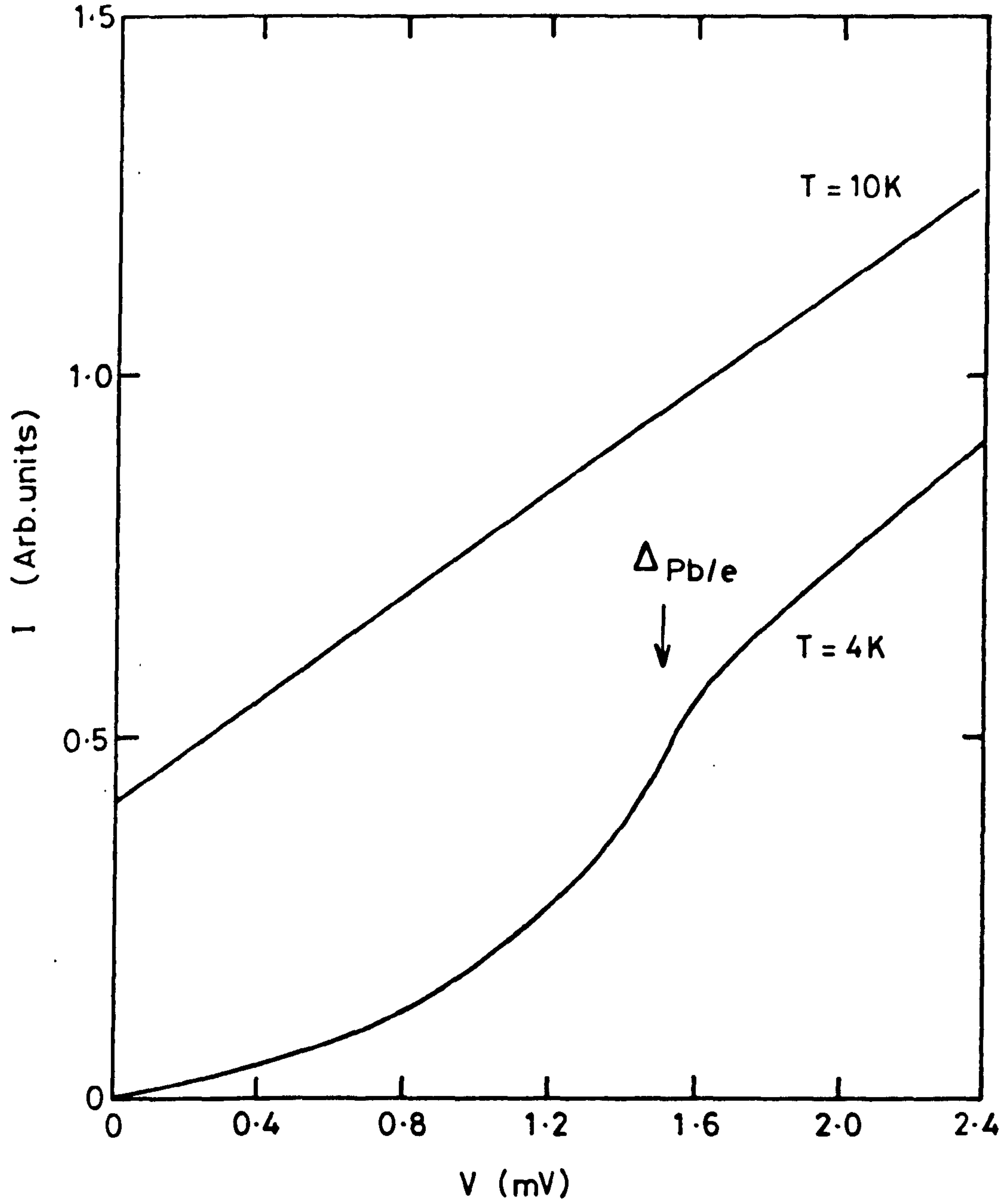

Fig 5.23 : Current-voltage characteristics for an Sn-BaSt$_2$-Pb device at low applied voltages and low temperatures (Sn electrode negative). The T = 10 K characteristic has been displaced along the current axis.

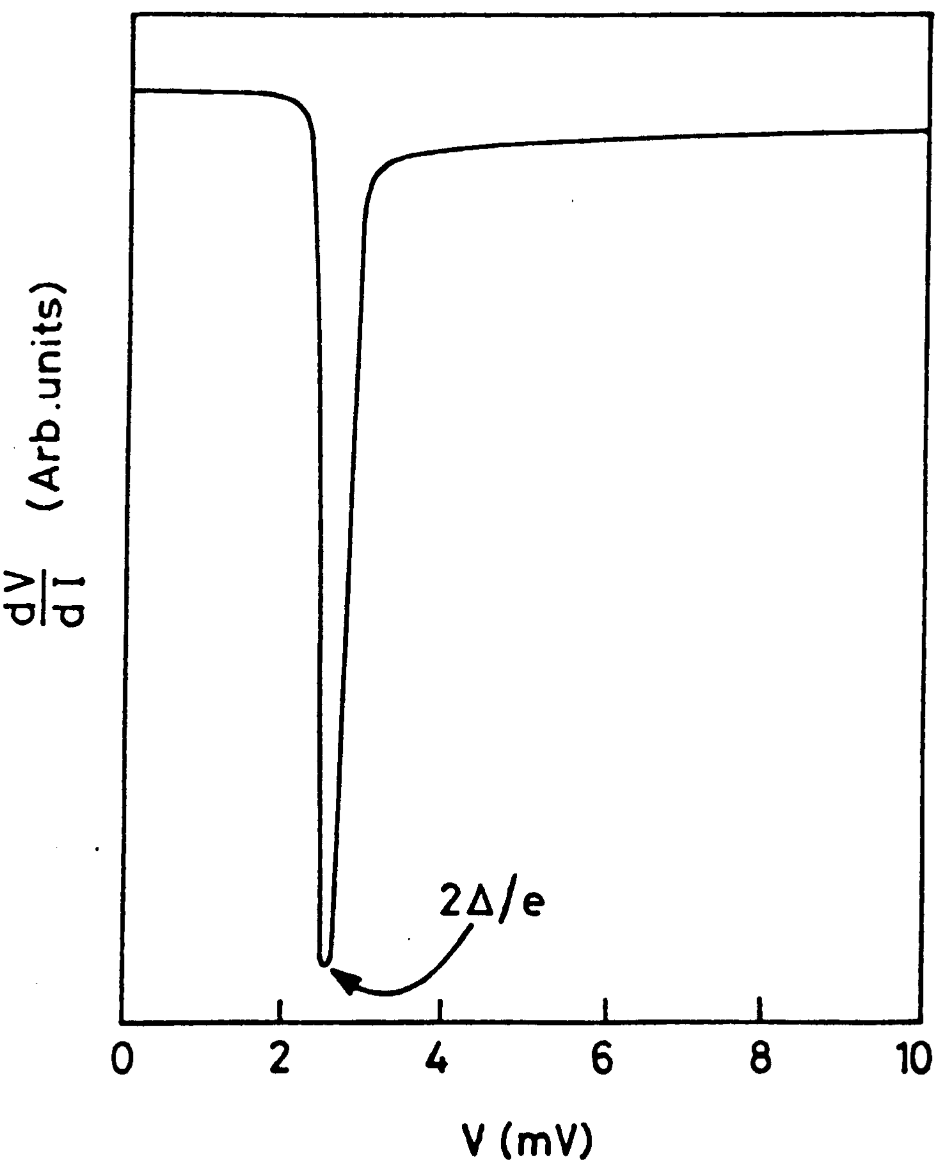

Fig 5.24: A plot of dV/dI versus V for a Pb/BaSt$_2$/Pb device at 4.2K. The base Pb electrode was negative and a modulation voltage of 30 μV rms was applied.

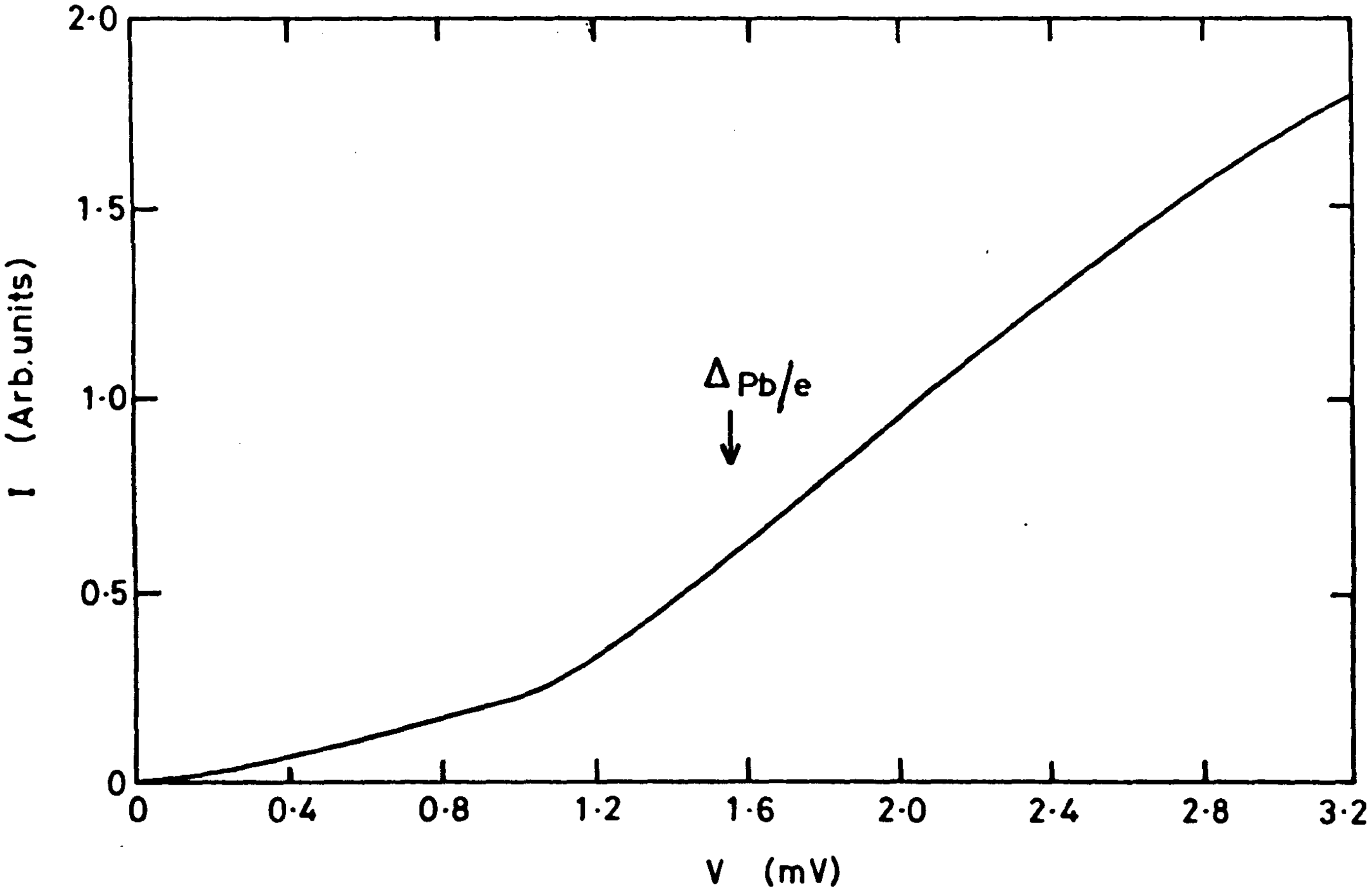

Fig 5.25: Current-voltage characteristic for an Sn-SnO$_x$-Pb device at low bias and 4.2 K (Sn electrode negative).

dominant transport mechanism at low bias and temperature. However, the results do not completely eliminate the possibility of conduction proceeding via tunnelling through the oxide and then through pinholes in the Langmuir film. Fig 5.25, a current-voltage characteristic for an Sn-SnO_x-Pb device at 4.2K is evidence in support of this statement. The device was made using a similar procedure to that employed for M-LF-M devices but no Langmuir film was incorporated. Although the resistance of these devices was found to be very low ($\lesssim 1\ \Omega$), insulating behaviour was found at liquid helium temperatures with some Sn-SnO_x-Pb devices. However, these devices generally broke down at applied voltages $V \lesssim 20$ mV. Fig 5.25 establishes beyond doubt that an electron tunnelling mechanism for charge transfer cannot be assumed in single layer Langmuir films simply on the basis of observing structure related to the energy gap of the superconducting electrode in the I-V characteristic. The best evidence for tunnelling in the organic film would be to observe inelastic electron tunnelling in these films in the bias range 50-500 mV.

5.9 INELASTIC ELECTRON TUNNELLING IN LANGMUIR FILMS

It will be clear from the discussion in this chapter that although measurements of the type described offer strong evidence for electron tunnelling in Langmuir films they do not unequivocally prove that this is indeed the predominant charge transfer mechanism. In particular it may be possible that the results describe a conduction process which can be attributed to electron tunnelling through the interfacial oxide layer(s) and then through defects in the Langmuir film. Consequently, the aim of these particular experiments was to observe evidence for inelastic tunnelling in the Langmuir film in the voltage range 50-500 mV.

For these experiments single layer films were fabricated on tin base electrodes and lead was used as a counter electrode. The choice of these materials was dictated by several considerations :-

(1) The resistance of junctions fabricated using aluminium base electrodes was generally found to be too high (> 1 M Ω) to allow the observation of inelastic tunnelling with conventional instrumentation.

(2) With aluminium base electrodes, the I-V characteristic is markedly non-linear even at applied biases as low as 50 mV. This point has already been discussed in some detail in section 5.5. Whatever the physical origins of this non-linearity, one important consequence of this marked voltage dependence of the current is that it produces a rapid variation in d^2V/dI^2 which masks the observation of peaks associated with inelastic tunnelling events. In contrast to this the current-voltage characteristics of tin-based junctions were found to be approximately linear up to applied voltages $V \simeq 0.3V$. In addition, the specific resistance of these particular junctions was usually in the range 25 Ω-5 k Ω which meant that the instrumentation described in section 4.5.2 could be used in an attempt to observe inelastic tunnelling in Langmuir films.

(3) Lead was preferred as the counter-electrode since it has a relatively high superconducting transition temperature (T_c = 7.2 K) and meant that devices could be simply immersed directly into the liquid helium.

Strong evidence for inelastic tunnelling in organic monolayers is presented in Figs 5.26 and 5.27. These are plots of d^2V/dI^2 against V for two different Sn-BaSt$_2$-Pb junctions at 4.2 K and at an applied bias of 50-500 mV. The lead electrode was biased positive in each case and the peak-to-peak modulation voltage was 4 mV.

For comparison purposes, a tunnelling spectrum of stearic acid was obtained from an Al-Al$_2$O$_3$-Pb junction which had been doped by the conventional liquid-phase doping technique(29) (Fig 5.28). The dopant

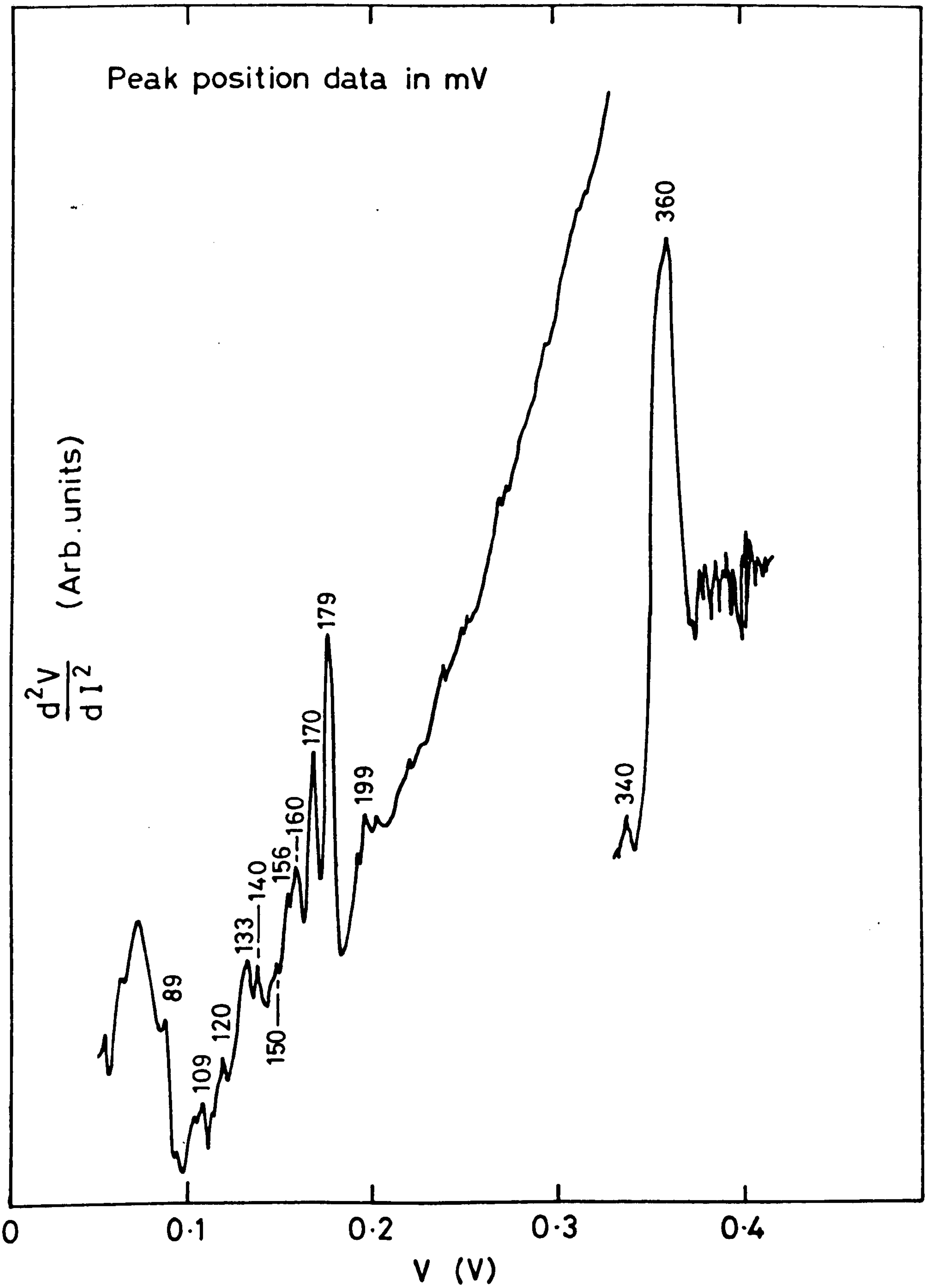

Fig 5.26: Inelastic electron tunnelling spectrum obtained from an Sn-BaSt$_2$-Pb device at 4.2 K using a modulation voltage of 4 mV p-p (Sn electrode negative).

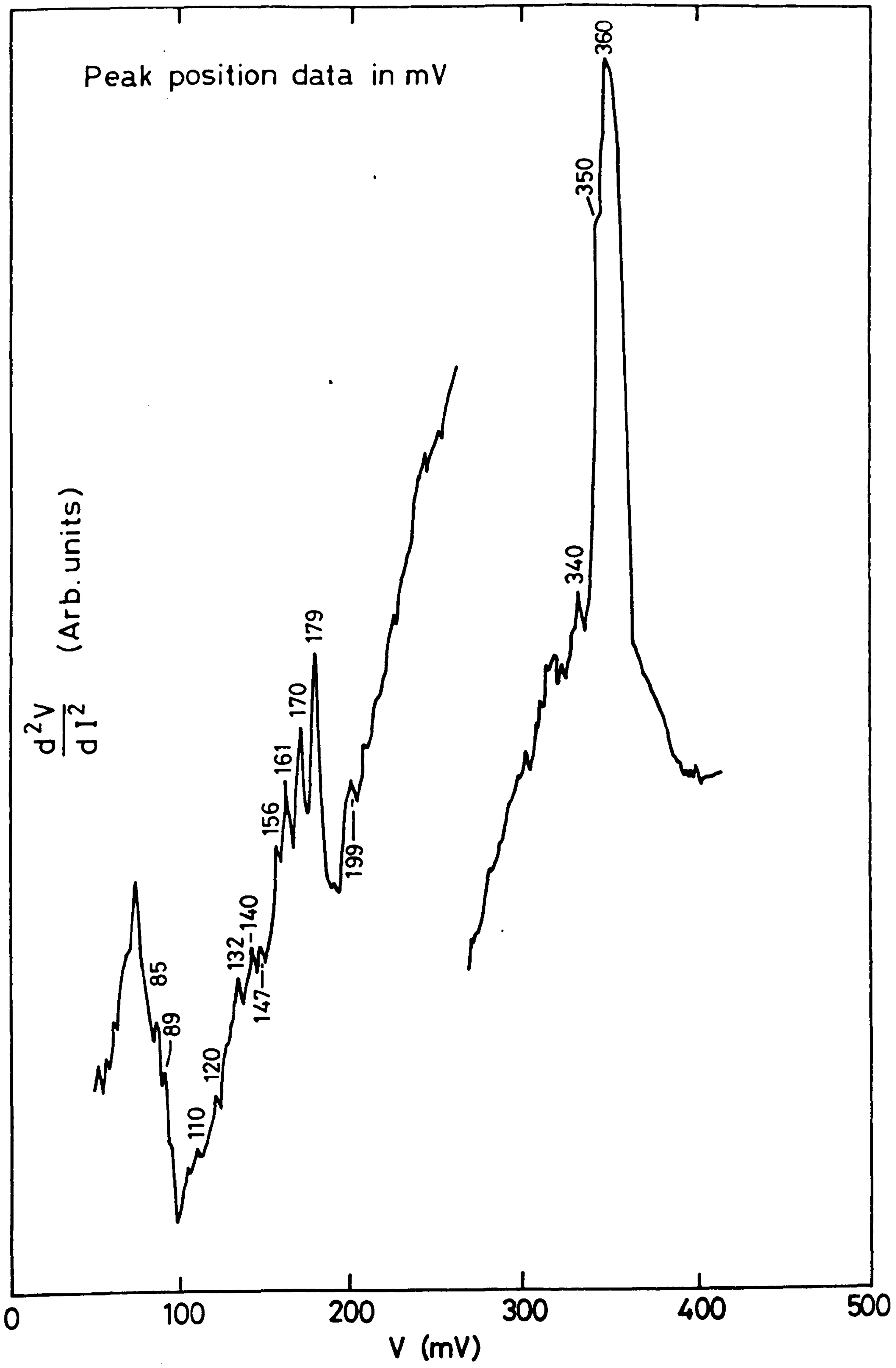

Fig 5.27: Tunnelling spectrum obtained from an Sn-BaSt$_2$-Pb device at 4.2 K using a modulation voltage of 4 mV p-p (Sn electrode negative).

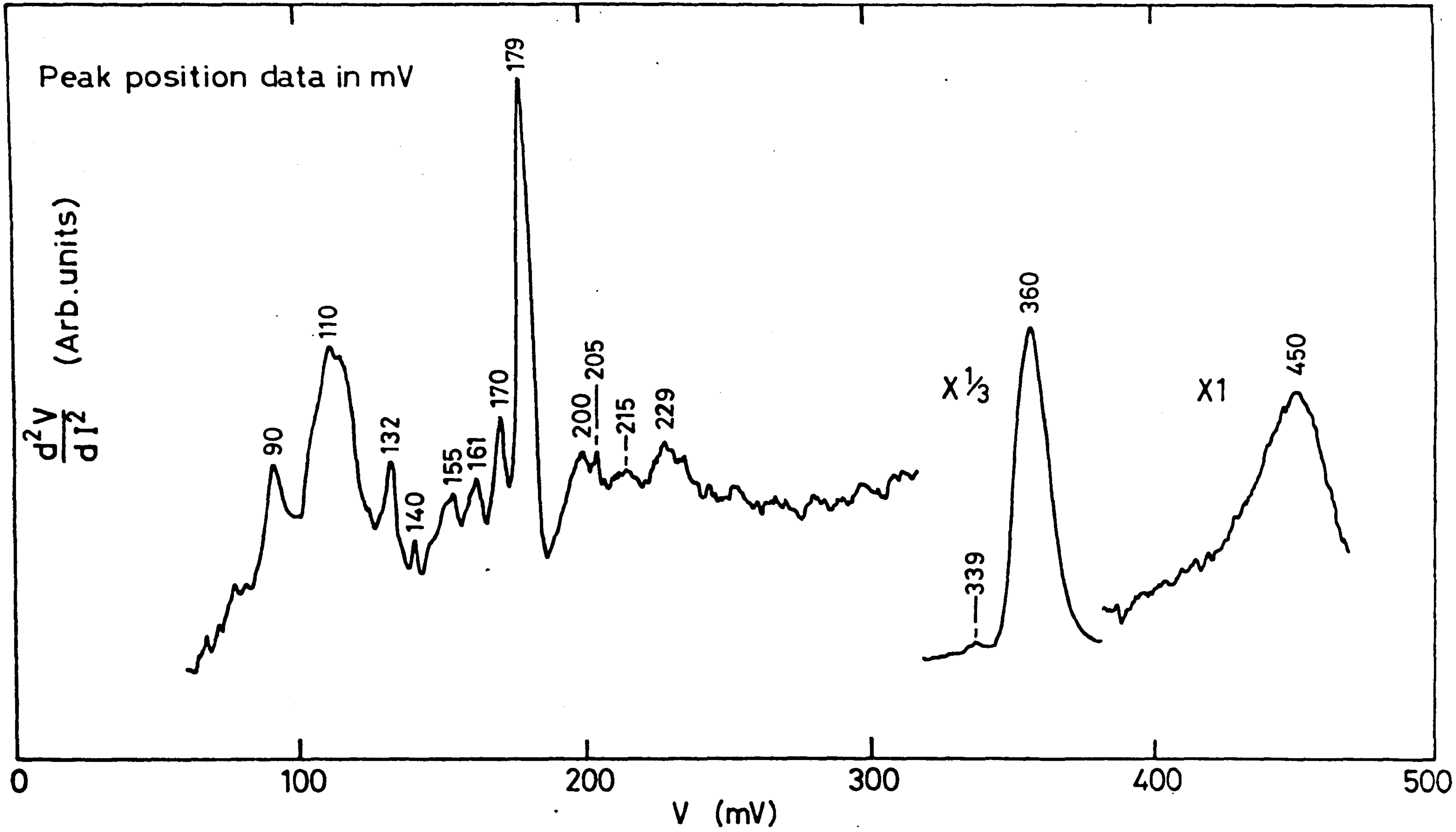

Fig 5.28: Tunnelling spectrum at 4.2 K obtained from an Al-Al_2O_3-Pb device liquid-phase doped with a 0.05 mg ml^{-1} stearic acid/Ethanol solution. The modulation voltage was 4 mV p-p and the Al electrode was biased negative.

solution was prepared by dissolving stearic acid in ethanol at a concentration of 0.05 mg ml^{-1}. The spectrum was obtained at 4.2 K with a peak-to-peak modulation voltage of 4 mV. The lead electrode was biased positive.

In Fig 5.29, infrared (IR) and Raman spectra together with another spectrum of stearic acid have been transcribed from Keil et al$^{(30)}$ for comparison with the present results.

For carboxylic acids, there are several regions of the IR spectrum from which data may be obtained for characterisation$^{(31)}$. Each will be dealt with in turn.

In the IR spectrum of saturated aliphatic acids, carbonyl group absorption takes place at 213 mV (1716 cm^{-1}). However, dissociation of the acid has a profound effect on this band which usually vanishes and is replaced by two new bands at about 200 mV (1600 cm^{-1}) and 180 mV (1440 cm^{-1}). These result from the resonance stabilised COO^- group. The two bands correspond to the antisymmetrical and symmetrical vibrations of the COO^- structure respectively. The frequencies also show minor variations depending on the nature of the metallic ion.

In the tunnelling spectra obtained from the Langmuir film junctions (Figs 5.26 and 5.27) the strong $C=O$ stretch occurring at 213 mV (1716 cm^{-1}) in the IR spectrum is not apparent. Instead, as expected in the case of dissociated fatty acids a weak broad band is noted at 199 mV ($\sim$ 1600 cm^{-1}) corresponding to the antisymmetrical stetching of the COO^- grouping. The symmetrical COO^- stretch occurs at 179 mV (1440 cm^{-1}).

Although there is no evidence of carbonyl group vibration in these particular spectra (Fig 5.26 and Fig 5.27) it has been noted in some of the other spectra obtained in the present work as a weak broad band at $\sim$ 215 mV. It is also present in the spectrum obtained from the

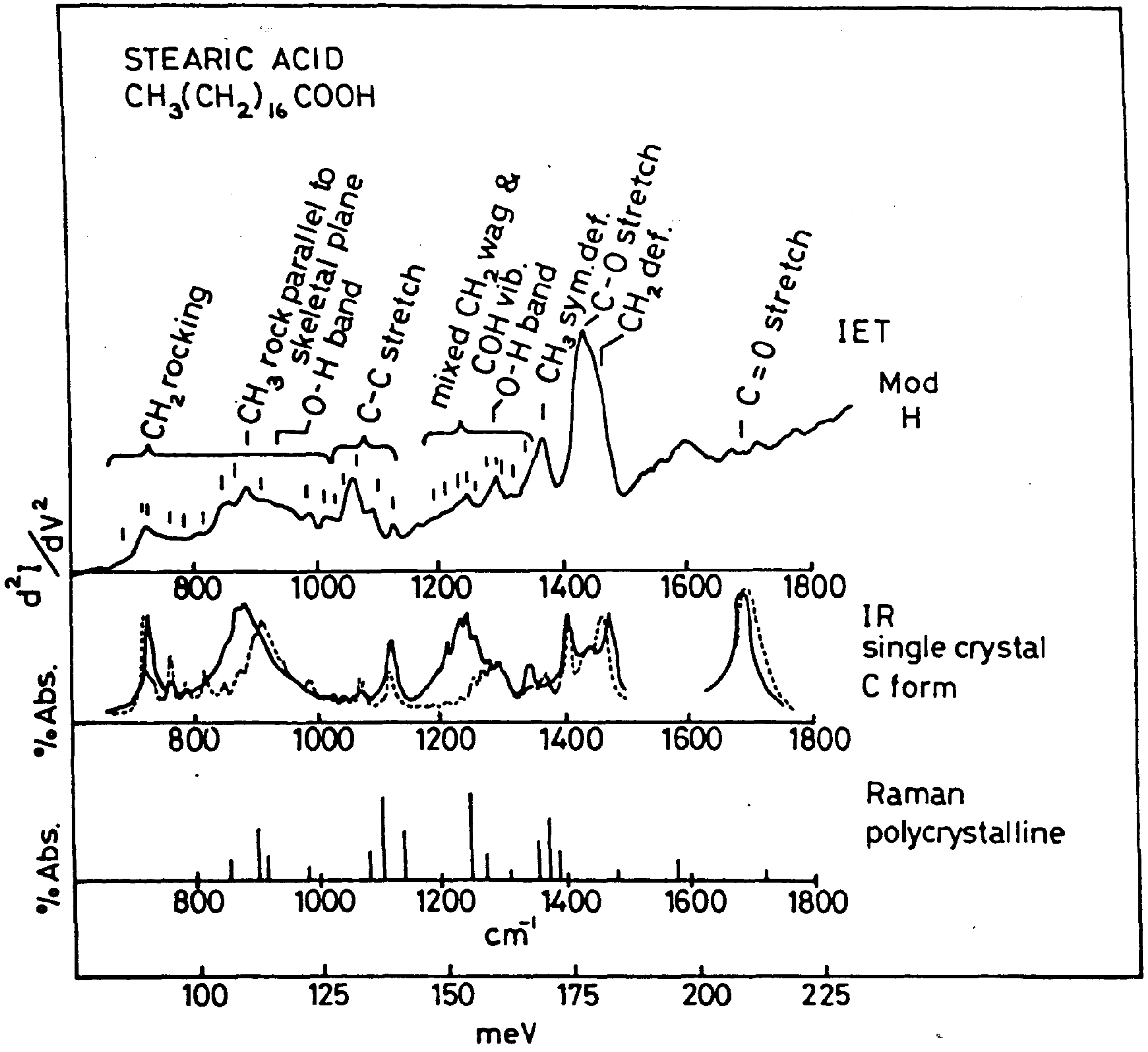

Fig 5.29: The tunnelling, single crystal infra-red and Raman spectra of stearic acid to 225 meV. The tunnelling spectrum was obtained from a liquid-phase doped $Al-Al_2O_3-Pb$ junction at 4.2 K (Data transcribed from Keil et al$^{(30)}$).

liquid-phase doped sample (Fig 5.28). Now generally, chemisorption of carboxylic acids is held to proceed via the formation of the salt of the acid with the base electrode metal(32). In the case where the adsorbate is a Langmuir film there is a further complication in that before transfer, the monolayer is already partially converted to the salt of any divalent cation in the subphase solution (see Chapter 3). Thus, the presence of a $C=O$ vibration implies that some of the carboxylic acid is most likely only physisorbed onto the substrate surface. This has considerable implications for the adherence of Langmuir films to the substrate electrode and will be investigated in more detail when the results of XPS analysis of the films fabricated in the present work are discussed (Chapter 7).

The free hydroxyl (O-H) stretch should be identifiable at about 450 mV (3600 cm^{-1}) but since the spectra were so noisy in this region and were therefore curtailed at about 420 mV it is not possible to say anything about this from Figs 5.26 and 5.27. Evidence from other tunnelling spectra reveals this as a broad peak at 450 mV. To some extent, this peak would be weakened anyway since the organic film is exposed to silica gel for about 12-15 hours and indeed the spectrum of stearic acid obtained from the liquid-phase doped junction shows a much stronger free OH stretch peak.

A broad bonded OH absorption band with many submaxima is usually noted between 312 and 345 mV(2500-3000 cm^{-1})(31) in the IR spectra of carboxylic acids. The main peak is near 375 mV with the main satellite band between 312 and 337 mV. The appearance of these bands is usually held to be strong evidence for the presence of a carboxylic acid but they are usually overlaid to some extent by the intensely strong CH absorption at 360 mV. There is evidence of this broad band due to the bonded OH stretch vibration in tunnelling spectra obtained from both the organic film and that obtained from the liquid-phase doped junction (Fig 5.28) with peaks at ∿ 340 mV. The peak at 375 mV is not discernible in any of the spectra however, perhaps because of being overlaid by the CH stretch.

A doublet is observed in the IR spectrum of stearic acid (Fig 5.29) between 156 and 160 mV (1250-1280 cm^{-1}). The higher frequency absorption is attributed to the coupled C-O and OH in-plane deformation modes. The origin of the second absorption is less certain. A coupled C-O and OH in-plane deformation often gives rise to another band between 172 and 180 mV(1375-1440 cm^{-1}) but usually found near 179 mV. Another absorption associated with a CH_2 deformation which has been modified by the adjacent CO group occurs at about 181 mV but is overlaid by the symmetrical vibration of the carboxylate ion in the case of salts of stearic acid.

All the tunnelling spectra show the effects of these vibrations and in addition the out-of-plane deformation of the hydroxyl of the carboxylic group. This occurs in the IR spectrum at about 118 mV but in the tunnelling spectra is usually shifted to about 120 mV.

Raman modes and vibrations associated with the carbon chain can also be assigned in the tunnelling spectra to the various rocking, bending and deformation modes of the CH, CH_2 and CH_3 groupings.

In Table 5.2, a comparison is made of the tunnelling spectra obtained from the organic film with that obtained from liquid-phase doped junctions and the IR and Raman spectra of stearic acid. When interpreting tunnelling spectra, it is necessary to remember however that the IR and Raman spectra are obtained at much higher temperatures, thereby allowing alterations in band positions, widths and intensities. An even more important factor is the possibility of alterations due to surface chemical effects(30).

Additional mechanisms of energy loss by tunnelling electrons have been recognised (see section 2.3). Phonons in the metal electrodes near the metal-insulator interface generally occur at low voltages (below 40 mV) and therefore are not obvious in the tunnelling spectra. However,

IR$^{(a)}$	Raman$^{(a)}$	IETS$^{(a)}$	IETS$^{(b)}$	IETS$^{(c)}$	IETS$^{(d)}$	Assignments$^{(31)}$	
90(m)		91(w)	89(m)	89(m)	90(s)		
100(w)		99(w)	98(sh)	96(sh)			CH_2 rock
	106,111,114(m)	103,112(m,d)	109(m)	110(w)	110(m)	Raman	
118(s)		121(w)	120(m)	120(m)	121(sh)	OH deformation	
	131,132(s)	131(m)	133(m)	132(m)	132(s)	Raman	C-C stretch
138(w)	139(s)	140(w)	140(m)	140(m)	140(m)		
150(w,d)		146,148(w,d)	150(w)	147(w)	147(s)		Mixed CH_2 and COH Vibration
	155,157	155	156(w)	156(m)	155(m)	Raman	
161(s)			160(s)	161(s)	161(s)	Coupled CO/OH deformation	
	168(s)	165(w)				Raman	
	171,173(s)	170(s)	170(s)	170(s)	170(s)	Raman	
		180(s)	179(s)	179(s)	179(s)	Symmetric COO^-/CH_2 deformation	
		200(m,b)	199,204(m)	199(m)	200,205(m)	Antisymmetric COO^- stretch	
213(s)					215(m,b)	C = O stretch	
	230,232,238(w)	230(m,b)			229(m,b)	Raman	
328-330 (Sh,b)	331		(340)	(340)	(339)	OH Absorbtion band	
350(sh) 360(s)	348,354(s) 356,360(m)	348(sh) 360(s)	350(sh) 360(s)	350(sh) 360(s)	360(s)	CH stretch	
		445(b)			450(b)	Free OH	

a - The data in these columns were taken directly from Ref (30) and Fig 5.29.
b - Present study (Fig 5.26) c - Present study (Fig 5.27) d - Present study (Fig 5.28)
Notations in columns 1-6 : w, weak; m, medium ;s, strong ; b,broad ; sh, shoulder; d, doublet.

TABLE 5.2: IR, Raman and tunnelling spectroscopy data (in meV) for stearic acid.

a very pronounced structure due to the molecular or lattice vibrations of the oxide is obvious from about 50-100 mV in Figs 5.26 and 5.27, and from 50-125 mV in Fig 5.28 and 5.29.

The most striking aspect of the tunnelling spectra obtained from the organic films is that they have a background which rises very steeply compared with the tunnelling spectra obtained by doping with conventional means. It has been found that with the Langmuir film junctions, the spectra obtained have either very steep backgrounds or no structure at all. The former always correspond to those junctions with resistivities close to the upper limit of resistance discussed earlier (see section 5.1) whereas the latter invariably resulted from junctions near the lower limit. The most successful junctions were those of intermediate resistance (100 - 500 Ω).

A second point to note in evaluating the significance of these tunnelling spectra is that despite the good correlation between repeat runs on the same sample and on different samples, it is true to say that it is more difficult to obtain inelastic tunnelling spectra from Langmuir films than from junctions doped by conventional means. These attempts were hampered by problems with the background and more particularly there was a high incidence of transient-like peaks in the Langmuir film tunnelling spectra , which were always reproducible on the same sample. Skarlatos et al(33) have found capacitance peaks associated with similar peaks and have attributed them to traps in the insulating layer at energies smaller than those previously reported(34). It may appear that as pointed out by Gundlach and Kadlec(10) for aluminium-based junctions, impurities picked up from the subphase or the atmosphere are present in the tin oxide. However, this is unlikely as an explanation, since the I-V characteristics of the tin-based junctions (unlike their aluminium counterparts) are still linear at about 300 mV bias. Moreover, the good correlation between the Raman, IR and tunnelling spectra together with the fact that junctions fabricated using tin oxide only show very low resistances (< 1 Ω) and break down at V $\lesssim$ 20 mV lead to the contention that truly inelastic tunnelling through the organic film is being observed here. If this were to be the case then it must mean that a significant proportion of the charge transfer across the Langmuir film must be attributed to electron tunnelling.

5.10 INTERNAL VOLTAGE AND AGEING EFFECTS

Considerable difficulties were encountered in the early stages of the work with sporadic internal voltage effects where some asymmetrical M-LF-M structures appeared to behave as batteries. The more important observations can be summarised thus :-

(1) Internal voltage effects were only found to occur in asymmetrical junctions and even with these the effects were highly irreproducible.

(2) At room temperature, it was typical to measure a voltage $V_o \sim 0.2$-0.4 V with a voltmeter connected across the junction.

(3) The internal voltage was found to be strongly time-dependent, often changing polarity with time.

(4) Although V_o was drastically reduced at liquid helium temperatures, it was still noticeable with a magnitude of the order of a few mV.

(5) On prolonged pumping in the experimental chamber of Fig 4.1, V_o was found to decrease to a very low value and sometimes to even change polarity.

(6) A similar effect to (5) was noted when a device was left with a 50 Ω termination connected across its terminals for about 2 hours.

(7) The effect was found to be negligible in asymmetrical junctions which were exposed to silica gel over long periods (> 12 hours) in an evacuated dessicator.

Internal voltages have been reported for single layer Langmuir films and multilayers by various authors(13,35-38). Leger et al(13) have measured ∿ 200 mV across their films and showed that the internal resistance of these 'batteries' varied as exp (E_o/kT) where E_o is an activation energy of 0.36 eV. Furthermore, at liquid helium temperatures the internal voltage was reduced to zero. The effect was discussed in terms of the difference in oxidation between the two metal electrodes (even when they were both aluminium) and of the movement of charged ions across the insulator in order to reach equilibrium.

Srivastava and co-workers(35-36) have studied the effect in more detail. They report that the internal voltage decreases linearly with the number N of monolayers, with higher voltages being obtained for molecularly unsymmetrical films (odd N) than for symmetrical layers. The voltage due to the unsymmetrical films were interpreted in terms of the net polarisation due to the molecules, and values of dipole moment were calculated on this basis. The voltage with unsymmetrical electrodes was discussed in terms of the work function difference between the electrodes. However, this interpretation (which regards the internal voltage as a direct result of the work function difference) has been criticised by Roberts et al(39) as unsatisfactory since it does not take into account the second unsymmetrical junction which must be present in the complete circuit.

From the observations of the present work it is probably reasonable to ascribe internal voltage effects to ionic diffusion occurring under the influence of the internal field due to the asymmetric electrode structure. It would appear that the effect is related to the presence of moisture in the device since in those devices where effort had been made for its removal, internal voltage effects were considerably reduced. Thus, the M-LF-M structure acts as an electrolytic cell with the voltage simply being the result of ionic movement due to differences in the electrode potentials of the two metal electrodes. The strong time dependence of the internal voltage is thus the result of the drying out of the device.

This explanation is not entirely satisfactory in that it was found that occasionally devices prepared under ostensibly similar conditions differed considerably with regard to the presence of internal voltage effects. It is probably reasonable therefore to assume that although these effects are probably related to the obvious differences in electrode materials and the presence of water they are also probably very sensitive to small variations in the ionic content and possibly in the in-plane compactness of the films, arising for instance from differences in deposition conditions (see Chapter 3). In the present work, it was found that if sufficient time (∿ 12-15 h) was allowed for the removal of water molecules once Langmuir film deposition had taken place and prior to counter-electrode deposition, the incidence of these effects was considerably reduced and sensible measurements of device properties could then be undertaken. This was therefore adopted as a standard step in the device fabrication procedure (section 4.2).

Another effect which may be related to the presence of water molecules in the organic films is shown in Fig 5.30. These are current-voltage characteristics recorded for a single layer Al-$BaSt_2$-Al sample at room temperature after various periods of storage under different conditions. It is apparent that there is a substantial decrease in the current with time, especially when the device is stored in room air. The current-voltage characteristic appears to become less time-dependent when the junction is stored under vacuum. Similar ageing effects (over more extended time periods) have been reported by Pollack and Morris(22) in aluminium oxide films where they were attributed to long-term ionic re-arrangement in the oxide. It is possible that this is an explanation of the present results, although the fact that the decrease in current with time is sensitive to

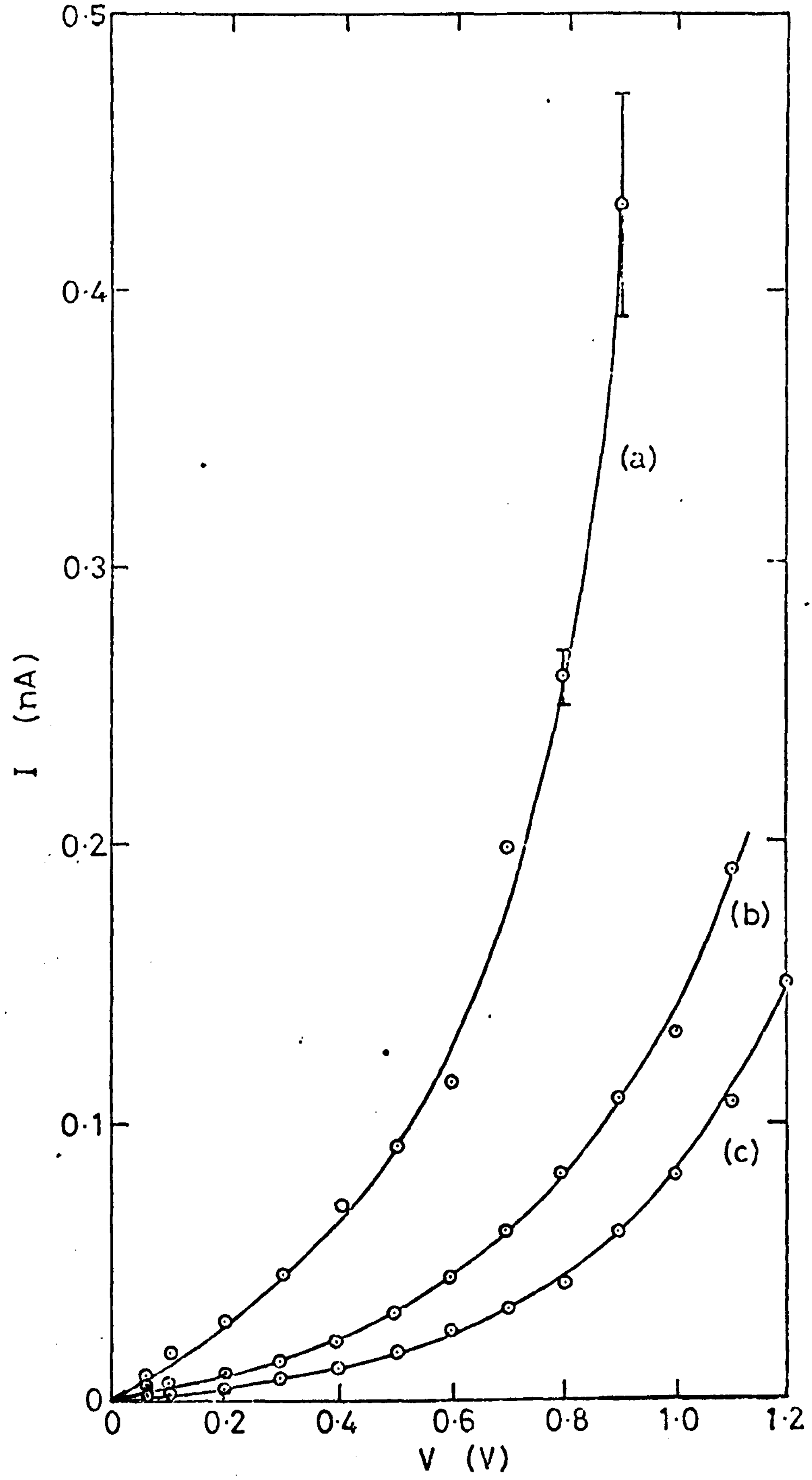

Fig 5.30: Current-voltage characteristics for a single layer Al-BaSt$_2$-Al device at room temperature (a) initially (b) after 18.5 hrs in room air and (c) after a further 60 hrs in low vacuum ($\sim 10^{-2}$ Torr).

the ambient suggests also the diffusion out of water molecules as a possible explanation.

For these reasons, it was usual to make all measurements either in vacuum or in an otherwise inert atmosphere. Under these conditions it was found that device properties were to all intents stable with respect to time over the several days needed to make the measurements.

5.11 THE ELECTRON TRANSPORT MODEL

It has been shown that the observed current-voltage relationship is correctly described by equation (2.47) or equations (2.36) and (2.37) which constitute the same variation. Furthermore, the temperature dependence of the current at a fixed applied voltage has been demonstrated to be of the form given by equation (2.53) consistent with a charge transfer mechanism involving direct electron tunnelling between the electrodes. A major difficulty in the interpretation of results is the extent of the role that needs to be ascribed to the inevitable oxide film(s) present in the completed M-LF-M structure. This has meant that although the observed functional form of the current-voltage and current-temperature dependence is correctly described by these equations, at best it is possible to obtain only qualitative agreement with the tunnelling model.

One complication that arises because of the uncertainty involved in assessing the true role of the oxide layer is that the superconducting electrode test[(27)] can no longer be held to substantiate unequivocally an electron tunnelling mechanism for charge transfer through the organic film itself. It has been shown that it is possible to obtain current-voltage characteristics at low biases and temperatures which are consistent with an explanation based on superconductive tunnelling through the oxide and then conduction through defects in the Langmuir film.

Although these observations do not prove conclusively that electron tunnelling is indeed the predominant conduction mechanism in single layer Langmuir films, more importantly, neither do any of them offer evidence for an alternative mechanism.

The most important evidence which establishes beyond doubt that the main conduction process which occurs in single layer films is truly electron tunnelling is the observation of inelastic tunnelling signals related to the interaction of tunnelling electrons with the organic film over a considerable energy range (40 - 500 meV). The significant point about these experiments is that only a small fraction of tunnelling electrons ($\sim$ 1%) lose energy to molecular oscillators in the Langmuir film. Thus, the observation of this small number of relatively rare inelastic tunnelling events constitutes unequivocal evidence for tunnelling through the film over an extensive voltage range.

Thus, conduction in single layer Langmuir film MIM devices occurs by direct electron tunnelling between the metal electrodes. There are several observations which support this contention :-

(1) An electron tunnelling model predicts the observed current dependence on voltage.

(2) It predicts the observed current dependence on temperature.

(3) A peak is observed in the $d(\ell n\ J)/dV$ versus V plot at $V = \phi$ as predicted by a tunnelling model.

(4) A markedly non-linear low bias current-voltage characteristic is observed when one of the electrodes is allowed to go superconducting.

(5) Structure is observed in the d^2V/dI^2 versus V plot which is consistent with the vibronic excitation of the molecules of the film by tunnelling electrons, and which corresponds well with the infra-red and Raman spectra of a bulk sample of the dissociated film material.

CHAPTER 6

CONDUCTION IN MULTILAYER FILMS

There have been a number of studies on the nature of the high field conduction process in Langmuir film multilayers(1-6) where N, the number of layers is in the range ∿ 3-9. Most of these workers have attributed the conduction process to either a Schottky mechanism or in some cases and for the thicker films to bulk-limited processes via the Poole-Frenkel or Poole effects. The essential physics of these processes has been discussed already in Chapter 2. This chapter describes the results obtained during the course of the present work from experiments aimed at elucidating the electron transport mechanism in these films, in particular through consideration of the temperature dependence of the current-voltage characteristic.

6.1 THE CURRENT-VOLTAGE DEPENDENCE

Current-voltage characteristics for a three and five layer Sn-$BaSt_2$-Pb device at room temperature are shown in Fig 6.1. They were obtained using the d.c. measurements apparatus and the evacuated (10^{-6} Torr) experimental chamber described in Chapter 4.

At low voltages $V \lesssim 0.2$ V, the characteristics are linear. As the applied voltage increases however, the current rises very rapidly with voltage until device breakdown occurs at $V \simeq 1.8 - 2.2$ V. The voltage required for significant departure from linearity increases slightly with increasing multilayer thickness as expected(2), but in general was significantly less than the values typically observed for inorganic insulating films such as Al_2O_3(7) of comparable thickness. As is apparent from Fig 6.1, for applied voltages $V \gtrsim 0.3V$ the characteristics display a clear asymmetry when the polarity of the applied field is reversed.

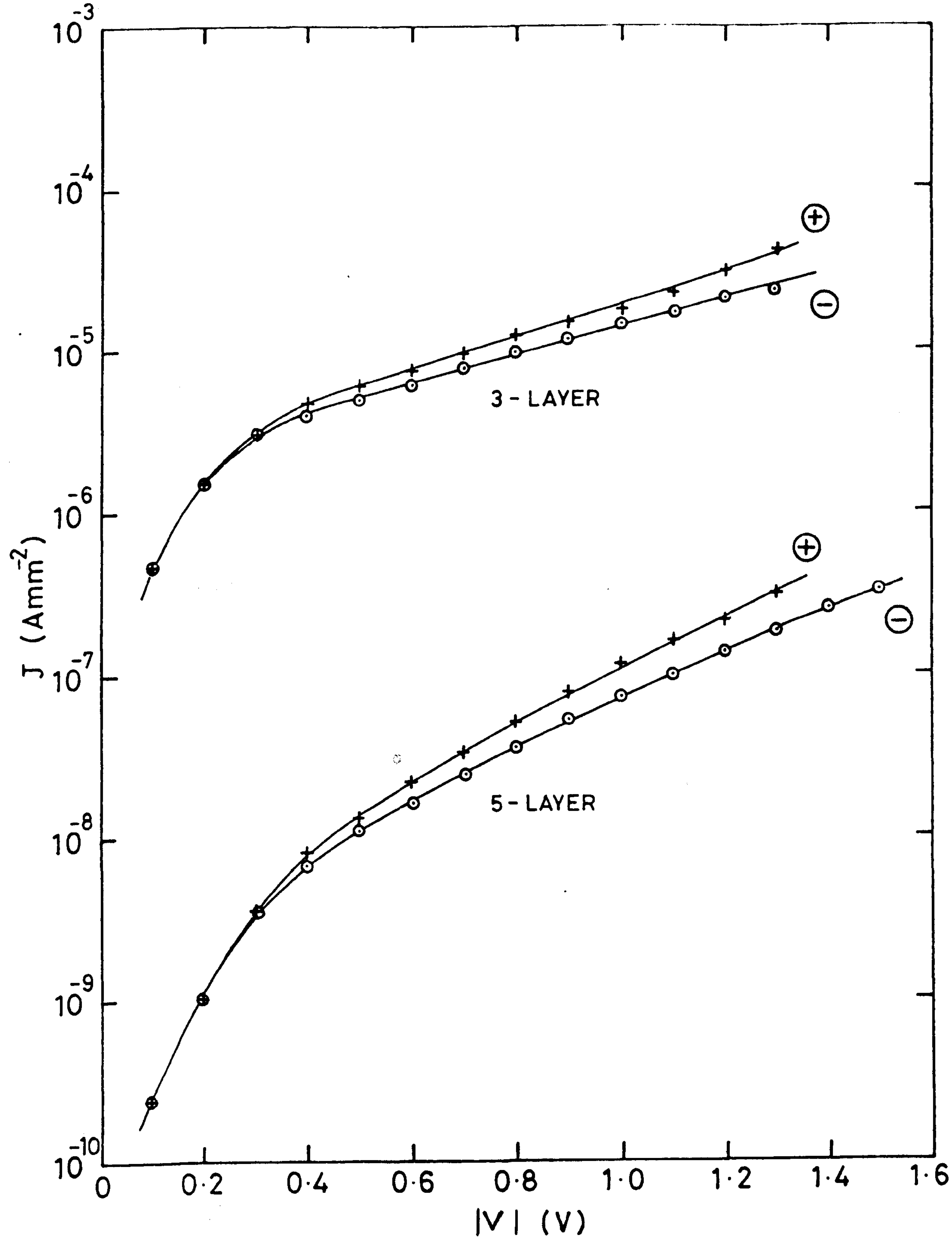

Fig 6.1: Current-voltage characteristics for a three and five layer $Sn-BaSt_2-Pb$ device at room temperature. The polarity of the Sn electrode is indicated.

Resistances calculated from the low voltage ($V \simeq 0.1$ V) linear region of the characteristics yielded a value of $\sim 1\ \mathrm{M}\Omega \pm 20\%$ for the three layer films and $\sim 1\ \mathrm{G}\Omega \pm 20\%$ for the five layer films for a mean device area of $0.25\ \mathrm{mm}^2$. Now, the current-voltage relationship for Schottky emission is given by equation (2.72) as

$$J = A_o T^2 \exp\left(\frac{-\phi_o}{kT}\right) \exp\left(\frac{\beta_s \mathcal{E}^{\frac{1}{2}}}{kT}\right)$$

where $A_o = 4\pi mek^2/h^3$ and ϕ_o are constants for a given system. This expression neglects the effects of any electron reflection at the barrier. Equation (2.72) can be written in the form

$$J = J_o \exp(\alpha V^{\frac{1}{2}}) \tag{6.1}$$

where $J_o = A_o T^2 \exp\left(-\frac{\phi_o}{kT}\right)$

and $\alpha = \beta_s/kT\, s^{\frac{1}{2}}$ (6.2)

From (6.1) it is apparent that a plot of ln J against $V^{\frac{1}{2}}$ should yield a straight line from whose slope a value for α may be computed. Two typical examples of such plots are shown in Figs 6.2 and 6.3 for a three-layer and five-layer Sn-BaSt$_2$-Pb device respectively. The straight line relationship obtained is strongly suggestive of Schottky emission over the Sn-BaSt$_2$ interface, however it cannot be taken as conclusive evidence. This is because an identical functional dependence of the current on the applied voltage is also given by equation (2.78)

$$J = A(T) \exp\left(\frac{\beta_{PF} \mathcal{E}^{\frac{1}{2}}}{kT}\right)$$

for the Poole-Frenkel mechanism of charge transfer. As discussed in Chapter 2, in the basic situation the two mechanisms will vary by a factor

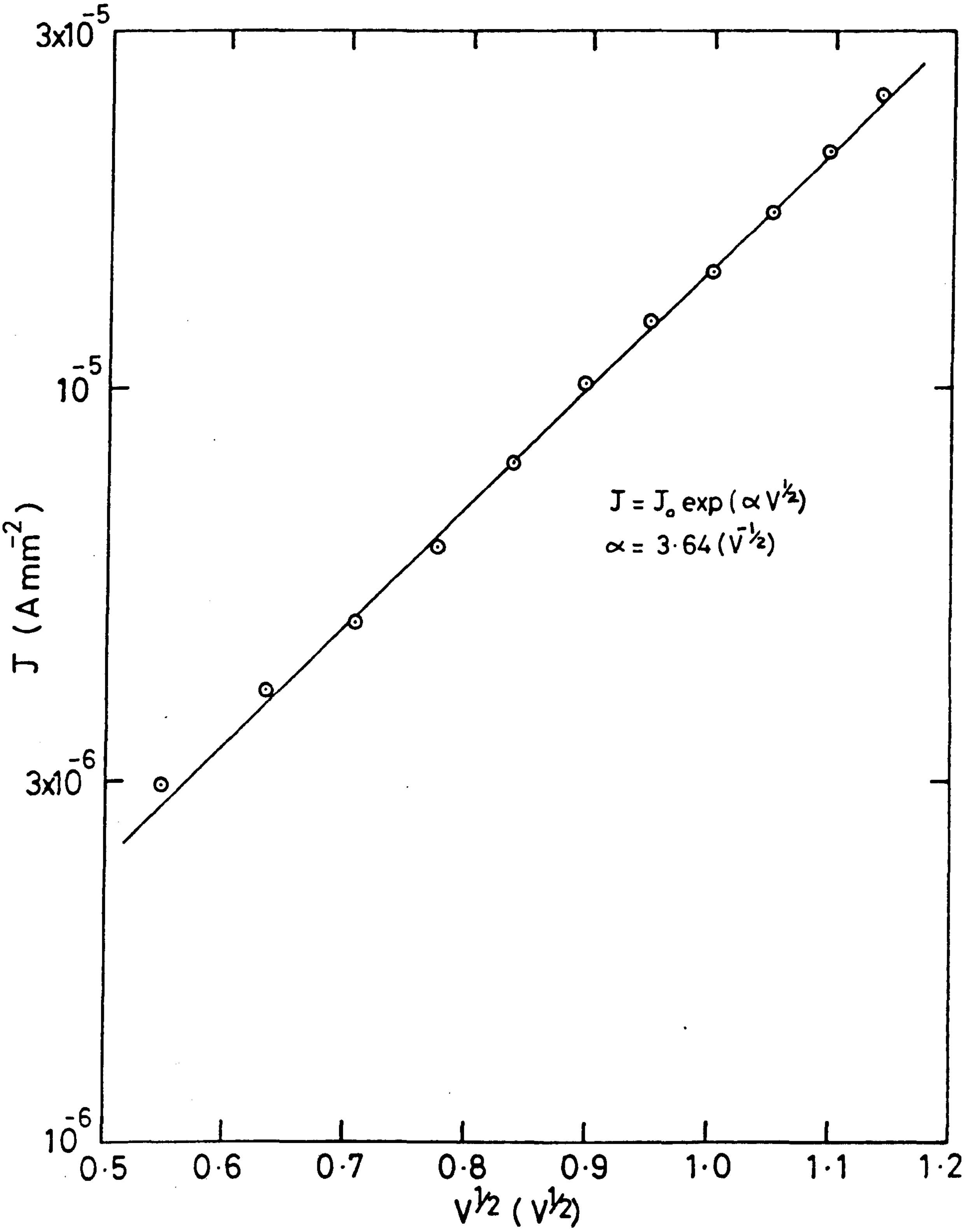

Fig 6.2: ln J versus $V^{\frac{1}{2}}$ plot for an Sn-3 x $BaSt_2$-Pb device at room temperature (Sn negative).

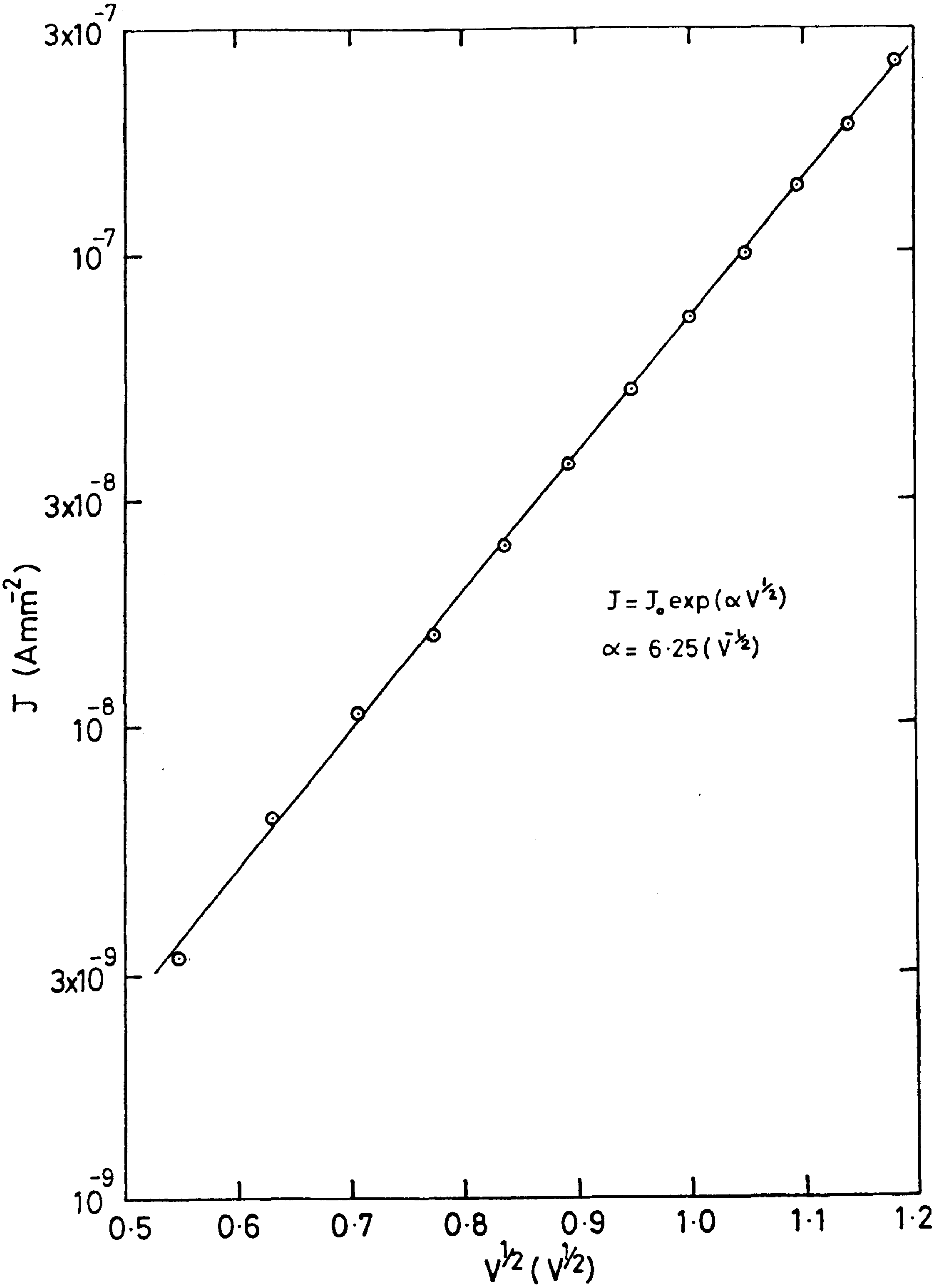

Fig 6.3: ln J versus $V^{\frac{1}{2}}$ plot for an Sn-5 x $BaSt_2$-Pb device at room temperature (Sn negative).

of two in the value of α and can thus be distinguished. The values calculated from the slopes of the ln J against $V^{\frac{1}{2}}$ plots are tabulated, together with calculated values of α for the two mechanisms, in Table 6.1.

TABLE 6.1 Values of $\alpha/V^{-\frac{1}{2}}$ from the equation $J = J_o \exp(\alpha V^{\frac{1}{2}})$

Base electrode (biased negative)	Langmuir film thickness/nm	$\alpha_{exp}/V^{-\frac{1}{2}}$	$\alpha_{calc}/V^{-\frac{1}{2}}$	
			Schottky	Poole-Frenkel
$Sn(SnO_x)$	7.5	3.64	10.50	21.00
$Sn(SnO_x)$	12.5	6.25	8.14	16.27

α_{calc} has been obtained assuming $\varepsilon_r = 2.6^{(8)}$.

It will be noted that neither Schottky emission nor the Poole-Frenkel effect fits the experimental data. However, the Schottky values are in much closer agreement and thus the electron transport mechanism is tentatively attributed to this effect. There is still another discrepancy between Schottky theory and experiment in that the value of α increases with increasing film thickness whereas the theory predicts the opposite relationship. In addition, as discussed in Chapter 2, in the case where the donor centres lie beneath the Fermi level, it is possible to have a virtually identical relationship for both Schottky emission and the Poole-Frenkel effect and thus the two mechanisms cannot be distinguished on the basis of a consideration of the value for α. One method that will separate the two mechanisms is to use the temperature dependence, as a plot of $\log(J/T^2)$ against $(1/T)$ will yield a straight line only for the Schottky process. These results are presented in the next section.

6.2 THE TEMPERATURE DEPENDENCE OF THE CURRENT

The temperature dependence of the current at fixed voltage was investigated for both three and five layer films of barium stearate. For these experiments, devices of the type Sn-$BaSt_2$-Pb were fabricated, located in the cryostat and the variation of the current with temperature measured in the range 80-300 K and at various fixed voltages.

Typical results for an Sn-3 x $BaSt_2$-Pb device at fixed voltages V = 1.0 V and V = 0.5 V are shown in Fig 6.4 and for an Sn-5 x $BaSt_2$-Pb device at V = 1.0 V in Fig 6.5. It is apparent that there is an almost exponential decrease in current between 300 K and ∿ 210 K for both multilayer devices and furthermore the current dependence on temperature is much weaker for $T \lesssim 210$ K. This suggests that a tunnelling mechanism of conduction at low temperatures probably gives predominance to a Schottky process at higher temperatures. Since the slopes at higher temperatures are the same in all cases, this is indicative that the barrier height ϕ_o is also comparable for both three and five layer devices. At lower temperatures, however, the slopes differ due to the different relative contribution of tunnelling and Schottky currents through the two multilayer structures.

The behaviour of the three layer device can be analysed in more detail by subtracting the temperature-independent current (I') from the total current (I) to obtain the Schottky contribution to the current. The temperature dependence of this current for a given voltage should yield a straight line when plotted as $\log (I-I')/T^2$ against the reciprocal temperature (1/T). Such a plot is shown in Fig 6.6. Now equation (2.72), which gives the current-voltage-temperature dependence for Schottky emission, can be written as

$$\ln\left(\frac{J}{T^2}\right) = \ln A_o + \left\{ \frac{\beta_s V^{\frac{1}{2}}}{k\, s^{\frac{1}{2}}} - \frac{\phi_o}{k} \right\} \frac{1}{T} \qquad (6.3)$$

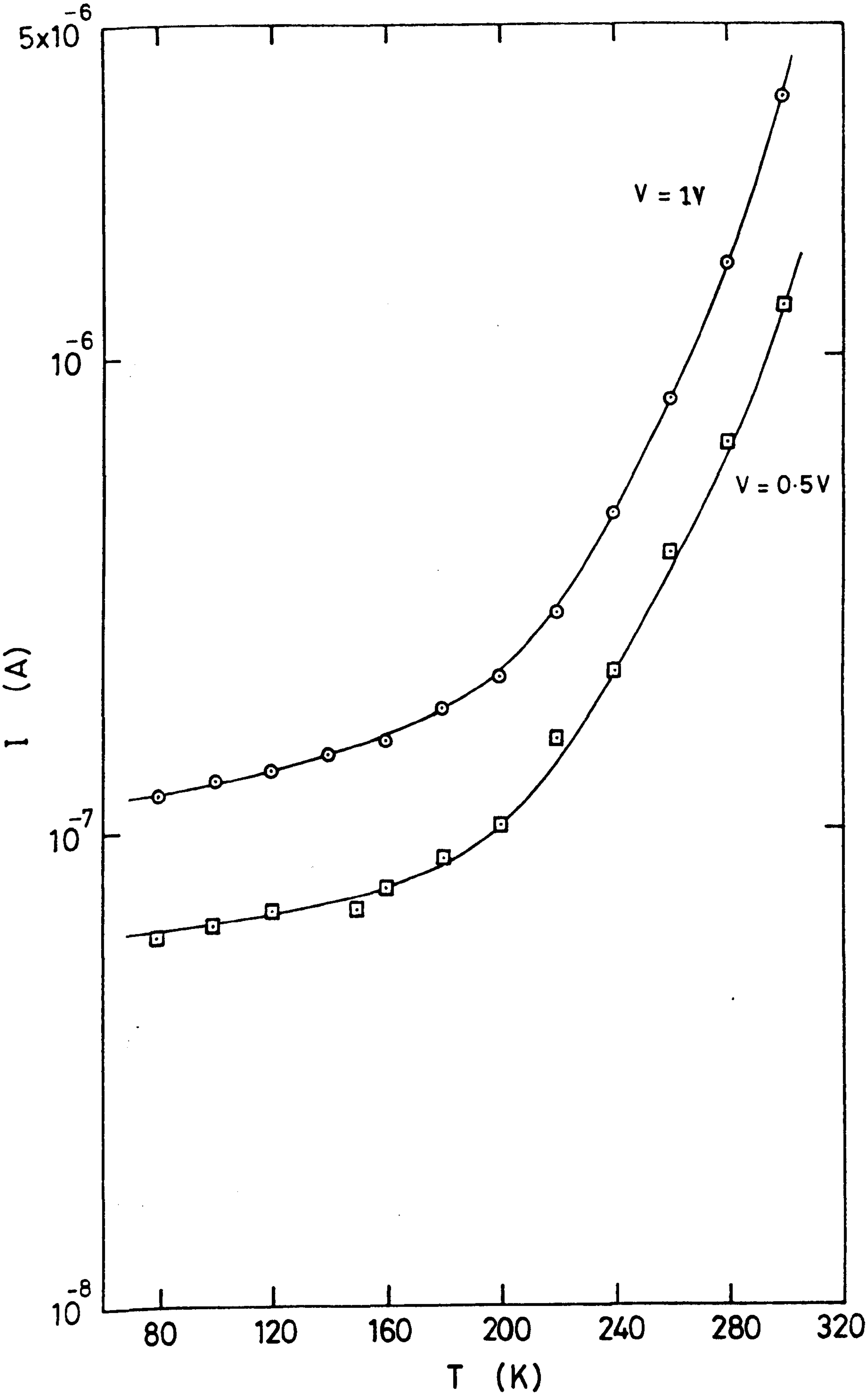

Fig 6.4: Temperature variation of the current through an Sn-3 x $BaSt_2$-Pb device at two fixed voltages (Sn negative).

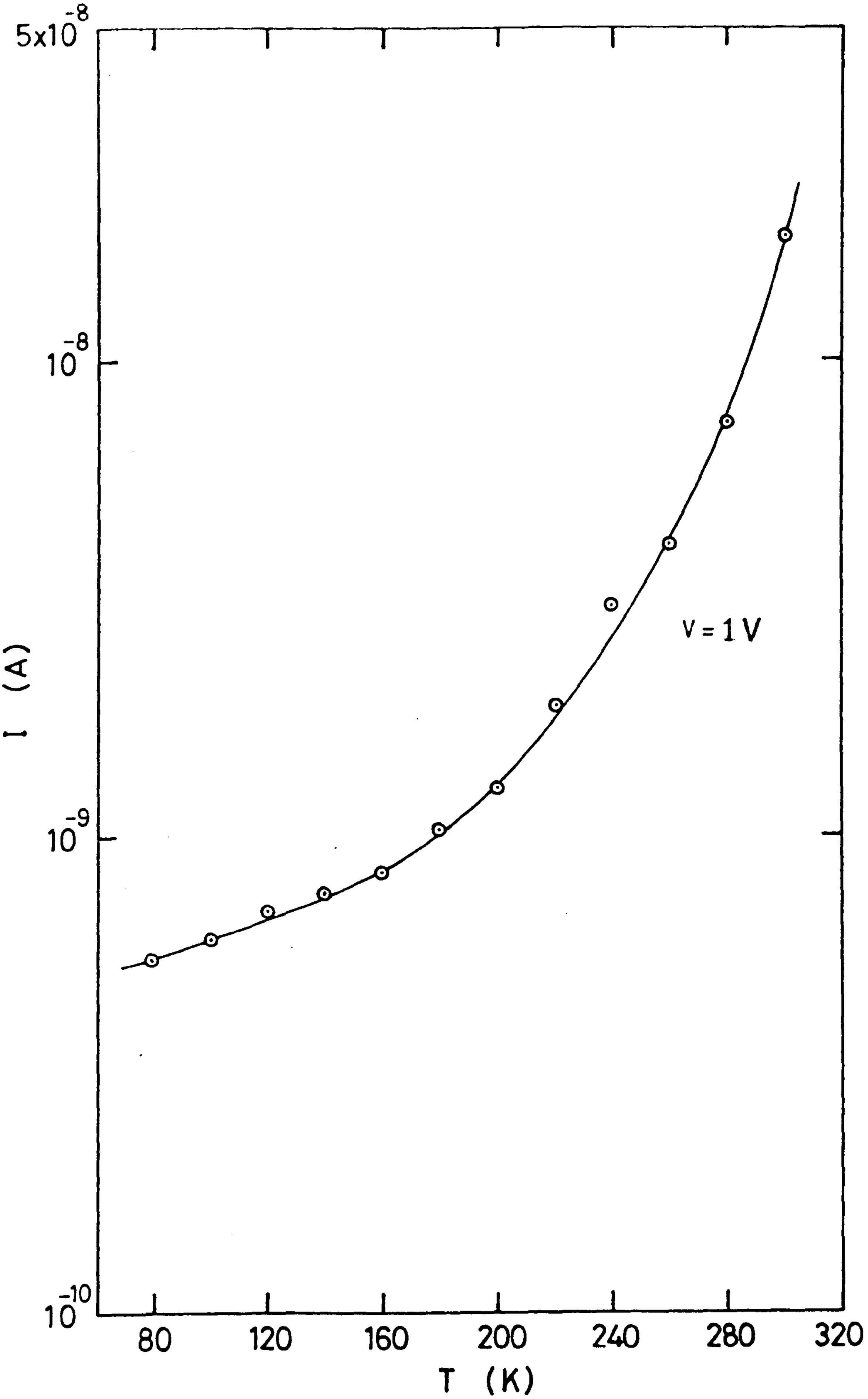

Fig 6.5: Temperature variation of the current through an Sn- 5 x BaSt$_2$-Pb device at a fixed voltage (Sn negative).

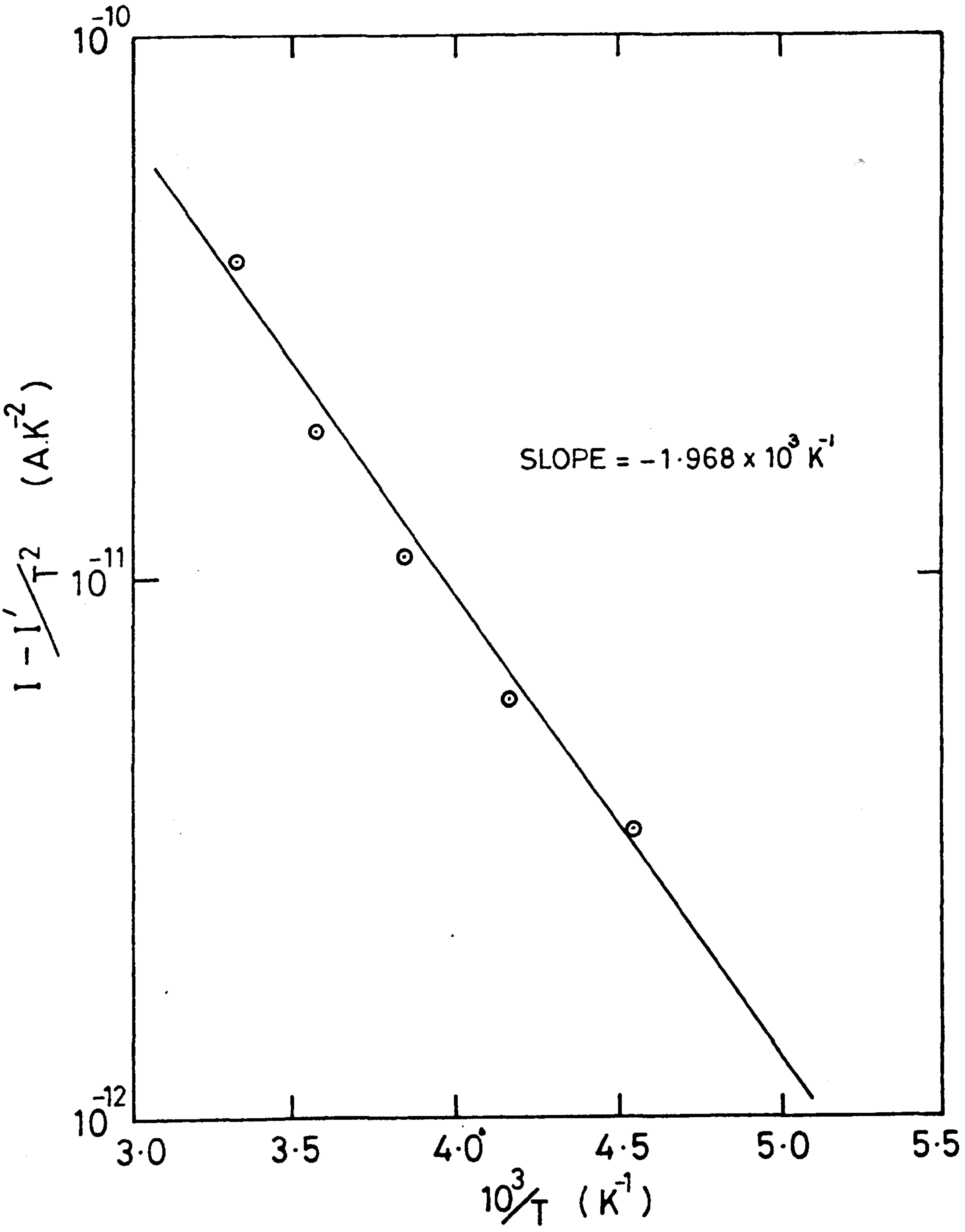

Fig 6.6: ln $(I-I')/T^2$ versus 1/T plot for an Sn-3 x $BaSt_2$-Pb device at V = 1.0V (Sn negative).

Thus, the slope (m) of the line in Fig 6.6 is given by

$$m = \frac{\phi_o}{k} - \frac{\beta_s V^{\frac{1}{2}}}{ks^{\frac{1}{2}}} \tag{6.4}$$

Multiplying throughout by k and re-arranging yields

$$\phi_o = km + \frac{\beta_s V^{\frac{1}{2}}}{s^{\frac{1}{2}}} \tag{6.5}$$

If a value of $m = 1.968 \times 10^3 \ K^{-1}$ is substituted into equation (6.5) and $V = 1.0$ V, $s = 7.5$ nm (the thickness of a 3-layer $BaSt_2$ film), and $\varepsilon_r = 2.6$ is used, a value for the zero-voltage, effective Sn-$BaSt_2$ interfacial barrier height of

$$\phi_o = 0.44 \text{ eV}$$

is obtained. It is assumed in this analysis that conduction is dominated by tunnelling at low temperatures (even though the current can still be described by a linear $\ell n \ I - V^{\frac{1}{2}}$ relationship) and by Schottky emission over the insulating barrier of height ϕ_o presented by the Langmuir film at high temperatures. The influence of the oxide film has been neglected since the value of ϕ_o calculated from the slope of the curve in Fig 6.6 depends only weakly on the thickness of the insulating film. In fact, an error of 100% in the thickness s results in an error in ϕ_o of only ∿8%(7).

6.3 ELECTRON TRANSPORT IN MULTILAYER LANGMUIR FILMS

It has been shown that the voltage and temperature dependence of the current satisfies the Schottky emission mechanism for both three and five layer Sn-$BaSt_2$-Pb devices for applied voltages $V > 0.2$ V and temperatures $T \gtrsim 210$ K. Below this temperature, and especially for the three layer devices, the current is only weakly dependent on the temperature and is probably due to electron tunnelling even though the current-voltage relationship is still described by $\ell n\ J \propto V^{\frac{1}{2}}$ to within the limits of experimental error.

From a Schottky plot of log $(I-I')/T^2$ against $1/T$, the zero-voltage Sn-BaSt$_2$ interfacial barrier height is determined as $\phi_o = 0.44$ eV. Although this is comparable to the value of ϕ obtained from the temperature dependence of tunnel currents in single layer Sn-BaSt$_2$-Pb devices (see Chapter 5) it is too low to be interpreted as simply the difference between the work function of tin and the electron affinity of barium stearate. However, similarly low values of ϕ_o ($\simeq$ 0.2-0.5 eV) have been reported previously for the Sn-stearate$^{(1-2)}$ and Al-stearate$^{(4)}$ interfaces. An apparently anomalously low value of ϕ_o has also been observed by Pollack$^{(7)}$ for the Al-Al$_2$O$_3$ interface where it is attributed to the establishment of a positive ionic space charge which under the influence of the applied field drifts towards the cathode. This positive space charge increases the effective field at the cathode, resulting in a decreased effective barrier height. It is suggested that the space charge may originate from a migration of either Al ions to vacant nearby interstices in the Al$_2$O$_3$ lattice or ionised negative ion vacancies. There is some evidence for ion migration in M-LF-M devices ; for instance, the transient currents that are found to occur on application of a voltage (see Chapter 4) and internal voltage effects can be understood on the basis of the movement of ions. Further evidence for positive ion incorporation in Langmuir film structures has been presented by Handy and Scala$^{(2)}$, based on observations made during the film transfer process and on the basis of autoradiograph studies of stearate films deposited on various metal substrates. Although most of this evidence is largely circumstantial it does offer a plausible explanation by invoking a similar model to that advanced by Pollack$^{(7)}$, for the low barrier heights found in the present study and by other workers for the Sn-stearate and Al-stearate interfaces.

It is apparent from the current-voltage characteristics that the magnitude of the current is dependent on the polarity of the applied voltage (Fig 6.1). This is again indicative of an electrode-limited conduction process (Schottky emission) rather than a bulk phenomena such as the Poole-Frenkel effect. However, the agreement in this regard between experiment and Schottky theory is at best only qualitative, since from equation (2.72) it is clear that the current depends exponentially on the barrier height, whereas the observed differences in the magnitudes of the currents with opposite polarities are not large enough to be due to electrode effects on this basis. However, in the light of the temperature dependence of the current, it is probably reasonable to conclude that conduction in multilayer Langmuir films of intermediate thickness (∿ 3-7 layers) occurs by Schottky emission over the metal-Langmuir film interfacial barrier. The temperature and voltage dependence of the current is at least in qualitative agreement with theory and yields a value for the effective metal-insulator barrier height ϕ_o of ∿ 0.44 eV. This low value for ϕ_o may be the result of a positive space-charge layer in the oxide adjacent to the negatively biased electrode which arises from the migration of metal ions on application of a voltage.

CHAPTER 7

STRUCTURAL CHARACTERISATION

Monolayer assemblies of organic molecules (Langmuir films) offer the possibility of obtaining uniform, structurally orientated layers whose thickness is accurately known and controllable. The technique however requires meticulous care and attention to detail. Consequently, it will have become clear that a substantial part of the present work involved the investigation and development of methods for the fabrication of high quality, defect-free films. This has been described in a previous chapter. This chapter is primarily concerned with the results of subsequent structural characterisation studies using two techniques ; X-ray photoelectron spectroscopy (XPS) and Auger electron spectroscopy (AES). These studies were prompted by the desirability of confirming the predicted structure of these films and where possible, correlating this with the results of investigations of electron transport phenomena. In addition, it was hoped that the use of these techniques would provide an improved understanding of the mechanism of adhesion of the Langmuir film to the metal substrate as this obviously has important consequences for the results of the electrical studies. Such experiments would also provide estimates of the electron inelastic mean free path length (IMFP) in the organic films and thus permit verification of the energy dependence of the IMFP found by workers(1) using other organic materials.

The chapter begins by briefly considering the basic principles utilised in XPS and AES before describing details of the instrumentation involved in these methods of surface analysis. The remainder of the chapter is taken up with some of the results obtained from the application of these techniques to the Langmuir films fabricated in the present work.

7.1 X-RAY PHOTOELECTRON AND AUGER ELECTRON SPECTROSCOPY: BASIC PRINCIPLES

Most surface analytical techniques involve the perturbation of the sample using either photons, electrons or ions and characterisation of the resultant emission.

In Auger electron spectroscopy the disturbance is produced by bombarding the specimen surface with low energy electrons (1-10 keV). Some of the atoms within the sample are ionised and electron re-arrangement can take place within the atom as a result. Thus, if for example, an electron from the K energy level is ejected (Fig 7.1), an electron from the L_2 level may take its place, releasing an amount of energy $E_K - E_{L_2}$. This energy may now be transferred to another electron possibly in the L_3 level, which is then ejected from the solid. This latter electron is termed the Auger electron and its energy E is given by

$$E \simeq E_K - E_{L_2} - E_{L_3} \qquad (7.1)$$

Since E_K, E_{L_2} and E_{L_3} are all characteristic of the particular element concerned, it is possible by measuring the energies and the number of Auger electrons to determine the chemical composition of the sample surface.

The energies of the Auger electrons is low (typically 20-1000 eV) so that although they may be produced from as far within the sample as the original electron beam penetrates, only those which are generated within the first few atomic layers ($\sim$ 2 nm) below the surface can escape with their original energies unchanged. Thus, the technique has immense surface sensitivity ($\sim$ 0.1 At %)$^{(2)}$. However, it is not capable of detecting hydrogen and helium since these elements do not possess sufficient energy levels for the Auger transition to occur.

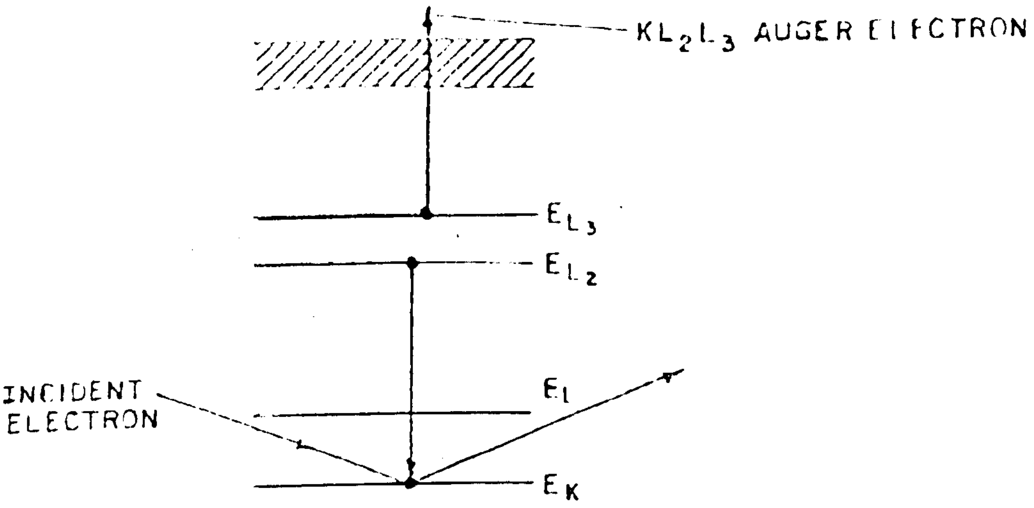

Fig 7.1: Schematic diagram illustrating a transition leading to the emission of a KL_2L_3 Auger electron (after Walls$^{(2)}$).

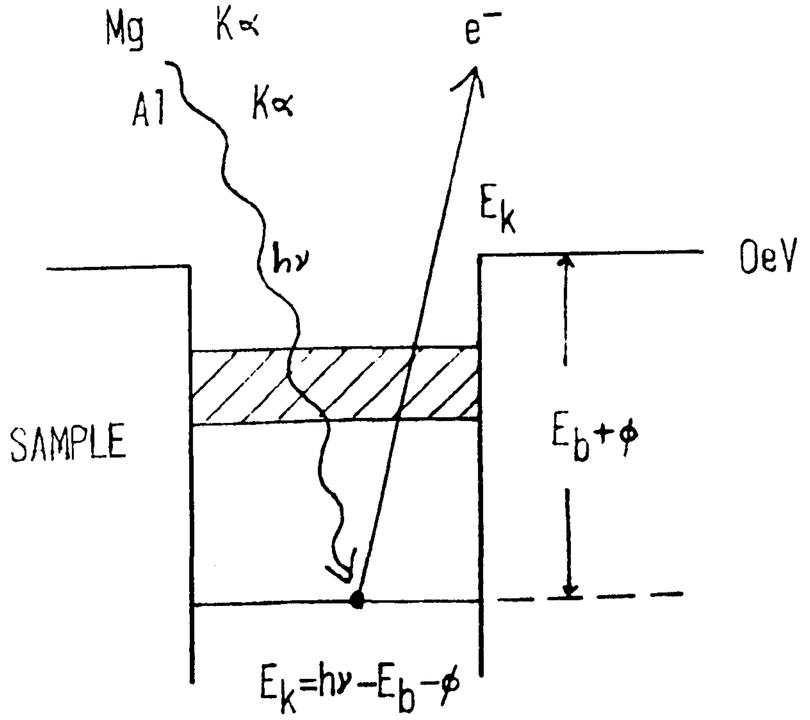

Fig 7.2: Schematic illustration of the photoelectron emission process (modified after Christie$^{(3)}$).

In XPS, the sample surface is irradiated by a source of low energy X-rays (generally $Al_{K\alpha}$/ 1487 eV or $Mg_{K\alpha}$/ 1254 eV) under ultra-high vacuum (10^{-8} - 10^{-11} Torr) conditions (Fig 7.2). Now, in addition to the valence electrons, which provide the bonding for the system, each atom present in the surface (except hydrogen) possesses core electrons not involved in the bonding. These core electrons are subject to a combination of many external forces. The positively charged nucleus provides an attractive force proportional to its atomic number Z, whilst the surrounding assembly of valence electrons gives rise to a complex repulsive force. The net result of all these interactions is referred to as the binding energy (E_b) of the core electron and is thus characteristic of the individual atom to which it is bound. The electron binding energies within any one element are far from fixed however, and small variations ($\lesssim$ 10 eV) in binding energy may occur due to changes in the valence electronic structure of the atoms concerned. Thus, these variations may be used to provide information on chemical bonding.

Upon irradiation with X-rays, photoionisation takes place in the sample surface (see Fig 7.2) with the resultant photoelectrons having a kinetic energy (E_k) given by the Einstein relation

$$E_k = h\nu - E_b - \phi \qquad (7.2)$$

where $h\nu$ is the X-ray energy and ϕ is the work function of the solid containing the atom. Since the energy levels occupied by electrons are quantised, the photoelectrons have a kinetic energy distribution N(E), consisting of a series of discrete bands essentially reflecting the "shell" form of the electronic structure of the sample.

The ejected photoelectrons enter the analyser of the spectrometer and are separated according to their energies ; they are then counted by a detector and the data recorded in the form N(E) versus E on an X-Y plotter.

	Auger Electron Spectroscopy (AES)	X-ray photoelectron spectroscopy (XPS)
Incident Particle	Electrons (1-10) keV	X-Rays (1254 eV and 1487 eV)
Emitted Particle	Auger electrons (20-2000 eV)	Photoelectrons (20-2000 eV)
Element Range	> Li (z = 3)	> He (z = 2)
Detection Limit	0.1 At %	> 0.5 At %
Depth of Analysis	∿ 2 nm	∿ 2 nm
Lateral Resolution	> 0.5 µm	> 1 mm
Spatial Resolution	High and visual display possible	None
Beam Damage	Possible on some insulating samples	Virtually none
Other Features	Quantification to within 10% with standards High reproducibility	Quantification to within 10% with standards. High reproducibility

Table 7.1 Summary of the main characteristics of Auger spectroscopy and X-ray photoelectron spectroscopy (modified after Walls(2)).

After ejection of the core electron as a photoelectron, the excited atom must decay back to the ground state. This may be done by filling the empty core-hole with an electron from another level, the excess energy being released as a photon (X-ray emission) or by imparting the excess energy to a third electron which is then released into vacuum as an Auger electron. These Auger electrons will thus also appear in the electron spectrum and can be used to supply additional information about surface composition.

As with Auger spectroscopy, although the X-ray photons penetrate deep into the sample, only those electrons which come from the outermost atomic layers emerge with their energies intact, since low-energy electrons have a very short mean free path in solids (1-10 nm)(3).

One major advantage of XPS from the point of view of the present work is that this technique is also the one that is most amenable to the widest range of sample materials since incident X-rays do not normally cause surface damage. Thus, this technique is the natural choice when analysing surfaces occurring in organic or polymeric coatings.

A summary of some of the capabilities and limitations of the two techniques is given in Table 7.1.

7.2 INSTRUMENTATION

The XPS/AES measurements were made mainly using a VG Escalab spectrometer. Some earlier AES experiments were however carried out on a Varian 10 keV spectrometer. The following description of the instrumentation used for the acquisition of the structural characterisation data pertains mainly to the VG instrument ; important differences in detail between the two spectrometers will be dealt with at relevant places.

The basic XPS unit can be divided into five main constituent parts : the X-ray source, the experimental chamber, the energy analyser, the electron multiplier/detector and the data recorder. For the AES instrument of course, the X-ray source is replaced by an electron gun (1-10 keV) to produce the primary electron beam. A schematic of the VG Escalab spectrometer is shown in Fig 7.3.

The VG instrument is fitted with a twin X-ray source incorporating both aluminium and magnesium anodes. To produce the X-rays a high voltage power supply is used to accelerate electrons into the target anode maintained at a high positive potential (typically 10-20 kV). The X-rays generated (Al $K\alpha$/1486 eV or Mg $K\alpha$/1253 eV) pass through a thin ($< 1\ \mu m$) aluminium window separating the X-ray source and spectrometer chambers, which serves to reduce cross-contamination of both source and sample. The sample surface is thus uniformly irradiated with a low flux of X-rays over a relatively large area ($\sim 1\ mm^2$).

The advantage of having both Al $K\alpha$ and Mg $K\alpha$ radiation available lies in the fact that photoionisation results not only in photoelectrons but in addition as discussed above (section 7.1), Auger electrons. Since the Auger electron energy is independent of the X-ray source used whilst the photoelectron energy is not, the <u>apparent</u> binding energy of Auger peaks changes (by 233 eV) on going from Al $K\alpha$ to Mg $K\alpha$ radiation (or vice versa). Thus a twin X-ray source may be used, not only to differentiate between photoelectron and Auger features in the spectrum, but also to resolve photoelectron and Auger peaks which may otherwise interfere with each other.

In order to allow emitted electrons to reach the analyser, the sample was mounted inside a high vacuum chamber, normally held at below 10^{-8} Torr, but able to reach much higher vacuum ($\sim 10^{-11}$ Torr) for high sensitivity measurements. This requirement of high vacuum conditions is quite general, not only in order to allow the constituent parts of the spectrometer (X-ray anode, electron multiplier and electron gun) to function effectively but also to reduce the build-up of contaminants on the clean sample surface.

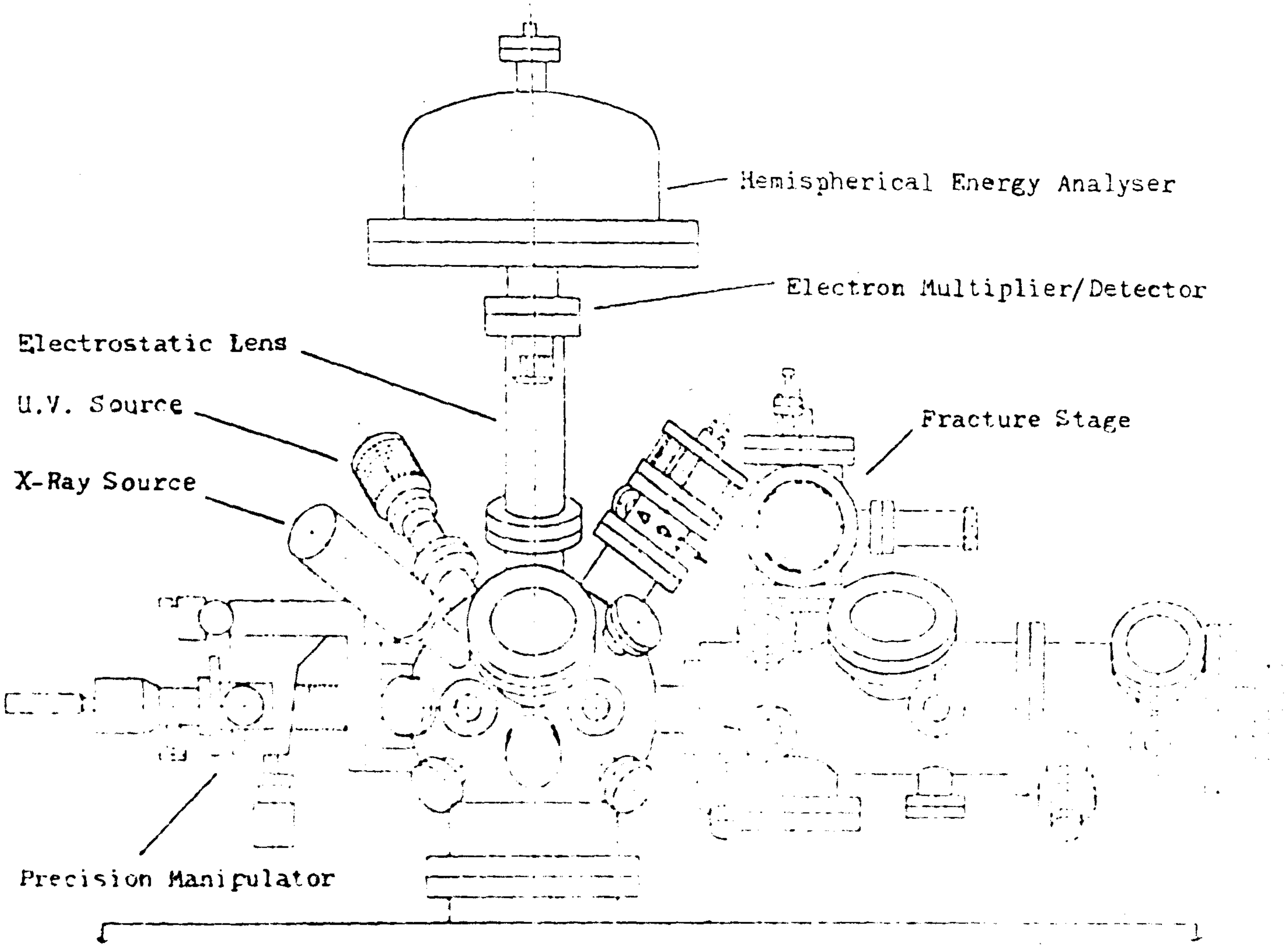

Fig 7.3: **Schematic of the VG Escalab Spectrometer (after Christie[3]).**

These low pressures were achieved using a bakeable stainless steel multi-chamber system and by the use of diffusion, and turbomolecular pumping and appropriate cryogenic traps.

An important difference in detail existed in this regard between the Varian and VG instruments. The former spectrometer is based on a single-chamber design, in which all of the sample mounting, preparation and analysis takes place. On the other hand, the VG spectrometer has several chambers each with its own pumping lines, thus having the advantage of rapid sample introduction (via an entry lock) and independent preparation and analysis chambers (see Fig 7.3). The length of time that the samples have to spend under UHV conditions before analysis has several important consequences for the present results and is discussed again at a later stage.

The electrons emitted from the surface of the sample were passed through an electrostatic lens and slit system and then into the analyser section, which operates by dispersing the electrons in an electrostatic field according to their energies. In the case of the Varian spectrometer, this was a cylindrical mirror analyser (CMA). This type is generally regarded as the most suitable for AES studies since it combines adequate resolution with rapid scan times and high sensitivity. In contrast, the VG instrument was fitted with a hemispherical analyser (HSA) which has the advantage of relatively better performance under ultra high vacuum conditions and is therefore favoured for XPS instruments.

The electrostatic lens served three important purposes. Firstly, it allowed the samples to be positioned well away from the entrance slit to the hemispherical analyser without seriously reducing the number of electrons entering the analyser. Secondly, unwanted high energy electrons were not focused by the lens, which resulted in an improved signal to noise ratio in the spectrum. Finally, since the lens forms an image of the sample at the entrance to the analyser, the area of the sample being analysed was determined by the entrance slit to the analyser, (generally 0.5-22 mm diameter), thus permitting selected area analysis to be undertaken.

The kinetic energy of electrons collected by the lens was reduced, prior to their entry into the analyser, by a voltage applied to a retard mesh positioned immediately in front of the entrance slit to the analyser. The analyser itself consisted of two concentric hemispheres maintained at a different voltage. Thus, only those electrons with a particular energy (proportional to this voltage) are focused onto the exit slit of the analyser and detected. In normal mode, the voltage difference between the two hemispheres was held constant and the voltage applied to the retard mesh swept between the desired electron energy limits.

The final detector was a single channel electron multiplier whose output was used to feed an amplifier and counter circuit. This signal was then plotted on an X-Y recorder in the form N(E) versus E. In the case of Auger spectra, since Auger freatures are comparatively small and occur on a large sloping background, it is usual to electronically differentiate N(E) so that the final data is obtained in the form d N(E)/dE versus E.

In addition to the basic units just described, both spectrometers had an ion gun to permit in situ surface cleaning and sputtering. In addition, the VG instrument also had facilities for sample heating and cooling; a sample fracture stage ; an evaporation source ; and gas handling facilities (see Fig 7.3).

7.3 FILM COMPOSITION

In order to confirm the predicted composition of the Langmuir films fabricated in the present work, mixed films of stearic acid/stearate in the thickness range 1-9 layers were fabricated on various evaporated metal substrates (see Chapter 3) and studied using both Auger and X-ray photoelectron spectroscopies. Typical results obtained using AES for a stearic acid/calcium stearate film (0-3 monolayers) on an Au substrate are shown in Fig 7.4. Results obtained from a stearic acid/BaSt$_2$ film on Ag(0-5 monolayers) using XPS are shown in Fig 7.5.

As expected, the peak heights for oxygen, carbon and calcium increase whilst those for the underlying gold substrate decrease with the number of monolayers (Fig 7.4). A similar situation is found with the XPS results of the stearic acid/BaSt$_2$ film on a silver substrate (Fig 7.5).

It will be noted that in the Auger spectra, there are several peaks which have been assigned to the elements sulphur and chlorine. In addition, even those spectra obtained from the bare substrates show evidence of carbon and oxygen. These are found to be an inevitable feature of all samples and reflects the need for high vacuum conditions when making AES/XPS measurements. It is known for instance that contaminants can build up at the rate of one monolayer per second even in vacua as low as 10^{-6} Torr(3).

The relative proportions of the elements have been standardised with respect to $CaCO_3$ and $BaCO_3$ and peak intensities are in reasonable agreement with expectations. The C/O/Ba proportions ($\sim$ 45/3/1) measured from Fig 7.5 are comparable to the proportions ($32/\lesssim 4/1$) of these elements predicted from an elemental analysis of barium stearate. The higher figure for carbon in the first case is attributed to the presence of free carbon present on the film surface. Both AES and XPS of course do not detect the element hydrogen.

Further confirmation of the step-like nature of the multilayer structures fabricated (compare with Fig 3.18) can be seen in Fig 7.6. Here, the peak intensity of the Ag3d$_{5/2}$ peak is plotted against distance along the substrate. The results were obtained from XPS measurements on a stearic acid/BaSt$_2$ film (0-5 monolayers) deposited on a silver substrate and demonstrate quite clearly the reproducible nature of the

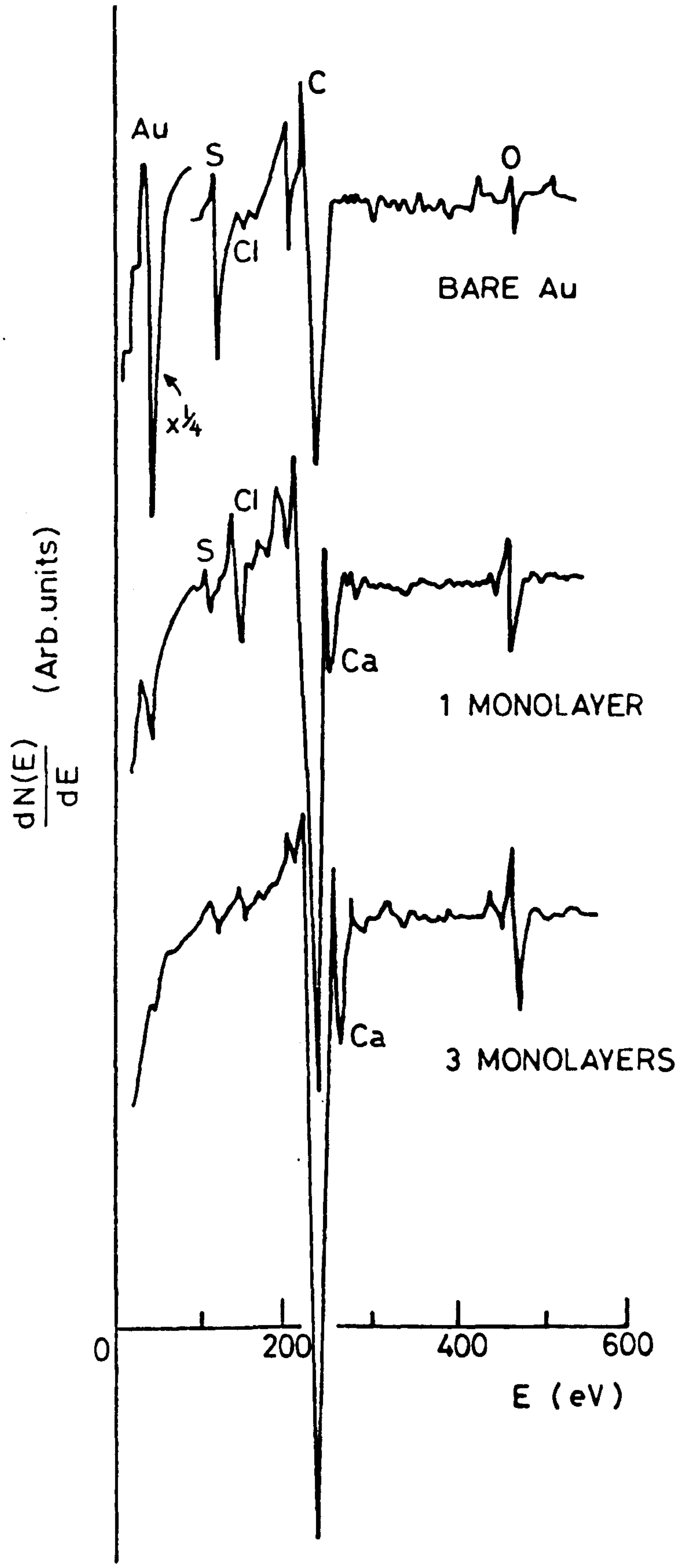

Fig 7.4: Auger Spectra obtained from a stearic acid/calcium stearate film (0-3 monolayers) deposited on an Au substrate.

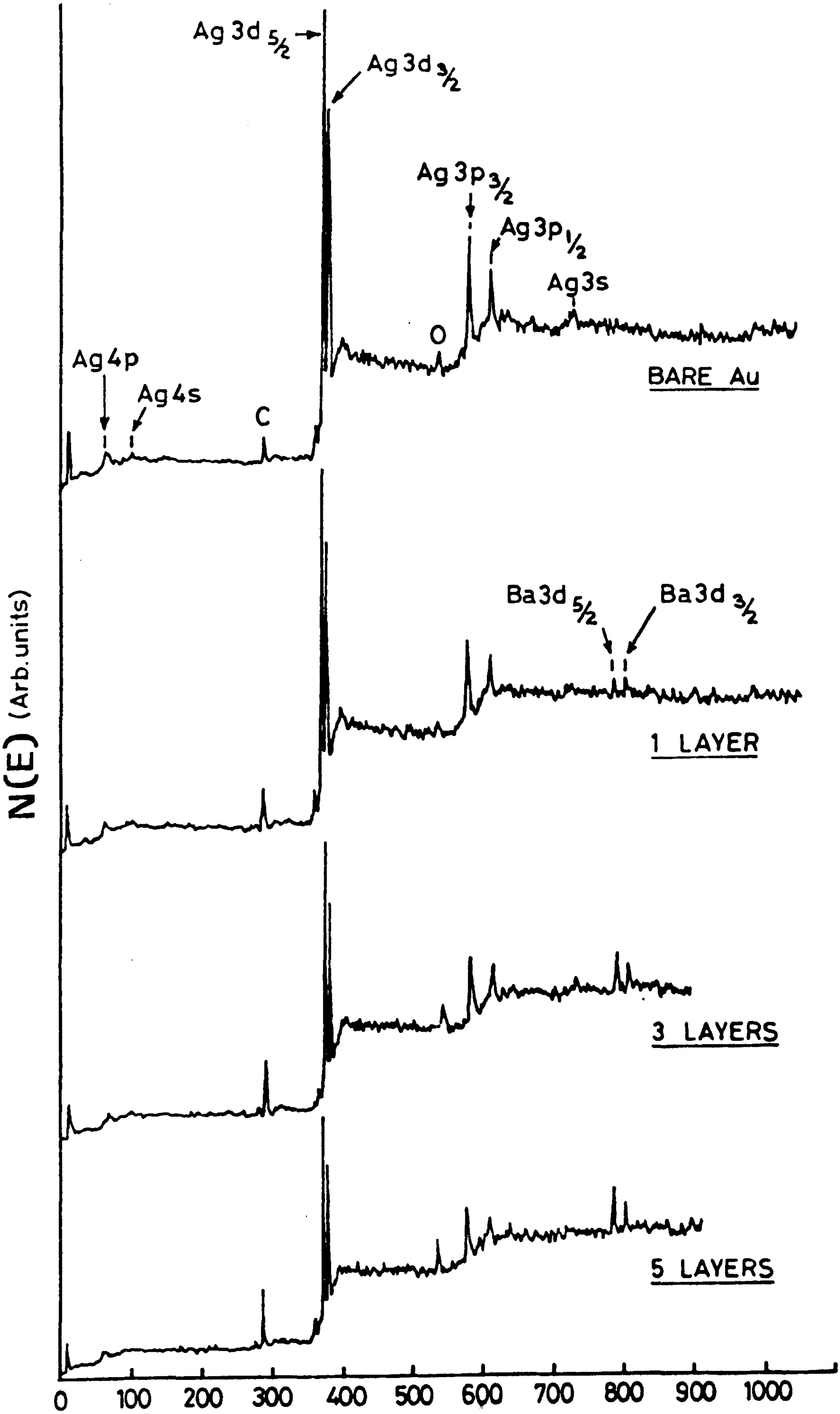

Fig 7.5: X-ray photoelectron spectra obtained from a stearic acid/barium stearate film (0-5 layers) deposited on an Ag substrate (B.E: Binding Energy).

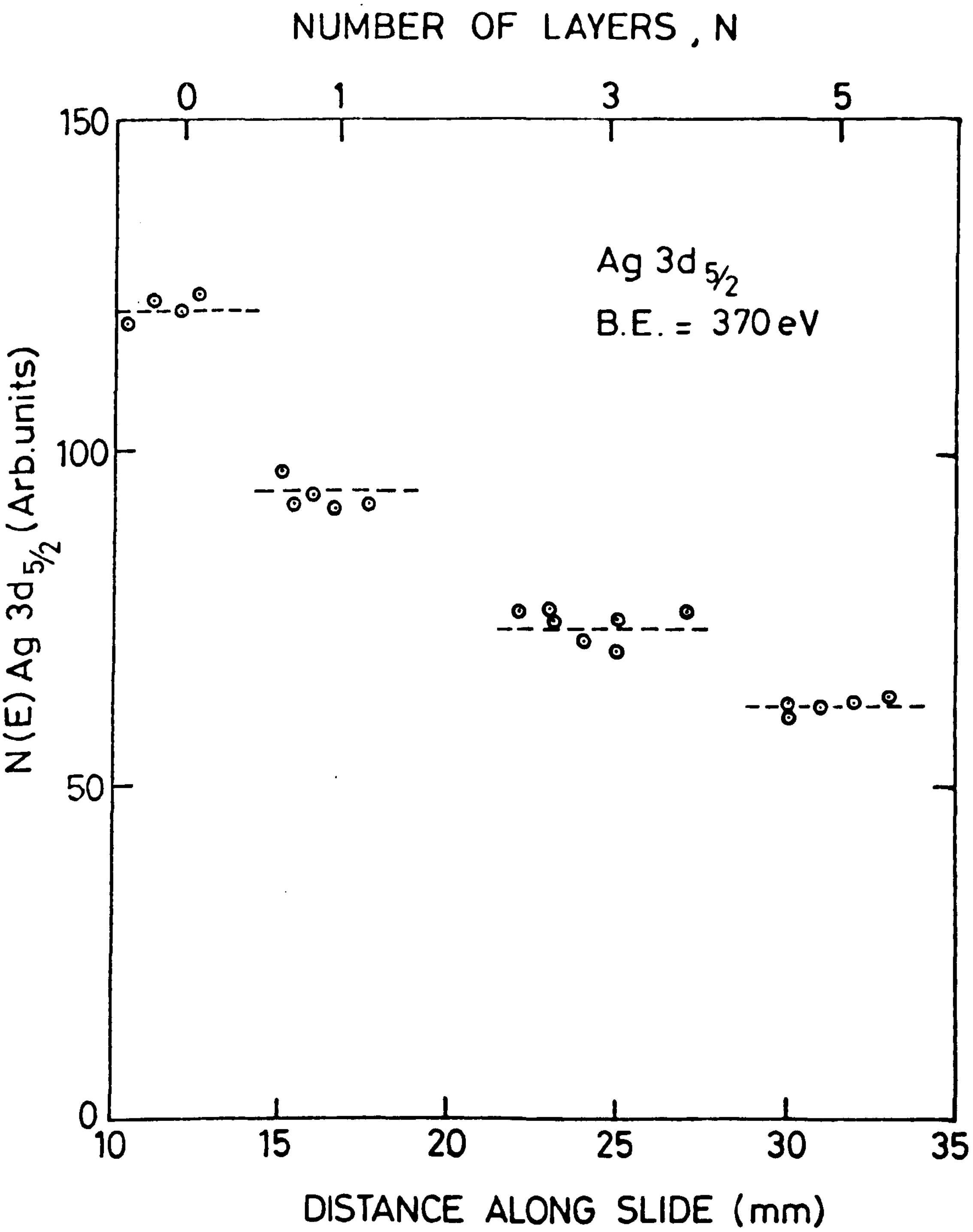

Fig 7.6: XPS peak intensities of the Ag $3d_{5/2}$ peak plotted against distance along the slide for a stearic acid/barium stearate film (0-5 layers step structure) deposited on an Ag substrate.

signal from the underlying substrate for a given number of monolayers.

It is important when making measurements on organic or other delicate materials to ensure that the surface of the sample is not damaged by the incident radiation. This is really only of significance in AES as X-rays do not normally cause appreciable surface damage and is one reason why XPS is preferred as a surface analytical technique for organics. With AES, it was found that bombardment of a sample with electrons of 2 keV and a 1 μA current (over a spot size of ∿ 1 μm diameter) nearly doubled the intensity of the underlying substrate signal in about a minute, thus indicating substantial surface changes. It was usual therefore when making AES measurements, to conduct preliminary experiments to determine values of beam energy (generally ∿ 1 keV and 0.5 μA were used) that induced minimal sample damage. No detectable change in the signal intensities of the substrate were noted as a result of possible X-ray beam damage in the case of XPS measurements.

7.4 ELECTRON MEAN-FREE PATHS IN LANGMUIR FILMS

The interpretation of Auger and X-ray photoelectron spectroscopy data often requires information on electron mean free paths as a function of electron kinetic energy in a variety of materials. Such information is obviously of great importance in determining the escape depth or the sampling depth from which the signal arises and is thus significant for the proper evaluation of the surface sensitivity of a particular experiment and for the quantification of results(1).

There is a considerable controversy in the literature concerning the values of electron inelastic mean free paths (IMFP) or attenuation lengths in organic materials(4-5). Cadman et al(4) have reported values which are considerably greater than for metals whereas other workers(5) claim that these values are essentially similar in the two classes of solids and should display an $E^{\frac{1}{2}}$ dependence on electron energy(1,6).

The usual method of determining IMFP(λ) values for organics consists of the deposition of a thin film of the material (to a known thickness) on an appropriate substrate, generally a metal. XPS and AES data is then determined for the main photoelectron and Auger lines of the substrates. The substrate peak intensities are a function of film thickness and are given by

$$I_d = I_o \exp(-s/\lambda\sin\Theta) \qquad (7.3)$$

where I_d/I_o is the intensity ratio of the substrate signal with an overlayer of thickness s to that in the absence of the overlayer and Θ is the electron emission angle determined between the sample plane and analyser axis.

The substrate core-level (Au 4f $_{7/2}$) peak heights, measured at a fixed emission angle $\Theta = 90^o$ as a function of the number of monolayers (stearic acid/barium stearate) are plotted in Fig 7.7 for a gold substrate. The solid line represents a best fit by eye to the data. From the slope of the line and equation (7.3), it is possible to derive a value for the IMFP (λ).

In Fig 7.8, IMFP data obtained in the present work are plotted on a compilation for organics by Seah and Dench$^{(6)}$. An approximate $E^{\frac{1}{2}}$ relationship can be demonstrated over the electron energy range 100-1500 eV in accord with the findings of Powell$^{(1)}$. However, IMFP values are higher than previous determinations by about a factor of two.

Brundle et al$^{(7)}$ have demonstrated that anomalously high IMFP values previously reported for organics obtained using the fixed emission angle, variable overlayer thickness method as conducted here can be attributed to substrate bare patch and surface roughness effects. It is also important in these experiments to ensure that signal intensities remain constant with time$^{(7)}$. With the earlier results reported from

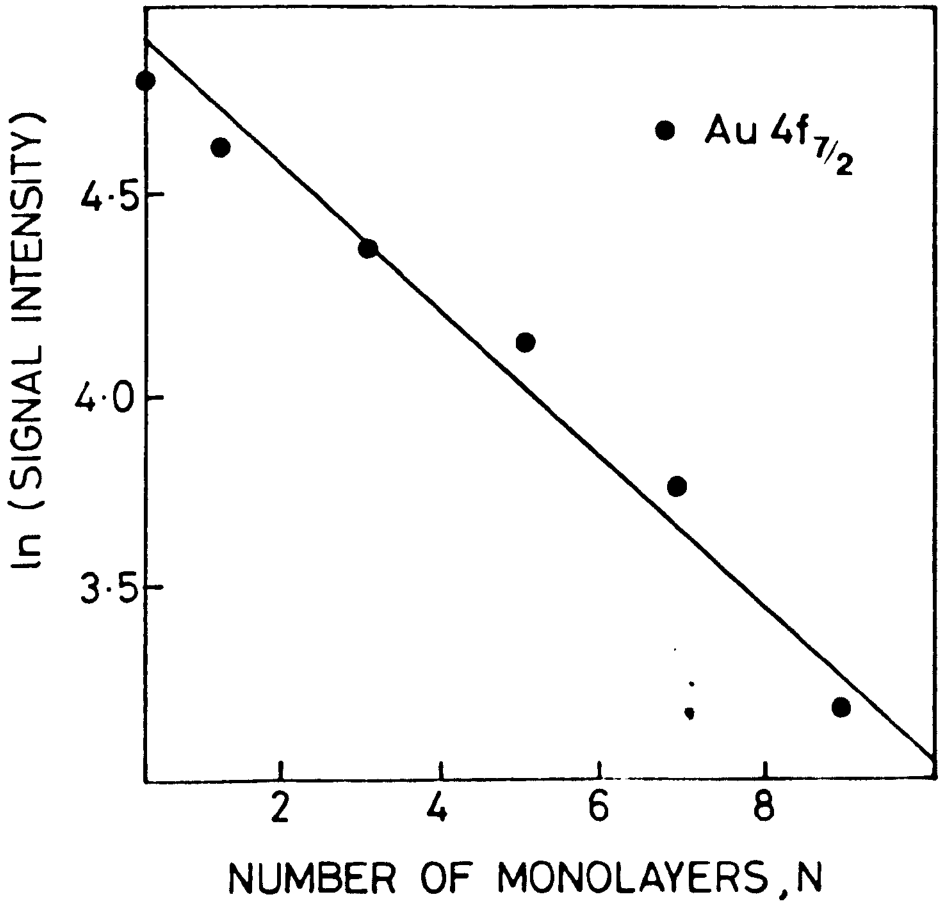

Fig 7.7: Substrate core-level (Au $4f_{7/2}$) peak intensities as a function of the number of monolayers for a stearic acid/barium stearate film (0-9 layers) on an Au substrate (see text).

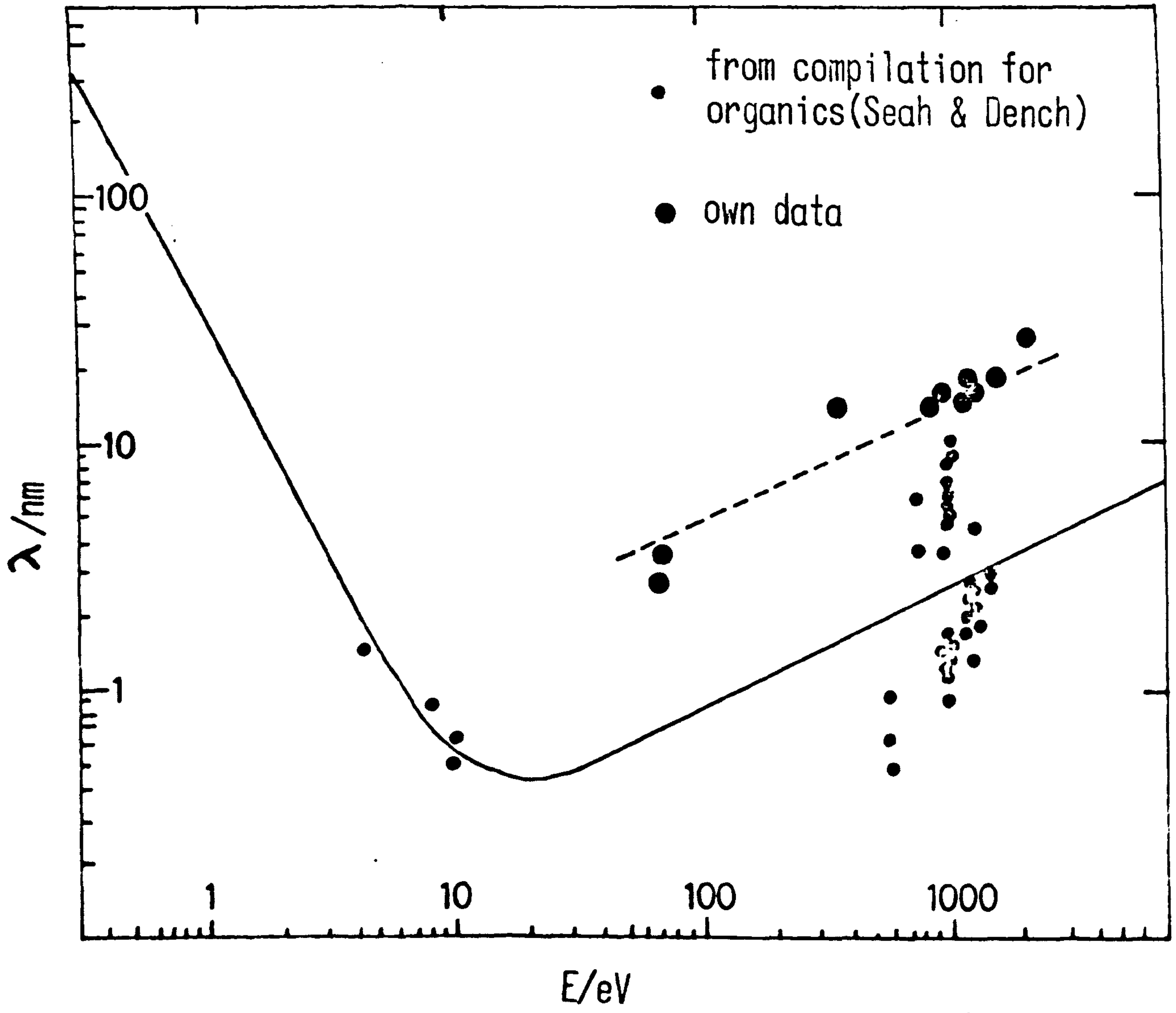

Fig 7.8: IMFP (λ) data plotted on a compilation for organics by Seah and Dench (6). The dotted line represents a $\lambda \alpha E^{\frac{1}{2}}$ dependence (see text).

this laboratory(8), no substrate bare patch effects or changes in signal intensities with time were noted. This was confirmed on the basis of additional experiments where :-

(1) the emission angle θ was reduced to 45° without the observation of any significant divergence from results obtained at the usual emission angle of $\theta = 90°$ (Bare patch effects were expected to become negligible at $\theta \gtrsim 55°$ in any case(7)).

(2) no change in signal intensities was noted as a result of possible beam damage and,

(3) no change in the signal intensities was noted with time as a result of possible film vapourisation in the high vacuum ($< 10^{-8}$ Torr) necessary for AES/XPS.

These results pertain to a situation where samples were put into vacuum and pumped down for ∿ 2 hours before making measurements. Subsequently, observations have been made where samples could be introduced into vacuum and measurements made in a few minutes and the results obtained are significantly different.

Fig 7.9 shows a series of traces of the Au $5p_{3/2}$ XPS signal from a gold substrate with a 9 monolayer thick film of stearic acid/barium stearate. There is an approximately 30s interval between successive traces. It is apparent that there is a steady increase in the signal with time. To eliminate the contention that the effect is possibly the result of beam damage, the X-ray flux was turned off for 35 minutes. The result can be seen in Fig 7.9. It would appear also that after some 40 minutes in vacuum the film vapourisation effect becomes much reduced and approaches equilibrium, thus explaining why no vapourisation effects were observed with the earlier measurements on similar substrates.

Recently, Hall et al(9) have carried out IMFP determinations using barium stearate multilayers. They report values (∿ 6.5 nm at 1480 eV) which

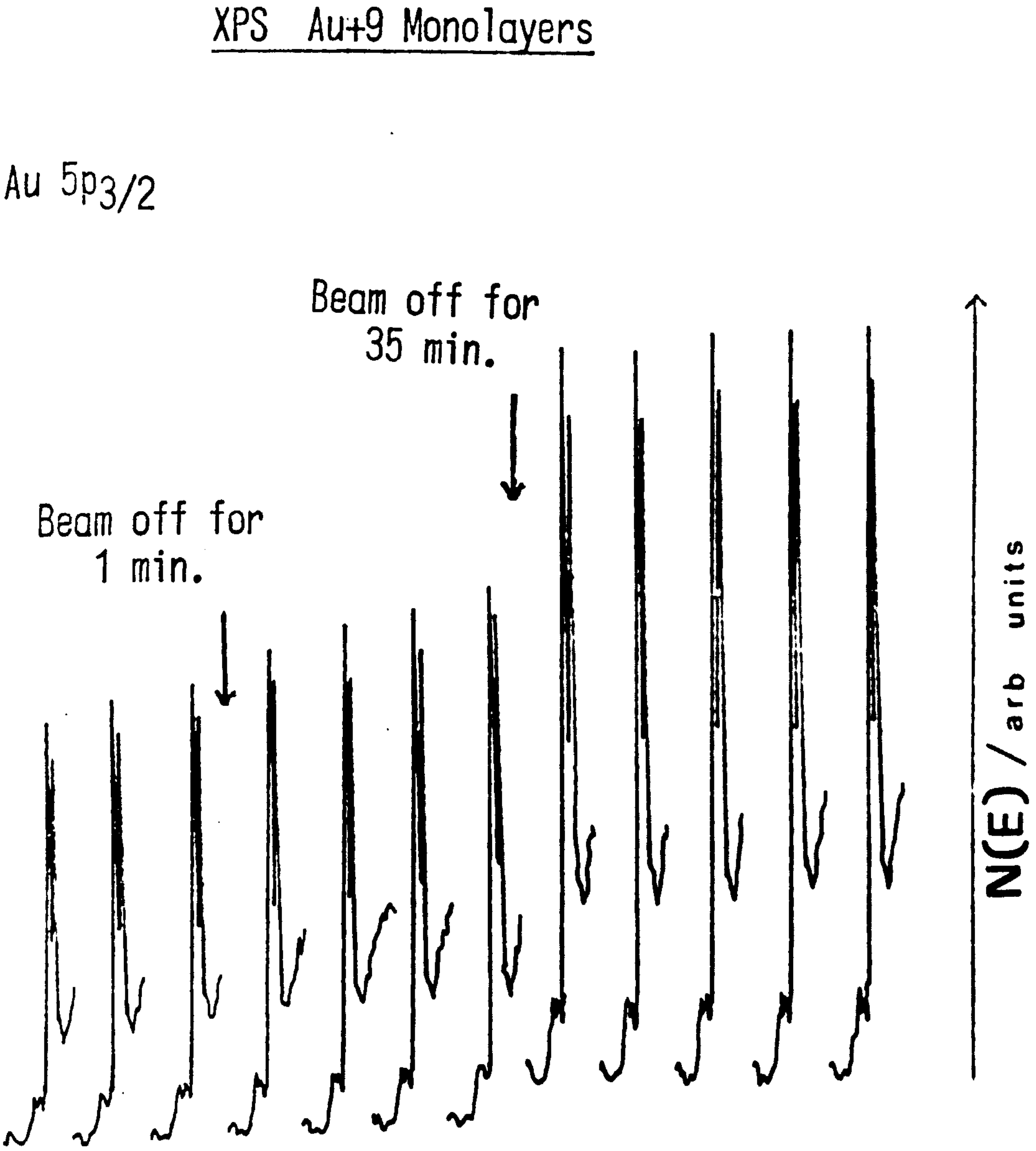

Fig 7.9: XPS $Au5p_{3/2}$ signals from a nine layer film of stearic acid/barium stearate on Au as a function of time. There is an approximately 30 s interval between traces except where indicated (see text).

are considerably lower than the results obtained in the present work. Hall et al utilised substrate cooling to 223 K in an attempt to reduce film vapourisation. The effect of cooling to liquid nitrogen temperature on the Ag $3d_{5/2}$/Ag $3d_{3/2}$ doublet from a silver + 1 monolayer (St.A/$BaSt_2$) sample fabricated in the present work is shown in Fig 7.10. There is a time interval of 90s to the first trace and 30s between traces. The important points which should be noted are :-

(1) the steady increase with time of the signal intensity, even though this is much reduced compared to the Au + 9 monolayers sample (Fig 7.9),

(2) since it is not possible to cool substrates subsequent to entry into the vacuum chamber, some film vapourisation is inevitable even if sample cooling is undertaken.

(3) after sufficient time has been allowed for thermodynamic equilibrium, the signal intensity still increases.

Langmuir film vapourisation effects have been reported previously by Gaines and Roberts(10). They showed that for barium stearate on quartz up to 10% of the film disappears in 30 minutes upon pumping at a 10^{-6} Torr vacuum at room temperature. After this length of time the removal of film becomes much reduced and approaches an equilibrium. Gaines and Roberts also report that for stearic acid films the losses are considerably greater and that vapourisation effects for both stearic acid and stearate films are substrate-dependent.

It is interesting to note that Hall et al(9) used germanium and copper substrates at 223 K in determining their IMFP values. Thus it is possible that the reason why they did not observe any film loss in vacuum is that these substrates are reactive and therefore interact more strongly with the first layer of the deposited Langmuir film. This will be in contrast to the results obtained in the present work where mainly gold

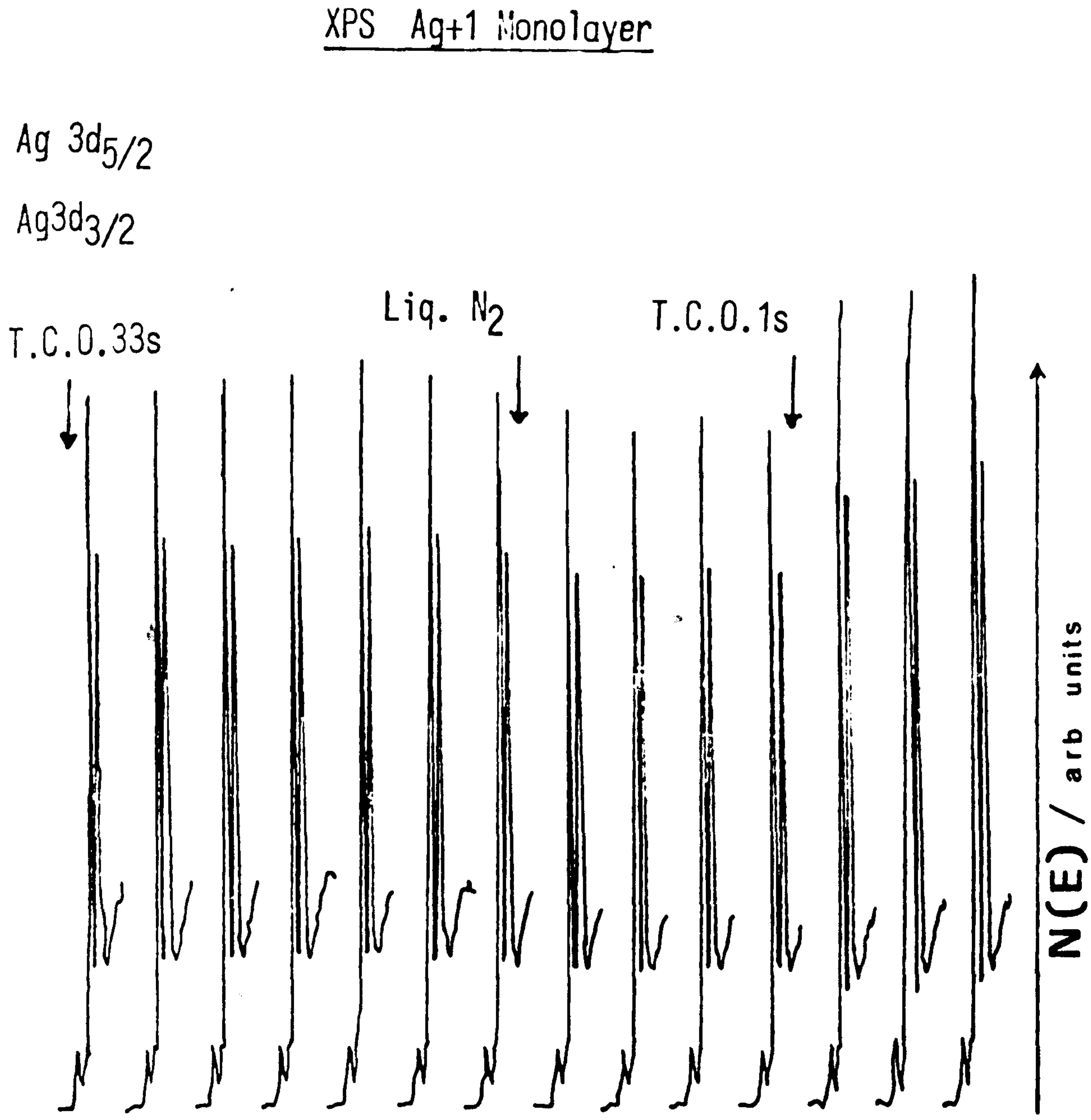

Fig 7.10: XPS Ag $3d_{5/2}$ /Ag $3d_{3/2}$ signals from a single layer film of stearic acid/barium stearate as a function of time. There is an approximately 30 s interval between traces. (T.C.= Time constant). (see text).

and silver substrates have been used. Nevertheless, the point remains that the results of IMFP determinations from Langmuir films(7-9,11) deposited on evaporated metal substrates (at least gold and silver specifically) must be interpreted in the light of the results reported here regarding film vapourisation in vacuum, even when substrates are cooled to 77 K.

7.5 LANGMUIR FILM ADHESION AND STACKING

It is generally believed that carboxylic acids are chemisorbed onto reactive metal substrates through formation of the salt of the acid with the metal substrate. Evidence in support of this comes mainly from tunnelling spectroscopy(12-13) and infra-red(14) measurements. With carboxylic acid Langmuir films however a further complication arises from the fact that before transfer onto the substrate the monolayer is already partially converted to the salt of any divalent cations in the subphase. Thus, in effect a mixed film of the acid and its salt is actually deposited on the substrate.

Fig 7.11 shows Auger spectra obtained from a bare tin substrate and a tin substrate with a single monolayer of stearic acid/calcium stearate. The most noticeable feature in the second spectrum in Fig 7.11 is the complete absence of any structure which could be associated with calcium in the monolayer. It is suggested that cation exchange has occurred during monolayer transfer and the substrate has actually become coated with tin stearate. In the case of spectra obtained from stearic acid/calcium stearate films deposited on gold substrates (Fig 7.4), no ion exchange is of course possible and evidence for calcium is observed in the spectra in a proportion which is in approximate agreement with that expected. Similar results have recently been reported for stearic acid/$CaSt_2$ films deposited on aluminium substrates(15)

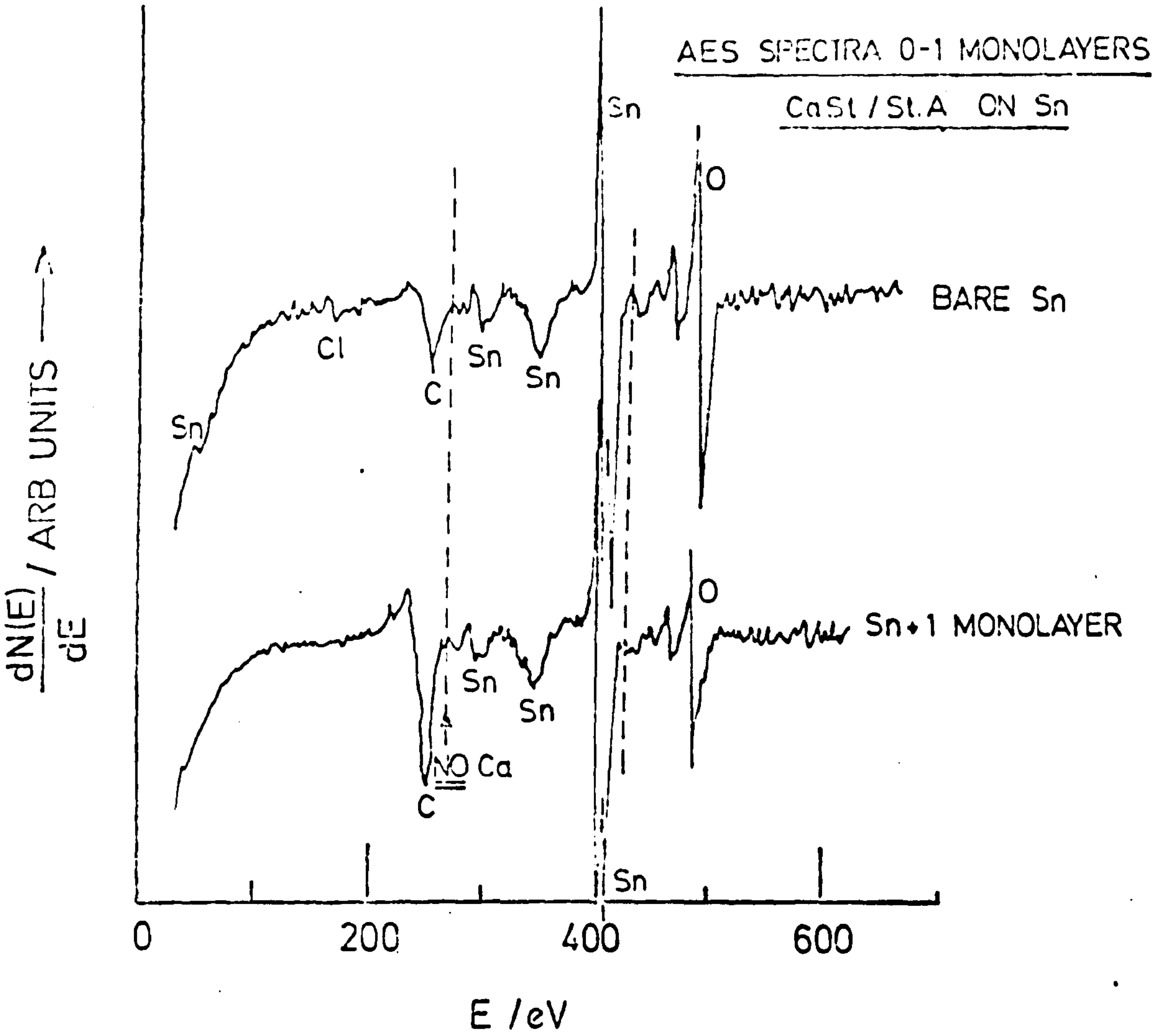

Fig 7.11: Auger Spectra obtained from a base Sn substrate and an Sn + 1 layer stearic acid/calcium stearate structure illustrating cation exchange with a reactive metal substrate.

Now the extent of vapourisation of a Langmuir film deposited on a solid substrate will clearly depend on the strength of the interaction between the film and the substrate. In the case of a reactive metal substrate the film will be chemisorbed through formation of the salt of the acid. When the transferred film already consists partially or completely of a salt of the acid, cation exchange occurs and the substrate actually becomes coated with the substrate metal salt of the acid. It is reasonable therefore to expect in this case that the deposited film will be strongly bound even under vacuum. With noble metal substrates no salt formation or ion exchange is possible and the film is only weakly adhered to the substrate. This is likely to be the reason for the longer IMFP values found in the present work using gold and silver substrates and also explains the differences found with regard to film vapourisation effects between these results (Figs 7.9-7.10) and those of Hall et al(9) using germanium and copper substrates.

This view is consistent also with the electrical measurements made in the present work with films fabricated on aluminium and tin substrates. Electrical measurements are extremely sensitive to pinholes and other defects in the insulating film and the results obtained here suggest convincingly that the Langmuir films fabricated are largely defect-free. If significant vapourisation of the film was occurring from these substrates it is extremely unlikely for instance that any evidence of inelastic tunnelling would be observed. Thus, although it is possible that a certain amount of physisorption of the acid does take place even with reactive metal substrates (see section 5.9), it is reasonable to surmise that with these substrates physisorption of the acid is limited and that the cohesion between adjacent molecules in the monolayer is sufficient to prevent significant film vapourisation.

It has been realised of course for some time that it is not possible to fabricate insulating Langmuir films on noble metal substrates. This has most commonly been attributed to the poor adherence of the fatty acid molecules to the metal surface. The results obtained here support this explanation but in addition it is argued that once transferred the film is also easily vapourised in vacuum during the evaporation of the top electrode. It is not surprising therefore that although deposition ratios of approximately unity (see section 3.4.3) have been observed during the transfer of these films, the completed M-LF-M devices have resistance values which are indicative of shorts.

With multilayer Langmuir films of course the interfaces between subsequent layers must also be considered and it would seem that in the absence of any functional groups deliberately introduced to promote interlayer interaction, the only forces responsible for layer-layer adhesion are those due to a Van der Waals type of bonding. However, in this context, there is considerable evidence of crystallisation processes and molecular re-arrangement in these organic films(16). These crystallites would appear to extend right through the film and as such would result in increased cohesion of the multilayer and a decreased probability of incorporating pinholes in the completed MIM structure. Since the interest here is in mechanisms which may possibly lead to the deterioration in 'electrical quality' of the organic films, the subject of multilayer cohesion was not directly explored in this work.

It is realised that the arguments presented here rely heavily upon the interpretation of the electrical measurement data. However, as the tunnelling process is extremely sensitive to pinholes and other defects, it is probable that these measurements provide the most convincing test of the integrity of a thin insulating layer. Consequently, the relationship between electrical measurements and Langmuir film adhesion has been stressed here and the arguments presented are consistent with the limited amount of experimental data available. The current interest in these films as thin, reproducible insulating layers should be extended to include further studies of the type reported here.

Finally, it is necessary in this brief discussion to examine the topic of monolayer stacking and orientation. It will be recalled (Chapter 3) that the transfer process was originally divided into three possible types; X,Y, and Z. This classification originates from the early work of Langmuir and Blodgett(17) where the normal mode was Y-type ; X-type was observed at extremes of pH and the possibility of Z-type deposition speculated, although not demonstrated. More recently, however, these basic distinctions have come under some criticism as the real process is understood to be considerably more complex. One of the major problems is that despite the observation of both Y and X-types of deposition (from the deposition ratio), X-ray studies of the resultant films(18-19) show the spacing of the carboxylate groups to be invariably twice the molecular length. This evidence therefore suggests that regardless of the pick-up mode, the resultant films are always of Y-type. In addition, other recent studies(20) of the process have proposed yet another mode of deposition (XY) which is a cross between the two original extremes.

In order to account for the apparent Y-type resultant film (as revealed by X-ray studies) Gaines(21) and others(22-23) have suggested that overturning may occur at some point during the X deposition mode. Another model(20) has proposed the formation of two distinct types of salt of the acid - the final form MSt_2 (where M is a divalent metal, specifically Pb(20)) and an intermediate form M^+St, where only the latter type is present in the monolayer on the subphase surface. The model suggests that transfer occurs only onto M^+St sites in the multilayer during substrate withdrawal but onto all available carbon chains on immersion of the substrate into the subphase. Thus the ratio MSt_2/M^+St defines the extent to which transfer occurs and the model explains in a consistent manner, without invoking any ideas of overturning, both the existence of XY and X deposition.

The main point of this discussion is to stress that the mode of film transfer and molecular orientation is considerably more complex than the original simple classification would seem to imply. Thus, it is most improbable that they can be predicted simply on the basis of the nature of the substrate (whether hydrophobic or hydrophilic) and the pH of the subphase during deposition. The observation made in this work where hydrophobic noble metal substrates (see section 3.4.3) do not pick up a monolayer on the first downstroke is therefore the result of a transfer process which is still not perfectly understood ; it is possible that minute variations, for instance in the substrate surface, are more significant in determining the mode of film transfer than originally thought. Although some work has already been done, many problems still remain and further studies are clearly necessary before a complete understanding of the transfer process emerges.

7.6 CONCLUSIONS

It is useful at this stage to summarise the important observations that have emerged as a result of the structural characterisation of films that has been undertaken in this work.

Auger and X-ray photoelectron spectroscopy studies have revealed that providing care is taken at all stages of the deposition process, the resulting Langmuir films are uniform and the results are in agreement with the predicted composition of these films and the tunnelling spectroscopy data. From these measurements, values for the electron inelastic mean freepath (IMFP) have been determined as a function of electron energy E. Although these IMFP values exhibit the expected $E^{1/2}$ dependence on energy they are greater (by a factor of ∿ 2) than previous determinations made by workers using other organic materials. The IMFP values in the present work have been determined on the basis of structures utilising gold and silver substrates and it is suggested that film vapourisation in vacuum from these inert surfaces is the probable reason for these differences. In the case of reactive metal substrates, AES studies show that cation exchange occurs between the transferred mixed acid/salt film and the substrate and that the final film is deposited as the substrate metal stearate salt. This film is more strongly bound to the substrate as it relies on a strong chemical interaction. The results of electrical measurements made on films deposited mainly on aluminium and tin substrates support this view since electrical and in particular tunnelling experiments are very sensitive to pinholes and defects in the insulating film.

It is suggested that further work is necessary to improve understanding of basic phenomena such as film adhesion and stacking and that the surface analytical techniques utilised here lend themselves conveniently to this application.

CHAPTER 8

CONCLUSIONS

This chapter is in the nature of a brief summary of the work undertaken and the main conclusions that have been arrived at in this study of d.c. conduction in Langmuir film MIM devices. The limitations of the work will be explained and suggestions made as to possible future development of the subject. Finally, some of the potential technological applications of these films will be considered.

8.1 CONDUCTION IN SINGLE LAYER FILMS

In the voltage range 1-1000 mV and between temperatures 4-300 K, electron transport in single layer Langmuir film MIM devices occurs predominantly by direct electron tunnelling between the metal electrodes. The current-voltage relationship at a given temperature is correctly described by equation (2.47) or equations (2.36) and (2.37) which constitute a similar variation. At a fixed applied voltage, the current is weakly dependent on the temperature. This dependence of the current on the temperature is given by equation (2.53). Both these observations are in accord with a tunnelling model of the electron transport process.

At very low applied voltages ($V \rightarrow 0$ V) and low temperatures(~ 4 K), structure related to the superconducting energy gap is clearly revealed in the current-voltage characteristic when one of the electrodes is allowed to become superconducting. Moreover, a plot of $d(\ln J)/dV$ against the applied voltage V yields a maximum at a bias corresponding to the metal-insulator interfacial barrier height ϕ.

All these observations constitute strong evidence that the predominant electron transport mechanism in single layer Langmuir films is indeed electron tunnelling. However, this interpretation of the data is complicated by the inevitable presence of an oxide film(s) in the completed MIM junction. Thus, it is possible to criticise this evidence on the grounds that the data can be interpreted as describing a conduction process which is dominated by electron tunnelling through the oxide and then via pinholes and other defects in the organic film. The relatively detailed studies undertaken in this work with the objective of ascertaining the role of the oxide film(s) would appear to support this view, certainly at least where aluminium electrodes have been used. With tin based electrodes, the oxide film is relatively conducting and electrical breakdown occurs at very low applied voltages (∿ mV). It can reasonably be concluded therefore that the oxide in this case is of less significance. Nevertheless, all the studies of the role of the oxide film in single layer M-LF-M junctions do underline the fact that a tunnelling mechanism of charge transfer cannot be assumed simply on the basis of observations of the type described above and those undertaken by previous workers(1-3).

Unequivocal evidence for electron tunnelling in single layer Langmuir film MIM junctions is however provided by the observation of inelastic electron tunnelling signals related to the interaction of tunnelling electrons with the organic film. Moreover, since only a small proportion (∿ 1%) of tunnelling electrons lose energy to molecular oscillators in the film, the observation of this small number of relatively rare inelastic tunnelling events is strong evidence for an electron tunnelling mechanism of conduction over an extensive voltage range. The good correlation obtained between the tunnelling spectra of stearic acid/stearate Langmuir films and other tunnelling spectroscopy, infra-red and Raman data thus establishes beyond doubt that the main conduction process which occurs in single layer Langmuir films is indeed electron tunnelling.

8.2 CONDUCTION IN MULTILAYER FILMS

Previous observations of d.c. conduction in multilayer Langmuir films of intermediate thickness ($N \approx 3$-9) have attributed electron transport in these films to either Schottky emission or to bulk transport processes, limited by the Poole-Frenkel or Poole effects. The present study has shown that the current-voltage relationship obtained for multilayer ($N \simeq 3-5$) Langmuir film MIM devices is compatible with the Schottky emission of electrons over the metal-insulator barrier. Moreover, this has been verified through a careful investigation of the temperature dependence of the current at fixed voltage. These results suggest that for applied voltages $V \gtrsim 0.2$ V and temperatures $T \gtrsim 210$ K, conduction in multilayer films of intermediate thickness does indeed occur through Schottky emission. Below this temperature, and especially for the three-layer devices, it would appear that electron tunnelling is also of significance.

8.3 FABRICATION METHODS AND FILM CHARACTERISATION

Electrical measurements provide the ultimate test of the integrity of a thin insulating layer. The investigations undertaken here have underlined the importance of a reliable and consistent technique for the deposition of Langmuir films onto solid substrates. In the present work, a sophisticated Langmuir film fabrication system has been designed and constructed for this purpose. Moreover, during the commissioning of this apparatus, several factors which have important consequences for the completed MIM device have also been investigated.

The films produced have been characterised using Auger and X-ray photoelectron spectroscopy as well as the electrical methods. The results demonstrate that, provided care is taken at all stages of the fabrication process, the result is a uniform film of predictable composition and substantially free of defects.

In addition, the Auger and X-ray photoelectron spectroscopy measurements have been used to obtain electron inelastic mean free path values for these films. These are higher than those previously reported$^{(4-5)}$. It has been shown that this is due to significant removal of the Langmuir film in vacuum, from the inert noble metal films used as substrates. In the case of reactive metal substrates, it has been demonstrated that the organic film is chemisorbed through formation of the salt of the substrate metal. Since it relies on a strong chemical interaction, this film is more strongly bound to the substrate and is therefore less likely to vapourise in vacuum. This view is supported by the results of electrical measurements in so far as these measurements are extremely sensitive to pinholes and voids in the insulating film.

8.4 SUGGESTIONS FOR FURTHER WORK

There are many areas of the subject which could benefit from further study. This section aims to briefly delineate some of these.

Although it is certain that the predominant conduction process in single layer Langmuir films is electron tunnelling there still remain a number of discrepancies between theory and experiment. Of these, the non-linear behaviour of the current-voltage characteristic in a voltage range where a tunnelling model predicts a linear relationship (section 5.5) and the observation that some of the data also yields a $\log I \propto V^{\frac{1}{4}}$ dependence is particularly worth noting. Although, this work has attempted to provide explanations for these discrepancies, problems clearly still remain, and further work is necessary before a complete understanding emerges.

The presence of internal voltage and ageing effects in these films, although most likely to be related to ionic transport, seem also to be sensitive to minor variations in conditions during deposition. In fact, many of the electrical and structural properties (e.g. monolayer orientation and stacking) of these films appear to be intimately related to the fabrication technique employed. It would be useful therefore to determine the nature of the relationship between factors such as subphase pH, surface pressure, ionic content of the monolayer and the subsequent electrical and structural properties of the transferred films.

In this work, a tentative model has been presented for the Al-Al_2O_3-stearic acid/stearate-Al system. It is obviously desirable to confirm this by conducting independent experiments and perhaps also through a judicious study of the consequences on the I-V-T characteristics of changes in electrode material. By extending this work to include MIM devices without an intervening organic monolayer, the effect of the oxide film(s) can be better understood.

One very strong possibility for further work is to extend the inelastic tunnelling experiments to novel Langmuir film systems. This technique offers considerable potential both for the routine assessment of films and for studying deliberately introduced reaction phenomena in the films and at the interfaces. Further exploratory work may well enable a more realistic appraisal to be made of the feasibility of realising this application.

With regard to conduction in multilayer films, this work could again be usefully extended by carefully determining the effects on the electrical characteristics of changes in the electrodes and the insulator thickness. For a complete study, it would be necessary also to confirm the magnitude of the interfacial barrier height as inferred from the Schottky plots with that measured, for instance, by photoemission.

Concerning those ideas presented in Chapter 7 regarding film adhesion and stacking, it is clear that there is considerable scope for further work. It is suggested that the spectroscopic techniques utilised in this study (including tunnelling spectroscopy) lend themselves conveniently to this application.

Finally, from the point of view of potential device applications, it is unlikely that fatty acid/salt Langmuir films will form the basis of many practical devices since these particular films have relatively low melting points. It is envisaged therefore that a considerable effort will be directed towards establishing techniques for the deposition of novel Langmuir film materials. The range of materials that could be deposited as Langmuir films through the use of suitable chemistry and the possibilities that this offers for potential device applications are enormous. The final section in this thesis briefly discusses some of these.

8.5 POTENTIAL TECHNOLOGICAL APPLICATIONS

The subject of potential technological applications has been extensively reviewed recently(6) and only the briefest outline of some of the possibilities is presented here.

It is natural to firstly consider potential applications which capitalise on the uniformity and thinness of Langmuir films. Since these films also possess excellent insulating properties and high dielectric strength, there are several areas where possibilities exist. Of these, the potential use of these films in low voltage, low loss capacitors and in several types of 'hot' electron devices(7), where a uniform insulating layer of tunnellable dimensions is required, is worth mentioning.

Langmuir films sandwiched between metal electrodes have also been shown to undergo 'electroforming' and to exhibit voltage controlled negative resistance, memory and switching phenomena(8-9). These properties suggest potential applications of these structures as resistive memory arrays(10) and in certain 'hot' electron devices to mention but a few of the possibilities.

The uniformity of Langmuir films and the critical control of film thickness that the technique affords may also find application for these films as tunnellable insulating layers between a metal and a semiconductor (MIS devices), e.g. in photovoltaic devices(11) and in conjunction with inorganic materials such as GaP and ZnS, in electroluminescent devices(12).

Potential applications also exist for Langmuir films as passivating layers for certain III-V compounds which do not possess a natural oxide layer of the required quality(13) and in various field effect devices(14). Since organic materials are more responsive than inorganic compounds to external stimuli such as pressure and ambient gases, the presence of an organic film within such a transistor device suggests possible applications of these structures as microelectronic gas detectors(15). With these particular devices, changes that occur in the surface state spectrum on exposure to various gases could be evaluated using advanced signal processing techniques(16).

An alternative approach for gas detector applications and indeed one that has implications for many other applications is to utilise the pyroelectric or piezoelectric effects(6). Thus, it may be possible to suitably modify organic molecules which possess the desired molecular symmetry and incorporate these in the form of Langmuir films into field effect structures. This possibility that the technique affords of assembling functional chemical and biological moieties within an insulating film suggests a whole host of applications in the transducer field ; for instance, field effect devices for monitoring immunological response and enzyme-substrate reactions have already been proposed(16).

Perhaps the most exciting (albeit more speculative at present) possibility that the Langmuir film fabrication technique offers, is the potential for constructing supermolecular 'organizates' designed to fulfil specific functions. Thus, it is possible, for example, to envisage a structure where specially synthesised co-operative groups of molecules are assembled to simulate the photosynthetic process. Structures that are even more ambitious than this have been discussed(6).

This brief outline of potential applications is by no means exhaustive. Numerous additional possibilities exist for the use of films fabricated through the Langmuir technique, both from the point of view of device applications and also as tools for the study of fundamental physical phenomena. It is to be hoped that the research undertaken here has brought the possibilities of realising some of these goals one small step nearer to fruition.

REFERENCES

CHAPTER 1

(1) I. Langmuir, Trans.Faraday Soc., 15 (1920) 62.
(2) K.B. Blodgett, J.Am.Chem.Soc., 56 (1934) 495.
(3) K.B. Blodgett, ibid., 57 (1935) 1007.
(4) G.L. Gaines Jr., Insoluble Monolayers at Liquid-Gas Interfaces, Wiley Interscience, N.Y. (1966).
(5) A.E. Alexander, Techniques of Organic Chemistry, vol I/Part IV (2nd Ed) Ch. XIII.
(6) V.K. Srivastava, Physics of Thin Films, 7 (1974) 311, Academic Press.
(7) B. Mann and H. Kuhn, J.Appl. Phys, 42 (1971) 4398.
(8) J. G. Simmons, J.Phys D: Appl.Phys., 4 (1971) 613.
(9) N. Yamamoto, T. Ohnishi, M. Hatakeyama and H. Tsubomura, Bull.Chem.Soc. Japan., 51 (1978) 3462.
(10) P.S. Vincett, W.A.Barlow, F.T.Boyle, J.A.Finney and G.G.Roberts, Thin Solid Films, 60 (1979) 265.
(11) P.S. Vincett and G.G.Roberts, ibid., 68 (1980) 135.
(12) J. L.Miles and H.O. McMahon, J.Appl.Phys., 32 (1961) 1176.
(13) I. Giaver and K. Megerle, Phys.Rev., 122 (1961)1101.
(14) R. M. Handy and L.C.Scala, J.Electrochem.Soc., 113 (1966) 109.
(15) S. Horiuchi, J. Yamaguchi and K. Naito, ibid., 115 (1968) 634.
(16) T.D. Clark, Mullard Res.Labs, Rep.No.512 (1964).
(17) J. Bardeen, L.N. Cooper and J.R.Schrieffer, Phys.Rev., 108 (1957)1175.
(18) I. Giaver, private communication.
(19) B. Mann, H.Kuhn and L.V. Szentpaly, Chem.Phys.Letts.,8 (1971)82.
(20) E.E.Polymeropoulos, J.Appl.Phys., 48 (1977) 2404.
(21) E.P.Honig, Thin Solid Films, 33 (1976) 231.
(22) A.Leger, J.Klein, M.Belin and D.Defourneau, ibid., 8 (1971) R51.
(23) M.A.Careem and R.M.Hill, ibid., 51 (1978)363.
(24) G.G.Roberts, P.C.Vincett and W.A.Barlow, J.Phys.C.,11 (1978)2077.
(25) F.J.Kampas and M.Gouterman, Chem.Phys. Letts., 48(1977) 233.
(26) M.H.Nathoo and A.K.Jonscher, J.Phys.C., 4 (1971)L301.
(27) A.K.Jonscher and M.H.Nathoo, Thin Solid Films, 12 (1972)S15.
(28) M. Sugi, K.Nembach, D.Mobius and H.Kuhn, Solid State Commun., 13 (1973) 603.
(29) M.Sugi, T.Fukui and S.Iizima, Appl.Phys.Letts., 27 (1975)559; 28 (1976) 240.
(30) M.Sugi, T.Fukui and S.Iizima, Chem.Phys.Letts.,45 (1977) 163.
(31) S.Iizima and M.Sugi, Appl.Phys.Letts.,28 (1976) 548.
(32) M.Sugi, T.Fukui, and S.Iizima, Phys.Rev.B., 18 (1978)725.
(33) M.Sugi and S.Iizima, Appl.Phys.Letts, 34 (1979)290.
(34) M.Sugi and S.Iizima, Phys.Rev.B., 15 (1977) 574.
(35) M.Sugi, K. Nembach, D.Möbius and H.Kuhn, Solid State Commun., 15 (1974) 1864.
(36) M.A. Careem and A.K.Jonscher, Philos.Mag., 35 (1977)1489.
(37) M.A. Careem, A.K.Jonscher and F.Taiedy, Philos.Mag., 35(1977)1503.
(38) A.K. Jonscher and M.A.Careem, Phys.Letts., A., 55 (1975) 257.
(39) A.K. Jonscher, F.Meca and H.M.Millany, J.Phys.C., 12 (1979)L293.
(40) A.K.Jonscher and F.Taiedy, J.Phys.C., 8(1975) L107.
(41) A.K.Jonscher and S.Buddhabadana, Solid State Electron., 21 (1978)991.
(42) M.H. Nathoo, Thin Solid Films, 16 (1973)215.
(43) T.M. Ginnai, D.P.Oxley and R.G.Pritchard,ibid., 68(1980) 241.
(44) K.H.Gundlach and J.Kadlec, Chem.Phys.Letts.,25 (1974)293.
(45) M.Sugi, T.Fukui and S.Iizima, Mol.Cryst.Liq.Cryst., 50(1979)183.

CHAPTER 2

(1) R.M.Eisberg, Fundamentals of Modern Physics, Wiley,N.Y.(1961).
(2) C.B.Duke, Tunnelling in Solids (1969), Solid State Physics - Advances in Research and Applications (10),Academic Press,N.Y.
(3) T.J.Coutts, Electrical Conduction in Thin Metal Films, Elsevier, Amsterdam (1974).
(4) N.F.Mott, Elements of Wave Mechanics,Cambridge Univ.Press,Camb.(1952).
(5) J.Frenkel, Phys.Rev., 36 (1930) 1604.
(6) A. Sommerfield and H.Bethe, Handbuch der Physik,Eds.H.Gieger and K.Schell (Julius Springer-Verlag,Berlin,1933)Vol.24/2,p.450.
(7) R.Holm, J.Appl.Phys., 22 (1951) 569.
(8) J.G.Simmons, ibid., 34 (1963) 1793.
(9) J.G.Simmons, ibid., 34 (1963) 2581.
(10) J.G.Simmons, ibid., 35 (1964) 2655.
(11) J.G.Simmons, Trans.AIME, 233 (1965) 485.
(12) C.K.Chow, J.Appl.Phys., 34 (1963) 2490,2599, 2918;36(1965)559.
(13) E.L.Murphy and R.H.Good, Phys.Rev., 102 (1956)1464.
(14) R.Stratton, J.Phys.Chem.Solids, 23 (1962)1177.
(15) D.R.Lamb, Electrical conduction mechanisms in thin insulating films, Methuen,London(1967).
(16) R.Fowler and L.Nordheim, Proc.Roy.Soc.,A119 (1928)173.
(17) T.E.Hartman, J.Appl.Phys., 35 (1964) 3283.
(18) I.Giaver and K.Megerle, Phys.Rev., 122 (1961)1101.
(19) J. Bardeen, L.N.Cooper and J.R.Schrieffer,ibid., 108 (1957)1175.
(20) W.L.McMillan and J.M.Rowell, Superconductivity, Ed.R.D.Parks, Ch.2.,Marcel Dekker,N.Y.(1969).
(21) R.Holm and B.Kirschtein, Z.Tech.Phys., 16 (1935) 488.
(22) J.G. Simmons, J.Appl.Phys., 35 (1964) 2472.
(23) D.V.Geppert, ibid., 33 (1962) 10; 34 (1963) 3.
(24) E.Pitteli, Solid State Electronics,6 (1963) 667.
(25) J.C.Penley, J.Appl.Phys., 33 (1962) 1901;Phys.Rev.,128(1963)596.
(26) F.W.Schmidlin, ibid., 37(1966) 2823.
(27) J.G.Simmons, Brit.J.Appl.Phys., 18 (1967)269.
(28) L.Y.L.Shen and J.M.Rowell, Phys.Rev., 165 (1968) 566.
(29) R.C.Jaklevic and J.Lambe, Phys.Rev.Letts.,17 (1966)1133.
(30) R.G.Keil, T.P.Graham and K.R.Roenker,Appl.Spectroscopy,30(1976)1.
(31) P.K.Hansma, Phys.Rep., 30C (1977)45.
(32) D.J.Scalapino and S.M.Marcus,Phys.Rev.Letts,18 (1967) 459.
(33) J.Lambe and R.C.Jaklevic,Phys.Rev., 165 (1968) 821.
(34) J.Kirtley,D.J.Scalapino and P.K.Hansma,Phys.Rev.B.,14(1976)3177.
(35) A.D.Brailsford and L.C.Davis, ibid., 2 (1970)1714.
(36) R.J.Jennings and J.R.Merril, J.Phys.Chem.Solids,33 (1972)1261.
(37) J.G.Simmons in Handbook of Thin Film Technology,Eds.L.I.Maissel and L.Glang, McGraw-Hill, N.Y.(1970)Ch.14.
(38) M.A.Careem and R.M.Hill, Thin Solid Films, 51 (1978)363.

CHAPTER 3

(1) I.Langmuir, Trans.Faraday Soc., 15 (1920) 62.
(2) K.B.Blodgett, J.Am.Chem.Soc., 56 (1934) 495.
(3) K.B.Blodgett, ibid., 57 (1935) 1007.
(4) J.Mingins and J.A.G.Taylor, A manual for the measurement of Interfacial Tension, Pressure and Potential at air or non-polar oil/water Interfaces, Unilever Research,(1974)unpublished.
(5) H.Braddick, The Physics of Experimental Method , Chapman and Hall, London (1963).
(6) G.L.Gaines Jnr., Insoluble Monolayers at Liquid-Gas Interfaces, Wiley Interscience, N.Y.(1966).
(7) H.Kuhn, D.Möbius and H.Bücher in Techniques of Organic Chemistry, Eds.A.Weissberger and B.W.Rossiter,Vol I/Part III B,Wiley, N.Y.(1972).

Chapter 3 Cont'd

(8) I.Langmuir and V.J.Schaefer, J.Am.Chem.Soc., 59 (1937) 2400.

(9) A.Müller, Proc.Roy.Soc., London, 114A (1927) 542.

(10) M.A.Careem, Ph.D.Thesis, University of London (1976), unpublished.

(11) B.Davdani, Ph.D.Thesis, Leicester Polytechnic (1978), unpublished.

(12) M.H.Nathoo, Thin Solid Films, 16 (1973) 215.

(13) G.G.Roberts, P.C.Vincett and W.A.Barlow, J.Phys.C., 11 (1978) 2077.

(14) N.Gerschfield in Techniques of Surface and Colloid Chemistry and Physics, Eds. Good, Stromberg and Patrick, Marcel-Dekker, N.Y. (1972).

(15) N.K.Adam, The Physics and Chemistry of Surfaces, Oxford Univ.Press (1941).

(16) K.B.Blodgett and I.Langmuir, Phys.Rev., 51 (1937) 964.

(17) T.D.Clark, Mullard Res.Labs., Rep.No.512 (1964), unpublished.

(18) M.W.Charles, J.App.Phys., 42 (1971) 3329.

(19) E.P.Honig, J.Colloid and Int.Sci., 43 (1973) 65.

(20) H.Hasmonay, M.Vincent and M.Dupeyrat, Thin Solid Films, 68 (1980) 21.

(21) B.Mann and H.Kuhn, J.Appl.Phys., 42 (1971) 4398.

CHAPTER 4

(1) B.Mann and H.Kuhn, J.Appl.Phys., 42 (1971) 4398.

(2) M.H.Nathoo, Thin Solid Films, 16 (1973) 215.

(3) B.D.Wallace, Electron Des., 14 (1974) 110.

(4) G. G.Roberts, P.C.Vincett and W.A.Barlow, J.Phys.C., 11 (1978) 2077.

(5) R.G.Keil, T.P.Graham and K.R.Roenker, Appl.Spectroscopy, 30 (1976) 1.

(6) A.F.Hebard and P.W.Schumate, Rev.Sci.Ins., 45 (1974) 529.

(7) J.Klein, A.Léger, M. Belin, D.Defourneau and M.J.L.Sangster, Phys.Rev.B., 7 (1973) 2336.

(8) J.Kirtley, J.Am.Chem.Soc., 80 (1980) 217.

(9) D.P.Oxley, A.J.Bowles, C.C.Horley, A.J.Langley, R.G.Pritchard and D.L.Tunnicliffe, Surface Interface Anal., 2 (1980) 31.

(10) J.Lambe and R.C.Jaklevic, Phys.Rev., 165 (1968) 821.

(11) I.W.N.McMorris, N.M.D.Brown and D.J.Walmsley, J.Chem.Phys., 66 (1977) 3952.

CHAPTER 5

(1) A. Müller, Proc.Roy.Soc.,London, 114A (1972) 542.

(2) H.H.Race and S.I.Reynolds, J.Am.Chem.Soc., 61 (1939) 1425.

(3) J.C.Fisher and I.Giaver, J.Appl.Phys., 32 (1961) 172.

(4) R.P.Madden, L.R.Canfield and G.Hass, J.Opt.Soc.Am., 53 (1963) 620.

(5) B.Mann and H.Kuhn, J.Appl.Phys., 42 (1971) 4398.

(6) R.M.Handy and L.C.Scala, J. Electrochem.Soc., 113 (1966) 109.

(7) R.M.Hill, Philos.Mag., 23 (1971) 59 ; Thin Solid Films, 7 (1971) R57.

(8) R.Stratton, J.Phys.Chem.Solids, 23 (1962) 1177.

(9) B.Mann, H.Kuhn and L.V.Szentpaly, Chem.Phys.Letts., 8 (1971) 82.

(10) K.H.Gundlach and J.Kadlec, ibid, 25 (1974) 293.

(11) G.G.Roberts, P.C.Vincett and W.A.Barlow, J.Phys., C, 11 (1978) 2077.

(12) E.E. Polymeropoulos, J.Appl.Physics, 48 (1977) 2404.

(13) A. Leger, J.Klein, M. Belin and D.Defourneau,Thin Solid Films, 8 (1971) R51.

(14) M.A.Careem and R.M.Hill, ibid., 51 (1978) 363.

(15) F.J.Kampas and M.Gouterman, Chem.Phys.Letts., 48 (1977) 233.

(16) T.E.Hartman, J.Appl.Phys., 35 (1964) 3283.

(17) T.E.Hartman and J.S.Chivian, Phys.Rev., 134 (1964) A1094.

(18) K.H.Gundlach and J.Holzl, Surface Sci., 27 (1971) 125.

(19) K.H.Gundlach in Advances in Solid State Physics, Vol.11, Ed. O. Madelung, Pergamon, Oxford (1971) p 237.

(20) L.Y.L.Shen and J.M.Powell, Phys.Rev., 165 (1968) 566.

(21) K.H.Gundlach and J.Antula, Thin Solid Films, 11 (1972) 401.

Chapter 5 Cont'd

(22) S.R.Pollack and C.E.Morris, J.Appl.Phys., 35 (1964) 1503.

(23) J. Furtlehner and J.Messier, Thin Solid Films, 68 (1980) 233.

(24) S.R.Pollack and C.E.Morris, Trans.Met.Soc.AIME, 233 (1965) 497.

(25) C.B.Duke, Tunnelling in Solids (1969) Solid State Physics - Advances in Research and Applications (10).

(26) S. Horiuchi, J.Yamaguchi and K.Naito, J.Electrochem.Soc.,115 (1968) 634.

(27) I. Giaver and K.Megerle, Phys.Rev., 122 (1961) 1101.

(28) T.D.Clark, Mullard Res.Labs., Rep.No.512 (1964), unpublished.

(29) P.K.Hansma, Phys.Rep., 30c (1977) 45.

(30) R.G.Keil, T.P.Graham and K.R.Roenker, Appl.Spectroscopy, 30 (1976) 1.

(31) L.J.Bellamy, The Infrared Spectra of Complex Molecules, Chapman and Hall,London, (1975).

(32) J.T.Hall and P.K.Hansma, Surf.Sci., 76 (1978) 61.

(33) Y.Skarlatos, R.C.Barker and A.Yelon,J.Appl.Phys., 47 (1976) 4593.

(34) E.Harari and B.S.H.Royce, Appl.Phys.Letts.,22 (1973) 106.

(35) S.K.Gupta, C.M.Singal and V.K.Srivastava,J.Appl.Phys., 48 (1977)2583.

(36) C.M.Singal, S.K.Gupta, A.K.Kapil and V.K.Srivastava, ibid., 49 (1978) 3402.

(37) E.P.Honig, Thin Solid Films, 33 (1976) 231.

(38) J.Tanguy, ibid., 13 (1972) 33.

(39) P.C.Vincett and G.G.Roberts, Thin Solid Films, 68 (1980) 135.

(40) R.H.Tredgold and C.S.Winter, J.Phys.D:Appl.Phys., 14 (1981) L185.

CHAPTER 6

(1) S.Horiuchi, M.Yamaguchi and K.Naito, J.Electrochem.Soc., 115 (1968) 634.

(2) R.M.Handy and L.C.Scala, ibid., 113 (1966) 109.

(3) M.H.Nathoo, Thin Solid Films, 16 (1973) 215.

(4) M.A.Careem and R.M.Hill, ibid., 51 (1978) 363.

(5) E.P.Honig, ibid., 33 (1976) 231.

(6) G.G.Roberts, P.C.Vincett and W.A.Barlow, J.Phys.C, 11 (1978)2077.

(7) S.R.Pollack, J.Appl.Phys., 34 (1963) 877.

(8) H.H.Race and S.I.Reynolds, J.Am.Chem.Soc., 61 (1939) 1425.

CHAPTER 7

(1) C.J.Powell, Surf.Sci., 44 (1974) 29.

(2) J.M.Walls in Methods of Surface Analysis, Loughborough University (1981), unpublished.

(3) A.B.Christie, ibid., unpublished.

(4) P. Cadman, G.Gossedge and J.D.Scott, J.Electron.Spect.,13 (1978)1.

(5) D.T.Clark and H.R.Thomas, J.Polym.Sci.Chem.Ed., 15 (1977)2843.

(6) M.P.Seah and W.A.Dench, Surface and Interface Anal., 1 (1979) 2.

(7) C.R.Brundle, H.Hopster and J.D.Swalen, J.Chem.Phys.,70 (1979)5190.

(8) T.M.Ginnai, R.E.Thurstans and D.P.Oxley, Vide Couches minces (1980) ; 201 (Suppl). Proc.Int.Vac.Congrs., p.435.

(9) S.M.Hall, J.D.Andrade, S.M.Ma and R.N.King, J.Electron Spect. Related Phenom., 17 (1979) 181.

(10) G.L.Gaines, Jnr., and A.W.Roberts, Nature, 197 (1963) 787.

(11) T.Ohnishi, A.Ishitani, H.Ishida, N.Yamamoto and H.Tsubomura, J.Phys. Chem., 18 (1978) 1989.

(12) R.G.Keil, T.P.Graham and K.R.Roenker,Appl.Spectroscopy,30(1976)1.

Chapter 7 Cont'd

(13) J.T.Hall and P.K.Hansma, Surf.Sci., 76 (1978) 61.

(14) L.J.Bellamy, *The Infrared Spectra of Complex Molecules* Chapman and Hall, London, (1975).

(15) A. Barraud, C.Rosilio and A. Ruaudel-Teixier,Thin Solid Films 68 (1980) 7.

(16) G.L.Gaines Jnr., *Insoluble Monolayer at Liquid-Gas Interfaces* , Wiley Interscience, N.Y.(1966).

(17) I.Langmuir, Trans.Faraday Soc., 15 (1920) 62; K.B.Blodgett, J.Am.Chem.Soc., 56 (1934) 495; 57 (1935) 1007.

(18) C.Holley and S.Bernstein, Phys.Rev., 52 (1937) 525.

(19) I.Fanteuchen, Phys.Rev., 53 (1938) 909.

(20) H.Hasmonay, M.Vincent and M. Dupeyrat, Thin Solid Films,68(1980)21.

(21) G.L.Gaines, Jnr., Nature, 186 (1960) 384.

(22) M.W.Charles, J.Appl.Phys., 42 (1971) 3329.

(23) E.P. Honig, J.Colloid and Interface Sci., 43 (1973) 65.

CHAPTER 8

(1) B.Mann and H.Kuhn, J.Appl.Phys., 42 (1971) 4398.

(2) A.Leger, J.Klein, M.Belin and D.Defourneau,Thin Solid Films, 8 (1971) R51.

(3) T.D.Clark, Mullard Res.Labs., Rep.No.512 (1964), unpublished.

(4) S.M.Hall, J.D.Andrade, S.M.Ma and R.N.King, J.Electron.Spect. Related Phenom., 17 (1979) 181.

(5) C.R. Brundle, H.Hopster and J.D.Swalen J.Chem.Phys., 70(1979)5190.

(6) P.S.Vincett and G.G.Roberts, Thin Solid Films, 68 (1980) 135.

(7) C.A.Mead, J.Appl.Phys., 32 (1961) 646; Proc.IRE, 48 (1960) 359.

(8) K.H.Gundlach and J.Kadlec, Phys.Status Solidi (a), 10 (1972)371.

(9) K.H.Gundlach and J.Kadlec, Thin Solid Films, 13 (1972) 225.

(10) J.G.Simmons and R.R.Verderber, Radio and Electron.Eng., 35(1968)265.

(11) I.M.Dharmadasa, G.G.Roberts and M.C.Petty, Electron.Letts., 16 (1980)201.

(12) J.B.Batey, G.G.Roberts and M.C.Petty, to be published in Thin Solid Films.

(13) G.G.Roberts, K.P.Pande and W.A.Barlow, Electron.Lett., 13(1977)581.

(14) G.G.Roberts, K.P.Pande and W.A.Barlow, Solid St. and Elect. Devices, 2 (1978) 169.

(15) R.W.Sykes, Ph.D.Thesis, University of Durham (1980), unpublished.

(16) G.G.Roberts, P.S.Vincett and W.A.Barlow, Phys.Technol.,12(1981)69.

APPENDIX 1

PROGRAM LISTINGS

```
100 PRINT"BEST SINH FIT"
200 DIM C(100),V(100),J(100)
300 PRINT"HOW MANY EXPL PTS"
400 INPUT N
500 LET N1=N-1
550 PRINT"EXPL CURRENT AND VOLTAGE"
600 FOR I=1 TO N
800 INPUT C(I),V(I)
900 NEXT I
1000 LET S1=0
1100 LET S2=0
1300 FOR I=2 TO N1
1400 LET H=V(I+1)-V(I)
1500 LET K=V(I)-V(I-1)
1700 LET P=2*(K*C(I+1)-(K+H)*C(I)+H*C(I-1))/(H*K*(H+K))
1800 S1=S1+P*C(I)
1900 S2=S2+C(I)*C(I)
2000 NEXT I
2100 A=SQR(S1/S2)
2200 LET S1=0
2300 LET S2=0
2400 FOR I=2 TO N1
2500 LET X=A*V(I)
2600 LET S3=(EXP(X)-EXP(-X))/2
2700 S1=S1+C(I)*S3
2800 S2=S2+S3*S3
2850 PRINT S1,S2
2900 NEXT I
3000 B=S1/S2
3050 OPEN1,4
3100 PRINT#1,"THE CONSTANTS IN I=BSINH(AV) ARE"
3200 PRINT#1,"A=  ";A
3300 PRINT#1,"B=  ";    B
3400 PRINT"WHAT STARTING VALUE FOR A"
3500 INPUT A1
3600 PRINT"WHAT INCREMENTS IN A DO YOU WANT"
3700 INPUT A3
3800 LET A2=A1+5*A3
3900 PRINT"WHAT VALUE FOR K"
4000 INPUT K
4100 FOR A=A1 TO A2 STEP A3
4200 LET S1=0
4300 LET S2=0
4400 LET S3=0
4500 LET S4=0
4600 LET S5=0
4700 FOR I=1 TO N
4800 X=EXP(-A*V(I)*V(I)/K)
4801 Y=(EXP(A*V(I))-EXP(-A*V(I)))/2
4802 J(I)=X*Y
4900 S1=S1+C(I)*J(I)
5000 S2=S2+J(I)
```

```
 5100 S3=S3+C(I)
 5200 S4=S4+J(I)*J(I)
 5300 S5=S5+C(I)*C(I)
 5400 NEXT I
 5500 D=(S1-(S2*S3)/N)/(S4-(S2*S2)/N)
 5600 D1=SQR((S4-(S2*S2/N))/(N-1))
 5700 D2=SQR((S5-(S3*S3/N))/(N-1))
 5800 R=D*D1/D2
 5850 PRINT#1,"CORR COEF IS   ";R
 5900 PRINT#1,"PRE EXP FACTOR IS   ";D
 6100 PRINT#1,"K=   ";K
 6200 PRINT#1,"A=   ";A
 6300 PRINT#1,"VOLTS ;I(EXPT);I(CALC);DEV"
 6400 LET S1=0
 6500 FOR I=1 TO N
 6550 T=D*J(I)
 6600 Z=T-C(I)
 6700 S1=S1+(Z*Z)
 6800 PRINT#1, V(I)   ;C(I)   ;T     ;Z
 6900 NEXT I
 7000 PRINT#1,"SUM SQRS OF CURRENT DEV= ";S1
 7100 NEXT A
 7200 PRINT"ANOTHER K? IF YES PUT 0;IF NO 1"
 7300 INPUT F
 7400 IF F=0 THEN 3900
 7500 PRINT"OTHER VALUES OF A? IF YES PUT 0"
 7600 INPUT G
 7700 IF G=0 THEN 3400
 7800 END
READY.
```

DERIVATIVE

```
READY.

 1 OPEN1,4
 5 DIM V(50),C(50)
 7 PRINT"▨"
 10 PRINT"HOW MANY POINTS ";:INPUT N
 20 PRINT"ENTER PAIRS OF V AND C"
 30 FOR I=1 TO N
 40 INPUT V(I),C(I):NEXT I
 45 FORI=1TON:PRINT#1,"V= "V(I)"  C= "C(I):NEXTI:PRINT#1
 50 FOR I=1 TO N-1
 60 DG=(C(I+1)-C(I))/(V(I+1)-V(I))
 70 DR=1/DG
 80 LC=2*DG/(C(I)+C(I+1))
 90 V1=(V(I)+V(I+1))/2
 100 PRINT#1,"V="V1"DYN G="DG"DYN R="DR"LC="LC
 110 NEXT I
 120 PRINT"REPEAT OUTPUT ";:INPUT Z
 130 IF Z=1 GOTO 50
 135 CLOSE1
 140 END
READY.
```

```
READY.

 5 OPEN1,4
 10 DIM T(50),J(50)
 30 PRINT"HOW MANY PAIRS OF DATA ":INPUT N
 40 PRINT"INPUT T AND J"
 50 FOR I=1 TO N
 60 INPUT T(I),J(I)
 70 NEXT I
 75 PRINT"INPUT J0 ";:INPUT J0
 76 PRINT#1,"J0 = ";J0
 80 A=0
 90 FOR I=1 TO N
 100 A1=6*(J(I)-J0)/(J(I)*T(I)*T(I))
 110 A1=SQR(A1)
 120 A=A+A1
 130 NEXT I
 140 A=A/N
 150 PRINT#1,"APPROX VAL OF A IS "A
 160 PRINT"INPUT LIMITS FOR A"
 170 INPUT AL,AU
 175 PRINT#1,"LIMITS OF A "AL" TO "AU
 180 PRINT"INPUT INCREMENT"
 190 INPUT AI
 200 E1=1E30
 210 FOR A3=AL TO AU STEP AI
 220 ER=0
 230 FOR I=1 TO N
 240 JC=J0*A3*T(I)/SIN(A3*T(I))
 250 ER=ER+(JC-J(I))*(JC-J(I))
 260 NEXT I
 270 PRINT#1,"A= "A3" SQ ERROR= "ER
 280 IF ER>E1 GOTO 300
 290 E1=ER:A=A3
 300 NEXT A3
 305 PRINT#1,"BEST VAL OF A IS "A
 310 PRINT"REPEAT WITH OTHER A'S";:INPUT Z
 320 IF Z=1 GOTO 160
 330 PRINT"REPEAT WITH ANOTHER J0";:INPUT Z
 340 IF Z=1 GOTO 75
 345 K=1.602E-19*A/(3.142*1.38E-23)
 350 PRINT#1,"K (BEST)= "K" J0 (BEST)= "J0
 360 PRINT#1,"    T             J(EXP)       J(CALC)"
 370 FOR I=1 TO N
 380 JC=J0*A*T(I)/SIN(A*T(I))
 390 PRINT#1,T(I),J(I),JC
 400 NEXT I
 410 CLOSE1
 420 END
READY.
```